

THE UNIVERSITY OF SYDNEY

DOCTORAL THESIS

Measurement of spontaneous parametric downconversion in atomically thick semiconductors

Author:

Loris MARINI

Supervisors:

Ass. Prof. Stefano PALOMBA
Prof. Benjamin J. EGGLETON

*A thesis submitted in fulfillment of the requirements
for the degree of Doctor of Philosophy*

in the

ARC Centre for Ultrahigh bandwidth Devices for Optical Systems (CUDOS)
School of Physics

February 26, 2019

Declaration of Authorship

I, Loris MARINI, declare that this thesis titled, "Measurement of spontaneous parametric downconversion in atomically thick semiconductors" and the work presented in it are my own. I confirm that:

- This work was done wholly or mainly while in candidature for a research degree at this University.
- Where any part of this thesis has previously been submitted for a degree or any other qualification at this University or any other institution, this has been clearly stated.
- Where I have consulted the published work of others, this is always clearly attributed.
- Where I have quoted from the work of others, the source is always given. With the exception of such quotations, this thesis is entirely my own work.
- I have acknowledged all main sources of help.
- Where the thesis is based on work done by myself jointly with others, I have made clear exactly what was done by others and what I have contributed myself.

Signed: Loris Marini

Date: 29/07/2018

“Nothing worth having comes easy” - Theodore Roosevelt

The University of Sydney

Abstract

Faculty of Science
School of Physics

Doctor of Philosophy

**Measurement of spontaneous parametric downconversion in atomically thick
semiconductors**

by Loris MARINI

The promises of quantum computing is to enable faster and more powerful computation than would ever be possible with a classical processor based on binary logic. Quantum photonics is one of many promising platforms for quantum computing, where information is encoded in the states of many photons, and processing results by their evolution through networks of quantum logical gates. The weak interaction between light and matter promises strong resistance to decoherence, thus allowing optical states to be transferred over long distances. However, this also poses computation challenges, which ideally requires the interaction between photons to be deterministic. A solution to the second problem was presented in the year 2000 by Knill, Laflamme and Milburn, who demonstrated how linear optical elements could be used to build a universal quantum computers by leveraging *photon bunching*, a quantum mechanical phenomenon that occurs whenever two photons are indistinguishable.

A common technique to prepare such states is photon heralding, where one photon of an energy-time entangled pair (*herald*), reveals the presence of the other (*heraled*) with a precision limited only by the measuring apparatus, and many heralded (identical) photons are used to encode and process information. Photon pairs are typically generated from a second-order nonlinear interaction known as spontaneous parametric downconversion (SPDC), or from a less-efficient third-order interaction through the process of spontaneous four-wave mixing (SFWM). In all existing platforms, materials for SPDC play two roles: they provide the necessary optical nonlinearity to generate down-converted fluorescent light, while ensuring that the fundamental and the down-converted modes all propagate with the same group velocity (phase-matching). A limitation of this approach is that both the linear and nonlinear optical properties must be simultaneously engineered, often resulting in narrow-band and non-reconfigurable operation. 2D materials promise to change this, thanks to their high nonlinearity, inherent broadband phase-matching, and highly configurable electro-optical properties.

Although predicted in such thin crystals, to date SPDC has only been reported in structures with many millions of atoms, stimulating experimental efforts to validate its scaling laws in structures only a few atoms thick. In this thesis we investigate group IV transition-metal dichalcogenides (TMDCs), one of the most promising 2D materials for nonlinear optics, and describe efforts towards the experimental observation of non-resonant SPDC from a diffraction-limited area. Because of the intimate connection between the classical second-harmonic generation (SHG) and the quantum SPDC, the efficiency of one process provides insights on the other. This guides the design of single-photon coincidence measurements required to demonstrate the strong temporal correlations of these entangled states. Measurements are hindered by the presence of a broadband, temporally uncorrelated background, attributed to photoluminescence. This work improves the understanding of the nonlinear quantum optical potential of these crystals, and provides a performance benchmark for these ultra-thin materials.

Acknowledgements

What makes a PhD hard is not the shear volume of new notions that need to be absorbed, or the many deadlines to face, or the constant realization that there is always someone that knows more than you do. What makes it hard is to find the courage to dig into unexplored territories, draw energy from a constant sense of uncertainty, manage risks, and all of this while keeping a healthy level of self-criticism to fuel continuous improvement. Luckily for me, I had around some truly amazing people with whom I shared this journey.

The first person I would like to thank is my wife Elisa, which has been an endless source of energy and support (both emotional and financial). I remember drawing endless diagrams of photons bouncing everywhere, and enjoying your intuition filling the cracks of my poor artistic skills. These words extend naturally to my family, which despite not having had the opportunity to experience the Journey of a PhD, believed in my choice every step of the way.

My next huge thank you goes to Dr. Fernando Diaz for his sharp intuition and scientific mind, as well as for unsurpassed BBQ abilities, and Dr. Blair Morrison for being passionate about sharing knowledge, using open source software and just chill with a nice cold beer. I would like to thank Dr. Alessandro Tuniz, which despite having joined NPAL only recently, has contributed to make the lab an enjoyable environment, and Robin Champhausen for the many long nights together in front of endless LabVIEW code. I would like to extend my gratitude to all Sydney CUDOS post-docs, and in particular Dr. Andrea Blanco Redondo, Dr. Birgit Stiller and Dr. Alessio Stefani for the countless quality discussions, adventures and emotional support. Among collaborators I would like to acknowledge in particular Dr. Luke Helt and Ass. Prof. Yurei Liu for showing extra care and passion for the topic and always be willing to help. I would also like to show my gratitude to graduate and undergraduate students I supervised and mentored, for they contributed in all sorts of ways to sharp my leadership skills.

My PhD experience would have been dramatically different without the support of the OSA and SPIE, two fantastic optical societies which I had the pleasure to contribute to and be inspired by. In particular I have been honored to host Dr. Jean-luc Doumont in Sydney late 2017, and share his talent with more than 200 people thanks to the financial support of the OSA. Finally, I would like to thank my supervisors Prof. Stefano Palomba and Prof. Benjamin J. Eggleton for enforcing a spirit of cooperation throughout the center of excellence, and for showing me the importance of a collaborative research environment.

The only way to truly understand what a PhD degree means, is doing it.

Ringraziamenti

Ciò che rende difficile un dottorato non è la quantità di nuove nozioni che occorre assorbire, o le scadenze da affrontare, o la costante consapevolezza che c'è sempre qualcuno che ne sa più di te. Ciò che lo rende difficile è trovare il coraggio di avventurarsi in territori inesplorati, trarre energia da un costante senso di incertezza, minimizzare i rischi, e tutto ciò mantenendo un sano livello di autocritica per continuare a migliore sempre. Fortunatamente per me, ho avuto accanto persone fantastiche con le quali ho condiviso questo viaggio.

La prima che vorrei ringraziare è mia moglie Elisa, che è stata una fonte inesauribile di energia e sostegno (sia emotivo che finanziario). Ricordo di aver disegnato infiniti diagrammi di fotoni che rimbalzavano ovunque, e di godere della sua intuizione riempiendo le crepe delle mie povere capacità artistiche. Queste parole si estendono naturalmente alla mia famiglia, che pur non avendo avuto l'opportunità di vivere il viaggio di un dottorato di ricerca, ha creduto nella mia scelta in ogni fase del percorso.

Il mio prossimo grande ringraziamento va al dott. Fernando Diaz per la sua intuizione e dedizione per la scienza, così come per le sue insuperabili doti culinarie, ed al dott. Blair Morrison per la sua insaziabile voglia di conoscenza, la sua passione per il software libero, e per le tante birre bevute insieme. Vorrei anche ringraziare il dott. Alessandro Tuniz, per aver contribuito a rendere il laboratorio un ambiente piacevole, e Robin Champhausen per le molte lunghe notti insieme davanti al codice LabVIEW. Vorrei estendere la mia gratitudine a tutti i post-doc di Sydney CUDOS, in particolare la dott.ssa Andrea Blanco Redondo, la dott.ssa Birgit Stiller e il dott. Alessio Stefanì per gli innumerevoli approfondimenti scientifici, e tanti avventurosi fine-settimana. Tra i collaboratori, vorrei ringraziare in particolare il professore associato Yurei Liu per le sue conoscenze in ambito di fabricazione, e il dott. Luke Helt senza il quale le fondamenta teoriche di questa tesi sarebbero state molto meno solide. Vorrei anche mostrare la mia gratitudine agli studenti universitari e laureandi che ho supervisionato, perché hanno contribuito in molti modi a migliorare le mie capacità di leadership.

La mia esperienza di dottorato sarebbe stata drammaticamente diversa senza il supporto della OSA e SPIE, due fantastiche organizzazioni alle quali ho avuto il piacere di contribuire e dalle quali ho tratto ispirazione. In particolare, sono stato onorato di aver ospitato il dott. Jean-luc Doumont a Sydney alla fine del 2017, per condividere il suo talento con oltre 200 persone grazie al sostegno finanziario dell'OSA, ed all'aiuto organizzativo di CUDOS. Infine, vorrei ringraziare i miei supervisori, il professore associato Stefano Palomba e il professore Benjamin J. Eggleton, per aver rafforzato lo spirito di cooperazione in tutto il centro di eccellenza, e per avermi permesso di percepire l'importanza di un ambiente di ricerca collaborativo.

L'unico modo per capire veramente cosa è un dottorato, è farlo.

Contents

Declaration of Authorship	iii
Abstract	viii
Acknowledgements	ix
Author Contributions	1
1 Introduction	3
1.1 Thesis Outline	5
2 Background	9
2.1 Nonlinear optics and SHG	11
2.1.1 Origin of the Second Harmonic Generation	13
2.1.2 SHG Efficiency	14
2.2 Quantum Optics, Entanglement and SPDC	17
2.2.1 Quantum interference	17
2.2.2 Coherence of light	18
2.2.3 Entanglement and its applications	19
2.2.4 Generation of entanglement	20
2.2.5 Spontaneous Parametric Downconversion	21
2.2.6 Efficiency of SPDC	23
2.3 Transition-metal Dichalcogenides	25
2.3.1 Electronic Properties of monolayer TMDC	26
2.3.2 Fabrication and characterization	28
2.4 SHG in TMDC	29
2.4.1 Reported second-order nonlinearity of WSe ₂ and MoS ₂	30
2.4.2 Efficiency of SHG in 2D TMDC	32
2.5 SPDC in 2D materials	33
2.5.1 SPDC in WSe ₂ and MoS ₂	34
2.6 Quantum Classical Correspondence in TMDC	36
3 Experimental Methods	39
3.1 Optical Table Overview	40
3.1.1 Femtosecond laser sources	40
3.1.2 Power and Polarization control	42
3.1.3 Beam size and divergence	43
3.1.4 Pump-probe synchronization and Autocorrelation	43
3.1.5 Integrated SPDC source	46
3.1.6 Illumination and Collection	47
3.1.7 Imaging and Spectroscopy	49

3.1.8 Fourier imaging	50
3.1.9 Single-Photon Detection	54
3.1.10 Time-correlated single-photon spectrometer	56
3.1.11 Other laser sources	57
3.2 Visible and NIR CCDs	57
3.3 Visible and NIR SPADs	60
3.4 Control of the illumination angle	62
3.4.1 Limitations and other techniques	64
3.5 Lasers and objectives: alignment and control	65
3.6 Measurement of the Second-order Coherence of Light	67
3.7 Photon coincidences with detection gating	69
3.8 Design and testing of a single-photon confocal imaging	72
3.8.1 Confocal factor and aperture size	74
4 Results	77
4.1 Breakdown Flashing in InGaAs Single-photon detectors	79
4.1.1 Temporal Characterization	80
4.1.2 Spectral Characterization	82
4.2 CAR in the measurement of photon simultaneity	85
4.2.1 Sources of accidental coincidences	85
4.2.2 Dark-count-limited CAR	87
4.2.3 Background-limited CAR	88
4.2.4 Types of loss and their effect	90
4.3 Simulations of loss and CAR in free-space SPDC	92
4.3.1 Model for the collection loss	92
4.3.2 Numerical Implementation	94
4.4 Measurement of femtosecond pulses: NanoFROG	95
4.5 SPDC from mono-layer WSe ₂	97
4.5.1 SHG in mono-layer WSe ₂	98
4.5.2 Brightness of SPDC from mono-layer WSe ₂	100
4.5.3 Simulated radiation pattern and collection loss	101
4.5.4 Dark-count-limited CAR for 1L-WSe ₂	103
4.5.5 Measured Coincidences from 1L WSe ₂	103
4.6 SPDC from multilayer MoS ₂	106
4.6.1 Material Choice	106
4.6.2 SHG Spectroscopy in 5L MoS ₂	107
4.6.3 Brightness of SPDC in 5L MoS ₂	108
4.6.4 Measured Coincidences from 5L MoS ₂	109
4.6.5 Background Characterization	111
4.6.6 Detection gating in 5L MoS ₂	113
4.7 Discussion	114
5 Conclusions	117
5.1 Outlook	119
Bibliography	121
Glossary	133

To my Family.

Author Contributions

Publications included in this Thesis

L. Marini, et al., "Deterministic filtering of breakdown flashing at telecom wavelengths", Appl. Phys. Lett. 111, 213501 (2017).

L. Marini, et al., "Constraints on downconversion in atomically thick films", J.Opt. Soc. Am. B 35, 672 (2018).

L. Marini, et al., "Spontaneous emission limits the observation of SPDC in atomically thick films", (In preparation for submission).

Not included in this Thesis

L. Marini, R. Camphausen et al., "Near-infrared sub-poissonian emission from lattice defects in hexagonal boron nitride HbN", (In preparation for submission).

Conference Posters and Presentations

L. Marini, et al., "Breakdown flashing at telecom wavelengths in InGaAs single-photon detectors", Australian Conference on Optical Fibre Technology, ACOFT (2016) - Presentation

L. Marini, et al., "Deterministic filtering of breakdown flashing at telecom wavelengths" Conference on Optics, Atoms, and Laser Applications, KOALA (2015) - Presentation

L. Marini, et al., "Stimulated Emission Tomography in Plasmonic Media" OSA Siegman International School on Lasers, ICFO (2016) - Poster

L. Marini, et al., "Time-correlatd single-photon monochromator for spectral measurements of ultra-weak optical signals" Topical Workshop on Quantum Optics, The University of Sydney (2017) - Poster

L. Marini, et al., "Constraints on downconversion in atomically thick films" Institute of Photonics and Optical Science, The University of Sydney (2017) - Poster

L. Marini, et al., "Spontaneous emission limits the observation of SPDC in atomically thick films" 24th Central European Workshop on Quantum Optics, DTU Denmark (2017) - Poster

Chapter 1

Introduction

In the past 60 years we have witnessed an unprecedented progress in the development of transistor-based information processing devices. Although implementations can vary substantially, information is typically encoded in a binary alphabet, and processing occurs through a large collection of nodes, whose binary states are deterministically controlled. For quite some time, the performance of these devices was limited by the density of transistors available in a chip. This spurred a large number of technological improvements, that led to the fabrication of active elements with a gap between source and drain as small as 5 nm, reaching a fundamental limit. This has encouraged developments in parallel architectures for computation, where distributed clusters of processing units are coordinated to increase the total computational power. However, the overall scaling of such distributed systems is at best linear with the number of processing nodes, and practically introduces a number of challenges and overheads. This has stimulated research into alternative ways to process information.

Based on quantum superposition and quantum entanglement, quantum computing promises to encode and process information in a radically different fashion, by harnessing quantum states of electrons, photons, ions or superconducting circuits. The approach differs from any classical architecture primarily in the way information is encoded. While the state of a classical system with n bits can be fully described with n binary values, by virtue of quantum superposition, n quantum bits (qubits) can simultaneously be in all combinations of the n states, requiring 2^n complex values to be fully represented. This exponential difference is at the heart of the potential of quantum computation and is what motivates most of the research in this field.

In particular, quantum computers based on photonics could play a key role in this race. Since the interaction between photons and matter is weak, their quantum state can be maintained over long distances at room temperature, a property that is necessary to take advantage of the extensive optical network already in place. In addition, photons seldom interact with each other, a fundamental property that allows to achieve extraordinary information densities necessary to power the back-bone of the modern Internet. High information densities to be carried through fibers, An exception to this, are indistinguishable (or quantum-mechanically identical) photons which interact deterministically in a process known as quantum interference, thus allowing to perform all-optical linear quantum computing at scale.

However, optical quantum information processing requires many dozens of such identical photons, which presents many challenges. The most promising techniques are either based on engineering the relaxation of a single electron in a quantum well (quantum dots), or by leveraging spontaneous nonlinear processes. The former generate more photons per unit of time (high brightness) with near unity conversion

efficiencies, while the latter have a much higher indistinguishability which is essential to perform quantum-interference with a large number of photons. In this thesis we focus on the second approach, and in particular on spontaneous parametric downconversion (SPDC). This is a second-order nonlinear optical phenomenon, where the energy of a single photon (input) is probabilistically converted into a pair of energy-time entangles photons (output).

Conventionally, the material used for SPDC in bulk crystals and integrated photonic chips plays two roles: it provides the necessary optical nonlinearity, while ensuring that the all optical modes propagate with the same group velocity so that they can interact over large distances (phase-matching). A direct limitation of this approach, is that both the linear and nonlinear optical properties of the medium must be simultaneously engineered, often resulting in narrow-band and non-reconfigurable operation.

Thanks to their high nonlinearity and quantum-confined nature, two-dimensional materials could be useful for the generation of entangled photon pairs via spontaneous parametric downconversion. We are particularly interested in transition-metal dichalcogenides (TMDCs) for their record-high nonlinearity [1–7], and their tunable nonlinear and linear optical response by either layer engineering, mechanical strain [8–10] and electrostatic doping [11–13]. By enabling inherently broadband phase-matching, and possessing a highly configurable electro-optical properties, this class of materials can be stacked to form a heterostructure and embedded into linear waveguides or resonant optical cavities. This allows to separate the task of designing an appropriate light-guiding structure, from that of optimizing the linear and nonlinear response. However, spontaneous parametric downconversion to date has only been reported in structures where the interaction length spans over many millions of atoms, leaving unclear how the dynamics of the phenomenon change when the material extends over only a few atomic planes.

In this thesis, we present a systematic description of the constraints associated with the observation of such quantum-mechanical phenomenon in a diffraction-limited area of transition-metal dichalcogenides (TMDC) atomically-thick films. The material studied in the context of this thesis are monolayer WSe₂ and five layer MoS₂. The first samples were fabricated in the ACT node of the Australian National Fabrication Facility, by the group of Ass. Prof. Yuerui Lu, and where exfoliated from the bulk, while the second was synthesized with chemical vapor transfer (CVT) by Liu Sheng in the group of Professor Xiong Qihua at Nanyang Technological University section 2.3.2.

We first adapt established quantum-classical relations to calculate the efficiency of generation of photon-pairs from a calibrated measurement of second-harmonic generation (SHG). Results are then used to numerically calculate the probability of photon coincidences given the experimental setup. Both classical nonlinear measurements and single-photon coincidence measurements are performed on different types of TMDC in free-space thus taking full advantage of the broadband phase-matching. Coincidence measurements are dominated by the presence of a weak, broadband, temporally uncorrelated background, which we attribute to photoluminescence. A detailed account of all sources of noise is given, along with suggestions to improve the measurements. This work improves the understanding of the nonlinear quantum optical potential of these crystals, and provides a performance benchmark for these ultra-thin materials.

1.1 Thesis Outline

Background

The aim of this thesis is to report on measurements of energy-time entangled photon pairs via spontaneous parametric downconversion (SPDC) in two-dimensional materials. In order to ease the understanding of this body of research it is important to introduce the fields of nonlinear optics, quantum optics and two-dimensional materials. Since the common theme in this thesis is nonlinear optics, the first section of chapter 2 focuses on the nature of the nonlinear optical response of a material, and derive analytical expressions for its efficiency. This is particularly useful to understand and characterize SPDC, whose efficiency is intimately related to that of the classical, and relatively more efficient, nonlinear optical process of second-harmonic generation (SHG). The second priority in this chapter is to introduce the field of quantum optics, and explain quantum interference and give a high-level description of the phenomenon of quantum entanglement. This paves the way to introduce the non-classical process of SPDC, and its potential in the generation of energy-time entangled pairs of photons. These states present non-classical correlations and are thus a promising route for optical quantum information processing. We then introduce two-dimensional materials and motivate the interest in quantum-optics such extremely confined structures. We focus on the family of transition-metal dichalcogenides (TMDCs) and derive analytical expressions for the efficiency of nonlinear interactions in mono-layer WSe₂ and five-layer MoS₂ which are the subject of the experimental results presented in chapter 4. Finally, we consider SHG and SPDC in two-dimensional films, and derive a simple analytical expression to estimate the efficiency of the second from a direct measurement of second-harmonic generation.

Experimental Methods

Nonlinear optical interactions in crystalline structures depend on both the pump polarization and its orientation relative to the principal axis of the crystal, requiring the measurement and control of incidence angles. Chapter 3 details the tools and methods built to measure SPDC in a diffraction-limited area of two-dimensional materials. The choice of a free-space setup simplifies the study the material nonlinear response and provides a benchmark for the performance of more elaborated structures, such as integration of two-dimensional material on waveguides or resonant cavities. However, the resulting interaction volume results in particularly inefficient interaction and limits the ability of these materials to dissipate energy. Avoid material damage while ensuring the detection of a sufficient nonlinear response, requires to concentrate a large photon flux in a short amount of time which we achieve with a tunable mode-locked femtosecond laser. The stable repetition rate has also two important consequences: it allows to reduce the noise via detection gating, and to reduce the uncertainty in the time of emission of photon pairs which is desirable in quantum computing networks based on linear optics [14].

Results

The overall goal of this thesis is to measure the generation of energy-time entangled photons generated via spontaneous parametric downconversion (SPDC) in planar two-dimensional films.

SPDC is a spontaneous second-order nonlinear optical phenomenon which, under perfect phase-matching, scales quadratically with the length of the nonlinear medium (see for instance eq. (2.52a)). Thus, it is not uncommon to find bulk or on-chip integrated sources with GHz generation rates, which can be fully characterized over millisecond timescales. However, when the same phenomenon is studied over a few atomic layers, the considerably smaller generation rates force instruments to operate over time scales of tens of hours, unveiling phenomena that would otherwise be unnoticed. In addition, while the use of intense optical fields and sensitive detectors can help maximize the signal intensity, any source of loss and noise in the system can severely limit the observation of this phenomenon.

With a focus on two-dimensional nonlinear films of transition-metal dichalcogenides (TMDCs), in this chapter we present efforts towards the measurement of simultaneity of spontaneous parametric downconversion energy-time entangled photon pairs. We start reporting on an often overlooked source of noise in coincidence measurements, namely breakdown flashing. This consists in the emission of light from the active area of SPADs (section 4.2.1, which can result in strongly time-correlated signatures which could be confused as a signature of photon-pair generation). We first introduce the phenomenon, and present the results of a careful characterization of its spectro-temporal properties in the single-photon avalanche photodiodes used in this thesis. Section 4.2 expands on the topic of noise, focusing on all sources of accidental coincidences. These are all the radiative emissions that, despite being uncorrelated with the entangled photon pairs, may result in two simultaneous photo-detections and thus be confused for the detection of an entangled photon pair. Lower-bounds for the coincidences over accidental ratio (CAR) are derived analytically for dark-count limited and a background-limited regimes in section 4.2.2 and section 4.2.3.

Section 4.3 discusses loss in single-photon coincidence experiments. Without it, there would be a one-to-one correspondence between the rate of photon pairs and that of true coincidences. In practice however, the latter scales quadratically with the inverse of loss, which thus becomes a crucial parameter in the prediction of the measurement CAR. In an experiment of SPDC at a planar, two-dimensional, nonlinear interface, energy and momentum conservation can simultaneously be satisfied by an infinite number of combinations of signal and idler. As a result the downconverted light does not propagate with well defined spatial modes, and the calculation of collection loss is not straightforward. Section 4.3.1 proposes a numerical model to extract the average radiation pattern of the downconverted light and calculate the collection efficiency.

Thanks to a fundamental connection between the spontaneous process of SPDC and its classical analog of second-harmonic generation (SHG), it is possible to calculate the expected rate of photon pairs (former) from the efficiency of the latter. Experimentally, this requires accurate knowledge of the pulse durations of two trains of light pulses one octave apart. The frequency-resolved optical gating (FROG) measurement of such temporal durations is described in section 4.4.

Section 4.5 is dedicated to a diffraction-limited area of a single-layer of tungsten diselenide (WSe_2). We first presents results of the classical measurements of SHG in section 4.5.1, where the average photon rates of pump and SHG light are found to be $2.3 \times 10^{16} \text{ Hz}$ and $2.4 \times 10^3 \text{ Hz}$ respectively, resulting in a second-harmonic generation efficiency on the order of 10×10^{-13} . From this we infer the expected brightness of SPDC in section 4.5.2, where the same quantities for the generation of telecom

photon pairs become 1.17×10^{16} Hz and 1×10^{-3} pairs/s, corresponding to an efficiency of 8.54×10^{-20} . We then simulate the radiation pattern and collection loss for this experiment in section 4.5.3 and present the result of the HBT coincidence measurement in section 4.5.5. After accounting for all sources of loss in the setup, we predict that in a dark-count limited measurement it would be possible to detect coincidences above noise with CAR>10, despite the extremely weak near-infrared signal generated. However, observations are dominated by accidental coincidences which are luckily to result from the direct-bandgap of WSe₂. The calculated CAR is 1.3×10^{-3} , thus confirm that the measurement is background limited.

Increasing the CAR requires a larger nonlinearity, a weaker (ideally absent) background, and a longer interaction length. To this end, we explore the 3R polyphase of five-layer MoS₂ in section 4.6. The symmetry of this material leads to a quadratic scaling of the second-harmonic generation (SHG) conversion efficiency with crystal thickness, and restores the indirect band-gap of the bulk leading to a comparatively weaker photoluminescence (PL) and thus even higher CAR. Through modeling and simulations under non-resonant pumping, we calculate a sub-Hz pair-generation efficiency from a diffraction-limited area of the material. While a dark-count limited measurement would successfully reveal the simultaneity of the entangled photon pairs, the temporal autocorrelation is dominated by accidental coincidences caused by a weak and broadband background.

It is however possible to synchronize the SPAD detections to the repetition rate of the laser cavity, and dramatically increase the measurement of CAR as described in section 4.6.6. Coincidence measurements performed over the course of eight days showed that the measurement of photon simultaneity is still hindered by a relatively brighter background emission.

Conclusions

Although photon simultaneity from pairs generated via spontaneous parametric downconversion (SPDC) in TMDC could not be confirmed experimentally, the results of this investigation guide the validation of established quantum-classical relations in deeply sub-wavelength media and provide a performance benchmark for more advanced structures based on these ultra-thin materials. Chapter 5 summarizes the key findings and suggests practical ways to reduce the sources of noise.

Chapter 2

Background

This chapter sets the scene to understand the rest of the work presented in this thesis. We start with a background on the field of nonlinear optics in section 2.1, with the aim to provide an intuitive understanding for the origin of a nonlinear optical response. Particular attention is given to second-harmonic generation, which is the key nonlinear optical phenomenon explored in this work. The propagation of pump and SHG fields in a nonlinear medium are described through a classical formalism, which allows to derive simple expressions for the conversion efficiency as a function of the material parameters and interaction length.

Section 2.2.1 starts with a synthetic historical background on the field of quantum optics, along with the description of the phenomenon of quantum interference with an example in the optical domain. Light coherence is discussed in section 2.2.2 along with both phase-sensitive and phase-insensitive measurement techniques. This sets the scene to understand one of the central instruments used to measure the simultaneity of two-photon states from spontaneous parametric downconversion (SPDC), namely the Hanbury-Brown and Twiss (HBT) interferometer. A phenomenological explanation of entanglement in a quantum-mechanical sense is given in section 2.2.3, which facilitates the understanding of the peculiar properties of photon pairs generated via spontaneous nonlinear processes. The generation and control of quantum entanglement in the optical domain presents some challenges, and section 2.2.4 describes two of the most common platforms, namely quantum-dots and nonlinear light-matter optical interactions, the latter of which is the subject of this thesis. In a medium with non-zero $\chi^{(2)}$, the energy of one photon can be instantaneously transferred to a pair of photons that are energy-time entangled, a phenomenon known as spontaneous parametric downconversion (SPDC) as discussed in section 2.2.5. This implies strong non-classical correlations which enable single-photon heralding, where the detection of one photon of a pair reveals energy and time (or position and momentum) of the other with arbitrary precision. The efficiency of such process is addressed in section 2.2.6.

After a few historical considerations on the discovery of 2D materials, section 2.3 introduces transition-metal dichalcogenide (TMDCs), a type of 2D material which experienced renewed interest after the discovery of graphene. Section 2.3.2 presents some of the techniques used to fabricate and characterize TMDCs, while some of the exotic electro-optical properties of this class of materials are addressed in section 2.3.1. In single-layer form, the breaking of inversion-symmetry leads to strong spin-orbit coupling, which shapes the spectro-temporal properties of spontaneous radiative emissions in these materials. An effort is made to describe these properties and provide a starting point to understand their effect on some of the single-photon measurements presented in this thesis. References provided here are far from being

exhaustive, and are only intended to aid the first exploratory steps in this vast field of research.

The crystalline structure of TMDCs allows to immediately write the form of their second order nonlinear susceptibility tensor. As it is the case in many crystals, only a few of the 27 elements that compose the second-order susceptibility tensor $\chi^{(2)}$ are non-zero. For mono-layer TMDCs there is one dominant symmetry, namely D_{3h} , which results in only four non-zero elements of $\chi^{(2)}$. However, symmetry properties change depending on how single-layers overlap to form thicker TMDC crystals, resulting in different layer-dependence of the second-order nonlinear optical response. Section 2.4 considers two types of stacking for multilayer TMDCs, namely 2H and 3R. Published values of the second-order susceptibility tensor for these 2D materials are reviewed, and the analytical expressions for the efficiency of second-harmonic generation derived in section 2.1 are adapted to the 2H and 3R polytypes. The focus is on mono-layer WSe₂ and five-layer MoS₂ which are the subject of the experimental results presented in chapter 4.

Section 2.5 introduces the research in TMDCs for the nonlinear generation of entangled photon pairs, thanks to their relatively strong nonlinear properties. The first clear advantage of using 2D materials for spontaneous parametric downconversion is modularity. Being confined to two dimensions they can be easily integrated in more complex structures such as photonic waveguides or resonant cavities, without significantly perturbing the group velocities (phase-matching) of the interacting modes. This translates into a separation of concerns, whereby the linear properties of the underlying structure can be controlled independently for the nonlinear properties of the 2D material that generates energy-time entangled pairs. The second motivation is the flexibility through their opto-electrical properties can be controlled; these include both mechanical and electrical stimuli as well as control of the in-plane geometry, the introduction of defects, and the stacking with different 2D materials to form heterostructures. These properties have no equivalent in conventional bulk or integrated nonlinear photonic structures, and thus offer a plethora of new opportunities to engineer the generation of entangled photon pairs with high coincidences over accidental ratio (CAR), or equivalently signal to noise ratio (SNR). In Section 2.5.1 the photon-probabilities are adapted for TMDCs, and analytical expressions derived for the rate of photon pairs expected to be generated in a diffraction-limited area of monolayer WSe₂ with 2H polyphase and five-layers MoS₂ with of polytype 3R.

Finally, section 2.6 points to the similarities between the classical process of SHG and the quantum process of spontaneous parametric downconversion. Although the latter cannot be explained with a classical theory of light, both processes are quadratically dependent on the medium effective $\chi^{(2)}$, are quasi instantaneous, involve a total of three interacting photons, and must conserve energy and momentum. From an input/output prospective, the only difference is the distribution of energy, with SHG requiring two simultaneous photons to annihilate into a single third photon, and SPDC requiring a single photon to spontaneously annihilate and transfer its energy to a photon pair. Formal mathematical arguments, followed by a large set of experimental evidence, have shown that it is possible to estimate the efficiency of SPDC by studying the efficiency of an appropriate SHG experiment. This leads to a simple linear expression for the average rate of SPDC photon pairs as a function of the average rate of SHG photons.

2.1 Nonlinear optics and SHG

When a particle with non-zero electric charge is accelerated, the electric field that surrounds it varies in time. Towards the end of the nineteenth century, Maxwell realized that this induces a non-zero magnetic field, and extended Ampere's circuit laws which at the time considered only charges moving at a constant velocity. Moreover, according to Faraday's law of induction, changes of magnetic field induce variations of the electric field. The result is an endless exchange of energy between the electric and magnetic field, which propagates in space and time in the form of an electro-magnetic wave. Electro-magnetic waves permeate the known universe and their study underpins all fields of science, from microscopy to astronomy. When these accelerations are controlled, one can transfer information between two remote points through free-space, which is at the heart of radio-telecommunication systems. Electrons in the atomic structure of a medium react upon the presence of an external electromagnetic field $\mathbf{E}(t)$. This causes a local displacement of charges thus generating a dipole-like field known as dielectric polarization $\mathbf{P}(t)$. If the intensity of the external electromagnetic stimulus is weak, its effect on the magnitude and direction of the polarization is linear. At high intensities however, higher order terms are required to describe the nonlinear polarization, which is the source of new propagating waves. Nonlinear optics is therefore the study of light-matter interactions where the optical power density (intensity) is high enough such that this relationship is nonlinear. The appearance of higher order terms in the polarization response enables the exchange of energy between two or more light waves.

In a medium with a total external charge ρ_{ext} and external current \mathbf{J}_{ext} , in the time domain, the electric and magnetic fields are related by Maxwell's equations

$$\nabla \times \mathbf{H}(t) - \frac{\partial \mathbf{D}(t)}{\partial t} = \mathbf{J}_{\text{ext}}, \quad (2.1a)$$

$$\nabla \times \mathbf{E}(t) + \frac{\partial \mathbf{B}(t)}{\partial t} = 0, \quad (2.1b)$$

$$\nabla \cdot \mathbf{B}(t) = 0, \quad (2.1c)$$

$$\nabla \cdot \mathbf{D}(t) = \rho_{\text{ext}}, \quad (2.1d)$$

where $\mathbf{H}(t)$ and $\mathbf{B}(t)$ are respectively the time-varying magnetic and electric field, and $\mathbf{B}(t)$ and $\mathbf{D}(t)$ the magnetic induction and the dielectric displacement. Equation (2.1b) states that temporal variations of the magnetic field are always balanced by a curvature in the electric field lines, while eq. (2.1a) describes how the curvature of the magnetic field is proportional to the sum of external currents and variations of \mathbf{D} over time. Due to the inseparability of the sources and sinks for the lines of the magnetic field, its divergence is always zero eq. (2.1c), while the electric displacement \mathbf{D} generates from external charges ρ_{ext} eq. (2.1d).

The coupled nature of eqs. (2.1a) and (2.1b) is the reason why when fields vary in time we refer to electro-magnetic fields, as opposed to just the electric and magnetic contribution. In vacuum, $\mathbf{D}(t) = \epsilon_0 \mathbf{E}(t)$ meaning that instantaneous variations of \mathbf{E} are followed by instantaneous variations in \mathbf{D} . However, in the presence of any charge the total dielectric displacement can be written as

$$\mathbf{D} = [\epsilon_0 \mathbf{E} + \mathbf{P}] = [\epsilon_0 \mathbf{E} + \epsilon_0 \chi \mathbf{E}] \quad (2.2)$$

where \mathbf{P} is the polarization and χ the impulse response of the medium polarizability. A similar relation can be written between the magnetic field, the magnetic induction and the magnetization \mathbf{M} , as $\mathbf{H} = \mathbf{B}/\mu_0 - \mathbf{M}$. This together with eq. (2.2) are known as constitutive relationships. For weak light fields χ is a an order-two tensor $\chi \approx \chi^{(1)}$. Assuming that the response of the medium is local, the constitutive relations in the time and frequency domain take the form (see also eq. 2.1.9 of Agrawal Nonlinear Fiber Optics, 4th Ed.)

$$\mathbf{P}(\mathbf{r}, t) = \mathbf{P}_L(\mathbf{r}, t) = \epsilon_0 \int_{-\infty}^{\infty} \chi^{(1)}(\mathbf{r}, t-t') \cdot \mathbf{E}(t') dt', \quad (2.3a)$$

$$\mathbf{P}(\mathbf{r}, \omega) = \mathbf{P}_L(\mathbf{r}, \omega) = \epsilon_0 \chi^{(1)}(\mathbf{r}, \omega) \cdot \mathbf{E}(\mathbf{r}, \omega). \quad (2.3b)$$

Substituting eq. (2.1a) in eq. (2.1b), one obtains a second order differential equation that contains both the electric field and the polarization and is known as the wave equation. If the medium is not conducting, with a zero macroscopic magnetization, and has zero net charge, the wave equation is homogeneous and takes the form [15]

$$\nabla \times \nabla \times \mathbf{E}(t) + \frac{1}{c^2} \frac{\partial^2 \mathbf{E}(t)}{\partial t^2} + \frac{1}{c^2 \epsilon_0} \frac{\partial^2 \mathbf{P}(t)}{\partial t^2} = 0, \quad (2.4a)$$

$$\nabla \times \nabla \times \mathbf{E}(\omega) + \frac{\omega^2}{c^2 \epsilon_0} \mathbf{k}(\omega) \cdot \mathbf{E}(\omega) = 0, \quad (2.4b)$$

where we ignored the spatial dependence, $\mathbf{k}(\omega) = \epsilon/\epsilon_0 = (\delta_{ij} + \chi_{ij}^{(1)}(\omega))$ is the linear dielectric tensor, δ_{ij} is the Kronecker delta, and we adopted the notation from [15] indicating with "·" both the product between two vectors and between a vector and a second-rank tensor. However, in the presence of intense light fields, the polarization can be expanded in Taylor series

$$\mathbf{P} = \mathbf{P}_L + \mathbf{P}_{NL} = \mathbf{P}_L + \mathbf{P}^{(2)} + \mathbf{P}^{(3)} + \dots, \quad (2.5)$$

as a sum of a linear and a nonlinear term. If the response in space is local, the second order of this can be written as

$$\mathbf{P}^{(2)}(\mathbf{r}, t) = \epsilon_0 \int_{-\infty}^{\infty} \int_{-\infty}^{\infty} \chi^{(2)}(t-t', t-t'') : \mathbf{E}(\mathbf{r}, t') \mathbf{E}(\mathbf{r}, t'') dt' dt'', \quad (2.6)$$

where the spatial dependence has been omitted. If the second-order impulse response of the medium is instantaneous, that is $\chi = \delta(t)$, convolutions become products and we can omit the spatial dependence [16]

$$\mathbf{P}(t) = \epsilon_0 \chi^{(1)}(t) \cdot \mathbf{E}(t) + \epsilon_0 \chi^{(2)}(t) : \mathbf{E}(t) \mathbf{E}(t) + \dots, \quad (2.7a)$$

$$\mathbf{P}(\omega) = \epsilon_0 \chi^{(1)}(\omega) \cdot \mathbf{E}(\omega) + \epsilon_0 \chi^{(2)}(\omega) : \mathbf{E}(\omega) \mathbf{E}(\omega) + \dots. \quad (2.7b)$$

The nonlinear polarization acts as a source term in the equation eq. (2.4a), which thus becomes inhomogeneous and in the time domain can be written as

$$\nabla \times \nabla \times \mathbf{E} + \frac{1}{c^2} \frac{\partial^2 \mathbf{E}}{\partial t^2} + \frac{1}{c^2 \epsilon_0} \frac{\partial^2 \mathbf{P}_L}{\partial t^2} = - \frac{1}{c^2 \epsilon_0} \frac{\partial^2 \mathbf{P}_{NL}}{\partial t^2}. \quad (2.8)$$

2.1.1 Origin of the Second Harmonic Generation

This thesis considers the generation of energy-time entangled photon pairs via spontaneous parametric downconversion (SPDC) which depends on the second-order nonlinear optical response of a material. This phenomenon is intimately connected to classical nonlinear process such as second-harmonic generation (SHG), so that the efficiency of one can be inferred from the other. Here we introduce SHG analytically, and find expressions that will be used in chapter 4 to derive simple expressions for the rate of SPDC photon pairs as a function of the average rate of SHG photons. The electric field of a monochromatic wave as a function of space and time can be written as

$$\mathbf{E}(\mathbf{r}, t) = \hat{\mathbf{e}} A(\mathbf{r}, t) \exp[i(\mathbf{k} \cdot \mathbf{r} - \omega t)] + \text{c.c.} , \quad (2.9)$$

where the direction of the electric field or polarization is given by the unit vector $\hat{\mathbf{e}}$, which is real (complex) for a linearly (elliptically) polarized wave, and can only have components along the plane orthogonal to the propagation direction. The monochromatic wave has an angular frequency ω , a wave-vector \mathbf{k} ($|\mathbf{k}| = \omega/c$ where c is the speed of light in the medium), a direction which is a linear combination of the unit vectors for the cardinal axis $\hat{\mathbf{e}}_x, \hat{\mathbf{e}}_y, \hat{\mathbf{e}}_z$. The space-time dependence is incorporated in the slowly-varying amplitude term $A(\mathbf{r}, t)$, which is a complex quantity and thus may account for a phase term other than the propagation term $\exp\{i(\mathbf{k} \cdot \mathbf{r} - \omega t)\}$.

Since nonlinear optics typically involves directional light sources (lasers), this is commonly written in terms of the primary direction of propagation, which we take along z:

$$\mathbf{E}(\mathbf{r}, t) = \hat{\mathbf{e}} A(\mathbf{r}, t) \exp[i(kz - \omega t)] + \text{c.c.} . \quad (2.10)$$

We now consider the case where the applied field in the time domain is the sum of two monochromatic components at angular frequencies ω_1 , and ω_2 and amplitudes A_1, A_2

$$\mathbf{E}_1 = \hat{\mathbf{e}} A_1 \exp(-i\omega_1 t) \quad (2.11)$$

$$\mathbf{E}_2 = \hat{\mathbf{e}} A_2 \exp(-i\omega_2 t) \quad (2.12)$$

$$\mathbf{E}(t) = \mathbf{E}_1 + \mathbf{E}_2 + \text{c.c.} . \quad (2.13)$$

Substituting this in the second term on the right-hand side of eq. (2.7a), the complex amplitude of the the second-order nonlinear polarization can written as the sum of the following five components:

$$P_{\text{SHG1}}^{(2)} = \epsilon_0 \chi^{(2)}(t) A_1^2 \exp[-i2\omega_1 t], \quad (2.14a)$$

$$P_{\text{SHG2}}^{(2)} = \epsilon_0 \chi^{(2)}(t) A_2^2 \exp[-i2\omega_2 t], \quad (2.14b)$$

$$P_{\text{SFG}}^{(2)} = \epsilon_0 \chi^{(2)}(t) A_1 A_2 \exp[-i(\omega_1 + \omega_2)t], \quad (2.14c)$$

$$P_{\text{DFG}}^{(2)} = \epsilon_0 \chi^{(2)}(t) A_1 A_2^* \exp[-i(\omega_1 - \omega_2)t], \quad (2.14d)$$

$$P(0) = \epsilon_0 \chi^{(2)}(t) [A_1 A_1^* + A_2 A_2^*] . \quad (2.14e)$$

The first two describe the frequency doubling of \mathbf{E}_1 and \mathbf{E}_2 and are thus referred to as second-harmonic generation (SHG), the third and forth represent sum frequency generation (SFG) and difference frequency generation (DFG), and the last term is

optical rectification which is constant in time. From eq. (2.14a) it is evident that the interaction of a plane wave at the fundamental angular frequency ω_F with the medium $\chi^{(2)}$, causes its frequency to double to $\omega_{SH} = 2\omega_F$.

More generally, when the applied electric field contains m frequency components, each may generate a nonlinear polarization, which in turn acts as source of new frequency components, and contributes to the nonlinear optical mixing. An example of this is the case of pulsed laser light. If the interaction length is much shorter than the pulse length, $d \ll c\tau_{pulse}/n$, and the amplitude (phase) of the applied field varies slowly in space (time), the nonlinear interaction is described by a system of $m+1$ differential equations. For an isotropic and lossy medium, the analytical form of this can be written as [15]

$$\frac{dA_{m+1}}{dz} + \frac{\alpha_{m+1}}{2} A_{m+1} = i \frac{\omega_{m+1}}{2n_{m+1}} D^{(m)} \chi_{\text{eff}}^{(m)} \prod_{u=1}^m A_u \exp(i\Delta kz) \quad (2.15)$$

where A_m, ω_m, k_m are the complex amplitude, angular frequency, and wave-vector of the $m - th$ interacting plane wave, and n_m, α_m are the refractive index and absorption coefficient of the medium at ω_m . A typical ultra-short laser pulse can have a very large number of frequency components, each separated by the free spectral range of the laser cavity. Since a complete analytical description of eq. (2.15) is impractical, it is custom to describe the interaction based on the central frequency of a pulse, and thus consider monochromatic interacting waves. The spatial dependence of the amplitudes A_m may be incorporated in the wave equation although this also complicates the analytical expressions (see page 3 of [15] for the Gaussian approximation of fundamental TEM₀₀₀ modes). In the next section we write the system of coupled differential equations for second-harmonic generation in a $\chi^{(2)}$ medium, and derive an expression for the efficiency of the process.

2.1.2 SHG Efficiency

Away from any electronic resonance, and in the absence of free charges, the coupled equations of eq. (2.15) for planar and monochromatic optical waves can be written as

$$\frac{dA_{SH}}{dz} + \frac{\alpha_{SH}}{2} A_{SH} = i \frac{\omega_{SH}}{2n_{SH}c} \chi_{\text{eff}}^{(2)} A_F A_F e^{i(2k_F - k_{SH})z}, \quad (2.16)$$

$$\frac{dA_F}{dz} + \frac{\alpha_F}{2} A_F = i \frac{\omega_F}{n_F c} \chi_{\text{eff}}^{(2)} A_F^* A_{SH} e^{-i(2k_F - k_{SH})z}, \quad (2.17)$$

where A_F, A_{SH} are the complex amplitudes of the fundamental and second-harmonic field respectively, α_{SH}, α_F are the absorption coefficients at the fundamental and second-harmonic, and the term $A_F^* A_{SH}$ accounts for the depletion of the pump field due to its conversion into the second harmonic. The relations between the amplitudes of the pulse envelope and its intensity is

$$\hat{I}_m = 2\epsilon_0 n_m c |A_m|^2, \quad (2.18)$$

$$\hat{P}_m = \hat{I}_m A_{\text{eff}}, \quad (2.19)$$

where \hat{I}_m is the peak intensity, \hat{P}_m is the peak power and A_{eff} the pulse effective area. Since these are all peak quantities, we can write the same equations in terms of

$$G_m = \sqrt{P_m},$$

$$\frac{dG_{SH}}{dz} = i \frac{G_F G_F}{\sqrt{\mathcal{P}_{F,F} A_{eff}}} e^{i(2k_F - k_{SH})z} - \frac{\alpha_{SH}}{2} G_{SH}, \quad (2.20)$$

$$\frac{dG_F}{dz} = i \frac{G_F^* G_{SH}}{\sqrt{\mathcal{P}_{F,F} A_{eff}}} e^{i(2k_F - k_{SH})z} - \frac{\alpha_{SH}}{2} G_F, \quad (2.21)$$

where we have incorporated all quantities that depend on the nonlinear medium in

$$\mathcal{P}_{m,n} = \frac{2\epsilon_0 n_m n_n n_{SH} c^3}{\left(\chi_{eff}^{(2)} \omega_m\right)^2}, \quad (2.22)$$

which has units of power, and depends on the linear refractive index at the fundamental ω_F and second-harmonic $\omega_{SH} = 2\omega_F$, and the effective material nonlinearity $\chi_{eff}^{(2)}$. In typical nonlinear interactions, the amplitude of the nonlinear generated field is much smaller than the pump amplitude and the mixed term $G_F^* G_{SH} \approx 0$. This is known as the undepleted pump approximation, where the amplitude of the pump during its propagation from $-d/2$ to $d/2$ can only change due to linear absorption

$$\frac{dG_F}{dz} = e^{\frac{\alpha_F}{2}(z+d/2)} G_F(-d/2). \quad (2.23)$$

Substituting this into eq. (2.20) we can write

$$G_{SH}(d/2) = \frac{G_F^2(-d/2)}{\sqrt{\mathcal{P}_{F,F} A_{eff}}} \frac{e^{i(2k_F - k_{SH})d/2} \left(e^{2ik_F - ik_{SH} - \alpha_F d} - e^{-\frac{\alpha_{SH}}{2} d} \right)}{2k_F - k_{SH} - i(\alpha_{SH} - 2\alpha_F)/2} \quad (2.24)$$

We define the conversion efficiency at the end of the waveguide ($z = d/2$), as the ratio between the power of the second harmonic wave at the output of the nonlinear medium and the input power of the fundamental. Written in terms of G defined above writes

$$\eta_{SH} = \frac{P_{SH-out}}{P_{F-in}} = \left(\frac{G_{SH}(d/2)}{G_F(-d/2)} \right)^2, \quad (2.25)$$

which upon substitution of eq. (2.24) yields

$$\eta_{SH} = 2 \frac{P_F d^2}{\mathcal{P}_{F,F} A_{eff}} e^{-d(\alpha_F + \alpha_{SH}/2)} \frac{\cosh[(2\alpha_F - \alpha_{SH})d/2] - \cos[(2k_F - k_{SH})d]}{[(2k_F - k_{SH})d]^2 + [(2\alpha_F - \alpha_{SH})d]^2}, \quad (2.26)$$

or equivalently

$$\eta_{SH} = \frac{P_F d^2}{\mathcal{P}_{F,F} A_{eff}} e^{-d(\alpha_F + \alpha_{SH}/2)} \frac{\sin^2[(2k_F - k_{SH})d/2] + \sinh[(2\alpha_F - \alpha_{SH})d/4]}{[(2k_F - k_{SH})d/2]^2 + [(2\alpha_F - \alpha_{SH})d/2]^2}. \quad (2.27)$$

In the absence of loss ($\alpha_{SH} = \alpha_F = 0$), and if dispersion is negligible so that the wave-vector of the fundamental is exactly half the wave-vector of the second harmonic ($k_F = k_{SH}/2$), this reaches a theoretical maximum

$$\eta_{SH}^{(0)} = \frac{\hat{P}_F}{A_{eff}} \frac{d^2}{\mathcal{P}_{F,F}} = \hat{I}_F \frac{\left(d \omega_F \chi_{eff}^{(2)}\right)^2}{2\epsilon_0 n_F^2 n_{SH} c^3}, \quad (2.28)$$

where we expressed the peak power and peak intensity as \hat{P} , \hat{I} to remind ourselves that these apply to a pulsed illumination under the continuous-wave approximation. The SHG efficiency scales quadratically with the sample thickness d and the effective second order susceptibility of the material $\chi_{\text{eff}}^{(2)}$, and linearly with the pump intensity. Equation (2.28) is adapted to atomically-thick nonlinear sheets of transition-metal dichalcogenide (TMDC) in section 2.4, and yields analytical expressions for the $\chi_{\text{eff}}^{(2)}$ of monolayer WSe₂ eq. (2.46a) and five-layer MoS₂ eq. (2.46b).

In section 2.2 we give a brief introduction to the field of quantum optics, then look at the process of spontaneous parametric downconversion as describe the formalism used to calculate its efficiency. In section 2.3 we introduce transition-metal dichalcogenides and show that their nominal thickness is close to 0.7 nm, between 5 and 6 orders of magnitude smaller than the thickness of a typical bulk crystal used for non-linear generation of single photons. From the analytical results, we show that the efficiency of SHG and SPDC are linked by a proportionality constant that does not depend on the optical properties of the material. Moreover, both efficiencies scale quadratically with the interaction length, and with the magnitude of the second-order susceptibility tensor of the material. These insights allow to perform an order-of-magnitude estimation of the expected efficiency of SPDC in TMDCs. The material of choice for optical entanglement generation via spontaneous parametric downconversion is LiNbO₃, from which can routinely generate photon pairs at a rate of 1×10^7 Hz. If the same material was thinned down to the nominal thickness of monolayer TMDCs, and phase-mismatching was negligible, we would expect a pair rate in the range 1×10^{-3} to 1×10^{-5} Hz (between 10 and 12 orders of magnitude weaker than in bulk). Taking into account that the second-order nonlinear susceptibility of the TMDCs considered in this thesis is one order of magnitude larger than LiNbO₃ (see section 2.4), our estimated pair rate would fall in the range 1×10^{-1} to 1×10^{-3} Hz. Remarkably, these back of the envelope calculations come very close to the actual values calculated in section 4.5.2 and section 4.6.3 where we find 2×10^{-3} Hz for monolayer WSe₂, and $\approx 5 \times 10^{-2}$ Hz for five layer MoS₂. Such low rates pose interesting challenges to the design of the measurement system, as detailed in chapter 3 and chapter 4.

2.2 Quantum Optics, Entanglement and SPDC

In the early development of optics, the two rival theories were the corpuscular theory (Newton), and the wave theory (Huygens). The double-slit experiment of Young in 1801 provided convincing experimental evidence in support of Huygens, followed by the explanation of diffraction by Fresnel in 1815. However, prior to 1901, the Rayleigh-Jeans Law and the theorem of equipartition of energy predicted that a black body (essentially any object at a temperature different from -273°C), should radiate an infinite amount of energy, and thus ought not to exist.

Instrumental to solve this *ultraviolet catastrophe*, was the work of Max Planck (1901) [17] who predicted that energy is exchanged between matter and radiation in packets, and that the population distribution in a black body wasn't uniform but followed the Bose-Einstein statistics. Soon after (1905), Albert Einstein formalized a principle known as the photo electric effect [18], which states that the energy of an electron in an atom can only be an integer multiple of a fundamental value, thus formalizing the concept of quanta of energy. These cognitive efforts, which are recognized by many as the birth of quantum mechanics, resulted in two Nobel Prizes in 1919 and 1921. A naive experimentalist would be tempted to think that to test Planck's theory one would simply need a perfect light sensor (detection efficiency $\eta = 1$ in an optical bandwidth W): if detections occurred in a discrete fashion one would accept Planck's hypothesis, or reject it otherwise. However, the very process of detecting light involves the absorption of optical energy from one electron, which as a consequence of the photoelectric effect, is discrete. Thus detections would be discrete even if the light flux was indeed continuous. This is why it took 75 years from the moment Planck published his paper, to the irrefutable experimental evidence that light ought be quantized by Kimble et. al. [19]. During this time-span many theorists developed what is today known as the semi-classical theory of light, optical waves are modeled classically, and energy discretization is only applied to matter (electrons in the atoms). Only a full quantum theory of light is fully compatible with the breath of experimental evidence collected to date.

2.2.1 Quantum interference

In 1801, Thomas Young devised an ingenious experiment to support his wave-like theory of light that came to be known as the *double-slit experiment*, demonstrating that the interference pattern of a light source diffracting on two carefully placed apertures is qualitatively identical to that created by water waves diffracting on two apertures in a pond. In 1927, Davisson and Germer performed a variation of Young's double-slit experiment, using an electron gun in place of a light source, and demonstrated that electron collisions on a photographic plate placed behind the apertures, resulted in a qualitatively identical diffraction pattern reported by Young more than a century earlier. This peculiarity came to be known as the *wave-particle duality*, which can only be fully explained by representing quantum states in terms of their wave function. This is a probability density function which evolves in space and time, and whose modulo squared is proportional to the likelihood that the state will be measured somewhere at some point in time.

Although many interference effects can be explained with both a classical and quantum description of light, there are exceptions with no classical counterpart. One such example is quantum interference, which in the optical domain occurs when

two photons' wave functions have the same distribution in all degrees of freedom (time, space, polarization and energy). The two photons are said to be *indistinguishable* and their evolution can no longer be described in terms of the original wave functions, but a in terms of the bi-photon wave function. This is qualitatively similar to the single photons case, with the only difference that its modulo squared is proportional to probability of the joined state. The bi-photon wave function cannot be factored into the wave functions of the two original states, a property known as *inseparability*. In quantum optics, this can be observed by engineering the quantum state of two photons generated either in the same or different medium, and guide them at the input of a four-port element such as a beam splitter. When the optical paths traveled by the two photons relative to the beam splitter is identical, the biphoton will evolve through only one of the two output ports, a phenomenon known as *photon bunching*.

In the year 2000, Knill, Laflamme, and Milburn [14] had the intuition to leverage this effect to perform highly efficient qubit logic gates, using only linear optical components. In order for this to work, it is important to generate identical single-photons on demand, with full control of their wavefunction (mode shape, energy distribution, polarization and time) and coherence [20, 21]. Passive optical components can be used to coherently mix these states, while active elements such as phase-shifters enable a dynamic reconfigurability of these photonic modes. After their evolution, these quantum states, are detected and their quantum state reconstructed experimentally. To date, this principle is at the basis of one of the most promising platforms to realize optical quantum computing [22, 23].

2.2.2 Coherence of light

The phase relationship between the electric field values at different locations or at different times defines respectively the spatial and the temporal coherence of a light source. For a fixed observer, the time scale over which the phase of a wave remains stable, is referred to as coherence time, while at a particular instant in time, the distance over which the phase remains constant is referred to as the coherence length. It follows that a monochromatic wave has an infinite coherence time, while a plane wave has a perfect spatial coherence. One way to measure coherence is via interferometry, where a distinction can be made between measurements that are sensitive to the electric field (first-order) and those sensitive to the its intensity (second-order). An example of the first is the Michelson interferometer, which in 2016 was instrumental to the detection of gravitational waves from a binary black hole [24], as well as the Hong-Ou-Mandel (HOM) interferometer [25], and the doubly-excited Mach-Zehnder (MZ) interferometer [26]. In a HOM interferometer two identical and independent sources are interfered at a beam splitter. When these are indistinguishable (i.e. identical in polarization, energy, spatial and temporal degrees of freedom) their wave functions become non-separable and the probability of detecting them at two different output ports of the beam splitter is zero. As a consequence, the second-order correlation function in zero vanishes. The degree of distinguishability can be controlled by introducing a variable delay, and manifests in a reduction in the rate of coincidences known as the Hong-Ou-Mandel dip [25]. Similarly, a Mach-Zehnder interferometer measures how indistinguishable are the wave functions generated by a source at two different times. A typical way to achieve this experimentally, is to excite a single-photon source with two consecutive pulses, generating two single

photons sequentially, and controlling their relative optical paths before they interact at a beam splitter. Provided that the optical paths are always adjusted so that their difference is always equal to zero, the coherence time of the source can be measured by tracking the bunching probability as a function of the temporal separation between the original pump pulses. For realistic sources, the width of the dip is a measurement of the temporal coherence of the source [20].

On the other hand, interference measurements that depend on the intensity of the light source are phase-insensitive and yield the second-order correlation function of light [27]. An example of this is the Hanbury-Brown and Twiss (HBT) interferometer, which depending on how is implemented, can measure the temporal or spatial correlations between one or two light sources. The history of HBT interferometry begins at the end of the Second World War, where advances in the field of radio astronomy led to the discovery of bright radio “stars” in the sky [28]. The standard instrument to measure the size of these stars was the Michelson interferometer, which registers the interference of light collected from two separate points. When the distance is varied, one can reconstruct a diffraction pattern resulting from the coherent interference of the amplitudes received, which is then used to infer the angular size of the emitting source (phase-sensitive measurement)¹. The Hanbury-Brown and Twiss interferometer was designed to overcome the resolution limit of amplitude interferometry by replacing amplitudes with intensities. The spatial correlation between two sources of light, that is, how likely these are to be in the same angular position, is inferred by correlating changes in the product of the intensities with the distance between the detectors. Analogously, if the separation between photo-detections is performed in time, the HBT interferometer measures the temporal second-order autocorrelation function $g^2(\tau)$ of an optical source, usually expressed as

$$g^{(2)}(\tau) = \frac{\langle I(t)I(t + \tau) \rangle}{\langle I(t) \rangle \langle I(t + \tau) \rangle} \quad (2.29)$$

where $I(t) = |E(t)|^2$ represents the intensity, and the angled brackets indicate an average taken over time [29, 30]. The basic ingredients for this measurement is a beam-splitter, a pair of photo-detectors and an optical delay stage to vary the delay τ . Intensities are recorded for each position of a linear and automated delay stage, leading to long experiment times, over which the optical alignment must be maintained. It is with such a device that in 1977 Kimble and his colleagues reported the unambiguous detection of a non-classical state of light [19].

2.2.3 Entanglement and its applications

Whenever two quantum mechanical systems are indistinguishable in one or more of their degrees of freedom, they may become entangled and thus manifest strong correlations that cannot be accounted for with a classical description of light. Such correlations are instantaneous, and underpin the realization of quantum communication protocols, such as quantum-teleportation or entanglement swapping. Analytically, entanglement results from the non-separability of the quantum state, meaning that the functional form that described the system cannot be written as a product of two separate quantities. Provided that there is some degree of quantum-mechanical

¹The angular diameter of Jupiter’s system of moons was measured in 1891 by Michelson, and in 1895 was used to measure the diameter of binary stars by K. Schwarzschild [28].

indistinguishability, such strong correlations can also be observed between particles that do not interact directly. This is known as entanglement swapping, where two independent pairs of entangled photons can entangle two photons created in separate points and kept at a distance from one another during the measurements [31]. Over the past two decades, this property has attracted interest for its applications to the manipulation of quantum information in the optical domain, which would provide robust propagation through long-distance fiber links [32]. Encoding of photonic qubits can be done in frequency bins [33], time bins [34], and broadband temporal modes, which are the building blocks for quantum information processing [35]. In the energy-time domain, entanglement has been successfully applied in metrology, where non-classical correlations can increase the measurement resolution [36]. A peculiar effect in the optical domain is dispersion cancellation, where energy-time entangled photons maintain strong temporal correlations regardless of any difference in their propagation velocity in the medium [37, 38]. Another notable example of the application of entanglement is code-division multiple access (CDMA), a well-known technique based on Hadamard codes, that allows to share the capacity of a classical communication channel. While CDMA can be implemented from the sum-frequency generation response of a nonlinear medium, in high-dimensional systems entanglement has been shown to outperform classical approaches [39]. Another interesting area of research is quantum-enhanced positioning and clock synchronization, where frequency-entangled modes are believed to lead to more accurate results [40].

2.2.4 Generation of entanglement

Generation of entanglement is non-trivial. In the optical domain, ideal sources of entanglement are deterministic, have high fidelity, are highly coherent, and have low loss [41]. Respectively, these properties imply that:

1. Excitations are always followed by the emission of a pair of entangled photons
2. The created two-photon state is close to the one desired
3. Wave-packets generated at different times would be quantum-mechanically indistinguishable, provided that any difference in generation times is compensated by a difference in optical paths leading to an interferometer.
4. We can rely on the presence of such states.

To date, entanglement between two photons has been produced through spontaneous parametric downconversion in nonlinear optical media, and by radiative cascades in single quantum emitters such as atoms [41, 42] and quantum dots [43, 44]. In practice, brightness and control of the time of emission often needs to be traded off with spectral purity and indistinguishability.

Engineering the electromagnetic environment of a medium consists in allowing only two energy states to be coupled with a continuum of radiative modes [45], in a fashion similar to that of a two-level atomic system. When such system is strongly coupled with a periodic optical pump, the excited state can be occupied almost deterministically. In particular, if the radiative transition lifetime is much shorter than the repetition period of the laser, each pulse is almost certainly followed by the emission of a single photon. For this reason these sources are referred to as *deterministic*,

despite electron excitation/relaxation are probabilistic in nature. Optical cavities can be used to control the density of optical states surrounding the emitter, and select only some emission lines. To date, the most challenging aspect of quantum dots is fabrication reproducibility, which is needed to ensure consistency between the wave-packets emitted by different dots, a necessary condition for linear-optics quantum computing. One way to directly generate entangled states from an atomic system is to use the radiative decay of bi-excitons. As the biexciton binding energy is defined as the energy gain for two excitons to bind into a molecule [46], this energy is also what determines the energy difference between the first emission (annihilation of one electron-hole pair out of two) and the second emission. If it happens that the two excitons can decay radiatively via two degenerate paths with different polarization, then the photons emitted will be entangled in polarization because indistinguishable in any other degree of freedom. This was demonstrated in electrically pumped InAs quantum dots operated at 20 K [47]. By cycling the bias voltage between two levels up to 1 GHz, electron-hole tunneling can be controlled and generate pairs of photons on demand. The realization of such a device has long been challenged by polarization splitting of the dot emission lines which effectively makes the two paths distinguishable in energy and compromises the entanglement [48]. The preparation of bi-excitons can be very efficient. In [49] the authors used a pulsed two-photon excitation (TPE) scheme to selectively target the formation of biexcitons, and demonstrated generation with near unity fidelity. A number of clever structures have also been proposed to engineer the isolation of pump and generated photons using optical micro-cavities (see [41] and references therein).

In a medium with a non-zero second-order (third-order) optical nonlinearity, one (two) pump photon(s) can annihilate spontaneously and generate an energy-time entangled bi-photon. Such processes are known as spontaneous parametric down-conversion (SPDC) and spontaneous four-wave mixing (SFWM). In both cases, the probability that a single pump photon downconverts spontaneously into a signal and idler is very low, with a time between downconversions that follows a Poisson statistics [50]. For this reason these processes are referred to as *probabilistic*. However, phase-matching in photonic waveguides can be engineered over lengths of many millions of atoms, and the spectro-temporal properties of these photons be crafted with very high precision. Owing to the strong temporal correlations between the photons of the pair, these can be used to herald single photons, just as the very early experiments of Grangier, Roger and Aspect in 1986 [51] followed by Hong and Mendel [52] soon after. Despite the low yield, there is a low variability associated with the quantum state of pairs generated at two different times. This enables engineers to design buffers of indistinguishable photons, and interfere/entangle them at will. For a recent review on SFWM and a detailed account of efforts to do so in silicon photonics we refer the reader to [23, 53]. In the following we focus on SPDC which is the subject of this thesis.

2.2.5 Spontaneous Parametric Downconversion

Spontaneous parametric downconversion (SPDC), is the annihilation of a single photon and the generation of a pair of energy-time entangled photons, conserving both energy and momentum [54, 55]. Predicted in 1967 and observed soon after in bulk crystals, the process occurs in media with a non-zero second order susceptibility $\chi^{(2)}$, and it is spontaneous, or equivalently stimulated by vacuum fluctuations. In

such nonlinear media the input photon can perturb the electron wave-function to a virtual state for a short amount of time, inversely proportional to the energy gap between the virtual state and the nearest available real state. When the electron relaxes, energy may be released into two radiative modes, named signal and idler photons. Since the initial and final quantum-mechanical states of the system are identical, the process is said to be parametric, to emphasize that there is no population transfer from one real level to another [16]. One of the formulations of the uncertainty principle states that the energy and emission time of a photon cannot be known with simultaneously arbitrary precision. Instead, the product of the two uncertainties has a lower bound. Importantly, this is not true in the case of energy-time entangled photons, where the higher our confidence on the sum of their energy, the more confident we can be that they are emitted at the same time [56, 57]. The magnitude of these correlations can be quantified unambiguously only from a coherent measurement of the bi-photon wavefunction (i.e. phase and modulo), as recently demonstrated with a clever implementation of optical gating [58]. Such strong correlations are often used for single-photon heralding, whereby the detection of one photon of the pair (herald) provides information on the existence of the other (heralded) at a specific energy and time.

Since its discovery, SPDC has been a standard platform for entanglement generation and the demonstration of non-classical states of light by means of photon heralding [59–61]. Although a single heralded single photon source has a Poisson photon statistics, one can improve the probability to find a single photon by combining multiple sources via *multiplexing*. First proposed in 2002 [62], spatial multiplexing was soon demonstrated experimentally with electro-optic polarization controllers [63, 64], followed by theoretical proposals in the time domain in 2011 [65]. However, higher-order photon components (multi-pairs) in practice limit the quality of the bi-photon state generated via SPDC, posing a challenge in large scale quantum circuits [66, 67].

A large number of integrated sources based on spontaneous parametric down-conversion have been proposed and demonstrated with small footprints, high brightness and excellent purity of generated the photon states. Entanglement in the polarization degree of freedom has been demonstrated extensively in lithium niobate, where phase-matching has historically been obtained alternating layers of material with different dispersion (periodically poling). Depending on the momentum conservation, this can result in type I phase matching [68, 69] or type II phase-matching [70–72]. Lithium niobate has used to demonstrate time-bin entanglement [73, 74], quantum state generation and manipulation [75, 76], and to demonstrate active control of the spatial correlations between photon pairs produced in SPDC in arrays of nonlinear waveguides [77, 78]. SPDC has also been largely studied in AlGaAs non-resonant waveguides, with many demonstration of entanglement in polarization [79–81], time-bin [82], and energy degree of freedom [83]. Like any spontaneous process, the downconversion probability is proportional to the number of radiative modes available for the two output photons. The density of these can increase with optical cavities, the efficiency of SPDC increases. For instance, in a micro-ring resonator the efficiency of second-order nonlinear processes scales linearly with the inverse of the ring radius, while third order processes scale with the inverse of the radius squared. In the undepleted pump approximation and in the absence of loss, SPDC scales linearly with the quality factor Q of the optical

cavity (while SFGM scales with Q^2) [84]. Some examples of such integrated optical cavities include micro-toroids [85, 86] and integrated resonators [79, 82, 83, 87, 88]. Spontaneous parametric downconversion has also been used for the creation of high-dimensional entangled photon states, such as photon triplets via simultaneous [89, 90] and cascaded parametric downconversion (PDC) [91, 92], recently also demonstrated at telecom wavelengths in a monolithic chip [93].

2.2.6 Efficiency of SPDC

In order to write the photon pair flux generated in a SPDC experiment we follow the formalism of density operators presented in [94] which incorporates loss in the nonlinear region as well as to use an intuitive description of the statistical properties of the generated photon states. Neglecting multi-pair generation, and in the undepleted pump approximation, we can write the probability that two-, one- and zero-photons leave the nonlinear medium (respectively P_2 , P_1 , P_0) in terms of the density operator wave-functions θ_2 , θ_1 and θ_0 [94]

$$P_2 = \int d\omega_1 d\omega_2 \theta_2(\omega_1, \omega_2, \omega_1, \omega_2) e^{-\frac{1}{2}d \cdot r[\alpha_F(\omega_1) + \alpha_F(\omega_2)]} \quad (2.30a)$$

$$P_1 = \int d\omega_1 d\omega_2 \theta_2(\omega_1, \omega_2, \omega_1, \omega_2) e^{-\frac{1}{2}d \cdot r[\alpha_F(\omega_1)]} - 2P_2 \quad (2.30b)$$

$$P_0 = \int d\omega_1 d\omega_2 \theta_0(\omega_1, \omega_2, \omega_1, \omega_2) - P_1 - P_2 \quad (2.30c)$$

where normalization of the probability density θ_0 imposes

$$\int \int d\omega_1 d\omega_2 |\theta_0(\omega_1, \omega_2, \omega_1, \omega_2)|^2 = 1. \quad (2.31)$$

If the dispersion is negligible, the pump and second harmonic propagate with similar group velocities, ($r = v_F/v_{SH} \approx 1$), and

$$\theta_2(\omega_1, \omega_2, \omega_3, \omega_4) = \frac{A_{1,2} A_{3,4}^*}{4\pi^2} \int d\omega d\omega' B_{1,2}(\omega) B_{3,4}^*(\omega') \int_{-d/(2v)}^{d/(2v)} d\tau d\tau' C_2, \quad (2.32a)$$

$$\theta_1(\omega_1, \omega_2, \omega_3, \omega_4) = \frac{A_{1,2} A_{3,4}^*}{4\pi^2} \int d\omega d\omega' B_{1,2}(\omega) B_{3,4}^*(\omega') \int_{-d/(2v)}^{d/(2v)} d\tau d\tau' C_1, \quad (2.32b)$$

$$\theta_0(\omega_1, \omega_2, \omega_3, \omega_4) = \frac{A_{1,2} A_{3,4}^*}{4\pi^2} \int d\omega d\omega' B_{1,2}(\omega) B_{3,4}^*(\omega') \int_{-d/(2v)}^{d/(2v)} d\tau d\tau' C_0, \quad (2.32c)$$

The probability densities $\theta_2, \theta_1, \theta_0$ are the product of a term $A_{m,n}$, that depends on the strength of the interaction, and a term $B_{m,n}(\omega)$ that depends on phase-matching and loss

$$A_{m,n} = \frac{z}{\zeta} \frac{i\chi_{\text{eff}}^{(2)} d}{2\bar{n}^3 v_D} \sqrt{\frac{\hbar\omega_m \omega_n}{3\pi\epsilon_0 A_{\text{eff}}}}, \quad (2.33a)$$

$$B_{m,n}(\omega) = \sqrt{\omega} \phi_P(\omega) e^{-\alpha_{SH}(\omega)d/4} \frac{\sin[(2k_F - k_{SH})d/2]}{[(2k_F - k_{SH})d/2]}, \quad (2.33b)$$

with $|z|^2$ representing the average number of photons per pump pulse at frequency ω_{SH} , and $|\zeta|^2$ the corresponding number of generated photon pairs at ω_F . If we indicate with $\alpha_{\text{SH}}, \alpha_F$ the attenuation of the pump and the down converted photons due to linear absorption, the terms C_2, C_1, C_0 are written as the product of a phase and amplitude terms

$$C_2 = e^{\frac{v}{2}[\alpha_{F,\omega_1} + \alpha_{F,\omega_1} - \alpha_{\text{SH},\omega}] \tau} e^{\frac{v}{2}[\alpha_{F,\omega_3} + \alpha_{F,\omega_4} - \alpha_{\text{SH},\omega'}] \tau'} \phi(\tau, \tau') \quad (2.34\text{a})$$

$$C_1 = e^{\frac{v}{2}[\alpha_{F,\omega_1} - \alpha_{\text{SH},\omega}] \tau} e^{\frac{v}{2}[\alpha_{F,\omega_3} - \alpha_{\text{SH},\omega'}] \tau'} e^{-[\alpha_{F,\omega_3} + \alpha_{F,\omega_4}]v|\tau - \tau'|/4} \phi(\tau, \tau') \quad (2.34\text{b})$$

$$C_0 = e^{\frac{v}{2}[-\alpha_{\text{SH},\omega}] \tau} e^{\frac{v}{2}[-\alpha_{\text{SH},\omega'}] \tau'} e^{-[\alpha_{F,\omega_1} + \alpha_{F,\omega_2} + \alpha_{F,\omega_3} + \alpha_{F,\omega_4}]v|\tau - \tau'|/4} \phi(\tau, \tau') \quad (2.34\text{c})$$

$$\phi(\tau, \tau') = e^{i(\omega_1 + \omega_2 - \omega)\tau} e^{-i(\omega_3 + \omega_4 - \omega')\tau'} \quad (2.34\text{d})$$

2.3 Transition-metal Dichalcogenides

In 2003 Novoselov and Geim reported the isolation of a chemically-stable single layer of carbon atoms from graphite [95], known as graphene. This was found to possess an excellent thermal conductivity, and to switch from a metal to a semiconductor upon application of a bias potential and mechanical strain. These properties make it attractive for a wide variety of applications, from high-speed electrical and optical devices [96–98], to energy storage and chemical sensors [99–101] and more.

In the last 15 years, the field of surface science has experienced an explosion of interest, with countless new materials being synthesized and studied, offering new opportunities for controlling light-matter interactions (see [102] for a recent review of the types of two-dimensional nanomaterials). Similar to graphene, transition-metal dichalcogenides (TMDCs) materials whose atoms are bound by strong covalent bonds in-plane, and weak van der Waals forces out of plane, and are thus known as van der Waals or *layered* materials. Their composition can be expressed with the formula MX₂, where M is a metal atom of the group IV (transition metal), and X₂ indicates two chalcogen atoms. While graphene is chemically inert and requires functionalization to interact with the desired molecules, single-layer TMDCs exhibit versatile chemistry with opportunities for catalysis, energy storage and sensing [103], and have been used for RNA sensing and DNA translocations [104, 105]. The oldest TMDC is molybdenum disulfide (MoS₂), with specimens dating over 2.9 billion years [106]. It is also the most studied TMDC with its structure determined for the first time in 1923. Like many other TMDCs, bulk MoS₂s has a large and indirect electronic bandgap at the K,K' points of the Brillouin zone. Remarkably, a direct band-gap appears when the material is thinned down to a single layer (three atoms thick), making monolayer forms of these materials good candidates for ultra-fast transistors, electrodes for Li-ion batteries, supercapacitors and more [11, 107]. The nonlinear optical response of a material depends on its intrinsic symmetry properties, specific orientation and strength of the optical field applied, and the microscopic transition dipole matrix. The latter, in general depends on the electronic environment such as the presence of optical cavities or excitonic resonances, and is in general frequency dependent. The nonlinear potential of transition-metal dichalcogenides (TMDCs) is primarily driven by their record-high nonlinearity, primarily resulting from their quantum-confined nature, which implies a reduced Coulomb screening and strong excitonic resonances (large exciton binding energy) [1–7]. Reported values of the second order susceptibility for WSe₂ and MoS₂ are comparable to monolayer GaAs which is known to be between $12 \times 10^{-11} \text{ m V}^{-1}$ and $50 \times 10^{-11} \text{ m V}^{-1}$ in the range 500–1500 nm [108], and up to one order of magnitude larger than the material of choice for optical entanglement generation via spontaneous parametric downconversion, namely LiNbO₃, whose largest component of $\chi^{(2)}$ is $6 \times 10^{-11} \text{ m V}^{-1}$ [16]. Depending on the exact arrangement of the metal and chalcogen atoms, the shape and form of the unit cell of these crystals changes, leading to different crystal symmetries and second-order nonlinear responses. Of eleven known variations (or polymorphs), only three are commonly found, namely the 1T, 2H and 3R forms, where the digit indicates the number of layers in the unit cell, and the letters refer to their symmetry: T (trigonal), H (hexagonal), and R (rhombohedral) [107]. As discussed in section 2.4, this plays an important role in determining the components of the second-order susceptibility tensor $\chi^{(2)}$ and thus the overall nonlinear response of the material under illumination with polarized light.

In order to distinguish the material contribution to the nonlinear optical response, from that of the electromagnetic environment, the crystal should be studied away from optically-resonant structures. A further simplification can be made assuming that the polarization of the excitation is also aligned to the crystal so as to probe the largest nonlinear response possible. With these two assumptions in mind, much of the interest in monolayer TMDC for non-linear optics lies in their intrinsic crystal symmetry breaking, and their strong exciton binding energy. In the paragraphs below, we give a brief overview of the most remarkable properties of these materials, introduce excitons from a phenomenological standpoint, and prepare for a literature review on the reported values of the second order nonlinear susceptibility of some of these 2D materials.

2.3.1 Electronic Properties of monolayer TMDC

The electronic properties of a single layer of transition-metal dichalcogenide are largely influenced by the inherent breaking of inversion-symmetry (one layer only) and the strong spin-orbit coupling, while strong excitonic effects dictate the spectral and temporal properties of their spontaneous radiative emissions (PL).

In bulk crystals, every atom of the lattice belongs simultaneously to three crystal planes, and is surrounded by a periodic electromagnetic environment in all directions in space. A consequence of this is Coulomb screening, which practically limits the coupling between the electron spin degree of freedom, and its orbit angular momentum. Due to the absence of a periodic structure out-of-plane, this coupling is restored in monolayers and its effect it to split the energy levels at the valley of the conduction band of the material. In TMDCs this coupling is dominated by the d orbitals of the heavy metal atoms [46]. Moreover, the explicitly broken inversion symmetry in TMDCs leads to valley-dependent optical selection rules, whereby electrons at the K (K') points must have opposite spins and can only be excited by a left (right) circularly-polarized photon. This is understood to arise from the insurgence of a non-zero effective magnetic field in momentum space (Berry curvature) and orbital magnetic moments [109]. In addition, time-reversal symmetry in TMDCs imposes that the spins of two electrons in the same point of the Brillouin zone must be anti-parallel, and that spin-up at the K point is degenerate with spin-down at K' point [109, 110]. Thus, the valley and spin indexes of electrons can be controlled by changing the handedness of the laser polarization. Because of the large separation between valleys in momentum space, these excitations are expected to be robust against scattering by long-wavelength phonons, a desirable feature in valleytronics, where information is encoded in the valley degree-of-freedom [110]. The broken inversion symmetry in monolayers is also responsible for the valley Hall effect where the application of an in-plane electric field, causes carriers in different valleys to flow to opposite transverse edges [110].

The electronic properties of TMDCs in close vicinity to the band gap are dominated by excitons. These are responsible for the appearance of a complex set of spectral features with three main peaks, historically marked as A, B, and C (see for instance figure 2a of [41]). First proposed by Yakov Frenkel in 1931, excitons are an elementary excitation of condensed matter that can transport energy without transporting net electric charge. The promotion of an electron in the valence band to the conduction band leaves behind a positively charged electron hole. An exciton is

formed when the Coulomb attraction between these particles is balanced by the repulsive forces from other electrons in the valence band, so that the electron-hole pair must be treated as a whole [111]. The energy necessary to separate an electron from a hole (electronic band-gap) can be higher than that required to create the bound electron-hole state or exciton (optical band-gap). In other words an exciton is energetically favorable compared to a non-bound electron-hole pair. The energy difference between the electronic and optical band-gap is a measurement of the strength of electron-hole interactions and is known as the exciton binding energy [112]. In bulk semiconductors, the lattice limits this interaction, so that collisions eventually lead electrons to recombine radiatively. In 2D TMDC however, the exciton binding energy can vary from 0.3 to 1 eV, and is large enough to overcome inhomogeneous broadening and be observed at room temperature [113]. Phenomenologically, a large binding energy means that the absorption and emission of a photon is more likely to occur when it involves the formation of an exciton, than when it does not. In turn, this implies a higher emission rate and a shorter lifetime for band-to-band transitions (10-100 ps compared to 10 ns for those that do not involve an exciton), with a lifetime ratio as large as 100 [41]. Higher order excitons such as trions and bi-excitons have also been observed in 2D TMDC such as monolayer MoS₂, albeit with smaller binding energies, requiring cryogenic temperatures to prevent inhomogeneous broadening [113–115]. Photoluminescence (PL) properties of single layer MoS₂ are indicated to have strong correlations with the surrounding dielectric environment. Blue shifts of up to 40 meV of exciton or trion PL peaks were observed as a function of the dielectric constant of the environment [116].

Vibration, Strain and other properties

Raman scattering of light with long-wavelength optical phonons has been studied extensively in 2H-MoS₂, where the six atoms in the unit cell give rise to 18 vibrational modes and four first-order Raman active modes (see [117–120] and references therein). Scattering of light by long wavelength acoustic phonons (Brillouin scattering) has been studied in multilayer graphene [121], as well as in WSe₂, TaSe₂ and MoS₂ [122–124]. One of the consequences of inversion symmetry braking is the insurgence of piezoelectricity. Metallic electrodes on multilayer MoS₂ deposited on a flexible substrate allowed to measure a 5% mechanical-to-electrical conversion efficiency when strained by 0.5 % [125]. Piezoelectricity was also studied on a suspended film of MoS₂ [126], using an atomic-force microscope probe to apply mechanical stress, which was monitored from the deflection of a laser beam on its cantilever. Under axial compression, strong interactions between adjacent layers lead to charge transfer from the metal to the chalcogen atoms with an ensuing semiconductor-metal transition at a critical pressure [127]. Experiments in a diamond anvil cell confirmed that mechanical stress changes the vibrational, optical and electronic properties of these layered nanomaterial, thus providing a platform for strong coupling of electrons, photons and phonons [128]. Magnetism is not expected in the ideal bulk MoS₂ but has been observed in real samples, which is associated with the presence of grain boundaries, crystal imperfections. Among more exotic properties of TMDCs, are topological semimetals (Weyl semimetals) with negative magnetoresistance, non-local transport and quantum oscillations [129] and superconductivity [130].

2.3.2 Fabrication and characterization

Studies on the exfoliation of TMDCs have been conducted since the 1960s. However, it wasn't until after the discovery of graphene that the deposition of high-quality single-layer sheets became widespread in the research community. The weak van der Waals forces in TMDCs allow exfoliation of the bulk and the isolation of monolayers. This top-down approach is simple, efficient and inexpensive. In a typical mechanical exfoliation process, thin TMDC crystals are peeled off from the bulk by using an adhesive tape. This is then brought into contact with a target substrate and removed, leaving behind single-layer and multilayer TMDC nanosheets. Despite its usefulness in an experimental setting, this process is not scalable and yields non-reproducible flake sizes, which may experience mechanical strain or be contaminated in the exfoliation process. Flakes can also be isolated by direct ultrasonication in a liquid, as used to disperse graphene [131, 132]. Another approach is electrochemical exfoliation, although it requires oxidization of the bulk which may affect the MoS₂ nanosheets [133]. On the opposite end is the bottom-up approach, which uses chemical-vapor deposition (CVD) or molecular epitaxy, the same technique that enables the fabrication of large area graphene sheets [134, 135]. Since the properties of TMDCs are strongly dependent on thickness, it is important to measure this accurately. This is challenging in exfoliated samples since their thickness is not uniform. One accurate but not practical method is atomic-force microscopy AFM. Far-field methods include Raman scattering, which relies on the layer-dependent vibrational modes of the lattice, and photoluminescence measurements which correlate changes in the PL brightness with the thickness-dependent direct-to-indirect phase transition of these materials. The TMDCs studied in the context of this thesis are monolayer WSe₂ and five layer MoS₂. The first samples were obtained by mechanical exfoliation of a bulk synthetic crystals of WSe₂, and drily transferred onto a quartz substrate with the same technique used for Graphene [136]. Device fabrication was supported by the ACT node of the Australian National Fabrication Facility, and was carried out by the group of Ass. Prof. Yuerui Lu. Monolayer flakes were identified from their optical contrast and from the shape and position of the electronic resonances, probed by photoluminescence spectroscopy using a femtosecond pump at 540 nm, to excited the material above bandgap. Unless otherwise stated, material damage was monitored by taking high resolution optical images and photoluminescence spectra of each sample before and after illumination. The peak and average power were closely monitored to avoid exceeding the power damage threshold of the crystals used. For reasons discussed in section 4.6, samples of multilayer MoS₂ required specific symmetry properties so as to guarantee the braking of inversion symmetry irrespective of the number of layers deposited. For this reason, 3R MoS₂ crystals were grown by the method of chemical vapor transport (CVT) using MoCl₅ as transporting agent [137]. Device fabrication and characterization was carried out by Liu Sheng in the group of Professor Xiong Qihua at Nanyang Technological University.

2.4 SHG in TMDC

The breaking of centrosymmetry in any material is a necessary requirement to observe a non-zero $\chi^{(2)}$ [16]. In the most general case, second-harmonic generation with a linearly polarized pump results in elliptically polarized light. The strength of each component depends on the elements of the susceptibility tensor (see for instance page 60 of [138]). In some TMDCs, such as hexagonal MoS₂, the relative intensity of horizontal and vertical polarizations generated in the doubling of a linearly polarized pump can be used to measure the crystal orientation [4, 139–141]. Depending on the particular monolayer and the way layers are arranged in multi-layer stacks, the resulting symmetry changes together with the form of $\chi_{\text{eff}}^{(2)}$. As an example, monolayers of tungsten diselenide (WSe₂) or molybdenum disulfide (MoS₂) have hexagonal symmetry with space group D_{3h}, for which only four elements of the second order susceptibility are non zero and are all identical

$$\chi_{\text{WSe}_2}^{(2)} = \chi_{xxx}^{(2)} = -\chi_{xxy}^{(2)} = -\chi_{xyx}^{(2)} = -\chi_{yxx}^{(2)}, \quad (2.35)$$

the effective $\chi^{(2)}$ can thus be written as

$$\chi_{\text{eff-WSe}_2}^{(2)} = \chi_{\text{WSe}_2}^{(2)} \sqrt{2} \cos(3\theta), \quad (2.36)$$

where θ is the angle between the polarization direction of the electric field and the principal axis of the crystal. When multiple layers are stacked vertically, the crystal symmetry depends on the number of layers; an odd number of layers possesses the same symmetry of a mono-layer (D_{3h}), and $\chi^{(2)} \neq 0$, while an even number of layers belongs to the space group D_{6h} (P6₃/mmc) [7]). In this second case, the nonlinear dipoles of any two adjacent planes are anti-parallel, all the elements of the tensor vanish, $\chi^{(2)} \approx 0$ [16], and the second harmonic response is inhibited.

However, molybdenum disulfide (MoS₂) can be grown in another polyphase referred to as 3R or trigonal, where the unit cell and bulk are non-centrosymmetric, and the parallel nonlinear dipoles across planes add constructively. In this phase the symmetry is c with space group C_{3v}(R_{3m}) [7], where 8 out of 27 components are non zero and many of them are degenerate

$$\begin{aligned} \chi_{C3v \ xzx}^{(2)} &= \chi_{C3v \ yzy}^{(2)} \neq 0, \\ \chi_{C3v \ xxz}^{(2)} &= \chi_{C3v \ yyz}^{(2)} \neq 0, \\ \chi_{C3v \ zxx}^{(2)} &= \chi_{C3v \ zyy}^{(2)} \neq 0, \\ \chi_{C3v \ zzz}^{(2)} &\neq 0, \\ \chi_{C3v \ zzz}^{(2)} &= \chi_{C3v \ yyy}^{(2)} = \chi_{C3v \ -yxx}^{(2)} = \chi_{C3v \ -xxy}^{(2)} = \chi_{C3v \ -xyx}^{(2)} \neq 0. \end{aligned}$$

In this case, indicating with θ_t the incidence angle of the pump on the material [142]

$$\begin{aligned} \chi_{\text{eff}}^{(2)} &= 2d_{\text{eff}} = (d_{15} \cos^2(\theta_t) + d_{33} \sin^2(\theta_t)) \sin(\theta_t) + \\ &- [d_{16} \cos(\theta_t) - (d_{15} + d_{31}) \sin(\theta_t)] \cos^2(\theta_t), \end{aligned} \quad (2.37)$$

which for normal incidence, $\theta_t = 0$ simplifies to

$$\chi_{\text{eff}}^{(2)} = 2d_{\text{eff}} = 2d_{16} = \chi^{(2)}. \quad (2.38)$$

Since the expression of $\chi^{(2)}$ does not change with number of layers in for the 3R polype, the overall nonlinear response increases with material thickness.

2.4.1 Reported second-order nonlinearity of WSe₂ and MoS₂

The authors in [143] measured the dependence of the second order nonlinear response of mono-layers WSe₂ on the excitation energy (room temperature). Across the two-photon resonance at the A exciton, the on-resonance SHG was found to be 15 times stronger than off-resonance, corresponding to a second-order susceptibility contrast of 4. In the former case, the effective volume second-order susceptibility, for a nominal thickness of 0.65 nm was estimated to be

$$\chi^{(2)}_{\text{WSe}_2-1\text{L}} = 6 \times 10^{-11} \text{ m V}^{-1}$$

with a conversion efficiency of 10×10^{-10} , an order of magnitude larger than what one would achieve if standard transparent nonlinear crystals was scaled to the same thickness. A contrast of over 3 orders of magnitude was reported in monolayer WSe₂ at cryogenic temperature for both the nonlinear optical response [2]. The depletion of the phonon population caused by cooling the material also allowed the discern exciton states beyond the 1s, such as 2p and 2s for both the A exciton and B exciton. Multi-photon transitions have also been investigated. Interestingly, when the pump was 2 photon resonant to the 1s state, the stronger SHG response was not followed by an increase in photoluminescence. This is because 1s states can only be accessed with one photon as opposed to 2p and higher energy exciton states. The frequency doubling resonant to the 1s state was found to result from two electric and one magnetic dipole interaction.

The measurement of optical second-harmonic generation from atomically thin samples of MoS₂ was also found to be three orders of magnitude stronger in monolayer compared to bulk [4]. The authors also reported the surface nonlinear susceptibility tensor d^s , and normalized for the contribution of the quartz substrate ($\chi^{(2)}_{\text{quartz}} = 6.2 \times 10^{-13} \text{ m V}^{-1}$). Upon conversion from C/V² to esu and finally to SI units (see page 50 of [16]), we find

$$\chi^{(2)}_{\text{MoS}_2-1\text{L}} = 32 \times 10^{-11} \text{ m V}^{-1}. \quad (2.39)$$

In [5] the setup was calibrated measuring the second order non linearity of Zinc Sulfide (ZnS). The reported surface nonlinearity was $\chi^{(2)}_{\text{MoS}_2-1\text{L}}^{\text{sheet}} = 2 \times 10^{-20} \text{ m}^2 \text{ V}^{-1}$ which for a nominal thickness of $0.68 \times 10^{-9} \text{ m}$ corresponds to

$$\chi^{(2)}_{\text{MoS}_2-1\text{L}} = 2.9 \times 10^{-11} \text{ m V}^{-1}. \quad (2.40)$$

The dispersion of $\chi^{(2)}$ in monolayer MoS₂ was also measured in [1]. They find that the maximum nonlinear response is obtained when the pump is resonant with the indirect band-gap at the Γ point of the Brillouin zone of MoS₂ (2.8 eV). In their experiment the pump energy was scanned from 1.2 eV to 1.7 eV and kept below the A and B excitons which are at 1.9 eV and above. The $\chi_{\text{Sheet}}^{(2)}$ of monolayer MoS₂ was

reported to increase eight times between off and on resonance. On resonance they report

$$\chi^{(2)\text{sheet}}_{\text{MoS}_2\text{-1L-res}} = 8 \times 10^{-20} \text{ m}^2 \text{ V}^{-1}, \quad (2.41\text{a})$$

$$\chi^{(2)}_{\text{MoS}_2\text{-1L-res}} = 11.9 \times 10^{-11} \text{ m V}^{-1}, \quad (2.41\text{b})$$

$$\chi^{(2)}_{\text{quartz}} = 0.08 \times 10^{-11} \text{ m V}^{-1}, \quad (2.41\text{c})$$

where the contribution of the substrate was subtracted. The dispersion of $\chi^{(2)}$ in monolayer MoS₂ has also been calculated by means of Density Functional Theory DFT and was found to increase of a factor of 4 when the two-photon energy of the pump was scanned from off-resonance to resonant to the A-exciton [144]. One outlier for monolayer MoS₂ is the one in [139] which reported

$$\chi^{(2)} = 10 \times 10^{-7} \text{ m V}^{-1}.$$

A close look at their results show that they report a peak second-harmonic intensity of $I_{\text{SH}} = 3.5 \times 10^6 \text{ W m}^{-2}$ for a peak pump intensity of $I_{\text{Pump}} = 1.8 \times 10^{13} \text{ W m}^{-2}$, corresponds to an average pump power of 1 mW. Summing over the two orthogonal polarizations of the SH response $I_{\text{SH}} = I_{\text{SH}\parallel} + I_{\text{SH}\perp} = 0.5n\epsilon_0c|\mathbf{A}_{\text{SH}}|^2$ and recalling that

$$|\mathbf{A}_{\text{SH}}| = \frac{1}{4} \frac{i2\omega}{2n_{2\omega}c} \chi^{(2)} d |\mathbf{E}_{\text{pump}}|^2, \quad (2.42\text{a})$$

$$\chi^{(2)} = \frac{\sqrt{I_{\text{SH-Tot}} 8n_{\text{SH}} n_F^2 \epsilon_0 c^3}}{\omega d I_{\text{Pump}}}, \quad (2.42\text{b})$$

we find $\chi^{(2)} = 152 \times 10^{-11} \text{ m V}^{-1}$, substantially smaller than the value of 10^{-7} claimed by the authors in [139]. Finally, in [7] the authors engineering the layer stacking and fabricated a 3R poliphase of multilayer MoS₂ that preserves inversion symmetry breaking. They measured a 40-fold increase of SHG with 7 layers, which corresponds to 6.5-fold increase in $\chi^{(2)}$. For reasons related to the electronic band-gap and symmetry, this material holds a potential for the measurement of simultaneity of entangled photon pairs generated via SPDC.

To put it in prospective, the second order susceptibility values quoted above for MoS₂ and WSe₂ are in the same order of magnitude of monolayer GaAs known between $12 \times 10^{-11} \text{ m V}^{-1}$ and $50 \times 10^{-11} \text{ m V}^{-1}$ in the range 500-1500 nm (see fig. 4a of [108]), and up to one order of magnitude larger than the material of choice for optical entanglement generation via spontaneous parametric downconversion, namely LiNbO₃, whose largest component of $\chi^{(2)}$ is known to be $6 \times 10^{-11} \text{ m V}^{-1}$ [16]. The practical adoption of a new platform for nonlinear conversion and/or nonlinear photon heralding depends on at least on three elements: a. the overall conversion efficiency, b. the ease of fabrication, and 3. the ease of integration with existing candidate platforms for information processing based on light (e.g. Silicon Photonics). While various integration approaches for incorporating non-centrosymmetric materials in the silicon photonics platform have been suggested, they all present fabrication challenges which are still subject of intense research [145, 146]. This thesis aims at providing quantitative insights on the potential of TMDCs focusing on sub-nanometer interaction lengths, thus minimizing the fabrication complexity and

isolating the contribution of the material form that of the waveguide medium. Our results provide a benchmark for more complex geometries, such as waveguides, ring resonators and photonic-crystal micro cavities.

2.4.2 Efficiency of SHG in 2D TMDC

Transition-metal dichalcogenides (TMDCs) are crystalline semi-conductors with a unit cell composed of a heavy atom surrounded by two chalcogenide atoms. These have typically large band-gaps and with a negligible macroscopic magnetization. These materials also have strong exciton resonances with large binding energies due to a reduced Coulomb screening resulting from the quantum confinement. In the presence of strong exciton resonances, the description of the nonlinear polarization as a product of the susceptibility tensor and the electric field is incomplete, and it is often necessary to use a fully quantum-mechanical treatment (see chapter 3 of [16]). The classical Hamiltonian becomes a quantum-mechanical operator that acts on quantum states as described by the Schrödinger equation. The solutions of this equation form a set of orthonormal functions of space and time, and can thus be used to represent any quantum state as their linear combination (superposition), as well as to anticipate the evolution of the state. Investigating the role of excitons in harmonics generation experimentally requires low-temperature setups, where samples must be isolated electrically and magnetically, to avoid contributions from the Stark, the magneto-Stark, and the Zeeman effects [147]. In this thesis we focus on non-resonant second-harmonic generation, and base our results on the classical description introduced briefly in section 2.1.2, modeling TMDC monolayers as an ultra-short waveguide. Since their nominal thickness ($d \approx 0.7 \text{ nm}$) is three orders of magnitude shorter than the wavelength of visible light ($400 \text{ nm} < \lambda_{\text{vis}} < 700 \text{ nm}$), the effect of dispersion can safely be neglected

$$\Delta k = k_F - k_{\text{SH}}/2 = 0. \quad (2.43)$$

Recall that eq. (2.26) has been obtained under the assumption that the optical wave at ω_F is quasi-CW, the average power of the SH generated as the result of the nonlinear interaction is

$$\hat{P}_{\text{SHG}} = \hat{P}_F \cdot \eta_{\text{SHG}} = \frac{\hat{P}_F^2}{A_{\text{eff}}} \frac{\left(d \omega_F \chi_{\text{eff}}^{(2)} \right)^2}{2\epsilon_0 n_F^2 n_{\text{SHG}} c^3} e^{-d(\alpha_F + \alpha_{\text{SHG}}/2)}. \quad (2.44)$$

In practice, measurements yield the cumulative spectrum of the SHG response over a long integration time, which upon normalization allows to calculate the average photon flux at the second harmonic frequency, \bar{R}_{SHG} . In a perfectly phase-matched SHG experiment, this can easily be related to the peak power \hat{P}_{SH} . We indicate with Δt_F and T_F the pump repetition period and pulse duration respectively. Since SHG is an ultra-fast process $T_{\text{SH}} = T_F$ and if we approximate $\Delta t_{\text{SH}} \approx \Delta t_F$ we can write

$$\hat{P}_{\text{SHG}} = \hat{R}_{\text{SHG}} \hbar \omega_{\text{SHG}} = \bar{R}_{\text{SHG}} \left(\frac{T_{\text{SHG}}}{\Delta t_{\text{SHG}}} \right) \hbar \omega_{\text{SHG}}, \quad (2.45a)$$

$$\bar{R}_{\text{SHG}} \approx \frac{\Delta t_F}{T_F} \frac{\hat{P}_F^2 d^2}{2\hbar \omega_F \mathcal{P}_{\text{FF}} A_{\text{SHG}}}, \quad (2.45b)$$

where we neglected the loss term as $e^{-d(\alpha_F + \alpha_{SH}/2)} \approx 1$. Note that eq. (2.45b) is the usual quasi-continuous wave (CW) expression for the generated SHG power (see eq. (2.28)) where any walkoff due to differences in the group velocities, as well as any dispersive pulse spreading are negligible, and the phase matching term set to unity. In particular this is expected to be valid even for illumination with femtosecond pulses (≈ 200 fs), since their envelope is more than 4 orders of magnitude longer than the thickness of a typical TMDC monolayer. Equation (2.44) is a second order equation in $\chi^{(2)}$. This can be solved for monolayer WSe₂ (1L-WSe2), and five-layer MoS₂ (5L-MoS2) to give:

$$\chi_{\text{eff-1L-WSe2}}^{(2)} = \sqrt{2} \chi_{\text{WSe2}}^{(2)} \cos 3\theta = \frac{1}{dP_F} \sqrt{\frac{4\hbar n_F^2 n_{SH} c^3}{\omega_F}} \sqrt{\bar{R}_{\text{SHG}} A_{\text{SHG}}} \quad (2.46a)$$

$$\chi_{\text{eff-5L-MoS2}}^{(2)} = \chi_{\text{MoS2}}^{(2)} = \frac{1}{dP_F} \sqrt{\frac{4\hbar n_F^2 n_{SH} c^3}{\omega_F}} \sqrt{\bar{R}_{\text{SHG}} A_{\text{SHG}}} \quad (2.46b)$$

2.5 SPDC in 2D materials

As discussed in section 2.2.5, spontaneous parametric downconversion has been observed in bulk and integrated structure and its scaling laws unveiled both theoretically and experimentally.

However, measurements have been limited to interaction volumes typically much larger than λ^3 , where λ is the wavelength of the light fields involved. One consequence of this is that the same medium must be used to guide both the fundamental and the down-converted light. While this is convenient to efficiently extract the downconverted light, both the linear and nonlinear optical properties of the medium must be simultaneously engineered, resulting in narrow-band and not reconfigurable operation. On the other hand, the relatively large $\chi^{(2)}$ of some 2D materials has stimulated research into their use to generate entangled photon pairs via nonlinear optical interactions. Such highly sub-diffraction sources of correlated photon pairs would be automatically phase-matched and inherently broadband. Moreover, the properties of the electromagnetic environment can be controlled by stacking the crystal planes of different materials, providing novel means to control the properties of the electromagnetic environment, and engineer the emission of photon pairs. In addition, the reduced thickness facilitates integration in more complex structures such as photonic waveguides or resonant cavities, without perturbing the group velocities (phase-matching) of the interacting modes. This translates into a separation of concerns. In particular, the optimization of intrinsic nonlinear properties is separated from the electromagnetic environment.

The use of 2D materials for SPDC is also motivated by the many opportunities to control their opto-electrical properties. These include mechanical and electrical stimuli as well as control of the in-plane geometry, the introduction of defects, and the stacking with different 2D materials to form heterostructures. Research into spontaneous parametric downconversion from 2D materials is also important from a fundamental prospective. While the way the process scales with length and material parameters is well known in bulk, it is interesting to see if and how the macroscopic description of the phenomenon holds for interaction lengths as short as the spatial extent of a few atoms. The only measurement of non-classical states of light from

sub-diffraction media has been reported from resonant SFWM in carbon nanotubes [148]. Although the pair generation rate was reported to be in excess of 16 kHz with a coincidence-over-accidental ratio CAR = 18 (limited by photon-phonon Raman scattering), the authors fail to provide coincidence measurements that unambiguously show the strong temporal correlations between signal and idler photons. To the best of the author's knowledge, experimental evidence of non-resonant SPDC from two-dimensional materials has not yet been reported.

2.5.1 SPDC in WSe₂ and MoS₂

Mono-layers of the group IV transition metal dichalcogenides (TMDC) are good candidates to explore the potential of this approach, thanks to their record-high nonlinearity [1–7]. Moreover, heterostructures, mechanical strain [8–10] and electrostatic doping [11–13] have all shown to offer a way to dynamically control their band-gap and their nonlinear response [143]. In particular in WSe₂ the efficiency of its SHG response undergoes a three orders-of-magnitude increase when the 2-photon laser energy is scanned across its A and B excitons [2]. Since the first of these resonances is just above the visible spectrum at 1.65 eV [149] it holds promise for the generation of telecom-band photon pairs via SPDC.

The analytical expressions in section 2.2.6 can be readily adapted to a mechanically exfoliated mono-layer of WSe₂ (crystal phase 2H and space group D_{3h}). Since all optical interactions occur over a length, $d = 0.65$ nm, much shorter than the wavelength they are intrinsically phase-matched, enabling broadband generation of photon pairs. Moreover, since the film is three orders of magnitude thinner than the optical wavelengths involved, any mismatch between the group velocities of the interacting waves can be neglected. The interaction occurs in an effective area A_{eff} over a length d , and the two-, one-, and zero-photon probabilities reduce to

$$P_2 = |A_{\text{FSH}}|^2 \left(\frac{\sinh(\Delta_{\alpha,2})}{\Delta_{\alpha,2}} \right)^2 e^{-(2\alpha_F + \alpha_{\text{SH}})d/2}, \quad (2.47a)$$

$$P_1 = 2 |A_{\text{FSH}}|^2 \left(\frac{\sinh(\Delta_{\alpha,1})}{\Delta_{\alpha,1}} \right)^2 e^{-(\alpha_F + \alpha_{\text{SH}})d/2} - 2P_2, \quad (2.47b)$$

$$P_0 = 2 |A_{\text{FSH}}|^2 \left(\frac{\sinh(\Delta_{\alpha,0})}{\Delta_{\alpha,0}} \right)^2 e^{-\alpha_{\text{SH}}d/2} - P_1 - P_2, \quad (2.47c)$$

where we defined

$$|A_{\text{FSH}}|^2 = \frac{|z|^2}{|\zeta|^2} \frac{\hbar\omega_F\omega_{\text{SH}}}{3\pi} \frac{d^2}{\mathcal{P}_{\text{FSH}} A_{\text{eff}}} \quad (2.48a)$$

$$\mathcal{P}_{\text{m,n}} = \frac{2\epsilon_0 n_m n_n n_{\text{SH}} c^3}{(\sqrt{2} \cos(3\theta) \chi^{(2)} \omega_m)^2} \quad (2.48b)$$

$$\Delta_{\alpha,2} = \frac{2\alpha_F - \alpha_{\text{SH}}}{d/4} \quad (2.48c)$$

$$\Delta_{\alpha,1} = \frac{\alpha_F - \alpha_{\text{SH}}}{d/4} \quad (2.48d)$$

$$\Delta_{\alpha,0} = \frac{\alpha_{\text{SH}}}{d/4} \quad (2.48e)$$

Note that $\mathcal{P}_{m,n}$ is identical to the one defined in eq. (2.48b) where we substituted the expression for the $\chi^{(2)}$ of monolayer WSe₂ in eq. (2.36), and θ is the angle between the polarization of the pump and the principal axis of the crystal. If the difference between the absorption at the fundamental and the second harmonic is negligible eq. (2.47) simplifies further

$$P_2 \approx e^{-\alpha_F d}, \quad (2.49a)$$

$$P_1 \approx 2e^{-\alpha_F d/2} - 2P_2, \quad (2.49b)$$

$$P_0 \approx 1 - P_1 - P_2. \quad (2.49c)$$

The average number of SPDC photon pairs at ω_F generated by a single pulse, $|\zeta|^2$, is related to the average number of photons per pump pulse at frequency ω_{SH} , $|z|^2$, via [94]

$$|\zeta|^2 = |z|^2 \frac{\hbar\omega_F\omega_{SH}}{3\pi} \frac{d^2}{\mathcal{P}_{F,SH} A_{eff}} e^{-\alpha_{SH}d/2}, \quad (2.50)$$

obtained because the normalization in eq. (2.31) simplifies to $|A_{F,SH}|^2 = 1$ for a perfectly phase-matched process. The quantities $|\zeta|^2, |z|^2$ are immediately related to the peak power of the pump, \hat{P}_{SH} and downconverted fields \hat{P}_F as

$$\hat{P}_{SH} = \frac{|z|^2 \hbar\omega_{SH}}{\Delta t_{SH}}, \quad (2.51a)$$

$$\hat{P}_F = \frac{|\zeta|^2 \hbar\omega_F}{\Delta t_F}, \quad (2.51b)$$

where Δt_m and $\hbar\omega_m$ are the pulse durations and the energy of each photon. We substitute eqs. (2.51a) and (2.51b) in eq. (2.50) and, given the instantaneous nature of SPDC, we assume $\Delta t_{SH} \approx \Delta t_F = \Delta t_P$. While in general the effect of loss in the nonlinear medium has to be considered [94, 150], here we neglect the loss ($e^{-\alpha_{SH}d/2} \approx 1$) since the material has an absorption coefficient of the order of $\alpha = 10^8 \text{ m}^{-1}$ [151] with a thickness of only $d = 0.7 \text{ nm}$ [143]. Since peak rate and power are related by the energy of a photon, $\hat{R} = \hat{P}/\hbar\omega$, we can write

$$\hat{R}_{SPDC-1LWSe2} = d^2 \frac{\hat{P}_{SH}}{A_{eff}} \frac{\omega_F}{3\pi} \frac{(\chi^{(2)} \sqrt{2} \cos(3\theta))^2}{2c^3 n_F^2 n_{SHG} \epsilon_0} = d^2 \frac{\hat{P}_{SH}}{A_{eff}} \frac{\omega_F}{3\pi} \frac{1}{\mathcal{P}_{F,SH}} \quad (2.52a)$$

$$\bar{R}_{SPDC-1LWSe2} = d^2 \frac{\Delta t_P}{T_P} \frac{\hat{P}_{SH}}{A_{eff}} \frac{\omega_F}{3\pi} \frac{(\chi^{(2)} \sqrt{2} \cos(3\theta))^2}{2c^3 n_F^2 n_{SHG} \epsilon_0} = d^2 \frac{\Delta t_P}{T_P} \frac{\hat{P}_{SH}}{A_{eff}} \frac{\omega_F}{3\pi} \frac{1}{\mathcal{P}_{F,SH}} \quad (2.52b)$$

which highlight the expected linear dependence of the pair rate on the pump intensity \hat{P}_{SH}/A_{eff} , and its quadratic dependence on both the medium thickness and the second order nonlinear susceptibility d , and $\chi^{(2)}$ respectively. For a five-layer MoS₂ in the 3R poliphase under normal-incidence illumination the effective second order susceptibility tensor reduced to a scalar eq. (2.38) and the expressions above simplify

in

$$\hat{R}_{\text{SPDC-5L-3R-MoS}2} = d^2 \frac{\hat{P}_{\text{SH}} \omega_F}{A_{\text{eff}}} \frac{(\chi^{(2)})^2}{2c^3 n_F^2 n_{\text{SHG}} \epsilon_0}, \quad (2.53\text{a})$$

$$\bar{R}_{\text{SPDC-5L-3R-MoS}2} = d^2 \frac{\Delta t_P}{T_P} \frac{\hat{P}_{\text{SH}} \omega_F}{A_{\text{eff}}} \frac{(\chi^{(2)})^2}{2c^3 n_F^2 n_{\text{SHG}} \epsilon_0}, \quad (2.53\text{b})$$

Photon pairs are expected to be generated in a broadband continuum of modes around ω_F on the order of the inverse period of a generated photon [84]

$$W = \frac{3\pi}{\omega_F/2}, \quad (2.54)$$

where ω_F is the pump central angular frequency. For a pump centered at 785 nm, this corresponds to a bandwidth of 127.3 THz which corresponds approximately to 270 nm. However, the wavelength of downconverted photons is $\lambda = 2\lambda_P$, and since $\Delta\lambda \approx \lambda^2 \Delta f/c$ we find that pair generation occurs in a 1 μm window. Collection of non-energy-degenerate photons is possible in theory, though spectral filtering is likely to reduce collection rate.

2.6 Quantum Classical Correspondence in TMDC

In spontaneous parametric downconversion energy and momentum must be conserved [54, 55] and the probability that the process occurs depends quadratically on the medium second order susceptibility $\chi^{(2)}$. The same conservation laws and scaling apply to the reverse (classical) process of SHG where two input photons give their sum energy to a single output photon. Although the two operate at two different regimes, in the lossless case the efficiency of one can be estimated knowing the efficiency of the other [84, 152]. The theoretical description of such connection was later expanded to incorporate scattering loss [150]. These predictions were followed by many experimental demonstrations where the joint spectral intensity (JSI) (probability distribution of the bi-photon state in the frequency domain) could be reconstructed with high fidelity with a conventional spectrometer [153–157], thus avoiding the complexity of tunable narrow band filters [158, 159] and lengthy and noisy coincidence measurements. Here, we approximate TMDC of one or few layers as an incredibly short waveguides, where light-matter interaction occurs in the diffraction-limited spot of focused laser beams (A_{SHG} or A_{SPDC} as appropriate). Following these principles, we can write the ratio between the average rate of generated SHG and SPDC, eq. (2.45b) and eq. (2.52b) respectively, and find

$$\bar{R}_{\text{SPDC}} = \bar{R}_{\text{SHG}} \left(\frac{A_{\text{SHG}}}{A_{\text{SPDC}}} \frac{\hat{P}_P}{\hat{P}_F^2} \frac{\Delta t_P}{\Delta t_F} \frac{T_F}{T_P} \frac{2\hbar\omega_F^2}{3\pi} \right) = \bar{R}_{\text{SHG}} K. \quad (2.55)$$

as expected, the generation rate of photon pairs from SPDC depends linearly on the rate of SHG photons collected via a proportionality constant K that depends on the ratio of effective areas, duty-cycle of the illumination ($T_P/\Delta t_P$ and $T_F/\Delta t_F$) and peak powers. Crucially, K does not depend on the linear or nonlinear properties of the material. Note that R_{SPDC} scales only linearly with pump power, whereas R_{SHG} scales quadratically, and the pump is centered at ω_{SH} while photon pairs are

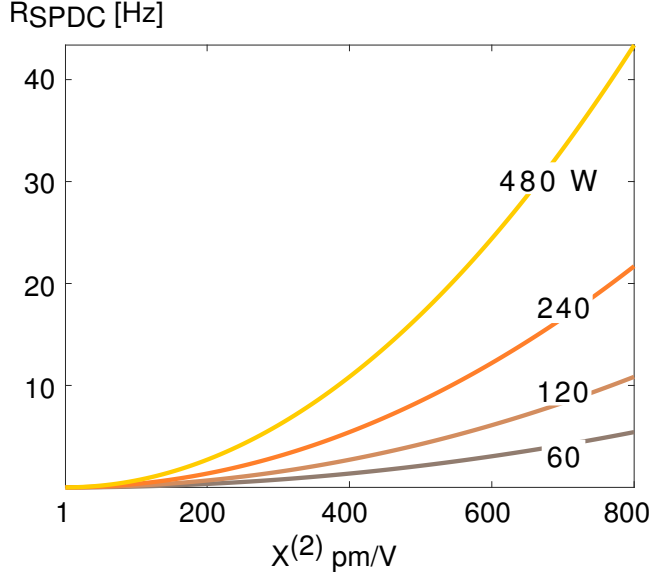


FIGURE 2.1: Expected quadratic scaling of the rate of photon pairs generated via SPDC from a TMDC mono-layer calculated using representative experimental values in eq. (2.52a), along with the linear refractive index of WSe₂ at the fundamental and second harmonic. Calculations show the expected linear scaling with pump peak power and assume illumination with a 80 MHz, 235 fs mode-locked pump.

collected near ω_F . Since the rate of SPDC photon pairs generated in a TMDC mono-layer can be inferred from the generate photon flux in a SHG experiment on the same material, eq. (2.55) is useful to investigate the potential of these mono-layers for parametric downconversion. Another way to calculate the rate of entangled photon-pairs produced in a SPDC experiment in monolayer TMDC, starting from the efficiency of a second-harmonic generation experiment, is to first calculate the $\chi^{(2)}$ and then evaluate eq. (2.52). Under the assumptions discussed in section 2.4.2, this can be calculated from the photon flux in a frequency-doubling experiment via eq. (2.46a) and eq. (2.46b). We substitute eq. (2.46a) in eq. (2.52b) and find

$$\bar{R}_{\text{SPDC}} = \bar{R}_{\text{SHG}} \frac{A_{\text{SHG}}}{A_{\text{SPDC}}} \frac{\hat{P}_P}{\hat{P}_F^2} \frac{\Delta t_P}{\Delta t_F} \frac{T_F}{T_P} \frac{2\hbar\omega_F^2}{3\pi} \quad (2.56)$$

which is identical to eq. (2.55). Equation (2.56) is strictly valid for WSe₂ only if the pump in the frequency-doubling experiment and the pump in the SPDC experiment are co-polarized, while it is always true for 3R-MoS₂ under normal pump incidence, since its SHG response is polarization insensitive.

In fig. 2.1 we plot eq. (2.55) for different $\chi_{\text{eff}}^{(2)}$ at a pump wavelength of 785 nm, $d = 0.7$ nm, and $n_F = 4.0$ and $n_{\text{SH}} = 5.1$ [151]. We imagine periodic illumination with a mode-locked laser at 80 MHz and 235 fs pulses so that $\Delta t_P/T_P = 1.88 \times 10^{-5}$ and $A_{\text{SPDC}} = 4.42 \times 10^{-13} \text{ m}^2$. A material different from WSe₂ would have different linear and nonlinear properties. Although the two are seldom independent quantities, within the assumptions of our model, the former appears in the term P_{FSH} at the denominator of eq. (2.52) which takes into account the linear refractive index of the material at the fundamental n_F and second harmonic n_{SHG} . On the other hand, the

intensity of SPDC on the effective second-order susceptibility tensor would remain quadratic as shown in fig. 2.1. With the same illumination parameters and geometry, the strength of downconversion in a material B can be estimated from that of material A as

$$\bar{R}_{\text{SPDC-B}} \propto \bar{R}_{\text{SPDC-A}} \left(\frac{\chi_{\text{eff-B}}^{(2)}}{\chi_{\text{eff-A}}^{(2)}} \right)^2 \left(\frac{n_A}{n_B} \right)_F^2 \left(\frac{n_A}{n_B} \right)_{\text{SHG}} \quad (2.57)$$

showing that it is preferable to uses materials with a small linear refractive index and a strong effective nonlinear susceptibility. As mentioned above, the photon rate of SPDC is related to that of SHG via a proportionality constant K , which incorporates any difference in power and effective area between the "stimulated" (SHG) and "spontaneous" (SPDC) measurements (as well as duty-cycle for periodic pulsed illumination), and is independent from the material linear and nonlinear properties already included in RSHG. Thus another way to predict how fig. 2.1 would look like in a different material is to calculate the ratio of the two SHG responses under the same illumination geometry and parameters:

$$\bar{R}_{\text{SPDC-A}} \propto \bar{R}_{\text{SPDC-B}} \frac{\bar{R}_{\text{SHG-A}}}{\bar{R}_{\text{SHG-B}}}. \quad (2.58)$$

Chapter 3

Experimental Methods

The first section of this chapter describes the organization of the optical table in section 3.1, from the excitation in section 3.1.1, to all modules for the control of power, divergence, angle, and position (see sections 3.1.2 and 3.1.3). Some of these are off-the-shelf systems, some had to be built ad hoc for the particular measurement. Section 3.1.4 describes the control of optical paths of ultrashort laser pulses, which is essential to both perform pump-probe optical mixing and accurate measurements of the pulses duration via frequency-resolved optical gating (FROG) interferometry described later in section 4.4. Section 3.1.5 describes the generation of time-correlated photon pairs used to test the optics and electronics of the setup to measure photon coincidences. The study of light-matter interactions at the nanometer scale requires high-quality imaging system and precise motion control. This, along with the imaging and spectroscopy system, and the Fourier imaging for the control of light incidence angle are described in section 3.1.6, section 3.1.7 and section 3.1.8. The system for single-photon detection and time-tagging is described in section 3.1.9, which prepares the reader to understand the design of a time-correlated single-photon spectrometer in section 3.1.10, designed to measure the emission energy of extremely weak light sources (see for instance the results in section 4.1.2).

Light detection instruments used in this thesis belong to two families. The first are based on arrays of charge-coupled device (CCD) and are introduced in section 3.2 together with a brief analysis of the sources of noise and their characterization. The second type are single-photon avalanche photodiode (SPAD), and are based on inversely polarized p-n junctions to generate a macroscopic current upon absorption of a single photon as explained in section 3.3. Sections 3.4 and 3.5 are dedicated to the control of incidence angle and illumination position of laser light on the samples, while the measurement of the second-order statistics of light ($g^2(\tau)$) is addressed in section 3.6. Section 3.7 describes the design of filter to ignore photo-detections received at specific time intervals, which is commonly known as detection gating. When studying ultrafast phenomena such as SPDC, this has the advantage of reducing the noise and increasing the sensitivity of the measurement.

Lastly, section 3.8 describes the design of a confocal collection system, as a way to improve the spatial resolution and thus filter-out a large portion of the background emission that may arise from areas surrounding the region directly illuminated by the pump beam. A higher-resolution single-photon imaging is finally described, which combines a three-dimensional motion control system with the SPADs.

3.1 Optical Table Overview

3.1.1 Femtosecond laser sources

Mode-locking requires a mechanism that results in higher net gain for short pulses compared to continuous-wave (cw) operation. With the help of a passive saturable absorber or an active dynamic mechanism to control the resonator loss, the phase relationship of the different transversal modes of a laser cavity can be arranged so that their interference results in bursts of light. We refer the reader to Cundiff and Haus for an introduction to frequency combs and ultrafast lasers [160, 161]. Various technological advances in the last two decades have led to a large range of commercially available laser sources based on mode-locking.

The experimental setup used throughout this thesis is shown in fig. 3.1. It is formed by a passively mode-locked laser cavity (Chameleon Ultra II from Coherent Inc.) with nominal pulse width $\tau_{\text{pulse}} \approx 225 \text{ fs}$ (FWHM) at 800 nm and repetition rate $\nu_{\text{rep}} \approx 80 \text{ MHz}$ (period $\approx 12.5 \text{ ns}$). Pulses thus extend for $67.4 \mu\text{m}$ in space, separated by $\approx 3.75 \text{ m}$. This Ti:Sapphire laser cavity can generate light pulses at a central wavelength of 800 nm, with an average output power of about 4 W, and a peak power density of $200 \times 10^3 \text{ W}$ ($1.6 \times 10^6 \text{ W cm}^{-2}$) for a 2 mm beam waist.

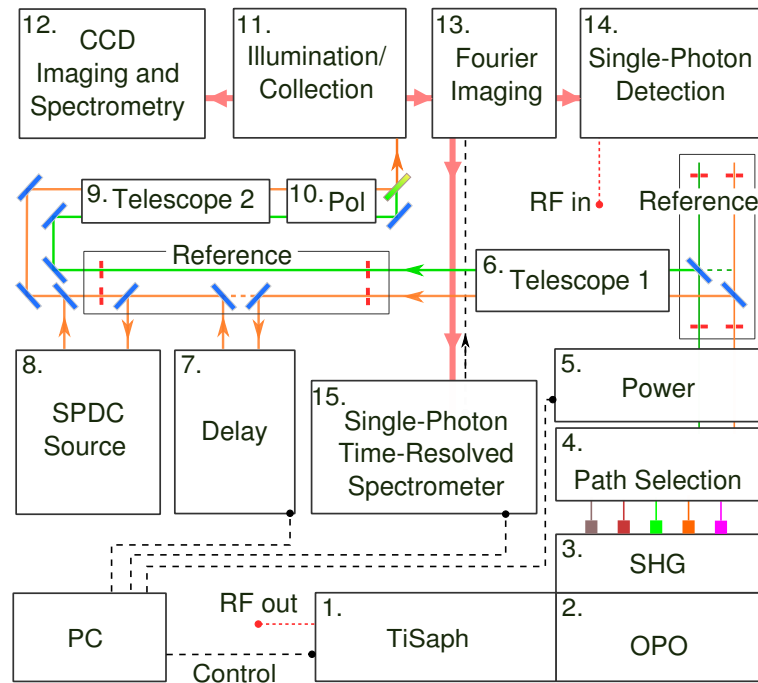


FIGURE 3.1: Optical table design. A source of mode-locked femtosecond pulses (350 nm to 4 μm) (1-2-3.) can be multiplexed (4.), power controlled (5.), expanded (6.) and delayed/interfered (7.). It can be used to pump an on-chip source of photon pairs (8.), and adjusted in diameter (9.) and polarization (10.) before entering the illumination and collection setup (11.). Results from the light-matter interactions can be analyzed classically with a dual imaging system and spectrometer (12.) or at the single-photon level (13-14.).

During normal operation, one-third of the optical power is released on the table, while the remaining 70 % circulates in a synchronously-pumped optical parametric

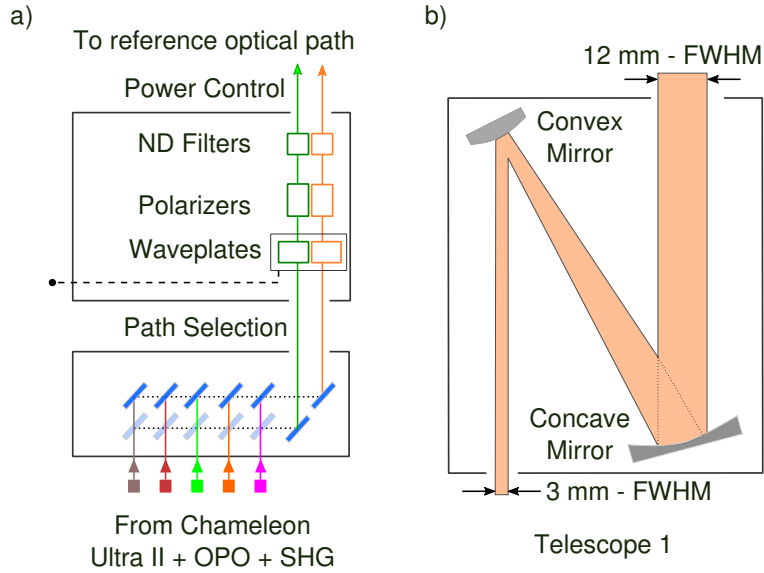


FIGURE 3.2: Schematic of the laser output, highlighting optical path selection and power control. a) The optical outputs can be conveniently selected and aligned to a reference path with two parallel sets of silver-coated flat mirrors on magnetic mounts; b) A 2f reflective telescope Altechna 6-RBE-Tx4-S with a magnification of 4 expands the optical beams to reduce the optical density and increase the divergence length.

oscillator OPO (2.). This system uses the nonlinear optical response of a periodically-poled nonlinear crystal to tunably down-convert the 800 nm pump into a NIR signal between 1050 - 1600 nm, and a IR idler between 2 μm and 4 μm . The lengths of the OPO and TiSaph cavities are identical, so that the signal beam is a femtosecond pulse train with the same 80 MHz repetition rate of the pump. This is particularly useful in pump-probe experiments (e.g. sum-frequency generation or four-wave mixing), where the temporal and spatial overlap between the interacting wave and the nonlinear medium is essential to observe their nonlinear interaction.

The central frequency emitted from the OPO cavity can be tuned by combining an active control of the cavity length and well as of the angle-dependent dispersion of the nonlinear crystal. The process is fully automatic and settings can be either accessed via the system controller or through a custom serial communication protocol. A LabVIEW interface allows sequential wavelength adjustments as well as scripting in more convoluted experiments. The optical outputs of Ti:Sapphire and OPO are cascaded with a broadband SHG module, which can optionally be used to double their frequency and increase the experimental capabilities. The SHG module features five optical ports, two for TiSaph and OPO signal, two for their second harmonics, and one for the idler of the OPO.

In ultrafast mode-locked lasers, the laser cavity supports a large number of longitudinal modes within the gain bandwidth of the active medium. The phase relation between each mode (resulting from x,y,z) is selected so that their constructive interference leads to short and bright pulses. There exists an inverse relation between number of longitudinal modes in the cavity and duration in time where interference can be constructive. Their product, known as the time-bandwidth product, is ultimately bound by Fourier relations and is minimum for Gaussian waveforms (transform-limited). The laser light emitted in such systems is inherently pulsed

with a low duty-cycle, meaning that a bright light pulse is always followed by a period of darkness. The extent of the latter (and thus the repetition rate of the laser) is dictated by the round-trip-time of the pulse inside the cavity, and thus by the cavity length. If one was to use a detector with a time constant much shorter than the period of the pulse train, information on the internal features of the periodic waveform would be lost and one would detect an average power level. In practice the average power can be calculated by integrating the optical energy carried by a large number of pulses over a time T , and normalizing for the integration time T . Peak power, it is generally referred to the energy rate of a single pulse, and is therefore calculated as the total energy carried by a single pulse, divided by its duration. In the limit of very small duty-cycles (very short pulses followed by long times of dark) the peak power can be several orders of magnitude higher than the average power, which is common in ultra-fast lasers. One can therefore convert between peak and average power \hat{P} and \bar{P} in W respectively as

$$\bar{P} = \hat{P}\tau_{\text{pulse}}\nu_{\text{rep}} \quad (3.1)$$

$$\hat{P} = \frac{\bar{P}}{\tau_{\text{pulse}}\nu_{\text{rep}}} \quad (3.2)$$

Since average optical power corresponds to the energy of a single photon c , multiplied the total number of photons in time T by divided. Therefore, one can explicit the link between average photon rate \bar{R} and peak photon rate \hat{R} in Photons/s

$$\hat{R} = \frac{\bar{R}}{\tau_{\text{pulse}}\nu_{\text{rep}}} \quad (3.3)$$

$$\bar{R} = \hat{R}\tau_{\text{pulse}}\nu_{\text{rep}} \quad (3.4)$$

In experiments of nonlinear wave mixing with ultrafast laser pumps it is often required to convert between peak power and average rate of photons since the former is what drives the nonlinearity while the latter is what can be measured in the laboratory with conventional detectors

$$\bar{R} = \frac{\hat{P}}{\hbar\omega}\tau_{\text{pulse}}\nu_{\text{rep}} = \frac{\bar{P}}{\hbar\omega} \quad (3.5)$$

$$\hat{P} = \frac{\bar{R}}{\tau_{\text{pulse}}\nu_{\text{rep}}}\hbar\omega = \hat{R} \cdot \hbar\omega \quad (3.6)$$

These simple relations are key to a correct calculation of the effective $\chi^{(2)}$ from classical non linear experiments.

3.1.2 Power and Polarization control

The next elements on the table are a path selection module (4.), a power control module (5.), and an optical telescope (6.). The first module is detailed in fig. 3.2 a) and consists of an array of silver-coated mirrors on two parallel rows. Their elevation and azimuthal angles are controlled with micrometric precision and their position secured by kinematic mounts (Thorlabs KB25/M) for versatile and repeatable placements. Control of the optical power is done with a conventional stack of half-wave

plates and linear polarizers. We use high peak-power half-wave plates, optimized for different wavelengths, to cover the spectrum between 350-1700 nm. Dedicated step-motors control the orientation of the wave-plates, which can either be adjusted manually, or through a custom LabVIEW interface. The latter is useful for automatic power normalization, where the optical power at the sample is monitored in real time, and used to compensate for power fluctuations, as well as non-flat spectral responses of dichroic mirrors and other interference filters. Polarizers operate in a broad spectral range with a high extinction ratio in order to filter only the desired polarization. These are formed by Edmund Optics calcite Glan-type prisms with MgF_2 anti-reflection coatings which transmit the extraordinary beam while absorbing the reflected ordinary beam.

3.1.3 Beam size and divergence

The divergence of a collimated beam of light is inversely proportional to its diameter. As a result, small laser beams are challenging to operate across a long optical table. In order to decrease the divergence of the laser beam, we expand the beams with an optical telescope in fig. 3.1, (6). In the simplest form this is composed of two consecutive refractive lenses of different focal lengths in either Galilean or Keplerian configuration. In the Galilean configuration, the beam is focused before being collimated. An aperture placed exactly at the focus of the first lens allows to spatially clean the beam and block any spurious divergent light that may leak from the laser cavity. The Keplerian geometry features a convex lens with a negative focus to diverge the beam, followed by a concave lens with a positive focal length to collimate the beam again. While this does not allow to perform spatial cleaning of the beam, the lack of a focus avoids distortions that might arise from photo-ionization of air and is more suitable for high power laser systems. A simplified ray diagram of the telescope used is shown in fig. 3.2 b. This is a fully reflective system with a magnification of 4, since it is inherently broadband and does not suffer from chromatic aberrations.

3.1.4 Pump-probe synchronization and Autocorrelation

Optical nonlinear interactions such as $\chi^{(2)}$ or $\chi^{(3)}$ occur over femtoseconds timescales, which are orders of magnitude shorter than the time between two consecutive pulses. As a consequence, nonlinear optical mixing of a pump and a probe beam occurs only if all pulses overlap in space and time. On the other hand, individual frequency doubling and tripling (SHG and THG) of each pulse train can be observed, provided that the medium nonlinearity and light intensity is sufficiently high. In pump-probe experiments it is important that the two optical trains are synchronous, so that for any given pump pulse there is a corresponding probe pulse. Any time-invariant offset between the two can be compensated, so that temporal fluctuations of the laser cavities can be tolerated, provided that their relative offset is constant. Since the OPO is synchronously pumped with pulses from the TiSaph cavity, their round-trip times (RTTs) are identical, making them ideal for pump-probe nonlinear mixing. However, a TiSaph pulse that travels inside the OPO cavity accumulates an additional 1.6 m optical path compared to one that reached the optical table directly.

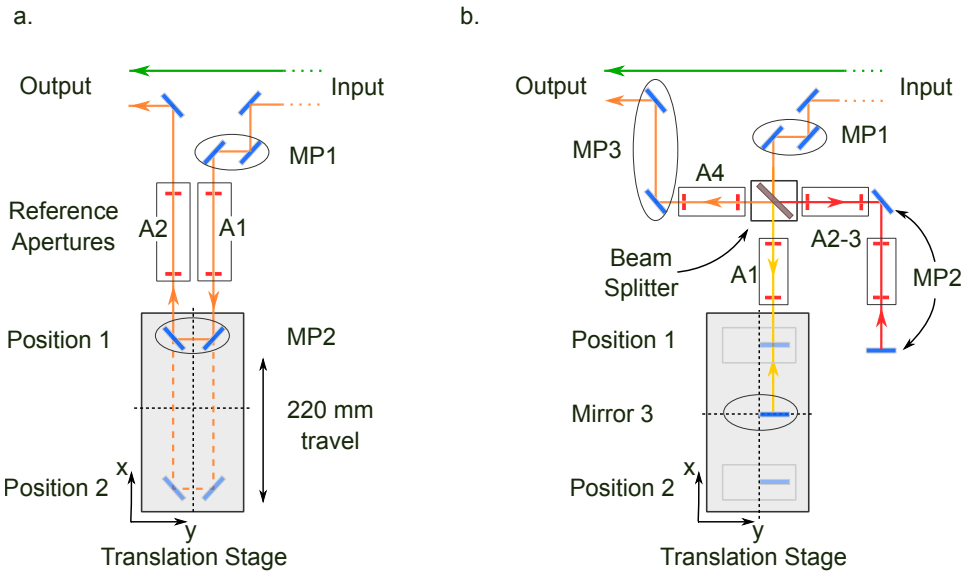


FIGURE 3.3: Schematics of the optical delay stage and its two configurations a) as a delay stage for the optical retardation of the probe pulse train relative to the pump, and b) for the measurement of the autocorrelation of the green pulse train. MP: mirror pair, A: Reference apertures.

The most accurate way to control the arrival time of an optical pulse on a reference sample is by varying the length of its optical path in free-space. This is achieved with an optical delay line (7.) composed of two 45° mirrors mounted on a linear translation stage controlled by a precision step motor. This system is also used in frequency-resolved optical gating (FROG) described in section 4.4, where pulses are interfered with themselves to measure their temporal duration and phase. The optical arrangement is shown in fig. 3.3 for pulse train synchronization (a) and for autocorrelation and FROG (b). In both applications optical temporal alignment can only be achieved if the resolution of the translation stage is much larger than the pulse duration with small backlash and good repeatability. Our optical delay stage has a quoted resolution of around 1.5 fs, a travel range of 220 mm and the ability to be driven at high speeds compared to stepper motor stages. The minimum delay is thus 3 fs, roughly twice as much as its resolution. The position of the two 45° mirrors can either be adjusted manually by deactivating the servo-control, or controlled by a LabVIEW interface through the calls to the instrument original driver.

Any small change in the optical paths can disrupt the time-overlap with a consequent loss of signal. For instance, a 90 μm -thick quartz window with an index of refraction ≈ 1.5 introduces an extra delay of ≈ 150 fs compared to one that propagates through the same length in air. By comparing this to the pulse width (see fig. 4.11 for measured via FROG traces and retrieved pulses) this can significantly perturb the temporal overlap.

Alignment for pump-probe synchronization

In most free-space nonlinear optics experiments, laser beams must be focused with high NA infinity-corrected objectives in order to reach the necessary light intensity. A routine procedure in these setups is to accurately position the focus of a laser

beam across the focal plane of the illumination lens. This is done by leveraging the translation property of the Fourier transform, which relates angular shifts in one space to translations in the conjugated space.

A pair of mirrors are generally used to control the incidence angle of the beams on the lenses, thus controlling the illumination. At the same time, unwanted angular drifts ϵ must be minimized in order to keep the illumination stable over time. This is notoriously more difficult to do in a setup with moving parts, such as an optical delay line. The largest tolerated angular drift can be calculated knowing the distance between the output of the delay line and the illumination stage in fig. 3.1 (≈ 10 m) and the diameter of a typical pupil (4 mm). It is immediate to see that an angular shift of 1° (0.017 rad) between position 1 and position 2 in fig. 3.3 a) would result in 17 cm shift at the Fourier plane of the objective, with consequent loss of coupling. Limiting such displacement to a fraction of a typical pupil diameter (say 1 mm) requires that $\epsilon \leq 0.005^\circ$. This can only be achieved if the laser beam is parallel to the direction of motion of the back-reflecting mirrors (x axis in fig. 3.3 a), both at the input and output of the delay line. The idea is that if the delay stage moves along x and the input beam is parallel to x, the angle of the output beam will not be affected by the position of MP2.

A useful technique is to use the patterned grid of anchor-points on the optical table as a reference for the linear stage as well as two sets of reference apertures A1 and A2. The most effective way to go about it is sequentially ensuring that in each segment the beam is parallel to either of the two symmetry axis of the translation stage (black dashed lines of fig. 3.3). We start from the mirror pair MP1 in fig. 3.3 a) and align the beam to the apertures A1. We then use the moving pair MP2 to align to the reference apertures A2. A way to test the quality of the alignment is to measure the power difference behind a partially-close aperture in A2 when the linear stage is at the two extremes of its range. Ideally, such variation is zero. In practice this is never the case due to the intrinsic divergence of the laser beams. If the divergence of the beam is measured, one can calculate how much its diameter would increase over a total length of $220\text{ mm} \times 2 = 0.44\text{ m}$ and estimate the expected power difference between the two extremes of the range. It is important to remember that this technique yields accurate results only if under the assumption that the transversal profile of the pulse is Gaussian, or any other functional form with a single maximum.

The final test is to image with a CCD the laser spot focused on a reference target (mirror) while toggling the delay stage between its two extremes. When done correctly, the overlap at the sample plane is maintained within 1/10 of the spot diameter FWHM when the delay stage is moved from one extreme to another of its range.

Alignment for autocorrelation

The alignment of the interferometer in fig. 3.3 b) follows the same general principles. Since femtosecond pulses are only a few tens of microns long, their autocorrelation typically scans over a few hundreds of microns, thus relaxing the requirement on ϵ . However, there are four ports to align which makes the process a bit more convoluted. One approach is to align the input beam to the apertures A1 which are positioned parallel to the x axis of the linear stage. This can be done conveniently via the mirror pair MP1 while blocking the left and right ports of the beam splitter to avoid distracting multiple reflections. We then adjust the moving mirror (Mirror 3 in fig. 3.3 b)) to ensure that the reflected beam is also aligned to A1. However,

discerning the incoming from the reflected beam can be challenging. A strategy is to follow the reflected beam through its backward path towards the laser with a semi-transparent target and maximize the overlap of the forward and backwards one. Care must be taken to avoid a perfect alignment of mirror 3 as the reflected power could enter the cavity and perturb the mode-locking. The azimuthal orientation of the beam splitter can now be adjusted so that the first reflection is aligned to A2 and the second reflection (the one coming back from mirror 3 and reflecting off to the left) aligns to A4. As for the variable arm, it is important the direct and reflected beams on the fixed arm of the interferometer are perfectly collinear. The mirror pair (MP2) in the fixed arm of the interferometer of fig. 3.3 b)) can be used to ensure that this is done correctly. The output of the interferometer should be two beams perfectly aligned to A4. Any further alignment to the rest of the optical table can be done using the mirror pair MP3.

3.1.5 Integrated SPDC source

In chapter 4 we describe the generation and measurement of energy-time entangled photon-pairs from atomically-thick nonlinear materials via a process of spontaneous parametric downconversion. Since these are generated at the same time, their simultaneity can be measured with a single photon HBT interferometer (see section 2.2.2). In its basic form, this consists of a beam-splitter, two single-photon detectors and a time interval analyzer. The relative time difference between consecutive photo-counts is analyzed in a histogram, which upon normalization, yields the second-order correlation function of the light source $g^2(\tau)$ as detailed in section 2.2.2.

Full system-tests (optical and electrical) require a light source with well known temporal statistics, possibly with distinct features in its intensity autocorrelation function. Although ambient light from incandescent or fluorescent lamps is a source of Super-Poissonian light, its flat autocorrelation function makes it hard to discern bugs in the time-stamp processing routines from its intrinsic intensity variations. The same holds for light from an attenuated laser (Poissonian), with the exception of a pulsed laser source which has a periodic intensity autocorrelation. However, this periodicity means that time differences between two channels are only accurate within multiples of the repetition period of the laser, which for an 80 MHz mode-locked TiSaph cavity is 12.5 ns. Moreover, filters may introduce optical reflections and introduce artifacts on the coincidence histogram.

One way to unambiguously measure the relative delay between channels is to generate a pair of energy-time entangled photon pairs and send them to two different detectors. To this end, we used a commercial integrated SPDC source pumped at 785 nm, to generate photon-pairs at 1570 nm with rates on the order of a tens of kHz. Pairs are then split probabilistically at a beam splitter and detected, yielding a periodic histogram, with a bright dominant peak and a number of size-peaks equally spaced of exactly the laser period. This constitutes an integration test, that is routinely performed before any coincidence measurement to assess the position in the histogram that corresponds to two simultaneously generated photons. Since this is the same energy range expected in all SPDC experiments of chapter 4, the same SPDC source can be used for a full integration test and confirm the expected inverse quadratic scaling of the rate of true coincidences with loss.

This SPDC source is also used to accurately measure the time-delay introduced by any optical element, and was instrumental in the calibration of a gated coincidence

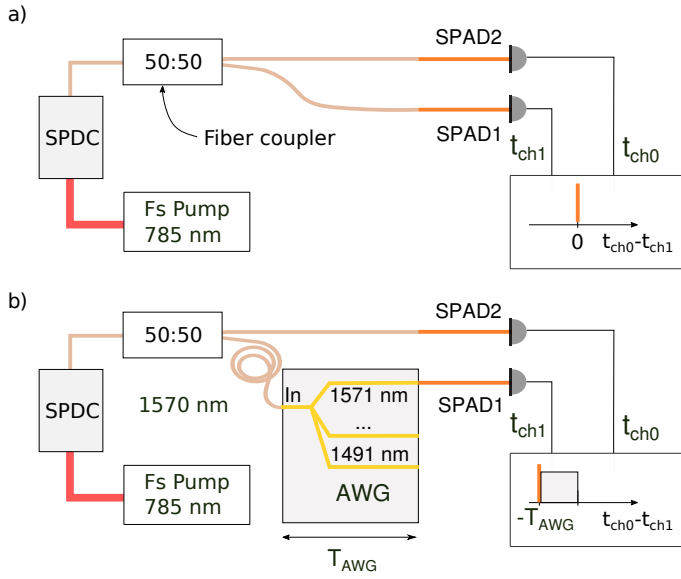


FIGURE 3.4: Entangled photon pairs from an integrated SPDC crystal can be used to accurately measure the propagation delay in a passive fiber AWG. a) A pump at 785 nm spontaneously downconverts into pairs of signal and idler photons around 1570 nm which are analyzed with a fiber HBT interferometer. Since optical and electronic paths are identical, coincidences are detected at $\tau = 0$. b) When the AWG is connected to one arm of the fiber coupler, the coincidence peak shifts of an amount equal to the optical path delay introduced. The jitter of the electronics limits the accuracy of the measurement.

measurement as described in section 3.7. The example shown in fig. 3.4 measures the optical path delay introduced by a fiber-coupled array waveguide grating (AWG) (20 nm channels) for detection of telecom photon pairs. Because optical and electronic paths are identical, coincidences are normally detected at $\tau = 0$. Any element connected between one output port of the 50:50 coupler and its associated detector shifts the coincidence peak by the optical path delay introduced. Crucially, the measurement is only limited by the jitter of the electronics.

3.1.6 Illumination and Collection

The study of light-matter interactions at the nanometer scale requires high-quality imaging systems and precise motion control. The central part of our optical setup is an off-the-shelf inverted microscope (Nikon Eclipse Ti-U), optimized for imaging in the visible part of the optical spectrum (shaded rectangle in the center of fig. 3.5). Samples can be moved with nanometer accuracy, thanks to a piezoelectric stage (90 μm range and nanometer accuracy and repeatability), and a long-range computer-actuated x-y stage. Sample positioning can be manually activated or computer controlled, thus enabling automatic light coupling and power measurement routines. The 3D confocal laser-scanning system described in section 3.8, shows an example of how integration between sample positioning and light detection leads to high resolution single-photon imaging.

A number of modules were designed and built around the inverted microscope to increase the breath of the possible measurements. Laser light can access both

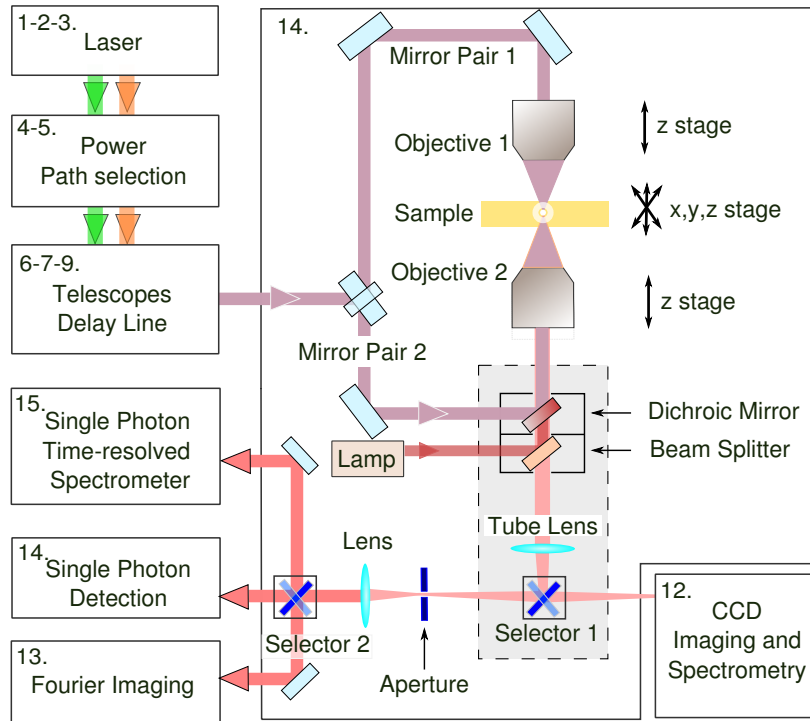


FIGURE 3.5: Schematic of the illumination and collection setup and how it interfaces with the rest of the setup as outlined in fig. 3.1. Dashed shaded rectangle: Nikon Eclipse Ti-U inverted microscope. Sample position is controlled with a computer-interfaced x,y,z stage and can be illuminated on either side. Light is collected through objective 2, focused via a tube lens and directed either to the left for single-photon detection and Fourier imaging (13-14-15.) or to the right for imaging and spectroscopy (12.).

sides of the sample via two separate objectives. Two rotating plates are used to accurately position dichroic mirrors, beam splitters and filters in the microscope tube. The top holder generally uses a dichroic mirror to reflect laser light towards the sample, while simultaneously collecting the emission light. Bright-field illumination is performed by loosely-focusing broadband incoherent light from a mercury lamp on the objective pupil through a beam splitter placed in the second holder.

The Nikon Eclipse Ti-U is designed to be used with infinitely corrected objectives, meaning that optical aberrations are corrected when the sample is placed at a distance f_0 from the objective (f_0 : objective focal length). In particular, when a scatterer is placed at the focal plane of a thin lens, the radiated far-field is mapped on the image plane at an infinite distance from the lens. As in any Fourier transform, information is preserved and uncertainty in direct space (position) is traded with uncertainty in spatial frequency (momentum). On the object plane one finds low uncertainty in position and highly uncertainty in momentum (omni-directional emission with several spatial frequencies). Spatial information is then restored by means of the *tube lens* which re-creates the image on a camera or sensor. Selector 1 in fig. 3.5 directs light to either imaging and spectroscopy tools (12.), described in section 3.1.7, or to Fourier imaging and single-photon detection (13-14-15.), described in sections 3.1.8 to 3.1.10. On the left-hand side, a removable spatial filter (aperture) performs confocal imaging. This is a high-precision circular window carefully aligned

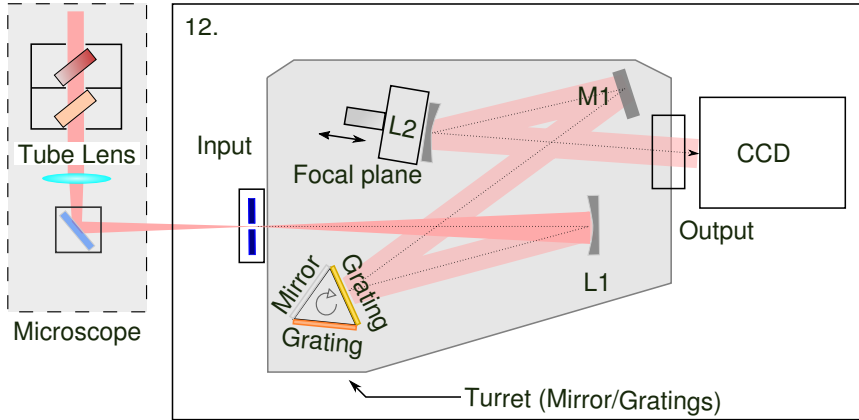


FIGURE 3.6: Schematic of the spectrograph and imaging system IsoPlane SCT320 . A rotating turret exposes either a mirror or two gratings to the collimating lens L1, while the folding mirror M1 directs the collimated beam to lens L2 which reconstructs the image on the CCD sensor.

on the image plane of the Tube Lens as detailed in section 3.8.1. This entire system allows to rapidly switch from imaging to spectroscopy and analyze intensity, polarization, energy and temporal statistics of any light source.

3.1.7 Imaging and Spectroscopy

Figure 3.6 shows a schematic of the spectrograph and imaging system represented as module 12 in figs. 3.1 and 3.5. It is a fully-reflective system with a focal length of 320 nm and a large focal plane size (27 mm x 14 mm). It features two interchangeable triple-facet turrets, one for the visible and one for the near infrared. Each turret has one metallic flat mirror for imaging and two metallic gratings, one with 1200 groove/mm (*high* resolution), and one with 600 groove/mm (*low* resolution). The turret is controlled by a step-motor with a resolution of ± 0.2 nm (± 0.05 nm repeatability) with fully-automated alignment. In high-resolution mode the maximum dispersion is 0.048 nm/pixel assuming a pixel size of 13 μm . A grating-based spectrometer transforms spectral information into space information. The advantage of a fully reflective design with large diffracting areas is low astigmatism at all wavelengths and higher fluence when imaging very narrow-line spectra. In spectrometer mode, light is diffracted by a variable vertical aperture with a minimum size of 10 μm and propagates through to L1. Since its distance from the aperture is equal to its focal length, light rays that reach the turret are collimated towards the flat grating on the turret at an incidence angle α . Each spectral component at a wavelength λ leaves the surface of the grating at an angle β , following to the grating equations:

$$m\lambda = d(\sin \alpha + \sin \beta), \quad (3.7)$$

or alternatively:

$$\beta = \arcsin \left(\frac{m\lambda}{d} - \sin \alpha \right), \quad (3.8)$$

where m is an integer and d is the grating period. Each spectral component stays collimated until it is focused by L2 (via the folding mirror M1) onto the image on the CCD sensor. For a fixed α , longer wavelengths will be diffracted at larger angles

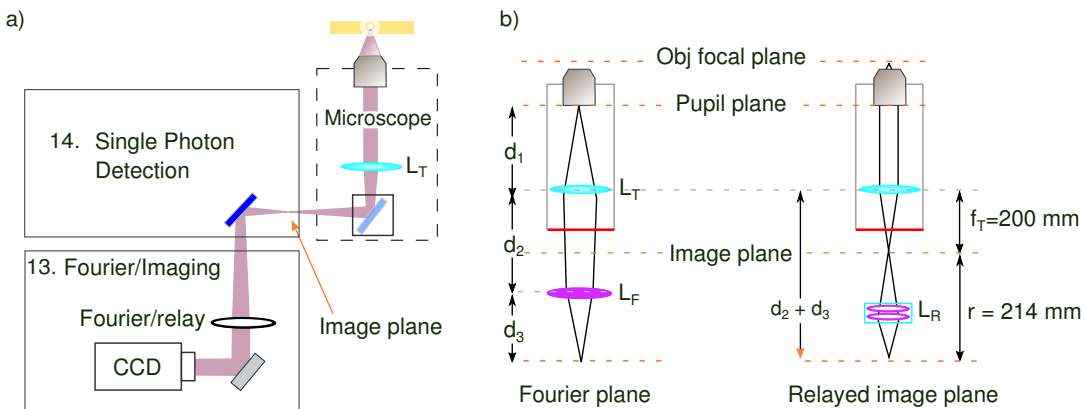


FIGURE 3.7: Schematic of the Fourier and Imaging system module in section 3.1, built to measure and control the illumination angle of laser beams incident on samples. a) The image plane of the objective is replicated by the tube lens outside the microscope body where a mirror directs light either to a 1:1 optical relay or a Fourier lens to image the objective pupil. b) Qualitative optical ray tracing diagrams for each case shown that the Fourier lens is calculated so that, together with the microscope tube lens, it images the pupil of the objective on the CCD array.

and thereby be detected by pixels further away from the center of the array. An open aperture removes the assumption that α is constant for a given wavelength, which degrades resolution.

To see how this can be problematic we recall that diffraction puts a lower-bound of $1.22\lambda/\text{NA}$ on the spatial extent of a light source, which in a magnified system corresponds to $\approx 100 \mu\text{m}$ in the visible/near-infrared. However, typical sources are not diffraction limited and are often embedded in a scattering medium which increases their effective volume. In imaging mode, the mirror side of the turret is rotated towards L1 and the aperture pulled away from the optical path.

Wavelength calibration is performed with a stable and well-characterized light source (IntelliCal) while intensity calibration requires ad additional software. Imaging is performed with two bi-dimensional CCD arrays based on Silicon and InGaAs as detailed in section 3.2. The complete system is controlled by LightField v6.1 which controls all aspects of the measurement such as exposure-time, camera gain, wavelength and intensity calibrations. The software provides an interface that allows automating measurements from any LabVIEW virtual interface. Logging of the experiment details can be done through experiment configuration files that can be modified and saved to memory. The software also deals with background acquisition and automatic subtraction of background files and filters for cosmic rays.

3.1.8 Fourier imaging

Being able to measure and control the angle of light incident onto a sample is important in a wide range of experimental settings. Some examples are structured illumination [162] (which increases optical resolution), filtering to increase the measurement signal to noise ratio, mode profiling in integrated photonic waveguides, optimization of grating coupling. Normally, accessing the Fourier plane and thus measuring the emission/illumination angles, is as easy as directly imaging the back-focal plane (BFP) or *pupil* of the objective (fig. 3.5). However, off-the shelf systems

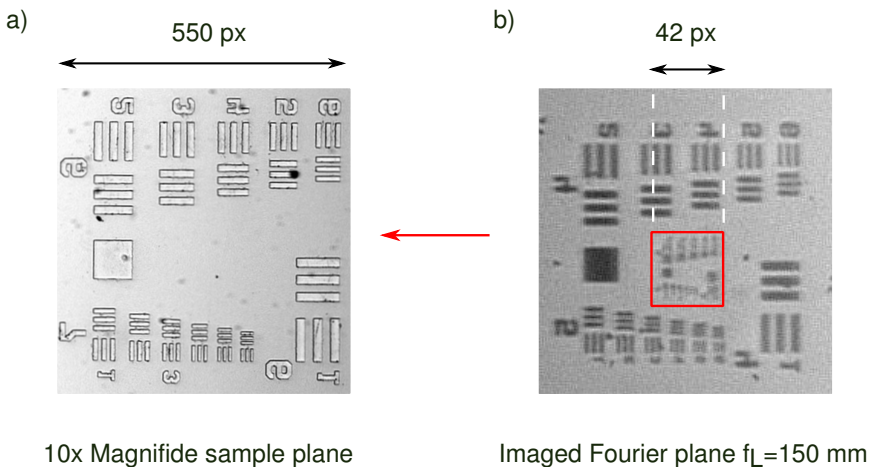


FIGURE 3.8: The magnification introduced by L_F can be confirmed experimentally by using a test target and a CCD camera: a) target imaged with a 10X Nikon objective through the tube lens L_T , b) objective replaced with the target sample and imaged through $f_F = 150$ mm via L_T on the same CCD camera.

rarely provide access to the tube lens which is often used as an additional degree of freedom to correct for aberrations. In the interest of reliable optical alignment and consistent image quality, our approach focused on relaying the image/Fourier planes outside the microscope.

Here we describe the design of the Fourier lens as a way to directly measure the angle of emission/illumination of light on a sample. For a description of techniques to control the angle, we refer the reader to section 3.4.

The goal is to choose a fixed position for a CCD camera, and design the optics so that the simple insertion of lens in the optical path allows to switch from imaging the sample plane to imaging the pupil plane of the objective. This lens will need to operate in synergy with the tube lens to form a new lens with the correct effective focal lens to relay the pupil (object) onto the CCD camera. In practice however, the system is part of a more complex structure as shown in fig. 3.10 and the image plane of the objective in our system is only 77 mm away from the body of the microscope (red line in fig. 3.7). This additional constraint requires to move the CCD sensor away from the microscope body and to map both the Fourier plane and the image plane onto it for conventional imaging.

A high level view of the system is shown in fig. 3.7 a). The image plane created by the objective lens L_O and the tube lens L_T is relayed onto the CCD sensor with a 1:1 achromatic relay lens L_R (Edmund Optics). When this is replaced with a suitable Fourier lens L_F , one can directly image the Fourier plane of the objective. Figure 3.7 b) shows two qualitative ray-tracing diagrams of the unfolded optical system comprising the objective and the tube lens placed at a distance d_1 from the pupil plane and with a focal length $f_T = 200$ mm. When the optics are dimensioned correctly, both the Fourier plane (left) and the image plane (right) are relayed at a distance $d_2 + d_3$ from L_T .

In order to validate these analytical results we perform an imaging test with a resolution target (Thorlabs R1DS1P) which is first imaged with a known objective (Nikon CFI Plan Fluor 10X) through the tube lens L_T resulting in a feature size of $550/10 =$

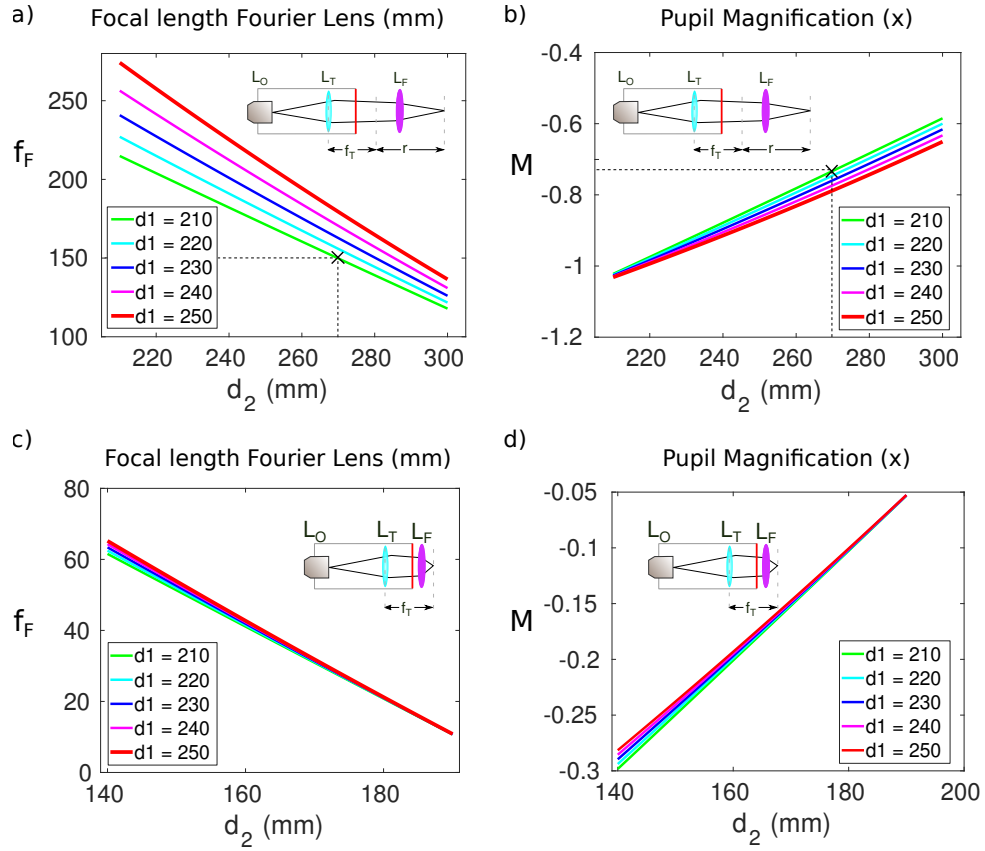


FIGURE 3.9: Focal length eq. (3.12) and magnification eq. (3.13) for the Fourier lens L_F when placed before a-b) and after the focal length of the tube lens c-d). Uncertainty on d_1 has only a minor impact on the optical magnification which is negative (inverted image). Design b-c) allows translate both image planes of a distance r . This facilitates the integration with the rest of the optical table, and introduces the smallest image compression thus facilitating the selection of lunch angles.

55 pixels in real space as shown in fig. 3.8 a). The objective is then replaced with the same target to serve as a reference for the pupil plane and is imaged with L_F yielding a feature size of 42 pixels. This corresponds to a measured magnification of $|M| = 0.76$ which is close to the analytical solution of $|M| = 0.73$

Fourier Lens Design

The sum of front and back focal lengths of Edmund Optics (90 mm) plus its physical length (34 mm) is $r = d_2 + d_3 - f_T = 214$ mm. In order to calculate the focal length of the Fourier lens L_F , we start from the thin-lens equation

$$\frac{1}{f} = \frac{1}{o} + \frac{1}{i} \quad (3.9)$$

where o and i are respectively the distance of the object and image from a lens of focal length f . Recalling that our object is the pupil plane at a distance $o_1 = d_1$ from L_T whose focal length is $f_1 = f_T = 200$ mm, we find the first intermediate image at

a distance i_1

$$i_1 = \frac{d_1 f_T}{d_1 - f_T} \quad (3.10)$$

Since we have a system of two lenses and propagation is linear, we can then propagate this new image onto the Fourier lens. With reference to fig. 3.7 this will now be at $o_2 = d_2 - I_1$ from the Fourier lens which then yields an image at

$$i_F = \frac{(d_2 - i_1) f_F}{d_2 - i_1 - f_F} \quad (3.11)$$

Recalling that we want the pupil to be imaged at a distance d_3 from the Fourier lens, we impose $i_F = d_3 = r + f_T - d_2$ and solve for f_F :

$$f_F = \frac{d_3 d_1 (d_2 - 2f_T)}{(d_2 + d_3) d_1 f_T - d_1 f_T} \quad (3.12)$$

The combined magnification for the two lenses is the product of the magnification of each lens, or simply the ratio of the back focal length over the front focal length of the equivalent lens. It can be shown that the expression takes the form [163]

$$M_F = \frac{f_T d_3}{d_2 (d_1 - f_T) - (d_1 f_T)} \quad (3.13)$$

Figure 3.9 a-b) shows results for f_F in a realistic range of focal lengths as a function of the distance d_2 . Since the microscope is designed to operate with infinity corrected objectives, the tube length d_1 can be in principle arbitrary so this is not reported in any manual or specification. Although the tube lens in Nikon Eclipse Ti-U cannot be taken out it is possible to confirm its position by direct inspection and take a reference of its position. Under the assumption that the pupil plane coincides with the edge of the objective closest to L_T , one can first image a test sample and measure d_1 directly. However, since the system is designed to accept objectives with different makes (and thus different para-focal lengths), d_1 can vary within ± 10 mm. If we account for a 5% measurement error we can safely place the estimate at $d_1 = (225 \pm 20)$ mm. The effect of this uncertainty is shown in fig. 3.9 where results are presented for a range of values for d_1 .

If we designed the Fourier lens so that $d_2 > f_T$ but imposing the same constraint on $d_2 + d_3$ we would require much shorter f_F and would experience a total magnification of around 0.2 as show in fig. 3.9 c-d). Since typical sizes for high-NA objectives are on the order of a few millimeters, the former solution is preferred. Practical considerations for L_F led to choose an off-the-shelf cemented doublets with NIR anti-reflection coating with $f_F = 150$ mm (Thorlabs AC254-150-B-ML). From fig. 3.9 a-b) this is expected to be positioned at $d_2 = 270$ mm from L_T and result in a magnification of the pupil of $|M| = 0.73$. These results are intended to provide a first order approximation of the focal lengths required. With real lenses the results are bound to deviate from these plots. In fact, the measured magnification in section 3.1.8 was found to be $|M| = 0.76$.

Any discrepancy is attributed to the propagation of uncertainties, the non-strict validity of the thin-lens assumption as well as residual alignment errors. One needs to take into account the thickness of the lens, particularly when using cemented achromatic doublets. Typically vendors provide detailed information on the glass

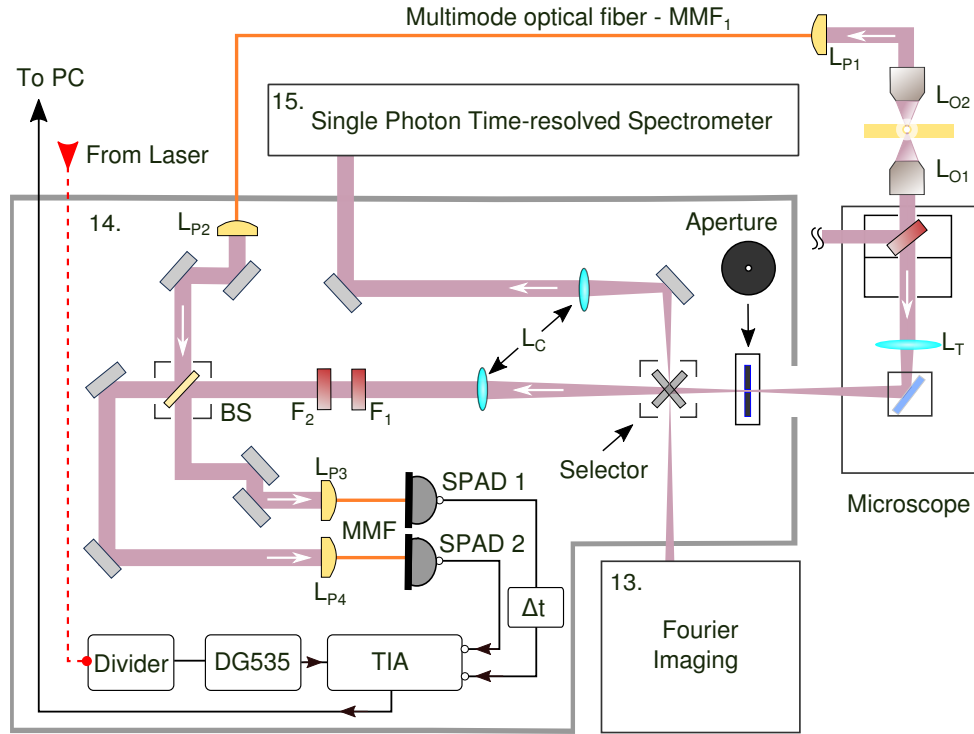


FIGURE 3.10: Schematic of the single-photon detection module. Light statistics can be measured with an HBT interferometer composed of a beam splitter (BS), a pair of visible/near-infrared free-running single-photon avalanche photodiode (SPADs) and a time-interval analyzer (TIA) which is connected to a PC for data-acquisition and processing. A pair of lenses (L_C, L_P) act as a telescope to achieve a 1:1 mapping between the image plane and the core of multi-mode fibers MMFs. A frequency-divider and pulse shaper can be used to gate detections in post-processing and enable ultra-low noise measurements. A small aperture may be used to filter the image plane and perform confocal imaging. Finally, the radiation pattern of the emission can be captured via Fourier imaging (setup 13.) or the intensity analyzed in energy and time (setup 15.) by means of an optical selector.

type, curvature and roughness in order to aid accurate modeling. Detailed calculations of the optical aberrations can be performed with free and open source options such as ‘rayopt’ written in Python¹, ‘OpticalRayTracer’ written in Java² one of the many licensed optical optimization environments such as ‘Zemax’. Particular useful for the impatient experimentalist as well as for the optics-newbie is ‘ray-optics’, a qualitative simulator written in JavaScript and running in the browser³.

3.1.9 Single-Photon Detection

The setup for single-photon detection couples to the side of the microscope of fig. 3.5 as shown schematically in fig. 3.10. Sample illumination and light collection is enabled on both sides of the sample plane as indicated by the pair of lenses L_{O2} and L_{O1} . This is particularly useful when samples are deposited on transparent substrates thinner than the Rayleigh range of the objective.

¹github repository ‘quartiq’ /rayopt

²<https://arachnoid.com/OpticalRayTracer/>

³github repository ‘ricktu288’ /ray-optics/simulator/

The first element after the tube lens L_T is a circularly-symmetric aperture, which works as a spatial filter. When its size is smaller than the point-spread-function of the optical system (given by the combination of the objective and the operating wavelength) both the axial and lateral resolution of the optical system increases as detailed in section 3.8. In the context of the measurements presented in 4, this was used to ensure that the pair of single-photon detectors collect light only from the illuminated area, thus reducing any ambient light, as well as spurious emission originating from areas immediately surrounding the illumination point. The second element is a four-port optical selector to direct light to either the single-photon spectrometer described in section 3.1.10, or to the Fourier imaging system detailed in section 3.1.8 or to a pair of visible/near-infrared single-photon detectors (SPADs) as detailed in section 3.3. This is simply made by pairing a flat mirror (PFR10-P01) with a cubic joint (ThorLabs CM1DCH/M). Alignment is optimized with pairs of protected silver-coated elliptical mirrors (PFE10-P01) fitted in suitable two-axis kinematic mounts (KCB1EC/M).

The divergent light coming from the tube lens of the microscope is first collimated with L_C (achromatic doublet AC254-300-X-ML - Thorlabs), and then delivered to the SPADs by means of multi-mode fibers (MMFs). Light is focused on the core of the MMFs with fiber-coupled reflective parabolic lenses L_{Px} in fig. 3.10, controlled with manual stages (KC1-S ThorLabs). The space between L_C and the beam-splitter is dedicated to interference filters (F_1, F_2), polarizers, isolators and all optical components used to condition light before detection.

The time-interval analyzer (TIA) is a four-channel SensL HRM-TDC , with a resolution of 66 ps root-mean square and a maximum combined detection rate of 4.5 MHz. Timestamps are sent to the PC in binary format and parsed by a dedicated LabVIEW and Python routine. A fast photodiode inside the Chameleon Ultra II samples the train of mode-locked pulses and returns a raw RF reference signal at 80 MHz. This is then converted to a rate of 125 kHz by the FPGA via an off-the-shelf pulse-picker controller. The down-clocked waveform is then fed into an active delay generator DG-645 , which outputs a synchronous train of 12.5 V and 100 ns TTL pulses ready to be detected by the TIA.

When the same light flux is detected with two independent SPADs, it is possible to measure the second order correlation function $g^2(\tau)$. We do this by time-tagging the photodetections with a time-interval analyzer (TIA) and process the data to construct a histogram of delays. For a more detailed description of this we refer the reader to section 3.6.

If available, the periodic reference signal from a laser cavity can be used to gate detections. Details of this can be found in section 2.2.2 where gate detection is used as a way to increase the CAR in coincidence measurements from SPDC. With the correct spatial filtering these can be used for visible/near infrared confocal scanning laser microscopy as described in section 3.8. Optionally, the beam splitter may be replaced with a dichroic mirror for simultaneous visible and near-infrared imaging. Single-photon detection in the visible requires a dark-count limited background. To this end, the structure of is fitted with a light-tight structure (ThorLabs BK5) which offers discrete mechanical strength and excellent opacity to visible and near-infrared light.

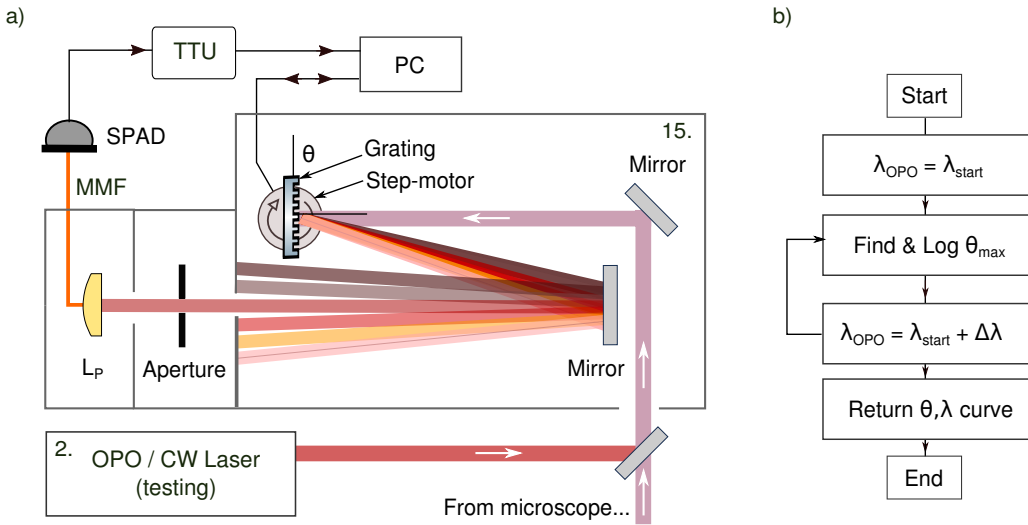


FIGURE 3.11: A dispersive element (grating), a single-photon avalanche photodiode (SPAD) and a time-interval analyzer (TTA) are arranged to form a time-correlated single-photon spectrometer. The module can be used in cascade to the confocal laser-scanning microscope (section 3.8), enabling frequency/time-resolved 3D confocal imaging. a) Optical layout: a collimated input beam is dispersed by a rotating metallic grating while a subset of its spectral content couples to a fiber through a reflective lens L_P . Calibration is performed using a reference and tunable source (OPO cavity/CW laser). b) Pseudo-code for the angle/wavelength calibration in labVIEW.

3.1.10 Time-correlated single-photon spectrometer

The visible CCD sensors described in section 3.2 have peak quantum efficiencies in excess of 70 %, low thermal and read-out noise, and large capacity wells. As a result, given a constant input photon-flux, longer integration times allow to accumulate the signal intensity leading to images with a higher SNR (SNR). The same is not true for near-infrared InGaAs CCDs, whose noise is dominated by dark counts and the read-out noise is typically much larger. While detection-gating can be useful, it requires additional hardware to synchronize detections to the arrival of the signal. Another limitation of CCDs is that, being designed to accumulate photo-electrons, they cannot provide information on the time of arrival of a photon, which is key to measuring molecule lifetimes (material-science, biology), light statistics (astronomy and quantum optics), as well as time of flight (eye-safe Lidars).

In order to overcome these limitations, we designed a time-correlated spectrometer (SPTCS), capable of measuring time-spectrum information in the near-infrared with superior SNR compared to the commercial imaging and spectroscopy system described in fig. 3.6. This can be cascaded with the scanning laser optical microscope, enabling 3D confocal imaging resolved in both frequency and time⁴. A schematic of the optical setup is shown in fig. 3.11 a), which corresponds to module 15 of fig. 3.1. Photo-detections are performed with the near-infrared ID230 SPADs (section 3.3), time-stamped with the TIA described in fig. 3.10 and analyzed by a labVIEW routine. The collimated input beam is dispersed by a rotating metallic grating while

⁴The dimensionality of the measurement could further grow if one used two SPADs with complementary polarizers (and polarization-maintaining fibers).

a subset of its spectral content couples to a MMF through a reflective lens L_P . If the spectral content of the input photon flux is constant, incremental rotations of the grating $\Delta\theta$ map to different wavelength ranges $\Delta\lambda$ being detected. The calibration procedure consists of tuning the OPO to a range of different wavelengths, and then comparing the spectra measured with the grating-based spectrometer, with those acquired from the IsoPlane SCT320 as a reference. The result is an angle-wavelength calibration, which allows to map a wavelength range to a set of angles.

The sensitivity of a spectrometer is a measurement of the smallest amount of photon flux Φ_{px} that can be detected above noise. Taking into account the quantum efficiency and gain of the Nirvana 640 (fig. 3.12) in free-running mode we find $\Phi_{px} = 1 \times 10^4 \text{ ph/s/px}$. In SPTCS this is $\Phi_{px} = 200 \cdot 2 = 4 \times 10^2 \text{ ph/s/px}$, and thus corresponds to a 20-fold increase in sensitivity (dark-count rate of 20 Hz and measured coupling loss of 50%). As in any grating-based spectrometers, the pixel resolution is a linear function of the distance between the detector and the diffracting element. For this particular implementation the measured resolution is 2 nm, which may be reduced to a value comparable to the IsoPlane SCT320 at the expense of the device footprint.

3.1.11 Other laser sources

Fianium SC400 is a high power fiber laser generating supercontinuum radiation between 400-2100 nm and 4 W average power, pulsedwidth 5 ps and 20 MHz repetition rate. Other laser sources used include a Toptica DL pro 0205446 CW tunable laser, 753-817 nm with 0.1 nm accuracy and 30 GHz mode-hop free tuning, a C-band Photonetics 1430-1650 nm, and a 785 nm laser used for continuous-wave pumping of the SPDC crystal described in section 3.1.5.

3.2 Visible and NIR CCDs

The imaging system of section 3.1.7 can be used for both imaging and spectroscopy. Detection is performed with bi dimensional CCD arrays, (Si Pixis 1024-BExcelon and InGaAs Nirvana 640), with a combined detection range that spans 1.5 μm as shown in fig. 3.12. The fundamental building block of a CCD camera is a bi-dimensional array of photo-active elements or capacitors, able to store electrons generated via the photoelectric effect. These are typically electrically-biased metal-oxide semiconductors that sit on a transmission layer used to transfer charges along the surface from one storage capacitor to the next. Photons incident on a single pixel of a CCD are absorbed with high probability and are converted to electrons (photo-electrons) which are then measured and rendered in a bi-dimensional intensity map or image. The ratio between the average rates of photoelectrons \bar{e} over the rate input photons \bar{p} represents the quantum efficiency η_{det} and can be interpreted as the average probability that a photon will be converted into an electron. Although the elementary units for a CCD sensor are electrons (photoelectrons), it is customary to read the output of a measurement in photo-counts or simply counts. The two are related by the gain of the detection circuitry which is specified in electrons/ADU (analog-to-digital unit), so that a gain of 10 means that 10 photoelectrons correspond to one count. If p photons are incident on a CCD with efficiency η_{det} and gain G the sensor

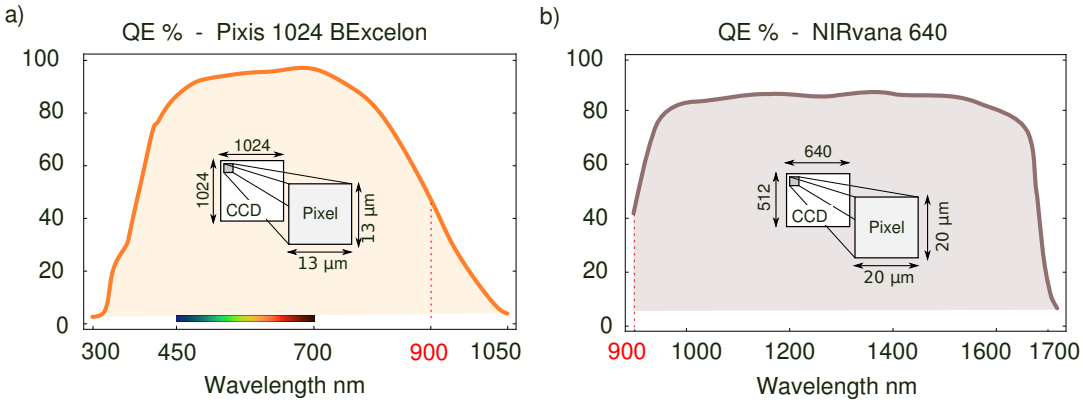


FIGURE 3.12: The combination of Pixis 1024-BExcelon and Nirvana 640 CCD sensors allows detection of a spectrum extending over $1.5\text{ }\mu\text{m}$. Quantum efficiencies are almost flat over the visible spectrum and the near-infrared, with a combined minimum of 40 % at 900 nm. Both sensor planes and pixel sizes are different between the two sensors. Together with the effective magnification provided by the objective and tube lenses in fig. 3.5 this is used to convert between pixels on the image plane and size.

will read:

$$\text{counts} = \frac{p \eta_{\text{det}}}{G} \quad (3.14)$$

This relation will be used in the calculation of the photon flux needed to achieve a target SNR in chapter 4. The gain is always greater than one and can be controlled by varying the electric bias across the p-n junction of the CCD. A high signal to noise ratio (SNR) is crucial for the measurement of faint sources of light such as those resulting from nonlinear optical mixing described in chapter 4. In a CCD matrix the pixel SNR is the ratio of the number of electrons accumulated in one pixel as a result of photo-absorption of signal photons, over those related to any noise process. Among these we can identify three dominant contributions: shot noise, thermal noise and readout noise.

Shot-noise is caused by the inherent randomness in the way photons and photoelectrons distribute in time. Photons from a perfectly stable and coherent source of light (laser above threshold) are randomly and uniformly distributed in time. Thus, the rate of photons (power) follows a Poisson distribution whose standard deviation is equal to the square root of the mean. If \bar{p} is the average photon flux, the mass probability function of the event "n photons arrive in 1 second observation time" is

$$\mathcal{P}(n) = \frac{\bar{p}^n}{n!} e^{-\bar{p}} \quad (3.15)$$

and its standard deviation is equal to the square root of the average number of photons $\sqrt{\bar{p}}$. The photoelectric effect which yields photoelectrons e is random and follows the same statistics. The shot noise, is the uncertainty in the number of photoelectrons in the integration time T is

$$N_{\text{Shot}} = \sqrt{e_{\text{signal}}} = \sqrt{e T} = \sqrt{\bar{p} \eta_{\text{det}} T} \quad (3.16)$$

The intensity registered by any detector can never be smaller than the shot-noise. *Dark noise* are detection events that are not associated to the absorption of photons.

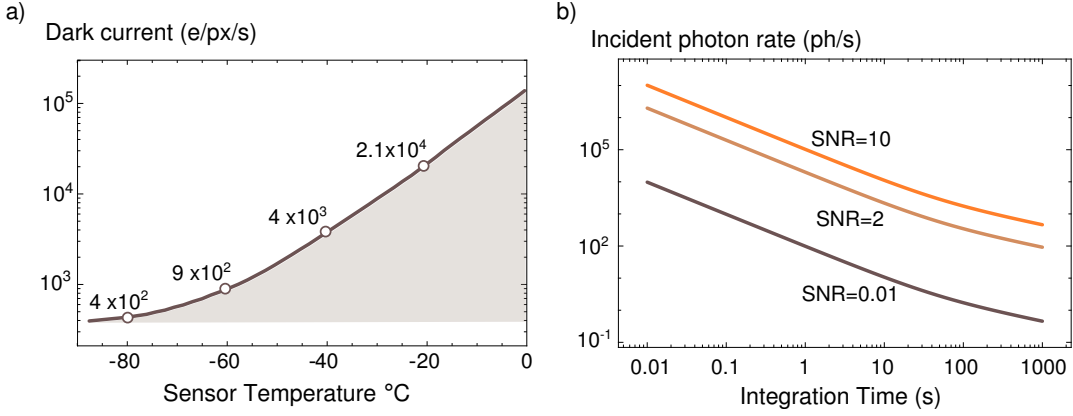


FIGURE 3.13: Dark-count rate and SNR for the InGaAs detector Nirvana 640. a) The minimum rate of photoelectrons accumulated by one pixel is $400 \text{ e}^-/\text{s}$ when cooled at -80°C , six orders of magnitude larger than the Pixis 1024-BExcelon at -70°C ($4 \times 10^{-4} \text{ e}^-/\text{s}$). b) More than 10000 photons/s are required for a SNR=2 over 1 second integration time for the Nirvana 640 at $\eta_{\text{det}} = 80\%$ with the best gain (65).

Instead, they results from the excitation of an electron from thermal fluctuations within the p-n junction of the charged coupled device. Dark counts also follow a Poisson statistics they fluctuate around their mean by as much as the square root of their mean value they are a source of noise that cannot be easily subtracted. Dark current I_{Dark} is a measurement of the magnitude of the uncertainty on the number of photoelectrons in a CCD per pixel and unit of time. For an integration time of T seconds the uncertainty in the number of photoelectrons introduced by the dark currents is equal to the square root of the total number of photoelectrons generated by photon absorption e_{signal}

$$N_{\text{Dark}} = \sqrt{I_{\text{Dark}} T} \quad (3.17)$$

As the temperature is decreased, the thermal energy in the semiconductor drops resulting in a smaller dark current. Section 3.2 (a) shows an example of dark current vs sensor temperature for a state of the art InGaAs CCD sensor Nirvana 640 from Princeton Instruments adapted from [164]. Depending on the gain this corresponds to either 400 (high gain: $1 \text{ e}^- = 1 \text{ count}$, pixel well capacity = 4×10^4), or 5600 photons (high-capacity: $1 \text{ e}^- \approx 14 \text{ counts}$, pixel well capacity = 6×10^5).

Readout Noise, which here we indicate as N_{Read} , arises from the uncertainty on the number of photoelectrons associated with quantifying the electronic signal in the CCD. It depends on the on-chip preamplifier that is used to quantify the number of electrons in each pixel. The signal to noise ratio (SNR) for a single pixel is simply the ratio of the total photoelectrons resulting from detection of *signal* photons e_{signal} over those resulting from all sources of noise

$$\text{SNR} = \frac{e_{\text{signal}}}{N_{\text{Shot}} + N_{\text{Dark}} + N_{\text{Read}}} = \frac{\bar{p} \eta_{\text{det}} T}{\sqrt{\bar{p} \eta_{\text{det}} T + I_{\text{Dark}} T + N_{\text{Read}}^2}} \quad (3.18)$$

where \bar{p} , T and η_{det} are respectively the average spherical photon-flux reaching the pixel, the integration time and quantum efficiency of the pixel. Since the grooves of the metallic gratings in the IsoPlane SCT320 (section 3.1.7) are orthogonal to the

optical table, the wavelength to angle mapping happens onto a plane parallel to the optical table. However, one rarely has a point-like source and light that reaches the CCD array typically extends vertically along a few tens of pixels. Since pixels within the same column represent the same spectral information the current that they accumulate can be combined, a process referred to *binning*. While this often increases the SNR in visible CCD arrays, InGaAs detectors have nominally larger N_{Read} and N_{Dark} and summing more rows does not necessarily improve the SNR. In a realistic scenario the incident photon flux is independent of the number of pixels binned M . However, both dark noise and readout noise increase linearly and the resulting SNR is

$$\text{SNR}_{\text{Binned}} = \frac{\bar{n} \eta_{\text{det}} T}{\sqrt{\bar{n} \eta_{\text{det}} T + M I_{\text{Dark}} T + M N_{\text{Read}}^2}} \quad (3.19)$$

Note that this is much larger than the one quoted by the manufacturer, which defines the spherical photon flux as the rate of photons that reach each single pixel⁵. For the Nirvana 640 CCD $I_{\text{Dark}} = 300$ [electrons/px/s] with a read noise of $N_{\text{Read}} = 120$ [electrons]. In low-light measurements, the choice of the binning factor can severely affect the resulting SNR and therefore the ability to detect the signal. An important parameter from an experimental stand-point is the rate of photoelectrons \bar{p}_{Th} from the signal required to achieve a target signal to noise ratio SNR_{Th} in a time T . Section 3.2 (b) shows that a photon flux higher than 10×10^3 photons/s is required for a SNR=2 over 1 second integration time for the Nirvana 640 at $\eta_{\text{det}} = 80\%$. The same drops to $\bar{p} = 100$ [photons/s] if one was willing to integrate for 15 minutes.

3.3 Visible and NIR SPADs

Single-photon avalanche detectors (SPADs), are used in a wide range of applications from bioluminescence detection, DNA sequencing, protein folding, light detection and ranging (LIDAR), single-molecule spectroscopy and fluorescence-lifetime measurements, as well as traditional and quantum-enabled metrology. For an overview of the technologies available, see [165]. The setup in fig. 3.10 is equipped with two pairs of free-running SPADs, one for the visible part of the spectrum (400 nm to 1060 nm) and one for the near-infrared (900 nm to 1700 nm).

The first are SPCM-AQRH - PerkinElmer , with a thermo-electrically cooled silicon active area of 180 µm in diameter and a detection efficiency of more than 65 % at 650 nm fig. 3.14 a). Upon detection of a photon, the hot-carriers generated during the avalanche amplification process are readily dispersed, leading to a dead time of 35 ns and a saturation rate of 20 MHz. The unit generates 15 ns long pulses of 2.5 V which are then time-tagged by a time interval analyzer SensL HRM-TDC .

Near-infrared single-photon detection with low noise generally requires cooling below -70°C in order to deplete the phonon population in the active area and prevent spontaneous detections. Off-the-shelf turn-key systems are based on three primary technologies, namely super conducting nano-wire detectors (with efficiencies in excess of 90 %), single-photon avalanche photodiodes and photomultiplier tubes. The first requires cryogenic cooling (1 K), does not suffer from spontaneous detections due to the release of trapped charges in the p-n junction (after-pulsing), and

⁵<http://www.princetoninstruments.com/calculators/signal-to-noise.cfm>

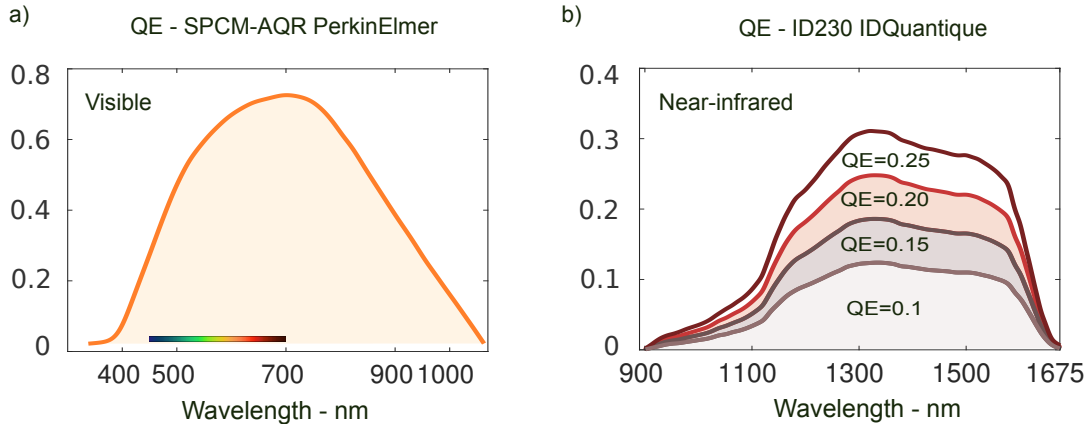


FIGURE 3.14: The combination of (a) SPCM-AQRH - PerkinElmer and (b) ID230 - ID Quantique single-photon avalanche photodiodes (SPADs) allows detection of single photons over a spectrum of $1.4\text{ }\mu\text{m}$. In the near-infrared, the bias voltage of the diode (and thus the resulting quantum efficiency) can be varied, which is particularly useful to limit the after-pulsing probability when operating at short dead-times.

reach dark-count rates $<100\text{ Hz}$. In contrast, SPADs are thermo-electrically cooled to $-90\text{ }^{\circ}\text{C}$, and are thus more compact, easy to maintain and cost effective. For a long time, InGaAs SPADs have been limited to applications with bright light sources, as they reported high dark count rates (10 kHz). Recent improvements on quenching electronics and semiconductor purity has led to ultra-low dark count rates, with a minimum of 10 Hz in a turn-key device. Remarkably, this is comparable with the best superconducting nano-wire detectors and find applications in many quantum-optics laboratories. Portability, however, comes with a reduced quantum efficiency, typically 20-30 %.

We use ID230 - ID Quantique ; its quantum efficiency curves are shown in fig. 3.14 b). The dead-time can be varied from 2 to $100\text{ }\mu\text{s}$, the temperature from -70 to -90 and the quantum efficiency from 0 to 25%. These parameters are linked in complicated ways. While both have a large active area and comparable dark count rate, InGaAs detectors must be operated in the range $-70\text{ }^{\circ}\text{C}$ to $-90\text{ }^{\circ}\text{C}$. Since the active area of the p-n junction must be thermally isolated, the coupling to the chip can only occur through an integrated and temperature-stabilized optical fiber. As a result, one typically needs to chose between SMF and MMF coupling before purchasing the device. If the spatial mode of the light collected in the fiber is important, such as in HOM (Hong-Ou-Mandel) quantum-interference measurements, it is preferable to use SMFs.

However, in addition to a loss of efficiency, free-space to fiber coupling is less flexible and any change in the optical setup (such as objective or wavelength used) and requires to redesign the coupling as described below. For this reason both SPADs were equipped with standard graded-index MMFs with a core diameter of $62.5\text{ }\mu\text{m}$.

Free-space to fiber coupling

Depending on the objective used, the wavelength of light, and the spacial extent of the emission, the coupling conditions from free-space to the core of the multi-mode fibers (MMFs) may change. Collection from an extended source requires the point

spread function (PSF) of the optical system comprised of L_{O1} , L_T , L_C and L_P to be smaller than the fiber core. If however we were interested in collecting light from a diffraction-limited point in a confocal fashion, we would need to make sure that the PSF is between one and two times larger than the fiber core.

Although it is possible to change the size of the optical beam that reaches the fibers to accommodate for these two contrasting requirements, this is likely to result in an increased alignment overhead. Instead, we optimize the light coupling from an extended light source on the image plane of L_{O1} and achieve the spacial selectivity required in confocal imaging by means of a circular aperture at the focal plane of L_T . When using large core MMFs, the light coupling problem simplifies to matching the size of the image at focal-plane of L_T with the core size of the MMFs ($62.5 \mu\text{m}$). In order to calculate the focal lens of L_C , we note that in all the experiments on atomically-thick materials described in chapter 4, sample sizes rarely exceed $6 \mu\text{m}$ along any of the two dimensions, requiring to used objectives with large magnifications (typically $\text{NA}=0.85$ and $M=100\times$) for imaging, illumination and collection. At an operating wavelength of $\lambda = 1 \mu\text{m}$, the PSF of the pair L_{O1}, L_T is $\approx (1.22 * 1/0.85) * 100 = 1.43 * 100 = 143 \mu\text{m}$ which is more than twice the diameter of the fiber's core. Thus, if the imaging system was diffraction-limited, a $6 \mu\text{m}$ feature at the image plane of L_{O1} would be mapped to $\approx (6 + 1.43) * 100 = 743 \mu\text{m}$ at the air-glass interface of the fiber. A 1:1 mapping onto the fiber's core requires a reduction of ≈ 12 times which we achieve with the L_C, L_P pair. The first lens with a $f_C = 400 \text{ mm}$ collimates the divergent rays coming from L_T , while the second ($f_P = 33 \text{ mm}$) recreates the image on the fiber core. The effective optical magnification is $33/400 = 0.0825$ which corresponds to an optical reduction of 12.12 times.

From the ratio of focal lengths between L_C and L_T ($f_C/f_T = 400/200 = 2$), one can quickly see that the size of the optical mode at the beam splitter is twice that available in the microscope's tube. Finally, it is important to note that if it was possible to access and replace L_T with a shorter focal length (15 mm) the same feature would be mapped to a size a bit smaller than $53 \mu\text{m}$, thus achieving a similar coupling with half the optical elements.

An additional note on the use of optical-fibers for single-photon detection regards the plastic protective jackets that surrounds the core. When made of dielectric material, these may not guarantee complete isolation from ambient light, an effect that can be appreciated in the visible spectrum due to the availability of SPADs with high quantum efficiency. In many experiments the fibers had to be replaced with custom fibers protected with a metal jacket.

3.4 Control of the illumination angle

The modules described in section 3.1 allow to characterize light in its energy, polarization, time, and angle degree of freedom. Controlling the angle is important in a number of applications such as the free-space coupling to a photonic chip, to the measurement of some components of the nonlinear susceptibility. In the context of this thesis, control of the illumination angle is particularly useful to increase the coincidences over accidental ratio (CAR) in single-photon coincidence measurements as discussed in chapter 4.

Here we describe how Fourier illumination allows to achieve such angle control in a compact, flexible, and cost-effective fashion. Fundamentally, this consists in

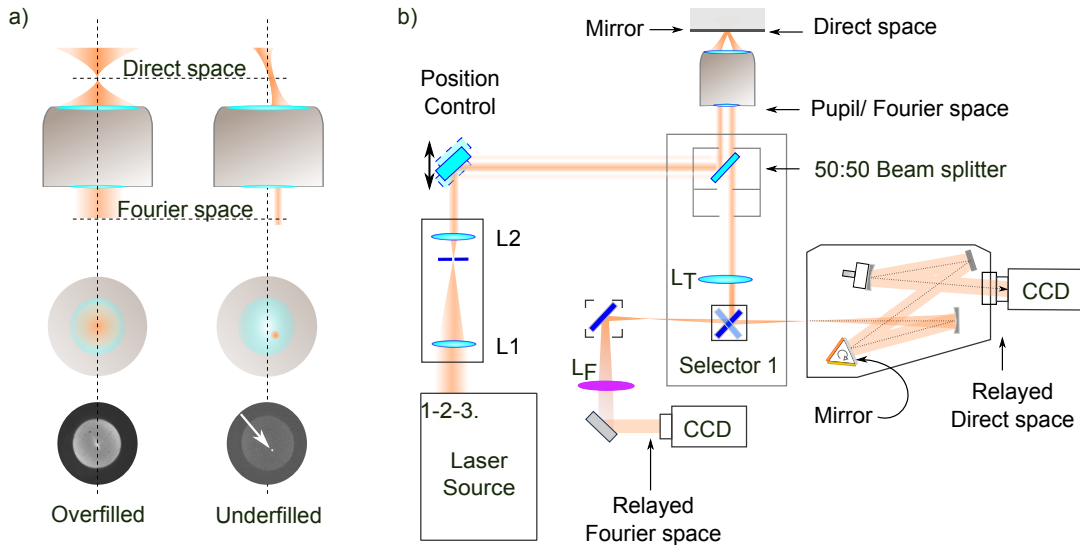


FIGURE 3.15: The incident angle of a laser beam on a static sample can be controlled by Fourier optics: a) Schematic and image of the pupil plane when this is over-filled (left) and under-filled (right) by a laser beam; b) By redirecting light to the two sides of the microscope, direct space and Fourier space are imaged allowing to control the incident angle and focal position.

leveraging the translation property of the Fourier transform: offsets in Fourier space correspond to phase delays in direct space and vice-versa. As a result, the phase-front of a laser beam on the image plane can be tilted simply by translating it across the input of a lens. The focus at the focal plane remains constant as long as the incidence angle of the beam on the lens does not change.

In order to accurately control the illumination angle with good accuracy, the diameter of a laser on the lens pupil must be several times smaller than the lens diameter. However, the length over which a beam maintains its collimation (Rayleigh range) scales linearly with the square of the beam diameter, and the size of an objective pupil tends to be inversely proportional to its numerical aperture (NA). As a result, high NA lenses typically require highly divergent beams. As an example we consider the optical table of fig. 3.1; if the distance between the source and the microscope is $z = 6\text{ m}$, a beam at a wavelength of $\lambda = 1\text{ }\mu\text{m}$ with an initial waist diameter $w_0 = 1\text{ mm}$ would reach the objective with a waist $w_0 \approx 2\text{ mm}$. From Gaussian optics, the minimum beam diameter with the smallest divergence at $1\text{ }\mu\text{m}$ is $w_0 = 1.4\text{ mm}$, leading to even smaller angular resolution.

In the absence of aberrations, one way to circumvent this problem is by leveraging the flat phase-front at the focus of a Gaussian laser beam, and simply interpose a lens between the input of the microscope and the objective. However, the distances involved in the setup in fig. 3.1 would require impractical focal lengths (longer than a meter). Our solution was to use a pair of lenses to produce an effective focal length much longer than the one of the individual optics. Conceptually this is equivalent to designing an optical telescope, with a convergent output beam, so that its waist falls precisely on the objective pupil at the required distance.

Figure 3.15 a) shows a schematic of the direct space (focal plane) and Fourier space (pupil plane) of a high-NA objective that is over-filled (left) and under-filled (right). The images of the pupil plane of Olympus LCPLN-100X-IR at the bottom

were acquired with a visible CCD using the setup described in fig. 3.7 and using a system of lenses so that the beam was focused on the pupil plane.

3.4.1 Limitations and other techniques

The first limitation of the Fourier illumination system described above derives from the uncertainty principle. If we want to control better the range of angles that reach the sample we must illuminate a smaller portion of the BFP, which in turn results in a correspondingly larger spot in direct space. In order to keep the intensity constant at the image plane the optical power at the input must increase quadratically. With ultra-fast lasers, this often leads to exceeding the power damage threshold of the optical elements (lenses, anti-reflection coatings) with consequent permanent damage of optics.

In addition, when the experiment requires simultaneously a large input photon flux and a single-photon output, the high intensity of the fields in a Fourier illumination system can lead to the generation of a weak and unpolarized photoluminescence background. In single-photon measurements this emission can severely affect the CAR. In a feasibility measurement of section 4.5.5 a near-infrared detection rate of a few kHz was routinely detected under illumination with a 775 nm and 1 mW femtosecond beam, focused to a 60 μm spot on the pupil plane of Olympus LCPLN-100X-IR (peak power density in excess of $6 \times 10^{12} \text{ W cm}^{-2}$). This stimulated the use of two lenses positioned at opposite sides of the transparent sample substrate. The first with a large numerical aperture is used for collection, while the one with a relatively smaller numerical aperture illuminates the sample.

Lastly, the transmissivity profile of the pupil is seldom uniform due to both Fresnel losses and the angle-dependent response of broadband anti-reflection coating. A phase-insensitive measurement of the pupil transfer function, which is generally tapered towards the edges, can be performed by illuminating the lens by a perfect spherical wave from the object side. In practice perfect spherical waves are not readily available, and the use of a known radiation diagram (such as a dipole emitter) yields satisfactory results (see [162] and references therein).

Alternative ways to control the illumination angle

One way to control the light incidence angle on a sample is to mount the latter on a goniometric stage, such as the Newport M-GON65-X and HXP100-MECA. However, their travel range is often limited to 10-20 degrees and they tend to have a large foot-print. A collimated beam of light can also be delivered with an optical fiber, which allows to easily change the illumination angle while maintaining the focus constant on the sample plane. Apart from vibrations and foot-print, ultra-fast pulsed lasers require hollow-core guidance to minimize nonlinearities and dispersion and thus preserve the spatio-temporal profile of the pulses. Two options with different guiding principles are narrow-band photonic-crystal fibers (PhCF), or broadband and much more expensive anti-resonant Kagome fibers with large mode field diameters

and insertion loss $< 2 \text{ dB m}^{-1}$ for radii of a few centimeters [166]⁶ Both solutions however rarely allow to collect light from both sides of the sample, a technique that can lead to more than one order of magnitude increase in CAR when measuring photon simultaneity from 2D materials.

3.5 Lasers and objectives: alignment and control

The radiation diagram of a point emitter is omni-directional and well localized in space. When this is brought at precisely one focal length away from a lens, the emission is mapped onto a well defined angle. An emitter perfectly aligned to the optical axis of the objective will correspond to normal emission in the Fourier plane; any in-plane displacement from the optical axis of the lens will also lead to a linear change in the emission angle in the Fourier plane, provided the distance between the lens and the emitter is kept constant. By virtue of reciprocity, a lens will focus a collimated beam of light into a small area at its focal length. As described in section 3.8, the size of the focus is given by $\Delta r_{min} = 0.61\lambda/NA$, where the effective is $NA_{\text{eff}} = D/2f$ where D is the diameter of the beam and f the focal length of the lens. A lens with an NA of 0.85 will focus a collimated laser beam ($\lambda = 1 \mu\text{m}$) to a diameter of $\approx 1.22/0.85 = 1.43 \mu\text{m}$, under the assumption that the beam evenly illuminates its back-focal plane (BFP). It is common to over-illuminate the BFP by a factor of 2, that is, the $1/e^2$ diameter of the beam should be twice as large as the BFP diameter. This results in the beam transmitted having only about 70% of the light in the un-truncated beam. One of the fundamental properties of Fourier transform is that translations in direct space correspond to linear phase shifts in Fourier space. In the laboratory we can introduce a linear phase-shift on the phase front of a laser beam simply by changing its incidence angle. This phase retardation changes the conditions for constructive interference at the focal plane and ultimately results in a shift of the focus. When aligning a laser beam to a lens it is important to maximize the transmitted optical power to avoid reflections and distortions of the intensity profile. One way to freely translate/tilt a laser beam in space is to use a pair of mirrors to *walk* the beam and control its incidence angle. Mirror pair 1 and 2 in fig. 3.5 are used to this end depending on whether the beam is aligned to the top or bottom arm. In the same setup a beam-splitter simultaneously reflects light upwards towards the objective (excitation), while allowing to collect the reflected downward light (emission) for analysis/imaging. Since the setup in fig. 3.5 features an inverted microscope, imaging can be accessed through the bottom objective. Coupled with the system in fig. 3.6, this can be used to provide a visual feedback on the quality of free-space coupling between a laser beam and the objective, other than to perform wide-field sample imaging.

⁶The hexagonal periodic structure in the cladding of PhCF can be seen as an effective Bragg grating, inside which light of the right wavelength undergoes destructive interference. Differently, Kagome fibers guide light by maintaining rapid phase modulations of the modes in the cladding which thus interact weakly those in the fiber core [167]. The resulting pattern resembles the one of Japanese woven baskets or *Kagome* from the Japanese combined word *Kago* (basket) and *me* (eye).

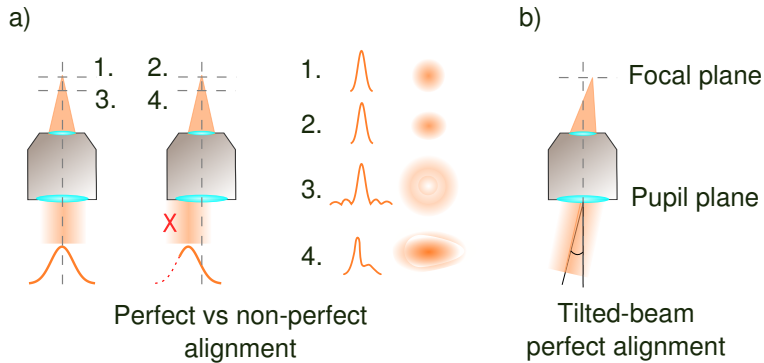


FIGURE 3.16: Gaussian beams through a high-NA lens. a) Experimental strategy to facilitate the alignment of a laser beam with the objective optical axis; small misalignments can hardly be noticed at focal plane where the intensity contrast between peak and wings is maximum 1-2. moving a fraction of the wavelength away from the focal plane the intensity asymmetries are clear and it is easier to adjust the beam position 3-4. b) controlling the position of the focus on the focal plane can easily be achieved by changing the incidence angle of the beam on the pupil plane (or Fourier plane).

Inverted Alignment

One obvious approach to perfect the coupling of optical power in free space is to probe and compare the input and output power at the two ports of the optical component. This technique applies to the majority of bulk optical components which can be manipulated freely in free-space. However, high-NA objectives used to probe nano-meter size features require a much greater level of accuracy. Moreover, there is a need for an agile technique that can adapt to a constantly changing optical environment (various dichroic filters, polarizers, beam sizes). Although one could bring the system to a known state for every optimization round, this is likely to introduce overhead, mistakes, and slow down measurements.

An effective technique is to place a flat mirror in the sample holder (piezo stage of fig. 3.5) and image its surface using the setup in fig. 3.6. This ensures that the object-plane and the image-plane of the objective are coplanar, so that the focus of an input collimated laser beam at the bottom objective will be perfectly aligned to the surface of the mirror. If the optical system is well aligned and calibrated, the reflected beam focus will appear in the center of the CCD plane in fig. 3.6. A pair of mirrors can be used to correct the angle and position of the beam and refine the alignment. With appropriate actuators and a good optical design, one can achieve a diffraction-limited accuracy in beam positioning and coupling. In practice however, the detection of a bright spot anywhere on the CCD plane is a necessary but not sufficient indication of good coupling. Figure fig. 3.16 a) illustrates the effect of non-perfect alignment from a qualitative stand point for a Gaussian beam profile. For each position 1-2 we show the typical CCD image for a mirror at the focal plane of the objective: it is very hard to distinguish a collimated and normally-incident beam that is collinear to the optical axis of the objective (ideal alignment) from one that is laterally off-set (non-ideal alignment). This effect is even more evident with high-NA objectives where the focus tends to be smaller and the intensity contrast larger, making it hard to detect asymmetries in the intensity profile with a regular CCD camera. A simple strategy to avoid this is to displace the object plane from the focal

plane in order to probe the intensity distribution of the focusing fields a few Rayleigh lengths away from the waist. This can vary between 1-100 μm depending on the NA of the lens and the beam diameter. The effect is a reduced peak intensity and a larger image size thus allowing to readily detect any unbalanced intensity distribution as shown in the images 3-4 of figure fig. 3.16 a). At this point, the mirror pairs can be used to straighten the beam in the same way as a pair of apertures; asymmetry in the intensity indicates a drift from the optimal input position in the objective, while a displacement of the center indicates a change in the angle of the collimated beam incident on the objective pupil. The general principles outlined here can be followed to align a laser beam to the upper arm of the illumination system in transmission.

3.6 Measurement of the Second-order Coherence of Light

In the following we focus on the temporal second-order correlation function of light and discuss its implementation in practice. We highlight what motivated the design of the apparatus presented in fig. 3.10 which was used to measure the simultaneity of entangled photon pairs generated in atomically-thick materials section 4.5 and section 4.6. As briefly mentioned in section 2.2.2, one way to measure the $g^2(\tau)$ of a light source is to use a beam-splitter, a pair of photo-detectors and an optical delay stage. However, with time-tagged single-photon detection, the experiment time can be reduced drastically and mechanical complexity can be traded with sophisticated electronics. We can write equation eq. (2.29) for a monochromatic and stationary source in terms of number of photons as $I(t) = \hbar\omega \cdot n(t)/\Delta T$ where $I(t)$ is the intensity of the incident light, $n(t)$ is the number of incident photons in the total observation time ΔT , and $\hbar\omega$ is their energy. If the emission of photons is a stationary, independent and identically distributed random process, this takes the form [30]

$$g^2(\tau) \approx \frac{\langle n(t)n(t+\tau) \rangle}{\langle n(t) \rangle^2} \quad (3.20)$$

Ideally, this ratio could be calculated directly from the autocorrelation of the detection times. In practice, it is often possible to approximate eq. (3.20) by correlating the output of a pair of non-ideal single-photon detectors connected to the transmitted (T) and reflected (R) output ports of a beam splitter [168]. This is particularly true at low photon rates, when the mean time between two photons is much larger than the detectors dead-time, and thus the probability that both detectors are in an OFF-state is negligible. Under this approximation, eq. (3.20) can be written as

$$g^2(\tau) \approx \frac{\langle n_R(t)n_T(t+\tau) \rangle}{\langle n_R(t) \rangle \langle n_T(t) \rangle}. \quad (3.21)$$

The combination of single-photon avalanche photodiodes (SPADs) and time-interval analyzer (TIA) introduces an intrinsic time-uncertainty (jitter), which cannot be compensated. Since this can arise from a number of different and uncorrelated sources, it is typically modeled as a Gaussian process with standard deviation σ_{jitter} , typically on the order of a few hundreds of ps. If two time-stamps are received with a time difference smaller than the jitter they should be considered simultaneous since

there is no way to distinguish them from noise. For this reason, time-tagged photo-detections are discretized, so that events that occur within a time window are considered simultaneous. Such time-window is commonly referred to as bin time and indicated as t_{bin} . The choice of t_{bin} has consequences on the visibility of the $g^2(\tau)$, since a large value can lead to distortion of the auto-correlation, while a small value can lead to a noisy histogram. We normally set $t_{\text{bin}} = 3\sigma_{\text{jitter}}$ as this ensures that more than 99% of truly simultaneous photons are represented in the same histogram bin. In the limit of a large observation time ΔT , $g^2(\tau)$ represents the conditional probability of detecting a photon at time $t + \tau$ given that we detected a photon at time t . We can write $g^2(\tau)$ in terms of the probability to find detections in t_{bin} as [169]

$$g^{(2)}(\tau) = \frac{P_{\text{RT}|\text{bin}}(\tau)}{P_{\text{T}|\text{bin}}P_{\text{R}|\text{bin}}}, \quad (3.22)$$

where $P_{\text{RT}|\text{bin}}(\tau)$ is the probability that we observe two independent detections with a time separation of τ in the bin time, and $P_{\text{T}|\text{bin}}$ ($P_{\text{R}|\text{bin}}$) is the probability of observing a detection in the T(R) arm of the beam-splitter in the same time. In order to calculate the numerator of eq. (3.22), we note that the number of correlated detections that are registered with a relative delay of τ during the observation time is $N_{\text{RT}}(\tau) = \eta_{\text{det}}\langle n_{\text{R}}(t)n_{\text{T}}(t + \tau)\rangle$, where η_{det} is the quantum efficiency of the detectors. In the limit of large ΔT we can thus write

$$P_{\text{RT}|\text{bin}}(\tau) = \left(\frac{N_{\text{RT}}(\tau)}{\Delta T} \right) t_{\text{bin}} = \frac{\eta_{\text{det}}\langle n_{\text{R}}(t)n_{\text{T}}(t + \tau)\rangle t_{\text{bin}}}{\Delta T}. \quad (3.23)$$

Indicating the number of detections on each arm of the beam-splitter as $N_{\text{R}} = \eta_{\text{det}}\langle n_{\text{R}}(t)\rangle$ and $N_{\text{T}} = \eta_{\text{det}}\langle n_{\text{T}}(t)\rangle$, eq. (2.29) becomes

$$g^{(2)}(\tau) = \frac{P_{\text{RT}|\text{bin}}(\tau)}{P_{\text{T}|\text{bin}}P_{\text{R}|\text{bin}}} = \left(\frac{\Delta T}{N_{\text{R}}N_{\text{T}}t_{\text{bin}}} \right) N_{\text{RT}}(\tau), \quad (3.24)$$

where $P_{\text{T}|\text{bin}} = N_{\text{T}}t_{\text{bin}}/\Delta T$ and $P_{\text{R}|\text{bin}} = N_{\text{R}}t_{\text{bin}}/\Delta T$. This last expression links the experimentally obtained coincidence histogram $N_{\text{RT}}(\tau)$ to the second-order correlation function of the light source $g^2(\tau)$. For a schematic of the implementation of a HBT interferometer, we refer to fig. 3.10, and in particular to the beam-splitter, SPADs and time-interval analyzer TIA. The latter, along with all the numerical routines that calculate differences in the detection times were tested with a function generator and showed no loss of information over time scales of tens of hours.

Quite unexpectedly, it was found that this particular model of the TIA generates random bursts of identical timestamps. In the time-analysis routines this would appear as a correlation with a sharp peak in $\tau = 0$, with the potential to compromise the reliability of the $g^2(\tau)$ measurements. A simple solution is to introduce a fixed electronic delay Δt in one arm of the HBT. This has the effect of translating the zero delay point on the histogram, so that simultaneous detections would appear at $\tau = \Delta t$ instead of $\tau = 0$. The accurate value of Δt can be measured directly from the coincidence histogram of an integrated source of entangled photon pairs such as that described in section 3.1.5.

We can identify at least four examples of light sources that will yield qualitatively different results when measured using an HBT interferometer. Incandescent filaments or fluorescent lamps emit thermal light which results from incoherent

multi-atom radiative processes. Here photons tend to be bunched, meaning that small temporal separations between photons are more likely than large ones. Since $g^2(0) = 2$ and tends to 1 for a long delay τ this is also called super-Poissonian light. The second classical example is a coherent and stabilized light source (attenuated laser above threshold). Here $g^2(\tau) = 1$ for any value of τ . This is referred to as Poissonian light, as the number of photons emitted in a given time interval follows a Poissonian distribution [29, 170]. Light sources for which large separations between two consecutive photons is more likely than small ones, bears the hallmark of a discrete particle nature. Since a single photon is an indivisible quantum of energy, for a perfect single-photon source the probability of recording two coincident detections is zero $N_{\text{RT}}(\tau)|_{\tau=0} = 0$, resulting in a dip in the coincidence histogram and associated $g^2(\tau)$ [171]. Another example is squeezed light, such as that emitted from a spontaneous parametric downconversion source like the one described in section 3.1.5 whose typical coincidence histogram shows a peak only for $\tau = 0$, because the photons detected are correlated, being generated at the same time.

3.7 Photon coincidences with detection gating

When pumped with high peak-power laser light, any material exhibits spontaneous radiative emissions (substrate impurities, strain, etc.). Two common filtering techniques to mitigate the impact of this background on $g^2(\tau)$ measurements are spectral and spatial filtering. Since the signal to noise ratio increase at the output of a filter is directly proportional to the degree of orthogonality between signal and noise, these are often ineffective in the measurements described in section 4.5 and section 4.6, where signal and noise are spatially and spectrally degenerate.

This section describes the design and implementation of a filter that operates in the time domain leading to a significant increase in signal to noise ratio as described in section 4.6.6. A slightly different implementation of the concept of temporal filtering was used in measurements of breakdown flashing in single-photon detectors as discussed section 4.1.2. While many off-the-shelf single-photon avalanche photodiodes provide this functionality to reduce the effective dark-count rate, the free-running SPADs described in section 3.3 cannot directly be gated. Instead, filtering in the time domain can be done on the timestamps generated by the time-interval analyzer.

Under pulsed illumination, a typical SPDC coincidence histogram is periodic with a large peak in $\tau = 0$ and a series of much smaller side peaks at a multiple of the laser period $\tau = \pm k T_{\text{rep}}$, where k is an integer. However, since there can be no SPDC between two consecutive pump pulses $kT_{\text{rep}} < \tau < (k + 1)T_{\text{rep}}$, any detection received in such interval must be background. Detection gating relies on the synchronization of excitation and detection, so that no background is observed when there is no signal to be detected.

The increase of coincidences over accidental ratio (CAR) that can be expected from detection gating depends on the ratio between the characteristic times, as well as from the repetition period of the laser, which dictates the maximum time-window where temporal filtering can be effective. If the lifetime of the signal is comparable with the illumination period of the femtosecond laser source, any attempt to reject the noise will also result in information loss, for the next pulse excites the electronic system before any lossless filter can operate. If however the signal is a stochastic process much faster than the background, filtering in the time domain reduces the total

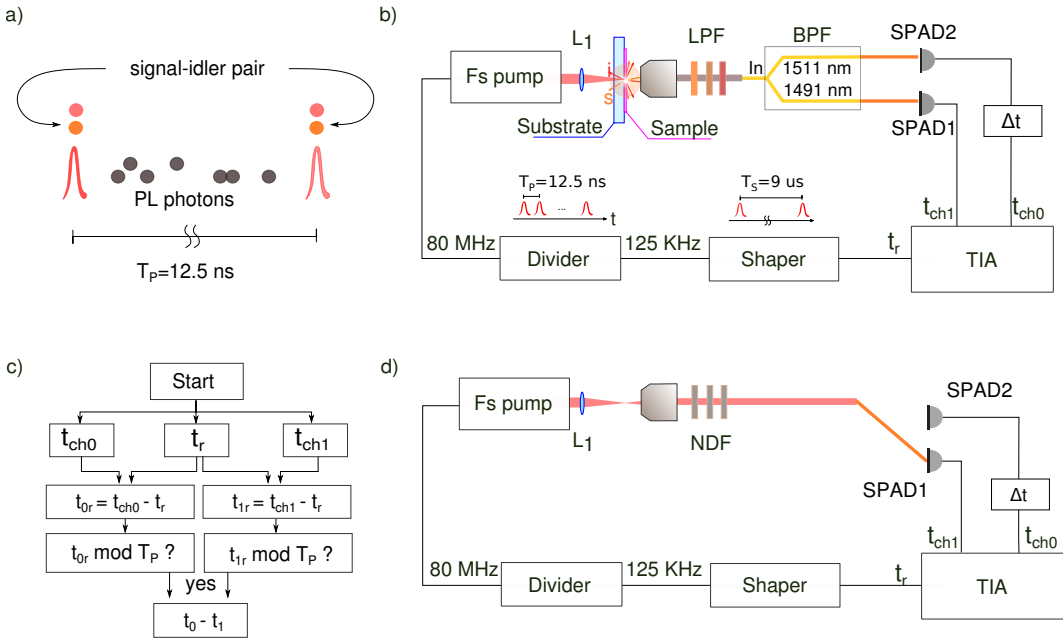


FIGURE 3.17: Gated detection can increase the CAR in measurements of simultaneity of entangled photon pairs. a-b) Pairs of energy-time correlated photons via SPDC of SFWM are generated within femtoseconds from the arrival time of a pump pulse, while photoluminescence photons can be detected at any time. Detection gating means to calculate time differences only if photo-detections occur within multiples of the laser repetition rate T_p (12.5 fs for an 80 MHz laser). c) Experimental setup for the measurement of SPDC photon coincidences from thin samples: a set of Long Pass Filters (LPF) rejects the pump and a Band Pass Filter (BPF) isolates signal and idler pairs. d) The reference clock t_R and the arrival of pulses can be synchronized by attenuating the pump with Neutral Density Filters (NDF) and calculating the time difference between its detection and the reference clock.

dark-count rate and increase the CAR. Detection gating can be particularly useful in coincidence measurements for spontaneous four-wave mixing (SFWM) or spontaneous parametric downconversion, since these occur over time-scales many orders of magnitude smaller than other spontaneous radiative processes. When generated, signal and idler pairs (orange dots in fig. 3.17 a), overlap almost perfectly with the arrival of a pump pulse on the sample.

The rest of this paragraph presents details of such gated coincidence measurements in a free-space setup, with a focus on single-photon coincidence measurements of SPDC in a two-dimensional material (sample) deposited on a transparent medium (substrate). Figure 3.17 (b) shows a schematic containing elements of the illumination module of fig. 3.5 with those of the single-photon detection module of fig. 3.10. A low-NA lens concentrates the optical power of a femtosecond laser source onto the sample, while a high-NA objective collects the downconverted light from the other side. A set of long-pass filters (LPFs) and a fiber based band-pass filter (BPF) select energy-correlated signal-idler pairs, which are then detected by two independent near-infrared single-photon avalanche photo-diodes (ID230 - ID Quantique).

A fast photo-diode in the Chameleon Ultra II generates a low-voltage electrical signal synchronous to the optical pulse train ($\approx 80 \text{ MHz}$). This pulse train cannot be directly detected by the time-interval analyzer SensL HRM-TDC (TIA), which has a

combined saturation rate of 4.5 MHz across four channels. To adjust the rate within the capability of the TIA we use a digital frequency divider with a scaling factor of 640, resulting in an analog reference waveform of $t_r = 125$ kHz. This is then shaped to a 2.5 V and 100 nm TTL pulse train which is then detected by the TIA. In order to quantify the the combined time-uncertainty we calculate the autocorrelation of the delta between a time series and itself. Timestamps from t_r were found to be equally spaced with a jitter smaller than 120 ps, which is less than half of that quoted for the SPADs.

The next step is the synchronization of the reference signal with the optical train, which are in general offset by the optical-electronic path difference. We measure the difference between reference time-stamps t_r and those corresponding to the detection of photons from a heavily-attenuated pump t_{ch0}, t_{ch1} . As shown in fig. 3.17 (d), the BPF is first removed and a set of anti-reflection coated neutral-density filter (NDF) attenuates the pump to a flux of ≈ 100 kHz, resulting in an average count rate of a few tens of kHz. Figure 3.17 (c) shows the pseudo-code for a gated coincidence detection. Since pump signal and idler are expected to be generated almost instantaneously, we only consider photo-detections whose distance from t_r is a multiple of the laser period T_p .

In practice, this condition is evaluated within an arbitrary tolerance level to account for jitter. As a rule of thumb, the width of the tolerance should be at least twice the jitter of the electronics as this guarantees that at least 95% of the signal detections are not discarded (Gaussian distribution of the jitter). This condition could be made more strict at the expense of data loss in an attempt to maximize the SNR. Intuitively, this works by leveraging differences in the shapes of the probability density function of the intrinsic jitter, from that of other noise processes. For dark-count limited measurements, the relationship between the tolerance and the amount of noise filtered is linear due to the statistical independence of dark detections (uniform distribution). If however the measurement is limited by a process with an exponential decaying probability density function (such as the photoluminescence process described above), a stricter condition could lead to a larger suppression of noise compared to the signal and thus be beneficial. Ultimately this trade-off depends on the specific noise process. In the measurement of chapter 4 the pair production rate was estimated to be on the order of 1 Hz, which accounting for the loss, corresponds to one coincidence every three hours. Given the low detection rate, any further loss increases the experiment time, so that the use of a small tolerance needs to be taken into account.

Although timestamps could be saved in memory and analyzed off-line, experiment times longer than a few tens of hours may result in many Tera bytes of data. To avoid the I/O bottleneck associated with such volumes of data, timestamps are processed on-line via dedicated labVIEW-Python routines (see Python/LabVIEW integration toolkit) and only those at the output of the filter are saved to disk. For a more user-friendly statistical monitoring and logging LabVIEW arrays are converted in NumPy arrays and processed using a dedicated Python script.

3.8 Design and testing of a single-photon confocal imaging

This section describes the design of confocal laser-scanning microscope (CLSM) with dual detection in the visible/near infrared. This system was used in the single-photon coincidence measurements of spontaneous parametric downconversion in mono-layers of transition-metal dichalcogenide (TMDC) presented in section 4.5.

The size of a feature in real space determines the extent of its spatial frequencies. In order for an imaging system to map an object to the image plane without loss of information, the number of spatial frequencies available must be inversely proportional to the object size. In 1873 Ernst Abbe realized that in far-field imaging systems the radius d of the smallest object detectable is $d = \lambda/(2NA)$ where λ is the wavelength of light and NA the numerical aperture. Rayleigh refined the above observation by defining the resolving power of an imaging instrument as the ability to separate two objects into two distinct images, giving a minimum lateral separation between two objects of [172]

$$\Delta r_{min} = \frac{0.61\lambda}{NA}. \quad (3.25)$$

In order to collect higher spatial frequencies and thus increase the resolution one can increase the density of the dielectric (higher refractive index), use media with a different dispersion relation such as metal or a meta-lens, or access the near-filed components with a micro-tip in (see for instance scanning near-field optical microscopes ⁷). In a far-field and linear optical system, improving the imaging resolution of a single sub-diffraction feature can only be achieved by increasing the density of the surrounding electromagnetic environment. Practically, this is done by placing the sample on a transparent substrate and using index-matching oils and oil-immersion lenses. A microscope image is a bi-dimensional representation of a volume (sample) that contains many light-scattering features. Since no realistic lens can have an infinitesimally shallow depth of focus and infinite resolution, the brightness of any one point of the image is the sum of the intensity of the desired point as well as all surrounding points, weighted by the azimuthal and radial impulse response of the optics. Confocal microscopy aims to reduce interference by using an aperture to collect light one point at a time. This acts as a spatial filter that exhibits low loss at the point of interest, and a high loss for any other neighboring point. When compared to conventional wide-field microscopy, confocal microscopy boasts a higher azimuthal and radial resolution [173, 174], and finds applications in measuring the emission statistics of sub-diffraction light sources such as quantum-dots, wafer inspection, non-invasive optical sectioning of a sample. If a point-like detection area is combined with a diffraction-limited illumination spot (focused laser beam) the amount of light scattered by points other than the one of interest is reduced, further

⁷One way to understand this limit is to think of the imaging problem as an information transfer through a linear medium following the formalism of the Green's function. The phase-front of a monochromatic electromagnetic wave in the far-field propagates as a result of a balance between oscillations in space and time, with associated spatial k and temporal ω angular frequencies. In vacuum, the relationship between the two is linear; since the phase velocity is constant and equal to c_0 , faster temporal oscillations of the electric fields result in faster spatial oscillations so that $\omega = c_0 \cdot k$. Such relations state that in order for an electro-magnetic wave to sustain itself during propagation, the speed at which it oscillates in space cannot be faster than a certain limit, thus limiting the range of spatial frequencies that can be relayed in the far field. In a lossless and homogeneous dielectric medium with linear index of refraction n , this relationship becomes $\omega = (c_0 \cdot k)/n$, also linear but with a different slope which is why a denser medium results in higher resolution.

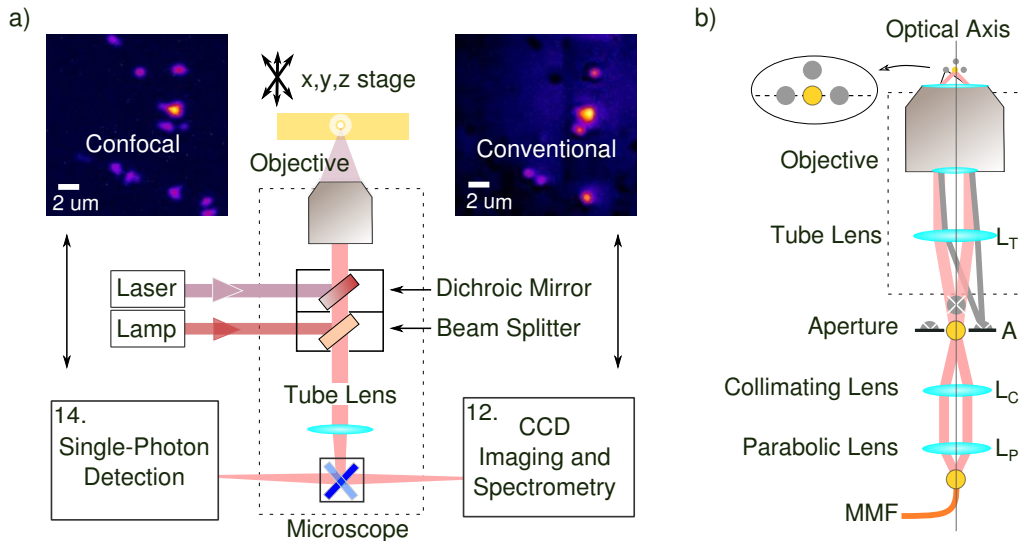


FIGURE 3.18: Schematic of a single-photon confocal laser-scanning microscope (CLSM). a) Incoherent light (Lamp) or laser light (Laser) are reflected towards the objective of a microscope by means of either an angled beam splitter or dichroic mirror. Illumination is fixed and the sample position controlled in 3D with a piezo-electric stage. The same image can be collected in a confocal (left image obtained with single-photon detectors) or wide-field illumination (right image). b) A simplified optical diagram shows that spatial selectivity is achieved with a round aperture at the focal plane of the tube lens of the microscope, and light is coupled to a multi-mode fiber.

improving the image contrast. In confocal microscopy the resolution gain comes at the cost of throughput, as images are formed by changing the sample position (or the illumination spot) and recording the intensity one point at a time.

Figure 3.18 (a) schematically shows our implementation of a single-photon confocal laser-scanning microscope (CLSM). The central element is an off-the-shelf microscope system (Nikon Eclipse Ti-U) that can direct light to the single-photon detection module described in fig. 3.10 or to the spectrometer and imaging system of fig. 3.6. A discussion of the optical design of the former, including lenses, fibers and coupling efficiencies, as well as details of the time-interval analyzer and single-photon avalanche photodiodes for single-photon detection can be found in section 3.1.9. To the left and right of the microscope are a confocal and bright-field image of test sample made of resonant gold nano-shells as described below. Figure 3.18 b) shows a simplified optical diagram of the CLSM. Light from the sample plane of an objective is relayed to the input of a multi-mode fiber (MMF). In between are the microscope tube lens L_T , a circular aperture A, a collimating lens L_C and a parabolic lens L_P for coupling light from free-space to a fiber. At the sample plane, the point of interest (yellow circle) is surrounded by an ensemble of other emitters (gray circles). When the former is at the working distance of the objective, and is aligned to the optical axis of the microscope, a magnified image will be found at the focal plane of L_T . When the aperture is also centered to the system optical axis, the focused rays of the point of interest will propagate to a second optical relay (the pair L_C, L_P) and reach the core of the fiber. Rays from all other scatterers will be off-center and thus

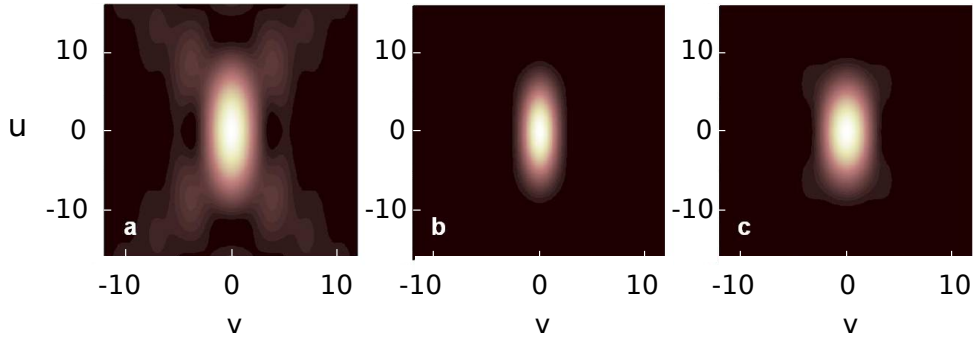


FIGURE 3.19: Comparison of normalized PSFs of a confocal optical system with an aperture of infinite size, one equal to an Airy unit, and one infinitesimally small.

be blocked by the aperture.

3.8.1 Confocal factor and aperture size

In the following we briefly describe the confocal factor and how to dimension A to meet a trade-off between spacial selectivity and loss, we describe the resolution tests that let to acquire the images in Figure 3.18 a) and conclude with a brief note on the use of a single-mode fiber simultaneously as a waveguide and aperture. The radiation pattern of a point-emitter at a wavelength λ and imaged with an effective numerical aperture NA in a medium with a linear refractive index n , is radially symmetric. Under the paraxial beam approximation, for a magnification $M = 1$ the scalar electric field can be written as [175]

$$E(u, v) = \int_0^1 e^{\frac{1}{2}iup^2} J_0(v\rho) \rho d\rho, \quad (3.26)$$

where J_0 is a zeroth order Bessel function of the first kind, u and v are normalized radial and axial coordinates related to the real radial r and axial z coordinates as $v = 2\pi r(\text{NA})/(\lambda)$ and $u = 2\pi z(\text{NA}^2)/(\lambda n)$ [172]. For a non-zero sized pinhole the collection intensity PSF becomes $I = |E|^2 * D$, where $*$ denotes the convolution operation and D is a typically the circularly symmetric step function $\text{circ}(v/v_A)$, for an aperture of radius of v_A . The total confocal point spread function becomes [176]

$$I_{\text{PSF}}(u, v) = |h(u, v)|^2 (|h(u, v)|^2 * \text{circ}(v/v_p)). \quad (3.27)$$

The confocal parameter is the ratio $\gamma = v_A/v_{\text{PSF}}$ between the normalized radius of the aperture v_A and that of the point spread function v_{PSF} . A $\gamma = \infty$ is equivalent to an infinitely large aperture while $\gamma = 0$ corresponds to the case of a completely opaque mask. Assumption perfect optical alignment, fig. 3.19 compares normalized PSFs of a confocal optical system with an aperture of infinite size, one equal to an Airy unit, and one infinitesimally small. In the first case the aperture has an infinite transmissivity and the resolution of the resolution of CLSM would be identical to that of conventional microscopy. The intermediate case shows that an aperture size of 1 airy unit achieves a resolution increase comparable to the extreme case of infinite confocal factor, without a much lower loss.

Resolution Tests

Once the size of the pinhole and the objective are chosen, the axial resolution can be measured directly in reflection by overfilling the objective with a laser beam and focusing it on a flat mirror. The reflected light is collected by the same objective, filtered by the aperture and its intensity recorded as a function of mirror distance with a combination of a SPAD and a TIA. For the test we operate at $\lambda = 800$ nm and use a standard single mode fiber (780HP Thorlabs) as a waveguide and aperture simultaneously (core diameter $4.4\text{ }\mu\text{m}$ and a mode filed diameter of $(5.0 \pm 0.5)\text{ }\mu\text{m}$ at 850 nm). Thus we evaluate the PSF at the input of the fiber using a NA=0.85 objective with an effective magnification M=111(Olympus LCPLN-100X-IR on Nikon system) which has a PSF of $(1.22 * 0.8 / 0.85) * 111 = 127.4\text{ }\mu\text{m}$. With $L_C = 200$ mm and $L_P = 15$ mm this is then mapped to a size $127.4 * 15 / 200 = 9.56\text{ }\mu\text{m}$ at the input of the fiber. If we approximate the input and fiber modes as a bi-variate Gaussian, we can define the confocal parameter γ as the ratio between they 1/e radii and find $\gamma \approx 0.58$. The theoretical and experimental intensity scaling was found to agree almost perfectly.

In order to measure the radial resolution of the system it is necessary to isolate and image a single sub-diffraction scatterer. We used a colloidal solution of 200 nm spheres made of a silica core coated with few nm of Au (AuSpheres nanoComposix). The metallic coating sustains localized surface plasmon polaritons which results in a strong and broad-band scattering cross-section from the visible to the near-infrared. The colloidal solution was diluted to 1 part in 100 in deionized water, and a drop was deposited for evaporation on a bare quartz cover-slide. Thanks to the surface tension of water, evaporation leaves the nano-spheres in circle, with single scatterers typically found in close proximity to the rim. Thanks to the large scattering cross-section, these can be seen with a standard bright-field illumination and a CCD camera. The radial resolution was measured by comparing the transversal profile of the same scatterer imaged with bright-field and single-photon laser-scanning confocal system. From the intensity profile we measure a ratio between the diameter of the confocal image and that of the bright-field image of $d_{cf} / d_{bf} = 0.82 \pm 0.041$, which is comparable to the theoretically predicted value of 0.78. Uncertainties arise from the non-perfect knowledge of the pixel size of the CCD sensor (Pixis 1024-BExcelon), as well as small alignment errors.

Objectives of different makes

In order to reduce chromatic and spherical aberrations, infinity-corrected objectives are often designed with a specific tube lens L_T . The distance between the two has in principle no impact on the quality of the image, while the focal length of the latter poses different requirements on aberration compensation. As a result preferences vary across manufacturers with Nikon systems designed with ≈ 200 mm, and Olympus and Zeiss ≈ 180 mm and ≈ 160 mm respectively. Since the magnification of a combination of two lenses is the ratio between their focal lengths, the effective magnification of an Olympus M=100 objective on a Nikon microscope is $100(200/180) = 111$, and 125 on a Zeiss.

Why not use a single-mode fiber as an aperture

There are two main approaches to implement a confocal laser-scanning microscope. The first is the one described in fig. 3.19 and uses multi-mode fiber to couple light for detections with single-photon avalanche photodiodes, and an aperture for the spacial selectivity. The second is to couple light to a SMF which acts simultaneously as a waveguide and spacial filter. The first reason why one should prefer the former is mere coupling efficiency. As visible from eq. (3.26), the radiation pattern of a point emitter extends to infinity while the size of the fiber core is finite. Efficient coupling between an incident electromagnetic mode $E_I(x, y, z)$ and the fiber fundamental (and only) mode $E_F(x, y, z)$ requires both the diameter and shape of the two modes to overlap. In integral for this can be expressed as [177]

$$\eta \propto \frac{\left| \int E_I^* E_F dA \right|^2}{\int |E_I|^2 dA \int |E_F|^2 dA} \quad (3.28)$$

which η is the coupling efficiency and the integral is carried over the cross-section area of the fiber. While the same is true for a multi-mode fiber, the large availability of optical modes ((tens/hundreds) extends this equation into a sum of overlap integrals, one for each of the available modes leading to an overall higher efficiency. With a realistic setup and laser beam, free-space to SMF coupling is typically $\eta \approx 60\%$ and is achieved when the size of the main lobe of the PSF (eq. (3.26)) matches the mode-field diameter of the fundamental mode of the fiber. For a MMF these numbers are much higher, with values of 95 % not being uncommon.

Another reason to prefer a MMF is simplicity. By decoupling the light coupling problem with the spacial filtering, if any of the parameters change (objective NA, magnification, emission wavelength), the setup only requires to change the aperture size. An approach with a SMF on the other hand, would require to re-design and align the lens pair L_C and L_P of fig. 3.19 b) so that the mode sizes are matched and a the coupling efficiency be large enough.

For details on the confocal factor and aperture size, resolution tests and design considerations we refer the reader to section 3.8.1.

Chapter 4

Results

"Two little mice fell into a bucket of cream. The first mouse quickly gave up and drowned, but the second mouse, he struggled so hard that he eventually churned that cream into butter and he walked out."

Catch me if you can.

SPDC is a spontaneous second-order nonlinear optical phenomenon which, under perfect phase-matching, scales quadratically with the length of the nonlinear medium (see for instance eq. (2.52a)). Thus, it is not uncommon to find bulk or on-chip integrated sources with GHz generation rates, for which a complete measurement of the intensity autocorrelation $g^2(\tau)$ requires only a few fractions of a second. However, when the same phenomenon is studied over a few atomic layers, the considerably smaller generation rates force instruments to operate over time scales of tens of hours, unveiling phenomena that would otherwise be unnoticed. In addition, while the use of intense optical fields and sensitive detectors can help maximize the signal intensity, any source of loss and noise in the system can severely limit the observation of this phenomenon. In this chapter we present efforts towards the measurement of simultaneity of spontaneous parametric downconversion entangled photon pairs, with a focus on two-dimensional nonlinear films of transition-metal dichalcogenides (TMDCs).

In section 4.1 we characterize radiative emissions from the active area of single-photon avalanche photo-diodes SPADs known as breakdown flashing, which if not properly accounted for can be mistaken for a signature of SPDC. We observe this effect in state-of-the-art near-infrared SPAD, and study its emission properties in the time and frequency domain. Although the spectrum of the emission extends over hundreds of nanometers, active quenching results in a well-defined time of emission, enabling deterministic filtering in the time domain.

Section 4.2 covers all sources of accidental coincidences and expands on the work published in [178]. These are all the radiative emissions that, despite being uncorrelated with the entangled photon pairs, result in two simultaneous photo-detections and thus be confused for the detection of an entangled photon pair. Lower-bounds for the coincidences over accidental ratio (CAR) are derived analytically for dark-count limited and a background-limited regimes in sections 4.2.2 and 4.2.3. Section 4.3 discusses loss in single-photon coincidence experiments and its effect in the measurement CAR. In an experiment of SPDC at a planar, two-dimensional, nonlinear interface, energy and momentum conservation can simultaneously be satisfied

by an infinite number of combinations of signal and idler. As a result the downconverted light does not propagate with well defined spatial modes, and the calculation of collection loss is not straightforward [178]. Section 4.3.1 proposes a numerical model to extract the average radiation pattern of the downconverted light and calculate the collection efficiency.

In section 4.4 we present frequency-resolved optical gating (FROG) measurements of the ultrafast pulses used to probe these non-linear interactions, which are essential to link efficiencies of the spontaneous process of SPDC with the classical analog of second-harmonic generation (SHG).

Section 4.5 uncovers the physical and experimental constraints for the detection of simultaneity of SPDC photon pairs from one-layer tungsten diselenide (WSe_2) under ultra-fast-pumping. Building on the quantum-classical relations of section 2.6, we conduct an appropriately designed second-harmonic generation experiment in section 4.5.1 and calculate the expected rate of photon pairs in a spontaneous parametric downconversion experiment in section 4.5.2. In section 4.5.3, the photon collection loss is estimated from numerical simulations based on energy and momentum conservation laws. From the estimated rate of SPDC photon pairs, section 4.5.4 shows the attainable CAR in mono-layer WSe_2 . In a dark-count limited measurement, with state-of the art superconducting nano-wire detectors this is predicted to be in excess of 10. However, in section 4.5.5 coincidence measurements show the presence of an incoherent background, where the probability of an accidental coincidence is more than six orders of magnitude larger than the expected rate of true coincidences. We attribute this to the direct band-gap and reduced Coulomb screening of monolayer WSe_2 , where one-photon spontaneous emissions are known to be up to five orders of magnitude more efficient than bulk.

In section 4.6 we explore materials with a stronger nonlinear response, indirect band-gap, longer interaction length, and higher damage threshold, with the aim to improve the measurement CAR. After motivating the choice of five-layer molybdenum disulfide (MoS_2), we present SHG and SPDC measurements respectively, from which we calculate a sub-Hz pair-generation efficiency from a diffraction-limited area of the material. Results of coincidence measurements in section 4.6.4 under 730 nm excitation indicate a weak background in the spectral range 1300-1650 nm. The intensity of this emission follows a similar spectral dependence as the photoluminescence response of the material, indicating that it might originate from the relaxation of excitonic states in the lattice. Single-photon spectroscopy shows a dominant contribution at 1560 nm, potentially extending to longer wavelengths. Detection-gating was explored as a means to filter-out any signal not synchronized with the repetition rate of the laser source, however measurements still indicate that a relatively brighter background emission dominates the measurement. From the expected generation rate, and the measured losses in the system we calculate a coincidences over accidental ratio two orders of magnitude below one. While experiments cannot confirm the presence of SPDC, we can equalize for the total loss in the system and advance the hypothesis that if present, the true rate of photon pairs generated at the sample plane must be smaller than $R_{\text{AC}}|t_{\text{bin}}|/(L_T)^2 = 0.155 \text{ Hz}$.

Finally section 4.7 summarizes the main findings and explore ways to improve the experimental setup.

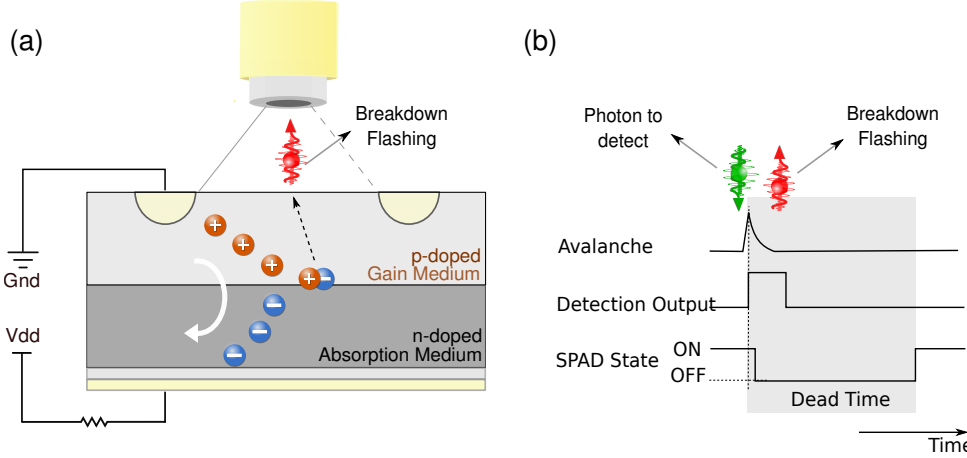


FIGURE 4.1: a) A p-n junction is reversely biased above breakdown voltage. Upon absorption of a photon the electron-hole pair formed is accelerated to generate a macroscopic current. After quenching radiative recombinations can occur thus leading to undesired photo-emission (breakdown flashing). b) Flashes occur between the onset of the avalanche and its termination by the quenching circuitry.

4.1 Breakdown Flashing in InGaAs Single-photon detectors

Single photon avalanche diodes (SPADs) are a well-established technology that finds applications in quantum communications, quantum information processing, imaging and sensing [179–181]. They rely on a current that is generated upon absorption of a photon by a cascaded amplification known as avalanche [182]. In this process electrons and holes can re-combine radiatively thus emitting a burst of photons. This effect can lead to false positives in temporal-correlation measurements, aberrations in single-photon lidar systems, cross-channel interference in SPAD arrays as well as a potential back-door to eavesdroppers in quantum key distribution networks [183–185]. Efforts have been made to contain these emissions, including the use of metallic trenches in arrays [Li2016d, 186, 187], narrow spectral filters and non reciprocal isolators. Although this effect has been observed in InGaAs p-n junctions, only qualitative and low resolution spectral measurements have been performed [188]. Fig. 4.1 shows a simplified diagram of a p-n junction reversely biased above breakdown voltage. Upon absorption of a single photon the electron-hole pair is accelerated through the gain medium where photo-ionization triggers a self-sustaining amplification process that yields a macroscopic current [189]. Subsequently the bias voltage is lowered (quenching) and radiation from hot-carriers recombinations can propagate to the rest of the optical setup causing cross-talk.

This section presents results of a careful characterization of the spectro-temporal properties of such breakdown flashing at telecom wavelengths in state-of-the-art InGaAs SPADs [190]. Measurements show that the emission spectrum spans hundreds of nanometers. In typical experimental conditions, photo-emissions can be as frequent as one every 8 detections. Moreover, the uncertainty in the time of emission can be on the order of 1 ns in actively-quenched junctions and allows to temporally isolate breakdown flashes from other uncorrelated processes. Time-domain

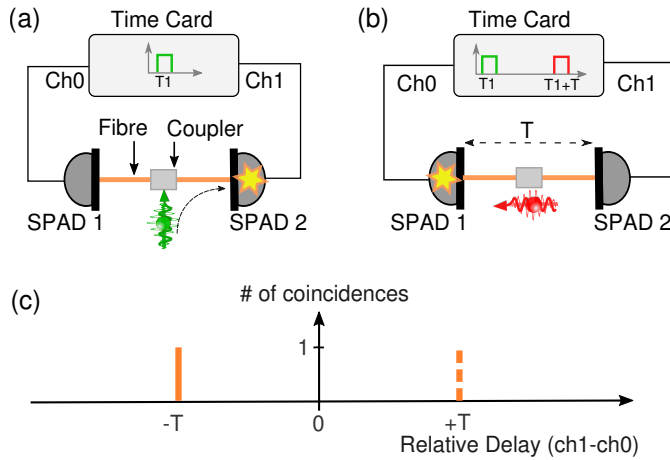


FIGURE 4.2: Two InGaAs SPADs are optically connected through a fiber coupler for the temporal characterization of breakdown flashes. a) A photon (green) is detected in SPAD 2 (star) leaving the detector inactive for its dead-time. b) The ensuing breakdown flash (red) is detected by SPAD1 after a delay T . c) This results in a coincidence at $-T$. A coincidence at $+T$ signals the breakdown radiation of SPAD 1.

filtering enables a dramatic increase in signal-to-noise ratio (up to 4 orders of magnitude) compared to the unfiltered case, and results in the first high-resolution spectral measurement of such weak effect. These results are important to understand the statistics of this broadband undesired emission, as well as to show that they can be suppressed very effectively without the use of expensive and narrow-band filters or non-reciprocal optical elements.

4.1.1 Temporal Characterization

The experimental setup consists of a Time Correlated Single Photon Counting (TC-SPC) scheme where two SPADs are optically connected to each other as shown in Fig. 4.2a. Impedance-matched transmission lines and dedicated fast electronics (SensL HRM-TDC) record the time of each photo-detection with a 300 ps error (detectors jitter). Detections are said to have a relative delay of T if their time difference Δ_T satisfies $\Delta_T < T_{\text{bin}}$ where T_{bin} is the bin time. Relative time differences, which are arbitrarily defined positive when Ch2 detects before Ch1, are then grouped in a histogram of coincidences.

The imperfect optical isolation of the fiber coupler as well as the large number of modes supported by the multi-mode fibers ($62.5 \mu\text{m}$ graded-index) allows a small fraction of background light (green in Fig. 4.2b) to reach SPAD 2. The electronic avalanche that triggers a detection event is followed by the emission of a breakdown flash (red) which is detected by SPAD 1. This results in a coincidence at $-T$, where T is the optical path connecting the two detectors. The symmetry of the setup as well as the absence of non-reciprocal elements allows the simultaneous detection of backflashes from both detectors. When the breaking radiation of SPAD 1 is detected by SPAD 2 the histogram would show a coincidence at positive times Fig. 4.2c. The mean time between the build up of an avalanche avalanche and the ensuing radiative recombination is assumed to be faster than the detector's jitter and can thus be neglected.

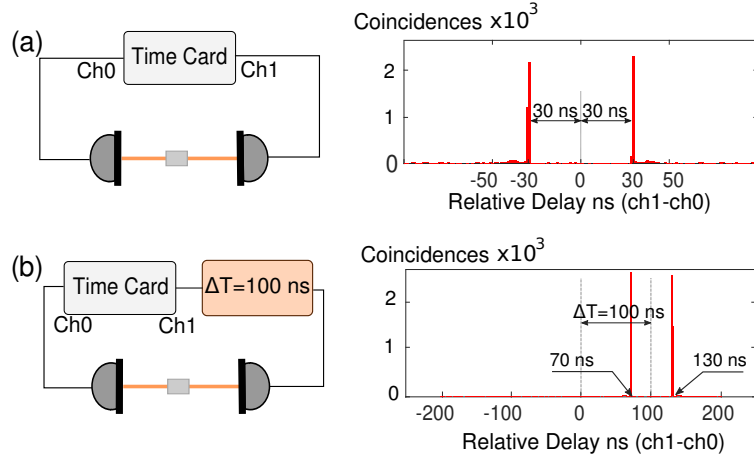


FIGURE 4.3: Experimental coincidence histogram collected over 60 seconds and 1 ns bin window. a) The histogram features two symmetric peaks around the origin. b) The introduction of a temporal asymmetry in any of the two channels causes a translation of the two peaks on one side only, ruling out the effect of reflections.

Fig. 4.3a shows the result of this measurement over 60 s, where the majority of the breaking radiation is tightly confined in a 2 ns window. This is in sharp contrast to the exponentially-decaying time distribution of breakdown flashes in passively-quenched SPADs [183, 185, 188] and suggests a rapid diffusion of hot carriers in InGaAs ID230 [190] by means of ultrafast quenching electronics [191]. The strong temporal confinement is particularly useful in large networks of SPADs where the knowledge of the network delays enables deterministic interference mitigation. Coincidences were obtained for an average of $R_1 = R_2 = 2000 \pm 130$ cps from background white light, with quantum efficiency $QE_1 = QE_2 = 0.25$, dead time $DT_1 = DT_2 = 10$ s and temperature -90°C .

We integrate the histogram in a $\tau = 2$ ns window centered around the left peak and find a total of 3565 detected flashes in 60 s. Assuming that the probability of multi-photon emission is negligible, this corresponds to $R_{\text{BF}} = 237.6 \pm 16$ flashes per second when accounting for the detector's quantum efficiency. The flashing probability is $P_{\text{BF}} = 0.12$, equivalent to one emission every 8.3 detections on average.

Although electronic reflections could result in strongly correlated timestamps over the same channel, cross channel correlations cannot occur due to the inherent electro to optical isolation. We test the absence of other electronic artifacts by introducing a constant 100 ns delay on one channel (DG645 - Stanford Research Systems) and observing the expected side-shift of the histogram (Fig. 4.3b). In order to confirm the optical nature of the measured traces, we vary the optical link between the two detectors with a 6 m standard multi-mode fiber 62.5 μm (30 ns propagation time). As expected both peaks move away from the origin by 30 ns as shown in Fig. 4.4a. Interestingly, similar coincidence histograms can be obtained in complete darkness where an average of 210 detections per second are initiated by the thermal background in the diode's junction Fig. 4.4b. This last result further confirms that breakdown flashes are independent from the absorption of a photon and arise from radiative recombination of hot carriers. Finally, two weak features are found to the sides of the main correlation peaks. Given the time constraints of the setup, these

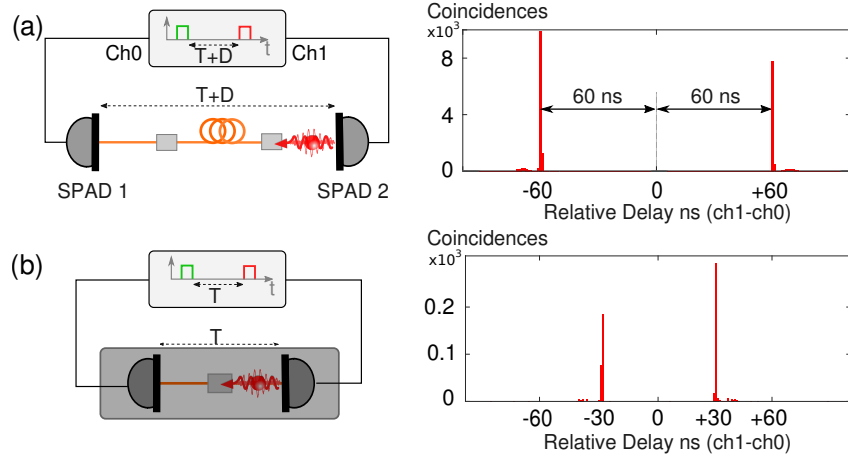


FIGURE 4.4: Longer optical links between the two detectors result in a simultaneous shift of the two peaks symmetrically around the origin
a) thus confirming the optical nature of the measured coincidences.
b) Avalanches initiated by thermal fluctuations (dark counts) can also generate breakdown flashes.

are manifestations of a temporally dispersive process that occurs after the onset of the first avalanche (first click). We note that the intrinsic group velocity dispersion of graded-index multi-mode fibers, typically on the order of hundreds of ps km^{-1} , cannot explain a delay spread of a few nanoseconds over a length of 3 m. We also note that these cannot be explained by two consecutive breakdown emissions, as a second flash would be characterized by the same temporal dynamics and thus appear in the same time bin as the primary flash. Moreover, after a first flash is detected both SPADs are inactive for a minimum dead-time of $DT = 10 \mu\text{s}$ much longer than the optical delay between the two SPADs. We tentatively attribute them to the transient response of the quenching electronics which could delay the radiative recombination of hot-carriers of a few nanoseconds. A direct measurement of the electronic impulse response would be needed in order to confirm this.

4.1.2 Spectral Characterization

Although the energy distribution of breakdown radiation is well understood from a theoretical standpoint a direct high-resolution measurement has so far remained elusive. This is primarily due to the weak nature of the emission which is often weaker than the intrinsic background noise of the detectors. An experimental upper bound for the spectral density of breakdown flashes can be calculated from the results in Fig. 4.3, considering that the sensitivity bandwidth is $w_D = 700 \text{ nm}$ and the saturation rate is $R_1 = 10 \times 10^5 \text{ Hz}$ for $DT_1 = 10 \mu\text{s}$. For a maximum quantum efficiency of 25%, the rate of detected breakdown emission in a 1 nm bandwidth can be estimated as $R_{\text{BF}, 1\text{nm}} = \text{QE}_1 \cdot R_1 \cdot P_{\text{BF}} / w_D \approx 4.3 \text{ Hz}$. The resulting signal-to-noise ratio would prohibit such spectral measurement ($SNR = 4.3/200 = 0.02$ for dark-count rate $R_{\text{BK}} = 200(15) \text{ Hz}$). However, while the temporal statistics of dark detections is well described by a uniform mass probability function, breakdown flashes always follow the onset of an avalanche. This strong temporal correlation allows us to perform off-line temporal filtering of the timestamps thus greatly increasing the SNR. The

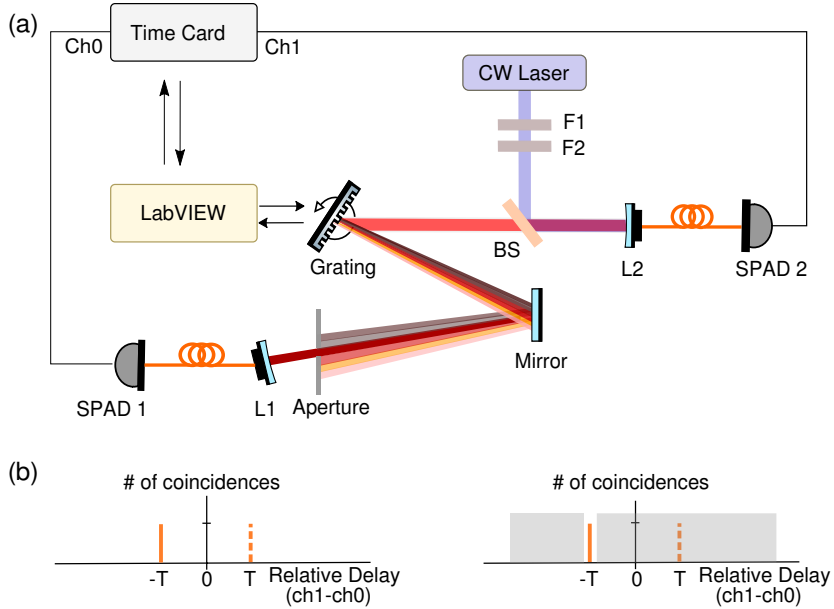


FIGURE 4.5: Experimental setup to characterize the energy distribution of breakdown flashes in ID230 [190]. a) A dispersive element in a time-correlated single-photon counting setup allows SPAD 1 to measure breakdown emissions from SPAD 2. b) Temporal gating leads to 4 orders of magnitude increase in SNR, thanks to a strong temporal correlation between the onset of an avalanche (detection) and hot-carriers radiative recombination (breakdown flash).

setup consists of a spectrally-resolved time-correlated single photon counting (TC-SPC) device (Fig. 4.5). A 100 kHz line-width CW laser centered at 1590 nm stimulates detection events in SPAD 2 which is the device under test.

The attenuated laser output is collimated ($L_1=L_2$: Thor-Labs RC08FC-P01), spatially filtered with a single mode fiber (SMF), spectrally filtered with a band-pass filter to suppress any amplified spontaneous emission (ASE) (F2: Santec OTF-320, 350 pm FWHM centered at 1590 nm) and weakly reflected to reach the active area of SPAD 2 (BS: ThorLabs BP208). Breakdown flashes originated in SPAD 2 propagate backwards through the same optical path, are diffracted by a rotating grating (Richardson Gratings 1200 grooves/mm blazed for 1300 nm) and are spatially filtered for wavelength selection before reaching SPAD 1. The spectral resolution of the system is measured to be 2 nm FWHM and limited by the optical path between the grating and L1. Breakdown emission is found to be broadband and extend from 1100 to 1600 nm. Fig. 4.6 shows the spectral distribution of the emission superimposed to the quantum efficiency of SPAD 1. We note that because absorption and multiplication occur in different materials of the semiconductor, the energy distribution of the flashes is unlikely to be correlated to the quantum efficiency of the source.

In order to understand the SNR gain introduced by the temporal gating we note that in TCSPC measurements, the SNR corresponds to the ratio between the rate of true coincidences R_{TC} and R_{AC} the rate of accidental coincidences:

$$CAR = \frac{R_{TC}}{R_{AC}} \quad (4.1)$$

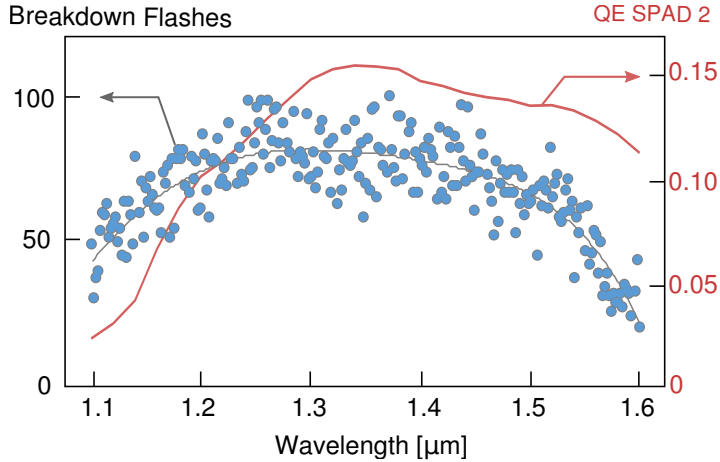


FIGURE 4.6: NIR spectral Distribution of breakdown flashes in ID230s. Circles (gray) represent background-free coincidence measurements over 180 seconds in 2 nm windows. The quantum efficiency of the detector (red) follows a different trend as absorption and multiplication of carriers occurs in two different materials of the diode heterostructure.

A true coincidence is registered when a detection in SPAD 2 is followed by the detection of the ensuing breakdown flash in SPAD 1. Accidental coincidences, on the other hand, can either occur in the absence of breakdown flashing (due to two simultaneous dark counts) or when a photo-detection SPAD 2 is followed by a dark count in SPAD 1. These can respectively be written as:

$$R_{TC} = R_{2_BF} \cdot QE_1 \cdot \frac{w_R}{w_D} \quad (4.2)$$

$$R_{AC} = R_{2_NBF} \cdot R_{1_BK} \cdot \tau \quad (4.3)$$

where R_{2_BF} and R_{2_NBF} are respectively the rate of detections in SPAD 2 that are followed by a breakdown emission and those that are not, and their sum is equal to the total count rate $R_2 = R_{2_BF} + R_{2_NBF}$. The dark-count rate of SPAD 1 is R_{1_BK} , and w_D , w_R , τ are respectively the sensitivity bandwidth of the detector, the spectral resolution of the monochromator and the width of the main peaks in the histogram. Typical values are $w_D = 700$ and $w_R = 2$ nm and $\tau = 2$ ns. The choice of quantum efficiency and dead-time is largely dictated by a trade-off between after-pulsing and dark counts [192]. In order to increase the saturation rate of the device under test (SPAD 2) we choose the minimum dead time $DT_2 = 2$ μs. However, the probability of after pulsing is a nonlinear function of the dead-time and can be limited drastically by tolerating a slightly lower quantum efficiency ($QE_2 = 10\%$). The settings for SPAD 1 are $QE_1 = 25\%$, $DT_1 = 10$ μs. From a total count rate of $R_2 = 5 \cdot 10^5$ cps, and the breakdown-flashing probability extracted in sec. 4.1.1 ($P_{BF} = 0.12$), we calculate a rate of true and accidental coincidences as $R_{TC} = 8.57$ and $R_{AC} = 0.035$ which results in CAR = 250. We note that this is more than 4 orders of magnitude larger than the signal to noise ratio that would have been possible without temporal gating: $SNR = 0.02$ (sec. 4.1.2).

To summarize, the emission is found to be broadband and not correlated with the

wavelength-dependent quantum efficiency of the detectors, and its emission probability (that is the probability to emit one or more breakdown flashes per avalanche, is estimated to be 12 % (or 0.12). The histogram of photon coincidences shows a highly localized probability mass function, in stark contrast to the exponentially decaying trend that is common in passively-quenched detectors. This is believed to result from the fast quenching electronics in ID230s which constrains radiative recombinations within a narrow temporal window from the onset of the avalanche. This narrow temporal autocorrelation can be leveraged to increase the coincidences over accidental ratio (CAR) and thus measure the spectral content of breakdown flashing with unprecedented resolution. Most importantly, this shows that the effect can be deterministically filtered in the time domain without the use of expensive and narrow-band non-reciprocal elements.

4.2 CAR in the measurement of photon simultaneity

The goal of this section is to describe all sources of accidental coincidences that disturb the measurement of time-correlations in entangled photon pairs and thus help define the coincidences over accidental ratio (CAR). We first derive two simple analytical expressions for the average CAR when measurements are only limited by dark-counts or background (photoluminescence). We frame the problem in terms of average rates of generation and detection of photons, so that our results do not depend on details of the downconversion process. We also include experimental parameters such as loss, bin time, and laser repetition rate, and discuss how and when each of these can be optimized to increase the CAR. We then focus on spontaneous parametric downconversion under ultrafast pumping (section 4.5), and derive specific expressions for mono-layers of transition-metal dichalcogenide (TMDC) at the interface between two dielectrics. Finally, we turn our attention to the Hanbury-Brown and Twiss (HBT) free-space setup described in section 3.1.9 (see fig. 3.10). We distinguish different sources of loss, and discuss their combined effect on the CAR, and the practical time required to observe a minimum number of true coincidences when accidental coincidences are primarily caused by dark counts.

4.2.1 Sources of accidental coincidences

A true coincidence corresponds to the simultaneous detection of each photon of an energy-time entangled pair, by a different single-photon detector in a Hanbury-Brown and Twiss interferometer. In the following, any other pair of such simultaneous detections are referred to as *noise* detections, and are the source of accidental coincidences.

Among the most common sources of accidentals are the thermal noise in the detectors (dark counts), radiative emissions from the material (background) or from the active area of single-photon avalanche photodiodes (breakdown flashing) [193], as well as the loss, where the detection of only one photon of a pair occurs simultaneously to that of a *noise* photon. We refer to the respective rates of these accidental coincidences as $R_{\text{AC-dark}}$, $R_{\text{AC-bkg}}$, $R_{\text{AC-bf}}$ and $R_{\text{AC-loss}}$ [178].

The probabilistic bunching of photon pairs at the beam-splitter of the HBT interferometer, can also introduce accidental coincidences, as the detection of the signal

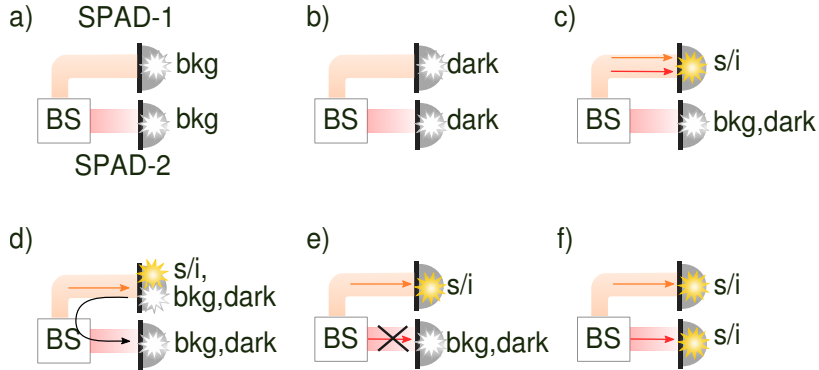


FIGURE 4.7: Breakdown of the processes that lead to accidental coincidences a-e) and true coincidences f): a-b) simultaneous dark and background detections; c) bunching of photon pairs at one output of the beam splitter followed by a dark or background detection; d) detection of breakdown flashing following any detection event; e) linear loss causes only one photon of the pair to be detected together with noise.

(any of the two photons of a pair) can occur simultaneously to that of noise (background or dark). We indicate this as $R_{AC\text{-bs}}$. The combined average rate of accidental coincidences can thus be written as

$$R_{AC} = R_{AC\text{-dark}}^{\text{nn}} + R_{AC\text{-bkg}}^{\text{nn}} + R_{AC\text{-bf}}^{\text{nn}} + R_{AC\text{-loss}}^{\text{ns}} + R_{AC\text{-bs}}^{\text{ns}}, \quad (4.4)$$

where the superscripts indicate cases that involve two coincident *noise* detections (nn), and those involving *noise-signal* detections (ns). The former are always present even if there is no generation of photon pairs, while *noise-signal* accidentals occur only in the presence of a mixture of signal and noise.

In order to be able to measure the simultaneity of SPDC photon pairs, the rate of true coincidences R_{TC} must exceed that of accidentals R_{AC} in the time bin of interest denoted by $t_{\text{bin}} = \tau^*$. While $\tau^* = 0$ when the arms of the HBT interferometer have the same propagation length, it is often preferable to work with $\tau^* \neq 0$ to limit the effect of anomalies in the time-tagging electronics (more on this in section 3.6). In order to perform a statistically significant measurement of temporal correlations the CAR must be larger than one

$$\text{CAR} = \frac{R_{TC}|t_{\text{bin}} = \tau^*}{R_{AC}|t_{\text{bin}} = \tau^*} \geq \text{CAR}_{\text{th}} > 1. \quad (4.5)$$

Since signal and idler photons are emitted at the same time, R_{TC} is equal to the number of true coincidences in the bin time $t_{\text{bin}} = \tau^*$. In particular, assuming that pair generation rate and loss are statistically independent process, the average rate of true coincidences is

$$R_{TC}|t_{\text{bin}} = R_{TC} = R_{\text{SPDC}}/L_T^2, \quad (4.6)$$

where R_{SPDC} is the calculated rate of photon pair generation on the sample, and L_T is the total loss that an SPDC photon experiences from generation to detection.

4.2.2 Dark-count-limited CAR

If the SPDC pump energy is sufficiently far from any optical resonance in the non-linear medium, the average detection rate from spontaneous radiative emissions can be neglected ($R_{\text{bkg-det}} \approx 0$). Although spectrally broadband, breakdown flashing in actively quenched single-photon detectors can be deterministically filtered and their contribution to the accidentals neglected ($R_{\text{AC-bf}} = 0$) [193]. Furthermore, if the rate of dark detections dominates over the rate of SPDC pairs, both $R_{\text{AC-loss}}$ and $R_{\text{AC-bs}}$ can be neglected because the number of accidentals due to *noise-noise* detections dominates over *noise-signal* ones. Under these assumptions eq. (4.4) reduces to

$$R_{\text{AC}} \approx R_{\text{AC-dark}}. \quad (4.7)$$

We can write the CAR analytically if we assume that the time at which dark-counts are detected is well described by a memory-less and white stochastic process with a uniform probability density function. Indicating the average rate of dark detections and the repetition rate of the laser respectively as $R_{\text{dark-det}}$ and ν_{rep} , the average rate of accidentals is

$$R_{\text{AC}}|t_{\text{bin}} \approx R_{\text{dark-det}}^2 \cdot t_{\text{bin}}, \quad (4.8)$$

which is the product of the probability to record two simultaneous dark detections in one bin ($R_{\text{AC-dark}} \cdot t_{\text{bin}}$)² and the number of bins in one second $N_{\text{bins}} = 1/t_{\text{bin}}$. The average CAR in such a dark-count limited measurement takes the form

$$\text{CAR} = \frac{R_{\text{SPDC}}}{L_T^2 R_{\text{dark-det}}^2 t_{\text{bin}}}, \quad (4.9)$$

which highlights the inverse quadratic dependence on the total loss L_T and thermal noise $R_{\text{AC-dark}}$ in the system. This suggests the use of single-photon detectors with a high quantum efficiency and low dark-counts, as well as reflective optics with high transmissivity, in a system to collect pairs efficiently. The effect of the bin time t_{bin} on the signal and noise is different, owing to different temporal statistics between the time correlated photon pairs (SPDC) and the uncorrelated thermal noise.

If the jitter is negligible, the number of true coincidences at $\tau = \tau^*$ does not depend on the bin time. In contrast, dark detections are more likely to lead to accidental coincidences in the same $\tau = \tau^*$ for large bin times. Overall, this means that CAR scales linearly with the inverse of the bin sizes as shown in eq. (4.9), and is strictly true only for t_{bin} much larger than the cumulative jitter of the electronics (TIA, SPADs, and all other electronic processing described in section 3.1.9). Although the dark count rate cannot arbitrarily be reduced, detection-gating can lead to a reduction of the total loss as discussed in section 3.7.

Under the assumption of perfect phase-matching, negligible multi-pair generation, and a constant pump intensity across the interaction volume (undepleted pump approximation), we can substitute eq. (2.52a) in eq. (4.9) and write the average coincidences over accidental ratio as

$$\text{CAR} = \frac{1}{12\pi c^3 \epsilon_0} \cdot \frac{\bar{I}_{\text{SH}}}{t_{\text{bin}}} \left(\frac{d}{L_T} \cdot \frac{\chi_{\text{eff}}^{(2)}}{R_{\text{dark-det}}} \right)^2 \frac{\omega_F^2 \omega_{\text{SHG}}^2}{n_F^2 n_{\text{SHG}} \omega_{\text{SPDC}}}, \quad (4.10)$$

where we assumed $L_A \approx 0$. The CAR increases quadratically with the second-order susceptibility $\chi_{\text{eff}}^{(2)}$ of the material, the interaction length d (thickness of the 2D material), the inverse of the dark count rate ($R_{\text{AC-dark}}$) and the inverse of loss L_T (eq. (4.21)). In this regime a higher pump intensity leads to a linear increase of CAR.

4.2.3 Background-limited CAR

When illuminated with a bright laser beam, any material exhibits some degree of spontaneous photo-emission. Examples are two-photon processes (such as linear photoluminescence, Raman scattering etc.), as well as three-photon processes (such as two-photon emission (TPE)), four-photon processes such as spontaneous four-wave mixing (SFWM) as well as higher order ones. In a coincidence measurement, this leads to a non-zero probability that two statistically-independent photon emissions are detected at the same time $R_{\text{AC-bkg}}^{\text{nn}} \neq 0$, resulting in a coincidence in the histogram for $\tau = 0$ (or any other time $\tau = \tau^*$). When the energy of emission does not overlap with the energy of the signal-idler pairs, its contribution to the accidental coincidences can be controlled with spectral filters, and the CAR greatly improved as a result. There are however situations where energy degeneracy between the uncorrelated background and the energy-time entangled pairs renders any filtering ineffective. It is this second class of processes that are of interest in this section.

If the intensity of such in-band background emission dominates over any other noise process, $R_{\text{AC-bkg}} \gg R_{\text{AC-dark}}$, the rate of accidentals is simply

$$R_{\text{AC}}|t_{\text{bin}} \approx R_{\text{AC-bkg}}|t_{\text{bin}}. \quad (4.11)$$

Despite the large simplification compared to eq. (4.4), writing an analytical expression for the right-hand-side of eq. (4.11) is not straightforward, as the assumption of uniform probability distribution that holds for thermal detections seldom applies to spontaneous emissions. For instance, for a single two-level electronic system under femtosecond pump illumination, the probability density function (pdf) of the time of emission is a decaying exponential [168]. For the experiments described in this thesis, a more realistic assumption is that the background results from many such emitters, as a typical diffraction-limited illumination spot interests thousands of atoms. Thus, an accurate calculation of $R_{\text{AC}}|t_{\text{bin}}$ would require to measure the pdf of the emission, $\Gamma(t)$, and calculate the probability of two simultaneous emissions conditioned to the arrival of a pump pulse.

In the following we consider the case of a pulse leading to two background detections, and show that a lower-bound on the CAR can be derived with two simple assumptions. The first, true for the experiments described here, is that the bin time is much smaller than the repetition period of the laser $t_{\text{bin}} \ll T_{\text{rep}}$. The second, is that the pdf of the emission is so short that can be approximated by a Dirac's delta, $\Gamma(t) = \delta(t)$. This implies that the emission lifetime is infinitely small, $E[\Gamma] = 0$, and the number of radiative emissions from the same system inside the span of a single laser pulse is unbound. As a result, any two detections received within a pulse repetition period T_{rep} would be recorded at the same time, $\tau = \tau^*$, thus leading to a minimum CAR. In reality $\Gamma \neq \delta(t)$, and one has a much lower chance to register a double simultaneous excitation and emission.

We can show this a bit more rigorously by writing down the probability of a background detecting after the arrival of a pump pulse as

$$P\{N_{\text{det/pulse}} = 1\} \approx \frac{R_{\text{bkg-det}}}{\nu_{\text{rep}}}, \quad (4.12)$$

where $R_{\text{bkg-det}}$ is the average rate of background detections, and ν_{rep} is the repetition rate of the laser. We now assume that if two emission occur come from two different electrons after illumination by one pulse they are statistically independent, and indicate with $P\{N_{\text{det/pulse}} = 2\}$ the probability of recording two background detections from one pulse. If the two SPD are identical, L_D (and thus L_T) is the same for both detectors. If $\Gamma = \delta(t)$, the pulse-wise probability of recording an accidental coincidence from background emission alone is simply

$$P_{\text{AC-bkg/pulse}} = P\{N_{\text{det/pulse}} = 2\} \approx \left(\frac{R_{\text{bkg-det}}}{\nu_{\text{rep}}} \right)^2, \quad (4.13)$$

and the corresponding rate of accidental coincidences is then

$$R_{\text{AC-bkg}} = \nu_{\text{rep}} \cdot P_{\text{AC-bkg/pulse}} = \frac{R_{\text{bkg-det}}^2}{\nu_{\text{rep}}}. \quad (4.14)$$

We now incorporate the temporal probability density function of the background light $\Gamma(t)$, with a corresponding lifetime given by its expectation $\bar{\Gamma} = \mathbb{E}[\Gamma(t)] \neq 0$, and show that eq. (4.14) is an upper bound which can be used to infer a CAR lower-bound without knowing the functional form of $\Gamma(t)$. The probability to detect an accidental coincidence after one pulse is

$$P_{\text{AC-bkg/pulse}} \approx \int_0^\infty \left(\frac{\Gamma(t) R_{\text{bkg-det}}}{\nu_{\text{rep}}} \right)^2 dt, \quad (4.15)$$

where the integral starts from 0 because radiative emission cannot precede the excitation ($\bar{\Gamma}(t < 0) = 0$). The rate of accidental coincidences can be found simply by multiplying this by the repetition rate of the laser. However, in a practical experiment any two detections that occur within a time difference t_{bin} are considered to be simultaneous. We can thus write a more general expression for the rate of accidentals

$$R_{\text{AC-bkg}} = \frac{R_{\text{bkg-det}}^2}{\nu_{\text{rep}}} \int_0^{t_{\text{bin}}} \int_0^\infty \Gamma(t) \Gamma(t + t^*) dt dt^* \quad (4.16)$$

and observe that when the bin time is small relative to the repetition period of the laser, $t_{\text{bin}} \ll T_{\text{rep}}$, we find

$$R_{\text{AC-bkg}} \approx \frac{R_{\text{bkg-det}}^2}{\nu_{\text{rep}}} t_{\text{bin}} \int_0^\infty \Gamma(t)^2 \leq \frac{R_{\text{bkg-det}}^2}{\nu_{\text{rep}}} t_{\text{bin}} \quad (4.17)$$

where the last inequality holds because $0 < \Gamma < 1$, $\forall t > 0$ and has unitary area by definition. Assuming that the rate of photon pairs scales linearly with the laser

repetition rate, we can write a lower-bound for the average CAR as

$$\text{CAR} \geq \frac{R_{\text{SPDC}}}{L_T^2 R_{\text{bkg-det}}^2 t_{\text{bin}}} = \frac{R_{\text{SPDC}}}{R_{\text{bkg-sample}}^2 t_{\text{bin}}}, \quad (4.18)$$

where the rate of background photons detected from each arm of the beam-splitter as a function of those emitted at the sample plane, is given by

$$R_{\text{bkg-det}} = R_{\text{bkg-sample}} / L_T. \quad (4.19)$$

Note that the effect of the beam-splitter is included in the detection loss of L_T under the assumption that the splitting ratio is even. Crucially, when both signal and noise are evaluated at the sample plane, the CAR lower-bound does not depend on the total loss in the system L_T since this would have a detrimental effect on both the true and accidental coincidences, and shows the same dependence on t_{bin} as in eq. (4.9). In the experiment results presented in section 4.5.4, the SPADs routinely recorded $R_{\text{bkg-det}} \approx 1 \times 10^3$ Hz. With a measured loss of $L_T = 88.8$, $R_{\text{bkg-sample}} \approx 88 \times 10^3$ Hz, with $R_{\text{SPDC}} = \bar{R}_{\text{SPDC}} = 0.002 \pm 0.0016$ pairs/s (eq. (4.29)), this corresponds to a CAR of 2×10^{-4} . In conclusion, the last equality in eq. (4.18) provides a CAR lower-bound and is obtained under the assumption that the background lifetime is zero (in practice much smaller than the jitter). In the case of radiative emissions from exciton in mono-layer TMDCs (direct band-gap), the typical lifetime is 3 ps [194], many times shorter than the smallest time constant in a coincidence measurement (jitter ≈ 300 ps), and thus practically instantaneous.

These derivations can be applied to the case of a measurement from a planar film of monolayer transition-metal dichalcogenide (TMDC). Under the assumption of perfect phase-matching, negligible multi-pair generation, and a constant pump intensity across the interaction volume (undepleted pump approximation), the average coincidences over accidental ratio can be written as

$$\text{CAR} \geq \frac{1}{12\pi c^3 \epsilon_0} \cdot \frac{1}{t_{\text{bin}}} \left(\frac{d}{L_T} \cdot \frac{\chi_{\text{eff}}^{(2)}}{R_{\text{bkg-det}}} \right)^2 \frac{\omega_F^2 \omega_{\text{SHG}}^2}{n_F^2 n_{\text{SHG}} \omega_{\text{SPDC}}}, \quad (4.20)$$

where we substituted eq. (2.52a) into eq. (4.18) and assumed $L_A \approx 0$. The CAR preserved the same dependence on second-order susceptibility, interaction length, and loss as predicted in eq. (4.10). The dark count rate is replaced with the background intensity $R_{\text{bkg-det}}$. Since this typically scales with pump intensity, to first order this counteracts the linear increase of photon-pairs thus removing the CAR dependence on pump power. The experiment time however is luckily to be affected as shown later in fig. 4.9.

4.2.4 Types of loss and their effect

In a free-space setup we can identify four contributions to L_T in a linear system

$$L_T = L_A \cdot L_C \cdot L_P \cdot L_D, \quad (4.21)$$

where L_A , L_C , L_P and L_D , respectively represent the loss due to the absorption of generated photon pairs in the nonlinear medium, due to the mismatch between the radiation pattern of the emission and the receiving lenses (collection efficiency), the

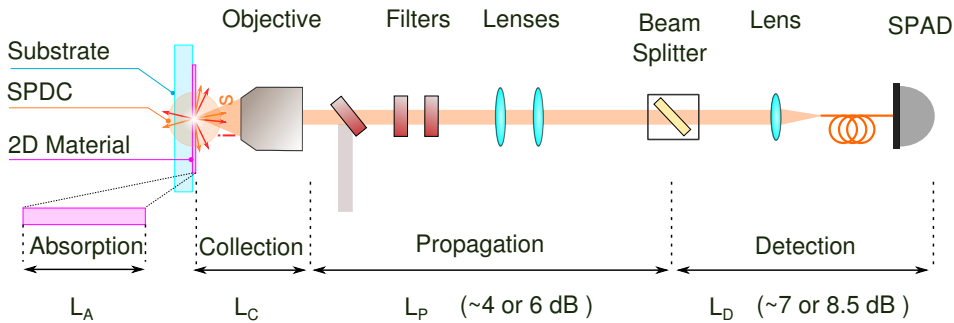


FIGURE 4.8: Breakdown of loss in a typical free-space setup for the measurement of photon simultaneity. A distinction is made between re-absorption of the photon pairs in the nonlinear medium (absorption), non perfect overlap of emission/collection radiation patterns as well as any reflection/absorption inside the objective (collection), loss due to filters and lenses (propagation), and the loss introduced by effect of beam splitter fibers and SPADs (detection). Brackets show values measured from the setup of fig. 3.10, assuming detection of photon pairs at 1550 nm and SPADs operated at $\eta_{\text{det}} = 10\%$ ($\eta_{\text{det}} = 0.14$ for ID230 - ID Quantique extracted from fig. 3.14).

absorption in the optical path between the objective and the beam-splitter (propagation loss) and, the quantum efficiency of the detectors along with the bunching at the beam splitter (detection loss). These are shown in fig. 4.8. The use of a beam splitter introduces a factor of 0.5 corresponding to the probability that both signal and idler photons bunch to one of the two output ports.

The effect of loss on the CAR depends on the nature of the noise and its relative magnitude compared to the signal. As shown in eq. (4.13), if emission and detection are statistically independent, the rate of accidental coincidences due to background light increases quadratically with its intensity, as a single laser pulse would have to generate two photo-emissions in order to lead to two simultaneous detections. This in turn scales increases linearly with the inverse of the total loss in the system, resulting in a net quadratic dependence on loss. However, energy conservation in SPDC means that photon pairs are always generated in pairs, and in principle the rate of true coincidences depends only linearly on the pair rate. On the other hand, a coincidence can only be measured if both photons are detected, leading to a quadratic dependence on loss. As a result, the net CAR does not depend on loss. A different case is the one of measurements limited by thermal noise. To first approximation this is independent of loss, which quadratically affects the rate of true coincidences, thereby appearing to the second power on the CAR. Another important effect of loss on the measurement is the experiment time, that is the time required to observe a given number of coincidence events. Figure 4.9 shows this in the case of dark-count limited measurement for different loss in the system. The rate of SPDC pairs at the sample plane is plotted against the observation time required to detect at least 5 true coincidences with a 95 % confidence. Calculations assume $t_{\text{bin}} = 1 \text{ ns}$ and a Poissonian probability density function of the time between two consecutive down-conversions. Starting from the SPADs of fig. 4.8 and moving towards the sample, we gradually remove loss while requiring a CAR>10, and find a minimum pair rate at the sample plane required for a successful measurement of photon simultaneity. The slope of the curves is -1, showing the expected linear inverse relationship between

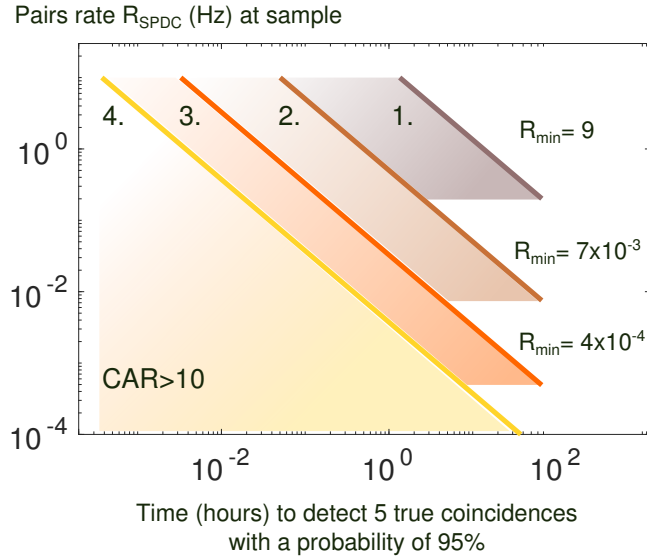


FIGURE 4.9: Minimum pair rate R_{min} Hz to guarantee a CAR>10 as a function of the observation time required to detect at least 5 true coincidences with a 95 % confidence. 1) realistic experimental setup with simulated collection loss, 2) ideal detection and propagation, 3) ideal detection and no loss ($L_T = 0$).

pairs rate and integration time.

Finally, it is important to note that if thermal noise and background were zero, the rate of detectable photon pairs would be unbounded, and loss would only have the effect of increasing the integration time of the experiment.

4.3 Simulations of loss and CAR in free-space SPDC

Photon pairs generated by SPDC in atomically-thick materials are emitted in the surrounding medium with a broad range of angle pairs. As such, this interaction is best probed in free-space, where substrates can be carefully chosen to be transparent and free from defects and impurities that could affect the measurement. In order to calculate the CAR it is important to quantify accidental coincidences as well as to estimate the total loss in the system. Once this is known, we can calculate a lower-bound for the rate of generated photon pairs (and corresponding minimum value of $\chi_{\text{eff}}^{(2)}$) required for a meaningful measurement of photon-simultaneity. With reference to eq. (4.21) and neglecting absorption loss, the total loss is the product of three terms $L_T = L_P \cdot L_D \cdot L_C$. While the first two can be measured directly in the laboratory, collection loss L_C depends on the emission angle of the pairs which in turn is constrained by momentum conservation at the nonlinear interface. In this section we describe the model and a tool to perform numeric simulations that includes all losses.

4.3.1 Model for the collection loss

Starting from basic principles of momentum and energy conservation, we describe a model of radiation patterns at a nonlinear and diffraction-limited interface between two uniform dielectrics. We model the pump $p(\omega_p, k_p, \theta_p, t_p)$ as a linearly polarized

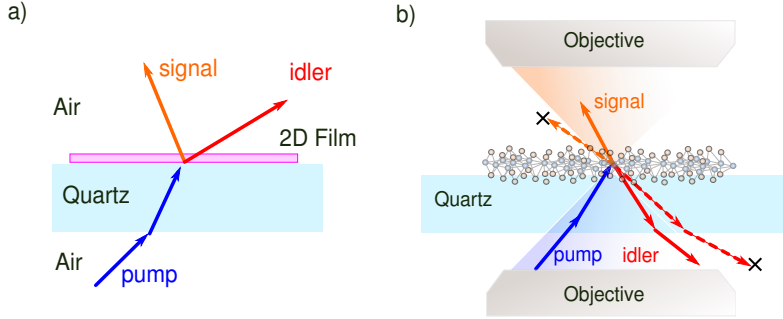


FIGURE 4.10: a) Momentum conservation at a flat interface between the mono-layer and its dielectric environment shapes the radiation pattern and the resulting probability of collecting both photons of a pair. b) Example of two combinations of signal and idler pairs, where two are collected and one is lost.

optical plane wave incident at time $t = t_p$ at the air/quartz interface with incidence angle $\theta = \theta_p$, angular frequency $\omega = \omega_p$ and wave-vector $k = k_p$. The process of spontaneous annihilation of a pump photon into signal $s(\omega_s, k_s, \theta_s, t_s)$ and idler $i(\omega_i, k_i, \theta_i, t_i)$ photons with $t_s = t_i$, is driven by the $\chi^{(2)}$ of the medium and constrained by energy and momentum conservation

$$k_p \sin(\theta_p) = k_s \sin(\theta_s) + k_i \sin(\theta_i), \quad (4.22a)$$

$$\hbar\omega_p = \hbar\omega_s + \hbar\omega_i, \quad (4.22b)$$

where p, s, i denote pump, signal and idler respectively, $\hbar\omega_x$ is the photon energy and $k_x \sin(\theta) \equiv k_{x//}$ is the component of the wave-vector parallel to the planar interface between the 2D material and the surrounding dielectrics [178]. This is schematically shown in fig. 4.10 a) at a quartz-air interface. Equation (4.22a) dictates the allowed departure angles θ_s and θ_i , and therefore shapes the radiation pattern of the down-converted light. Starting from an incident pump photon $p(k_p, \theta_p)$ we fix the energy of signal and idler photons symmetrically around of $\hbar\omega_p/2$ and find θ_i for $0 \leq \theta_s \leq 2\pi$

$$\theta_i = \arcsin \left(\frac{k_p \sin(\theta_p) - k_s \sin(\theta_s)}{|k_i|} \right). \quad (4.23)$$

In order to understand the effect of each term we start from the simple case of $\theta_p = 0$ and degenerate SPDC in a homogeneous dielectric environment, $|k_s| = |k_i|$. When the two photons leave the interface in the same semi-space eq. (4.23) has the real solution $\theta'_i = -\theta_s$ which becomes $\theta''_i = \pi - \theta_s$ if the pairs departs in two opposite sides of the medium. Since these two events are equally likely, the joint probability distribution along a unitary circle centered at the interface is uniform and the pair emission is omni-directional. When $\omega_s \neq \omega_i$ and $\theta_p = 0$, the idler departure angle becomes $\theta_i = \arcsin(-k_s/|k_i| \sin(\theta_s))$ which may yield complex solutions if $k_s > |k_i|$, a condition that does not depend on the photon emission angles. Considering that there are an infinite number of equally-likely solutions to eq. (4.22b) this is expected to happen with a 50% chance. If the dielectric environment surrounding the nonlinear medium is non homogeneous and ω_s and ω_i are energy degenerate, it is possible that $k_s > |k_i|$ which results in complex θ_i . However, since θ'_i and θ''_i are

equally likely, there is always the corresponding case $k_s \leq |k_i|$ so the overall radiation diagram maintains its uniform shape. An angular dependence of the emission probabilities can however arise for $\theta_p \neq 0$ when $k_{p//} - k_{s//} > |k_i|$. This alters the probability to find a pair in the far field and leads to a directional radiation pattern.

4.3.2 Numerical Implementation

Numerical simulations are performed with an ad-hoc toolkit designed to model the free-space spontaneous parametric downconversion of a pump photon in a 2D nonlinear material deposited at the interface between two dielectrics. The aim is to enable a simulation of the signal-idler departure angles, the collection loss, true and accidental coincidences, and their ratio (CAR).

We define key properties for photons (such as angular momentum, energy and wavelength), pulsed laser fields (such as peak and average power, power density, repetition rate, pulse duration etc.) and of single-photon avalanche photodiodes and CCD sensors, (quantum efficiency, gain factor and dead-time). A ‘medium’ class defines basic properties of an optical medium such as linear refractive index, thickness, and linear absorption. All optical element involved in the experiment such as dichroics, beam-splitters, filters, including the nonlinear two-dimensional film inherit from the same class and expand their attributes and methods. Objectives are modeled as thin lenses in the paraxial approximation, with a uniform apodization function, and have additional properties such as numerical aperture, working distance and pupil diameter. The nonlinear medium also has an associated $\chi^{(2)}$ which is estimated from classical nonlinear measurements. Internally, the sample is represented as an ordered collection of media (such as air, nonlinear-film, substrate, and air). The same applies to the experimental setup, which will feature all lenses, filters, beams-slitters and detectors that are encountered by a propagating photon from its generation on the sample to its detection by a SPAD.

Before describing the principles that guided the design of this tool, we note that for the purpose of calculating the instantaneous collection probability of a photon we would need to write the system Hamiltonian, solve for the photon wave-function and calculate the expectation of the photon number operator at each point of the setup. Here we employ a classical and macroscopic picture. Photons propagate from one element of the setup to the next, with an average probability inversely proportional to the experienced propagation loss. If $N/2$ photons reach the end of one section out of a total of N , the photon probability $p \rightarrow 0.5$, for $N \rightarrow \infty$. In this sense, a probability change from $p = 1$ to $p = 0.5$ would ideally lead to detect one out of two input photons on average. Equivalently, if we had two constant fluxes of N identical photons with $p = 1$ and $p = 0.5$ respectively, they would correspond to classical optical fields with a normalized average power $P = 1$ and $P = 0.5$. This approach is computationally efficient and offers an intuition of the performance of the system. Such probability is updated during propagation to account for any reflection at the dielectric interfaces (linear Fresnel coefficients) and absorption/collection losses. At any given time, there is a very small probability to generate a pair of photons (section 2.5.1). However, to rounding errors that would derive from manipulating small numbers, the probability calculations assume deterministic downconversions ($R_{SPDC} = 1$). To find the true rate of collected photon pairs, the results can then be conveniently scaled by the true rate of downconversion events (section 2.5.1).

Starting from the excitation, a pump plane wave departs from the front lens of the illumination objective with a specific momentum (angle) and reaches the nonlinear film. Following eq. (4.23), θ_s is varied and θ_i calculated thus accumulating a large range of possible signal and idler pairs. Pairs are then individually propagated towards the collection lens(es) and the detectors. If the departure angle of each individual photon exceeds the numerical aperture of the collection optics, it is lost and its probability assigned to zero. Assuming that the density of propagating states at the interface is uniform in momentum space, all candidate downconversions occur with the same probability. The average probability of collecting both photons of a pair, needs to account all possible ways momentum can be conserved (eq. (4.23)). Information on each photon of the many possible pairs is recorded at each pump incidence angle. The output of an SPDC simulation is a dataset with tens of thousands of photons at the input of the beam-splitter of fig. 4.7 (hundreds of signal-idler pairs for hundreds of pump incidence angle).

Simulating single-photon coincidences

With this as an input, a coincidence simulation performs a probabilistic separation of pairs at the beam-splitter and accounts for their probabilistic detection, updating the probabilities and locations in the dataset. The routine that calculates the average CAR, computes the average probability $R_{\text{TC}}|t_{\text{bin}}$ that pairs split and are both detected in the bin time t_{bin} , as well as the average probability $R_{\text{AC}}|t_{\text{bin}}$ to record an accidental coincidence in the bin time eq. (4.5). Recall from eq. (4.4) that accidentals can be caused by at least five different processes

$$R_{\text{AC}} = R_{\text{AC-dark}}^{\text{nn}} + R_{\text{AC-bkg}}^{\text{nn}} + R_{\text{AC-bf}}^{\text{nn}} + R_{\text{AC-loss}}^{\text{ns}} + R_{\text{AC-bs}}^{\text{ns}}. \quad (4.24)$$

At the moment of writing this manuscript, the toolkit can account for $R_{\text{AC-dark}}^{\text{nn}}$, and offers a lower bound for the CAR in the presence of a dominant contribution from $R_{\text{AC-bkg}}^{\text{nn}}$, as discussed in section 4.2.3. The computation of the radiation patterns and collection loss is independent from the simulation of single-photon coincidences and calculation of the CAR. This results in a computationally efficient and modular code that facilitates the exploration of the effect of each degree of freedom on the experimental feasibility. The toolkit can easily be extended to incorporate the radiation pattern of more complex structures, such as ring resonators and nano-pillars, whose numerical analysis via finite element method simulations [195].

4.4 Measurement of femtosecond pulses: NanoFROG

Thanks to a fundamental connection between the spontaneous process of SPDC and its classical analog of second-harmonic generation (SHG), it is possible to calculate the expected rate of photon pairs (former) from the efficiency of the latter, assuming that the durations of all pulses of light involved are known accurately. Measuring the dynamics of an event typically requires to observe its evolution via a detector, probe, etc. faster than the event being measured. However, a Gaussian optical pulse of 200 fs has a bandwidth larger than 2000 GHz, which is prohibitive for any electronic circuit and thus cannot be measured directly. A typical way to circumvent this is to measure the pulse autocorrelation to infer the pulse temporal duration. The general principle of an autocorrelation is to measure the product of a function

with a delayed version of itself. Starting from an optical beam, a beam-splitter creates two identical copies of the pulse which then interfere at another beam-splitter. They then mix via some form of nonlinear optical process, and the result of this interaction is detected with a conventional (slow) detector. The time-series of intensities recorded at each relative delay constitutes the autocorrelation trace. Typically one needs an a-priori knowledge of the pulse envelope in time in order to extract meaningful conclusions from an autocorrelation trace. Without this, there is an infinite number intensity and phase solutions for each autocorrelation trace, leaving the pulse structure practically unknown. Being a phase-insensitive measurement, the autocorrelation cannot reveal the inner structures of the pulse such as variations of the instantaneous frequency over time (chirp). A solution to this is Frequency Resolved Optical Gating (FROG), a robust approach to fully characterize an ultrashort pulse which has been successfully used from the UV to the near-infrared [196] with durations of only a few femtoseconds. To measure a FROG trace instead of recording the intensity of the multiplication between the pulse and its delayed self, the spectrum is measured at each delay.

Thus, a FROG trace contains information on delay, intensity and frequency, which can be analyzed numerically and allow to retrieve both the amplitude and phase of the pulse. There are many ways to implement a FROG and each has strengths and weaknesses. For a detailed description we refer the reader to [197] and references therein.

Here we report the measurement of the pulse envelope via a collinear FROG, where illumination and collection are performed via the same lens in a reflection geometry. Pulse multiplication is performed via SHG at a diffraction-limited Au feature at the sample-plane of the microscope setup of fig. 3.5. Since each pulse propagates through the same setup used for all nonlinear measurements (see for instance section 4.5.1), all dispersion effects are automatically accounted for, providing an accurate measurement of the pulse width at the sample plane. The spectrogram observed in a SHG and collinear (C) FROG measurement can be written as [198]

$$I_{\text{C-FROG}}(\tau, f) = \left| \int_{-\infty}^{+\infty} (E(t) + E(t - \tau))^2 \exp(i2\pi ft) dt \right|^2. \quad (4.25)$$

where τ is the relative delay between the pulses, and f is the frequency measured. By expanding this expression, four contributions can be recognized. The most important term is of the form

$$I_{\text{FROG}}(\tau, f) = \left| \int_{-\infty}^{+\infty} (E(t) + E(t - \tau)) \exp(i2\pi ft) dt \right|^2. \quad (4.26)$$

The other three contributions represent the sum of the SHG of the pulse and the SHG of its delayed copy; a cross-term between the interference of the SHG pulses, and the interference of the SHG of each pulse with the product between the fields. While these terms are always present in any SHG FROG, a non-collinear geometry typically allows to spatially isolate the first from the last three terms. In order to extract the FROG trace it is sufficient to apply a low-pass filter to the trace detected [198]. Figure 4.11 shows results of two FROG measurements of the TiSaph and OPO lasers described in section 3.1.1 at $\lambda = 900$ nm and $\lambda = 1550$ nm, respectively. The autocorrelation part of the measurement setup is described in section 3.1.4, where

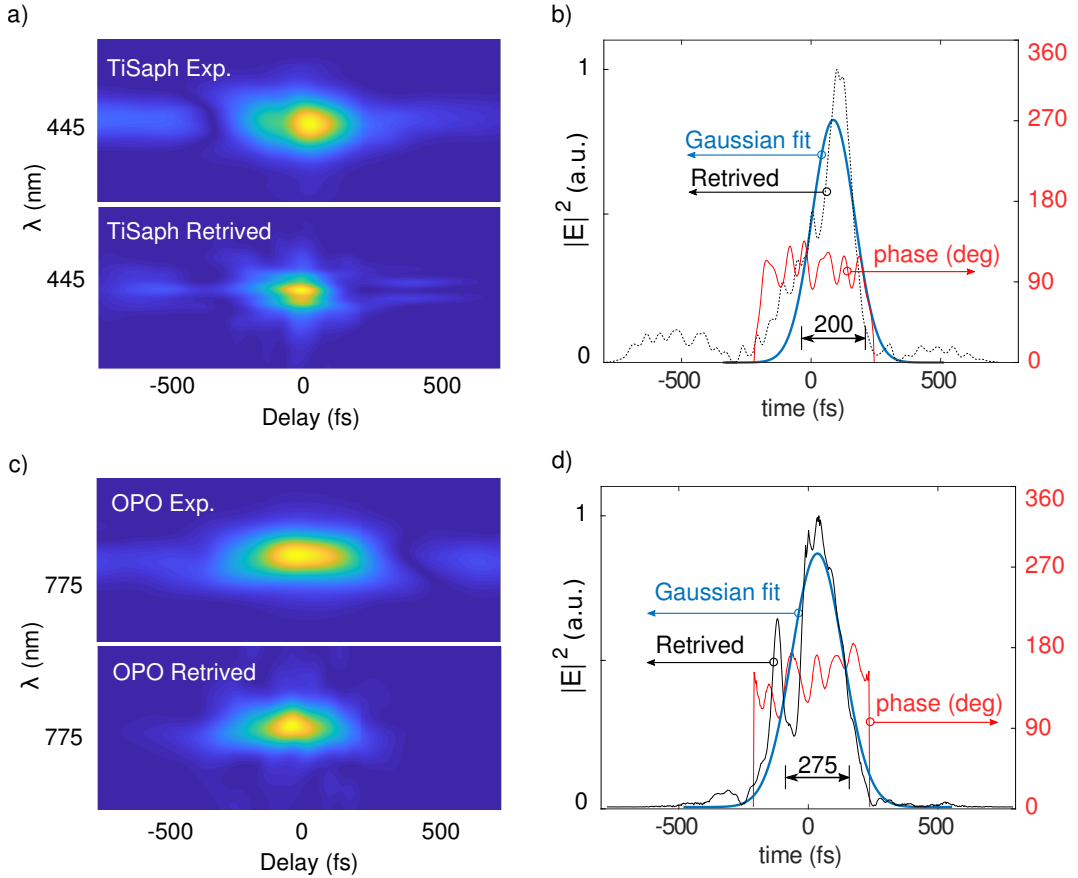


FIGURE 4.11: Measurement of amplitude and phase of femtosecond pulse trains from a TiSaph mode-locked laser $\lambda = 900\text{ nm}$ and a synchronously pumped OPO $\lambda = 1550\text{ nm}$: a,c) Experimental and retrieved FROG traces showing the spectrum around the second-harmonic of the fundamental, b,d) retrieved intensity and phase of Ti-Sapphire and OPO pulses. From a Gaussian fit we estimate these to be 200 and 275 fs (FWHM).

one half of the pulse train travels back and forth on a fixed-length arm, while the other travels a variable distance thanks to a mirror mounted on a motorized linear stage as detailed in fig. 3.3 (b).

4.5 SPDC from mono-layer WSe₂

This section presents experimental efforts aimed at measuring spontaneous parametric downconversion in a single-layer tungsten diselenide (WSe₂). Section 4.5.1 first introduces the results of the classical nonlinear measurement of SHG, from which we infer the expected brightness of SPDC in section 4.5.2. The radiation pattern of the down-converted light is simulated in section 4.5.3, allowing to calculate all terms of loss. From the coincidence results obtained with our Hanbury-Brown and Twiss (HBT) in section 4.5.5 we conclude that the measurement is limited by the presence of a relatively brighter background.

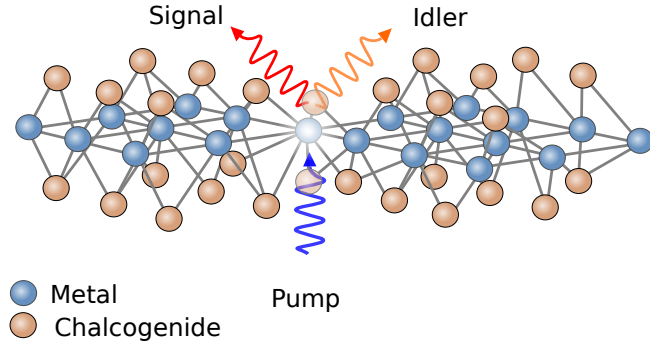


FIGURE 4.12: SPDC from a mono-layer of transition-metal dichalcogenide WSe₂. A pump photon (yellow) is incident from free-space onto the nonlinear film and spontaneously annihilates into a signal (orange) and an idler photon (red).

Our starting point is a TMDC mono-layer as sketched in Fig. 4.12 where both illumination and collection occur in free-space. We perform second harmonic generation (SHG) experiments and harness the correspondence between stimulated and spontaneous nonlinear optical interactions [84, 94, 150, 152–157] to calculate the expected brightness of SPDC. Our results include estimates of SPDC emission patterns as well as linear propagation and collection losses. We show that a pump at normal incidence leads to omni-directional pair emission and a maximum pair collection probability. The small interaction volume limits the pair generation efficiency of our structure to be well below typical waveguide-based integrated sources and, as such, the observation of SPDC from a TMDC mono-layer could prove challenging. However, we calculate that for dark-count limited measurements, the signal to noise ratio for such sources of photon pairs, known as the coincidence-to-accidental ratio (CAR) [199], could still be larger than 10. Our results pave the way to the experimental demonstration of localized SPDC in atomically-thick films and provide a benchmark for the performance of other structures based on these materials.

4.5.1 SHG in mono-layer WSe₂

Following the quantum-classical relations of section 2.6, a first step in obtaining an estimate of a potential SPDC generated photon pair flux is to measure the photon flux generated in an appropriate SHG experiment (recall eq. (2.52a)). We focus on the specific TMDC of WSe₂, which is known to exhibit strong light matter interactions. The left inset of Fig. 4.13 shows our experimental setup for probing the SHG response from a mono-layer of WSe₂. The nonlinear film is deposited on a quartz substrate and both illumination and collection occur in air. A mode-locked femtosecond laser (80 MHz, 275 fs) centered at the fundamental wavelength of 1570 nm is focused through air by an infinitely-corrected objective (NA=0.85). We fit the intensity profile of the spot at focus with a rotationally-symmetric bi-variate Gaussian of diameter of 1.6 μm at $1/e^2$ of its peak. We calculate the effective area of the pump at focus as $A_{\text{SHG}} = 7.854 \times 10^{-13} \text{ m}^2$ by modeling the intensity profile of the pump as a cylindrical beam with diameter $0.625 \times 1.6 = 1 \mu\text{m}$ for energy conservation. A non-polarizing beam-splitter is used to both reflect the pump towards the sample and collect the generated SHG light which is then diffracted by a metallic grating and detected with a high-efficiency CCD array. The pump is carefully removed in

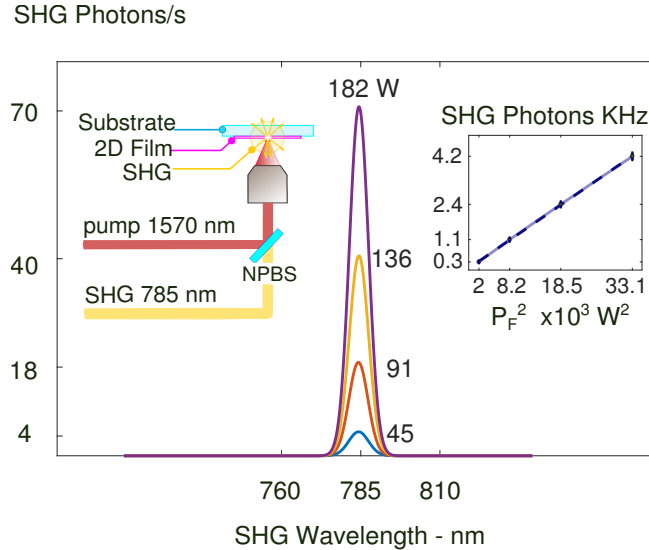


FIGURE 4.13: Calibrated SHG spectra for different peak powers of a 80 MHz mode-locked pump centered at 1570 nm. Left inset: schematic of the experimental setup. Illumination and collection occur through the same lens ($NA=0.85$) and a non-polarizing beam-splitter (NPBS) is used to spatially separate input and output. Right inset: expected quadratic power dependence of SHG intensity.

the detection path by means of interference filters. Fig. 4.13 shows spectra of the frequency-doubled light centered at half the pump wavelength 785 nm demonstrating that we are able to collect across the entire generation bandwidth. Intensities were calibrated to account for all collection, propagation and detection losses and thus represent the estimated SHG photon flux that is generated by the WSe₂ monolayer and propagates in 4π sr on both sides of the sample. Spectra are presented for different peak powers corresponding to average power values ranging from 1 to 4 mW and were collected over 60 s. The blue solid line in the right inset of Fig. 4.13 is the ratio R_{SHG}/P_F^2 which overlaps perfectly with the line of best fit (dashed line). The SHG data in the right inset of fig. 4.13 can also be used to calculate the effective nonlinearity $\chi_{\text{eff}}^{(2)}$ of WSe₂ monolayer [178]. In order to measure the medium $\chi_{\text{eff}}^{(2)}$ we follow the expressions in eq. (2.28). Written in terms of the peak photon flux \hat{R}_{SHG} at the SHG

$$|\chi^{(2)}| = \pm \frac{2c^{3/2}n_F}{d\hat{P}_F} \sqrt{\frac{A_{\text{eff}}n_{\text{SHG}}\hat{R}_{\text{SHG}}\epsilon_0\hbar}{\omega_{\text{SHG}}}} e^{-\frac{1}{2}d(\alpha_F + \frac{\alpha_{\text{SHG}}}{2})}, \quad (4.27)$$

where \hat{P}_{SHG} and the fundamental \hat{P}_F is respectively the peak power of the second-harmonic and fundamental, A_{eff} is the effective area of the interaction, and d is the thickness of the monolayer. We calculate this for each of the four measured points and find

$$\chi_{\text{1L-WSe}_2}^{(2)} = (6.63 \pm 1.72) \times 10^{-12} \text{ m V}^{-1}, \quad (4.28)$$

which is one order of magnitude smaller than what was reported under resonant

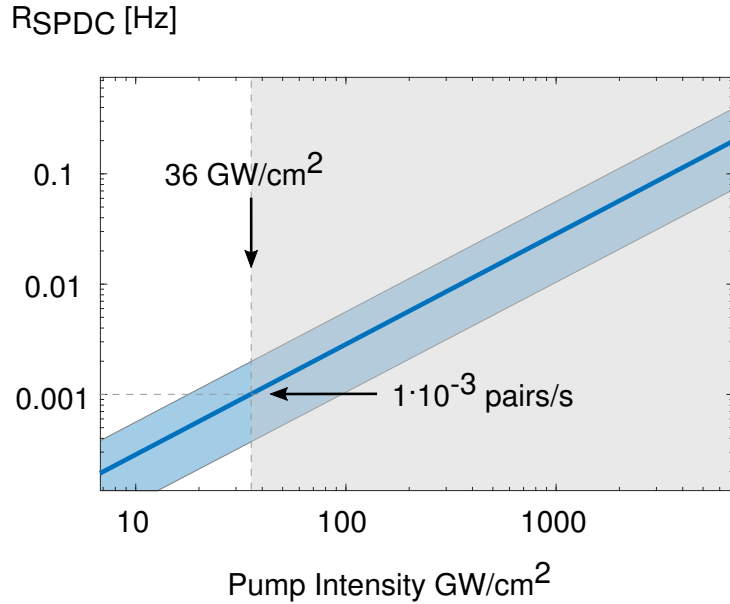


FIGURE 4.14: While the rate of SPDC photon pairs increases linearly with pump intensity, the power damage threshold of mono-layers WSe₂ (36 GW cm⁻²) practically limits the maximum rate to 1 mHz (outside the gray shadowed area). The shaded blue area represents the uncertainty in the calculation.

pumping at room temperature in [143]¹. We attribute the difference to the non-perfect alignment between the crystal principal axis and the pump polarization.

4.5.2 Brightness of SPDC from mono-layer WSe₂

In Fig. 4.14 we plot the predicted rate of SPDC pair generation in a mono-layer of WSe₂ via eq. (2.52a) as a function of average pump intensity ($P_{\text{P}}/A_{\text{SPDC}}$). As an example, we consider the source to be a Coherent Ultra II commercial laser system where the pump for the SPDC experiment is generated by synchronously pumping an OPO cavity with the same pulse train used in the SHG measurements ($T_{\text{F}} = T_{\text{P}}$). The duration of the pulses is taken from a FROG measurement as discussed in section 4.4 and are $\Delta t_{\text{F}} = 275$ fs and $\Delta t_{\text{P}} = 235$ fs. While, theoretically, we could achieve higher and higher rates simply increasing the pump power, in practice the damage threshold of WSe₂ will limit the achievable rate. We experimentally find this damage threshold to be 36 GW cm⁻² (corresponding to an average optical power on sample of 3×10^{-3} W), which in turn bounds the rate of SPDC-generated pairs to

$$\bar{R}_{\text{SPDC}} = 0.002 \pm 0.0016 \text{ pairs/s} \quad (4.29)$$

or 1 pair every 16.7 minutes on average. The uncertainty, which is represented by the shaded blue area, is calculated assuming that all quantities in eq. (2.52a) are known with an error of 5 % with the exception of R_{SHG} whose variance is estimated from the four measured data points in the right inset of fig. 4.13. Yet while this rate is considerably smaller than what can be obtained in phase-matched bulk crystals [200],

¹In the same work it was found that the SHG under resonant pumping was 15 times stronger than off resonance, which indicates a four-fold increase in the second-order susceptibility, a value comparable to what has been predicted in a similar TMDC via density functional theory [3].

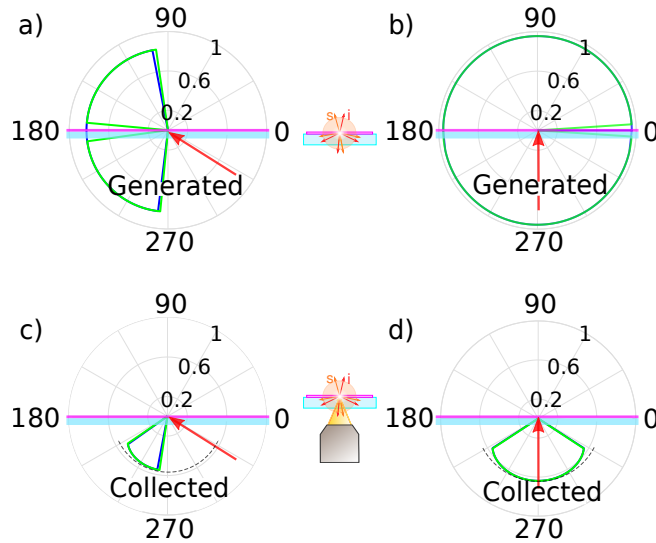


FIGURE 4.15: Simulated radiation pattern of down-converted light from a single-layer of WSe₂ which enables a calculation of the collection loss L_C adapted from [178]. Energy and momentum conservation lead to isotropic emission of signal (blue) and idler (green) photons for normal pump incidence (red arrow in a,b). Single sided photon collection (c,d) further restricts the range of angles collected reducing the probability to collect both photons.

201] and could make the experimental observation of SPDC challenging, in the next section we identify the main contributions of noise and loss in a free-space measurement setup and show that a CAR greater than 10 could in principle be achieved with state-of-the-art single-photon detectors. Such a measurement would set a record for photon pair generation from 2D quantum confined materials as well as enable the experimental exploration of scaling laws involving excitonic resonances. Results are obtained for illumination at 1570 nm with $\omega_{\text{SH}} = 2\pi \times 3.82 \times 10^{14} \text{ rad s}^{-1}$, $A_{\text{SHG}} = 7.85 \times 10^{-13} \text{ m}^2$, $L = 0.7 \text{ nm}$, $n_F = 4.0$, and $n_{\text{SH}} = 5.1$ and errors are calculated under the same assumptions detailed above for the calculation of R_{SPDC} .

4.5.3 Simulated radiation pattern and collection loss

We solve eq. (4.23) numerically for a large number of downconversion events of a pump photon at 785 nm into pairs at around 1570 nm from a single layer of WSe₂ on a quartz substrate. We assume the material extends over an infinite plane at the boundary between two dielectrics and to be rotationally symmetric so that we can restrict solutions along the plane of incidence of the pump. The presence of a higher density dielectric introduces an angle dependence in k_s and k_i and care must be taken to select the relevant wave-vector. We calculate linear Fresnel coefficients at all dielectric interfaces between the nonlinear film and the air-immersion lenses and include all losses due to absorption.

Figure 4.15 shows the photon departure angles of signal (blue) and idler (green) photons in a normalized polar plot discarding downconversion events that lead to evanescent waves. The distance from the origin represents the probability of finding the photon in the far field. Results are presented for two relevant moments: immediately after the pair is generated a-b) and after collection by a NA=0.85 lens

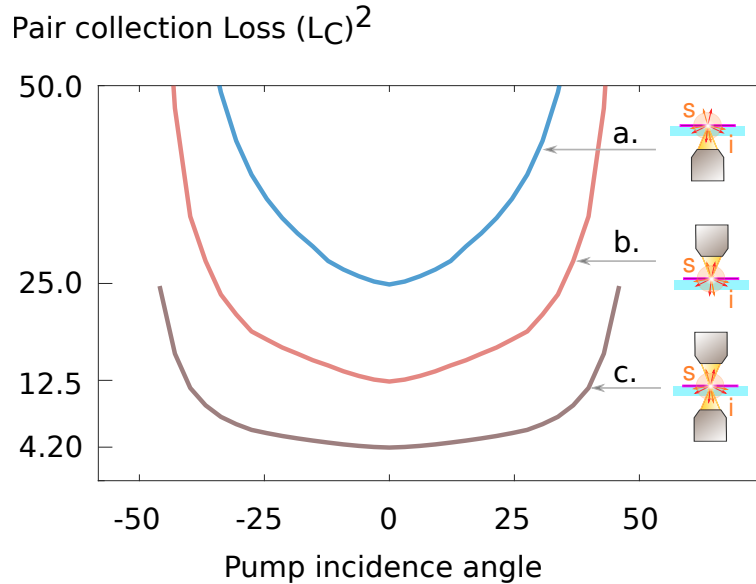


FIGURE 4.16: Simulated collection loss of SPDC photon-pairs generated in an atomically-thick film on quartz with $\text{NA}=0.85$. The presence of a dielectric with a higher density leads to sharper departure angles of s,i pairs and total-internal reflection at the quartz-air interface thereby increasing the pair collection loss. Normal pump incidence spreads the departure angles evenly resulting in a higher chance to collect and detect a pair.

from the air-quartz interface c-d). The angular dependence of transmission coefficients shapes the radiation diagram breaking its circular symmetry (dashed line in fig. 4.15). Upon detection, photons that can be collected experience linear propagation loss while all others are lost and have a zero probability to be detected.

Figure 4.16 shows that the pair collection loss is minimum for normal pump incidence $\theta_p = 0$ which corresponds to isotropic emission of the down-converted light. Our results show that by using two air-immersion objectives one on each side of the mono-layer ($\text{NA}=0.85$ and transmissivity of 0.65), 1 in 4.2 pairs may be successfully collected on average, corresponding to a photon collection loss $L_C \approx 2$. Single-sided collection from the higher-density dielectric causes a higher pair collection loss due to the additional glass-air interface. The first step to calculate the CAR is to estimate the rate of true coincidences, which is proportional to the probability that both photons of a pair are detected. However, since signal and idler can be emitted in both sides of the nonlinear medium, their collection probabilities may differ substantially. We therefore calculate the average pair loss L_C^2 as the inverse of the probability that both s,i are collected and detected.

Since the momentum is larger in the higher-density dielectric photons generated in the higher density dielectric have sharper departures angles and a higher probability to experience total internal reflection at the quartz-air interface. This also affects the pair collection loss making its angular dependence sharper, as visible by comparing Fig. 4.16a-b.

Importantly, under normal pump incidence the CAR increases six-fold by collecting from the air side as opposed to the quartz side. The use of an index-matched lens is likely to dramatically reduce optical reflections thus represents an effective way to improve the collection efficiency. However, given the weak signals expected, this

would require ultra-pure index-matching solutions that do not fluoresce in the spectral region of the signal and idler. The laser light that exits the laser cavity has a well defined momentum (collimated beam), and a less defined position (intensity profile extends over a few mm (or thousands of wavelengths)). After passing through the objective, the situation is reversed with the energy well localized in space (focused beam) thanks to a large superposition of momenta. Thus, by controlling the diameter of the beam at the input of the objective, it is possible to reach a trade-off between uncertainty in momentum and position, a technique known as Fourier illumination. We refer the reader to section 3.4 for a detailed implementation as well as a discussion on its limitations in the context of these measurements. Alternatively one can leverage the transparency of the quartz substrate and use a low-NA lens for illumination and a high NA-objective for collection as shown in fig. 4.21 of section 4.6, in the context of coincidence measurements form multi-layer MoS₂.

4.5.4 Dark-count-limited CAR for 1L-WSe₂

From eq. (4.29) we note that the maximum expected rate of SPDC photon pairs from mono-layer WSe₂ is five orders of magnitude smaller than typical dark count rates ($R_{\text{AC-dark}} \approx 100 \text{ Hz}$). Under the assumption that dark counts were the only disturbance in the system $R_{\text{AC-loss}} = R_{\text{AC-bs}} = R_{\text{AC-bkg}} = 0$, we can approximate the average rate of accidental coincidences R_{AC} as (see eq. (4.7))

$$R_{\text{AC}} \approx R_{\text{AC-dark}}. \quad (4.30)$$

L_P and L_D may vary considerably depending on the experimental setup with a maximum quantum efficiency QE=0.95, and lens transmissivity between 0.6 and 0.95. We can now predict the CAR in an non-optimized setup where collection occurs in air. Figure 4.17 shows the calculated CAR ($t_{\text{bin}} = 1 \text{ ns}$) as function of pump angle and lens numerical aperture for typical values of quantum efficiency of avalanche photodiodes and superconducting nanowires, respectively QE=0.1 and QE=0.9 and $R_{\text{AC-dark}} = 10 \text{ Hz}$. The material considered is mono-layer WSe₂ for which $\bar{R}_{\text{SPDC}} = 0.002 \text{ pairs/s}$ eq. (4.29). With $L_T = 88.8$ (L_C , L_P , L_D respectively 3.2, 3.9, 7.1) we expect one true coincidence every 7885 generated pairs.² Despite the loss, we anticipate that CAR ≥ 10 can be achieved with single-sided collection and normal pump incidence when thermal noise in the detectors is the only source of noise.

4.5.5 Measured Coincidences from 1L WSe₂

In spontaneous parametric downconversion signal and idler photons are generated at the same time. When analyzed with a Hanbury-Brown and Twiss (HBT) interferometer, light from a SPDC source, a sharp correlation peak appears as evidence of their simultaneity. Here we describe the results of such experiments, where the source of nonlinearity is single layer of tungsten diselenide (WSe₂), deposited on a quartz substrate and illuminated in free-space.

²The value of L_D implies a detection efficiency of 0.14 (or 14 %) and has been extracted from the specifications of the popular ID230 InGaAs SPADs (ID-Quantique) at 1550 nm operated at 10 % efficiency.

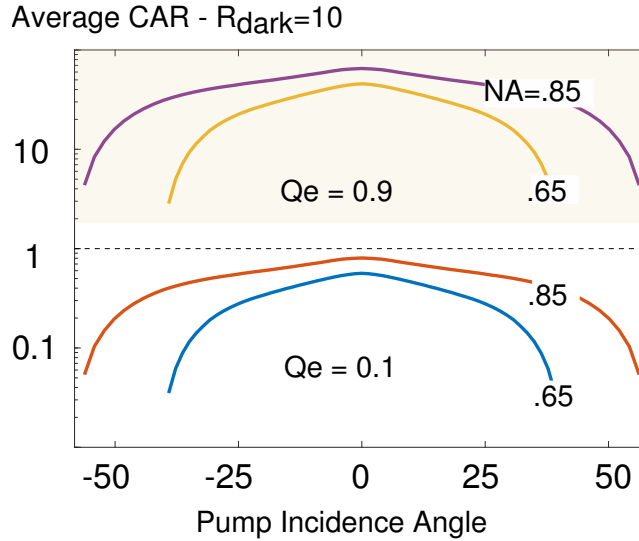


FIGURE 4.17: Simulated collection loss for unilateral collection of $\bar{R}_{\text{SPDC}} = 0.002$ pairs/s for the best detector configurations existing to date: SPADs ($R_{\text{AC-dark}} = 10$, QE = 0.1) and super-conducting nanowire ($R_{\text{AC-dark}} = 10$, QE = 0.9) adapted from [178]. Despite the measurement is dark-count limited, the CAR is expected to be largely above one for normal pump incidence and high efficiency detectors ($t_{\text{bin}} = 1$ ns).

Figure 4.18 (a-b) show respectively the experimental setup, and the results of a single-photon coincidence measurement performed over the course of 30 minutes, for a bin width of 1 ns. In order to detect the time differences between emitted photons, the HBT interferometer uses a beam splitter (BS) and two single-photon avalanche photodiodes (SPADs), and approximates the second order autocorrelation function ($g^2(\tau)$) of the light source (for details see section 2.2.2 and section 3.1.9). We expect a correlation peak at $\tau = 0$, since no electronic delay is used, and the optical paths from the beam splitter (BS) to the single-photon avalanche photodiodes (SPADs) are the same. However, the histogram shows a flat and incoherent emission, with the exception of two weak features symmetrically arranged around $\tau = 0$, and corresponding to breakdown flashes as discussed in section 4.1.1. To confirm that the SPDC measurement is background limited we apply the measured linear loss 88.8 to the calculated pair rate at the sample plane in eq. (4.29), which assumes an illumination peak power of $3.6 \times 10^{10} \text{ W cm}^{-2}$. Moreover, from the measured average of 30.96 accidentals per 1 ns bin in a total integration time of 1800 s we find

$$R_{\text{AC}} = 1.72 \times 10^{-2} \text{ Hz}, \quad (4.31a)$$

$$R_{\text{TC}} = 2.53 \times 10^{-7} \text{ Hz}, \quad (4.31b)$$

$$\text{CAR} = 1.47 \times 10^{-5}. \quad (4.31c)$$

In order to test the measurement setup, the two-dimensional material was substituted with an on-chip SPDC source described in section 3.1.5. Figure 4.18 (c-d) show the setup and results from such experiment. The crystal is pumped with the same femto-second pulse train used before, slightly red-shifted to a central wavelength of 775 nm to overlap with the crystal phase matching. Light collection and pump

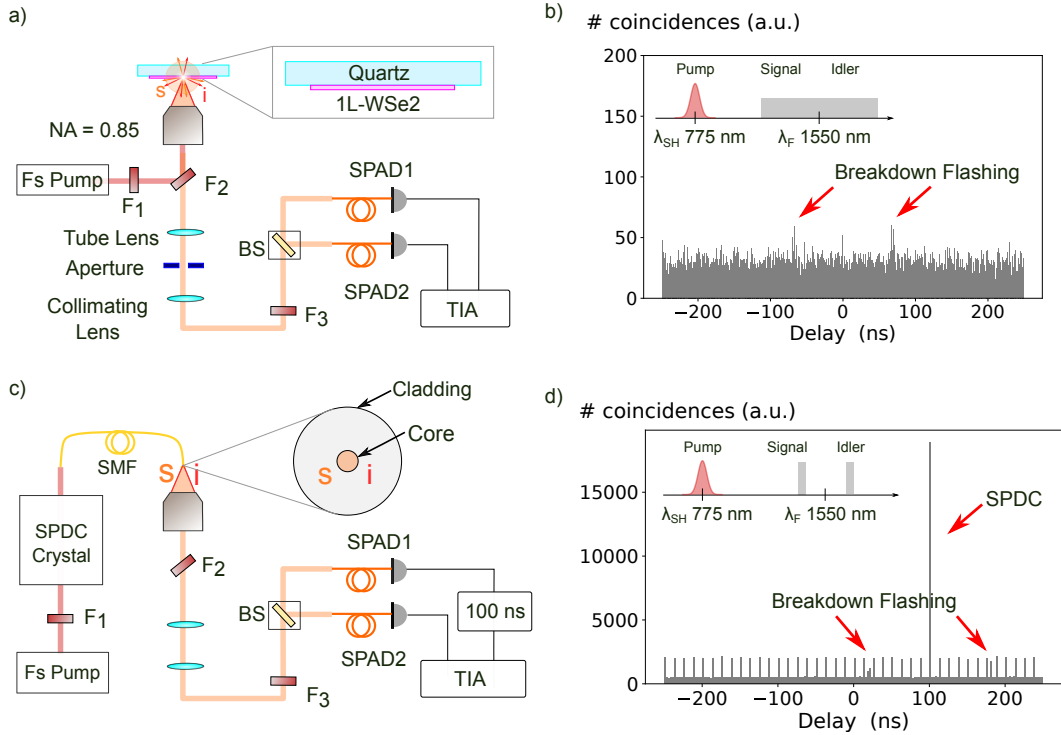


FIGURE 4.18: Experimental setup for the measurement of simultaneity of SPDC photon pairs from mono-layer WSe₂ (a): Pump photons from a 775 nm mode-locked Ti:Saph laser spontaneously down-convert to pairs at 1550 nm, and a beam splitter (BS) and two single-photon avalanche photodiodes (SPADs) allow to detect their simultaneity. (b) The measurement is dominated by an incoherent background, which reveals the signature of breakdown flashing from the two SPADs. (c-d) When the two-dimensional material is replaced with a bulk SPDC source, the same periodic illumination generates pairs of signal and idler photons, resulting in a characteristic periodic autocorrelation, shifted to $\tau = +100$ ns thanks to the use of a fixed electronic delay on one of the two channels of the time-interval analyzer (TIA).

rejection is performed with the same optical setup, while a fixed electronic delay of 100 ns is added to one channel of the time-interval analyzer (TIA), shifting the zero of the histogram to +100 ns. Results in fig. 4.18 (d) show the expected periodic autocorrelation, with a pronounced peak in $\tau = +100$ ns corresponding to true coincidences, and a number of size-peaks which represent the generation of signal-idler pairs by consecutive pump pulses. Given the strong overlap between the pump that illuminates WSe₂ and the material direct electronic band-gap (A exciton nm pump 725 nm), accidental coincidences are likely to be generated by electron-hole recombinations. In the next section we describe attempts to control such emission by choosing a transition-metal dichalcogenide material with a higher-energy resonances, and a layer stacking engineered to take advantage of an indirect band-gap as well as a larger second-harmonic response.

4.6 SPDC from multilayer MoS₂

Spontaneous parametric downconversion in WSe₂ mono-layers can provide broad-band and sub-diffraction generation of heralded single-photons, thanks to a strong nonlinearity and band-gap tunability. However, the direct-bandgap of mono-layer WSe₂ results in a large quantum yield for one-photon processes which are the dominant source of accidental coincidences (noise), in the measurement of spontaneous parametric downconversion (SPDC) photon coincidences (see section 4.5.5). In addition, their thickness limits both spontaneous and stimulated conversion efficiencies. In this section we explore multilayer MoS₂ in 3R polytype, which compared to the mono-layer, exhibits a non-direct band-gap, a larger interaction volume, and a higher power-damage threshold. These properties could lead to a higher SPDC conversion efficiency, as well as a lower optical background. The aim is to experimentally confirm the expected increase in coincidences over accidental ratio (CAR), as well as to establish the feasibility of an unambiguous simultaneity measurement of the energy-time entangled photons pairs generated via spontaneous parametric downconversion.

4.6.1 Material Choice

With specimens dating over 2.9 billion years molybdenum disulfide (MoS₂) is the oldest and most studied material in the family of transition-metal dichalcogenide (TMDC) (see section 2.3). Its linear and nonlinear properties have been studied extensively, and chemical-vapor deposition (CVD) techniques have been refined to achieve excellent growth control, material thickness and purity. In the context of this work MoS₂ is an attractive material for SPDC photon-pair generation at telecom wavelengths, as it promises a weaker background emission compared to WSe₂, and a comparatively larger second-order nonlinear response. The first is expected because A and B excitonic resonances in MoS₂ are at 680 and 620 nm (1.823 - 2 eV) respectively [202, 203]. Illumination at 775 nm is thus non-resonant, and the efficiency of its incoherent radiative emissions (background) is expected to be considerably weaker. The second property is particularly attractive as it contributes quadratically to the rate of SPDC photon pairs (see eq. (2.52)). Published values of $\chi_{\text{1L-MoS}_2}^{(2)}$ range from 2.9 to 11.9, and $32 \times 10^{-11} \text{ m V}^{-1}$, with an average value four times larger than what we measured in WSe₂³[1, 4, 5]. With more pairs generated, the coincidences over accidental ratio of the measurement in fig. 4.17 could thus increases up to 16 times.

Single layers of TMDCs however presents two major limitations. The first is a direct band-gap which, given the large pump intensities, can lead to single as well as multi-photon absorption and a consequent high rate of accidentals. The second limitation is the short interaction length d , which as shown in eq. (2.52a), contributes quadratically to the pairs generation rate. Interestingly, as their thickness increases, TMDCs undergo a transition from direct (monolayer) to indirect band-gap (bulk),

³From the works in [1, 4, 5] we calculate an average of $\chi^{(2)} \approx 25 \times 10^{-11} \text{ m V}^{-1}$. The variability in the results of these measurement is due to differences in pulse durations, material growth and orientation, and instrument calibration, as well as the presence of strong excitonic resonances. In mono-layer MoS₂ at room temperature, density functional theory predicts the $\chi_{\text{1L-MoS}_2}^{(2)}$ to increase up to four times if the pump is two-photon resonant to the A-exciton [3], with a SHG efficiency that could be up to sixteen times stronger for the same input pump power.

and the quantum yield of one-photon processes reduces exponentially as a result [204]. In five-layers MoS₂ this has been reported to be more than three order of magnitude weaker than single layer [203]. However, a complication with multi-layer stacks of MoS₂ and any TMDC for nonlinear optics is symmetry. In naturally-occurring MoS₂ (2H polyphase), Bernal stacking restores the broken inversion symmetry in even number of layers. As a result the second harmonic generation (SHG) vanishes [137], $\chi^{(2)} \approx 0$, and the SPDC pair generation rate can be expected to be practically zero. Although the former is restored in 2H polyphase for odd number of layers, its strength scales only marginally with thickness leading to limited practical benefits.

One solution to this is to synthesize MoS₂ in the 3R polyphase, so that centrosymmetry is broken for any number of layers and the strength of the SHG response increases quadratically with layer number [7]. For more than 5-6 layers linear absorption becomes significant and balances the increase of SHG which slowly saturates. In the next sections we describe the results of classical and single-photons coincidence experiments with five-layers MoS₂ in the 3R polyphase. Since the combined thickness is still much shorter than the wavelength of light, nonlinear optical interactions can be considered perfectly phase-matched and eq. (2.52a) holds.

4.6.2 SHG Spectroscopy in 5L MoS₂

The first step to infer the efficiency of SPDC from multilayer MoS₂ is to observe the frequency-doubling of a bright pump in the same wavelength range of the prospective signal-idler pairs, as discussed in section 4.5.5. In order to appreciate the contribution of the material resonances, we illuminate in the range 1100-1550 nm (0.8-1.127 eV), and perform SHG spectroscopy. As shown in section 4.5.3, the pair-collection loss can be minimized by illuminating with a normally-incident laser beam.

In order to concentrate the diameter of the collimated laser beam on the sample we approximate normal incidence with a low-NA lens, while collection occurs through a high-NA lens at opposite side of the material. This is the same transmission geometry later used for the coincidence measurements described in section 4.6.4, which is important to link the efficiencies of quantum (SPDC) and classical (SHG) experiments through section 2.6. A reflective telescope expands the optical parametric oscillator (OPO) of fig. 3.1 to 12 mm, which is then focused with a 25 mm lens to $\approx 12 \mu\text{m}$ (effective numerical aperture 0.24). Short-pass filters isolate the near-infrared pump from the converted light, which is then analyzed with the grating-based spectrometer of fig. 3.6. Spectra are normalized to account for propagation and detection loss, resulting in an estimate of the collected spectral-densities of the SHG photon flux. As a control experiment, we repeat the measurement in reflection, where illumination and collection occur through the same high-numerical aperture lens (NA=0.85).

Results are shown in fig. 4.19 (a) for the transmission (dashed lines) and reflection setups (solid lines), which are described schematically in fig. 4.19 (b). From the transmission experiment, we calculate a SHG conversion efficiency of 2.1×10^{-12} away from electronic resonances ($\lambda_{\text{SH}} = 775 \text{ nm}$), which increases ten-fold to 1.9×10^{-11} when two photons of the pump overlap with the A exciton ($\lambda_{\text{SH}} = 625 \text{ nm}$)⁴. From

⁴The respective photon rates were $3.6 \times 10^5 \text{ Hz}$ and $3.2 \times 10^6 \text{ Hz}$, with a measured pump peak intensity of $1.7 \times 10^9 \text{ W cm}^{-2}$ at the sample plane, corresponding to a pump average photon rate of $\approx 1.7 \times 10^{17} \text{ Hz}$ and average power of $22 \times 10^{-3} \text{ W}$

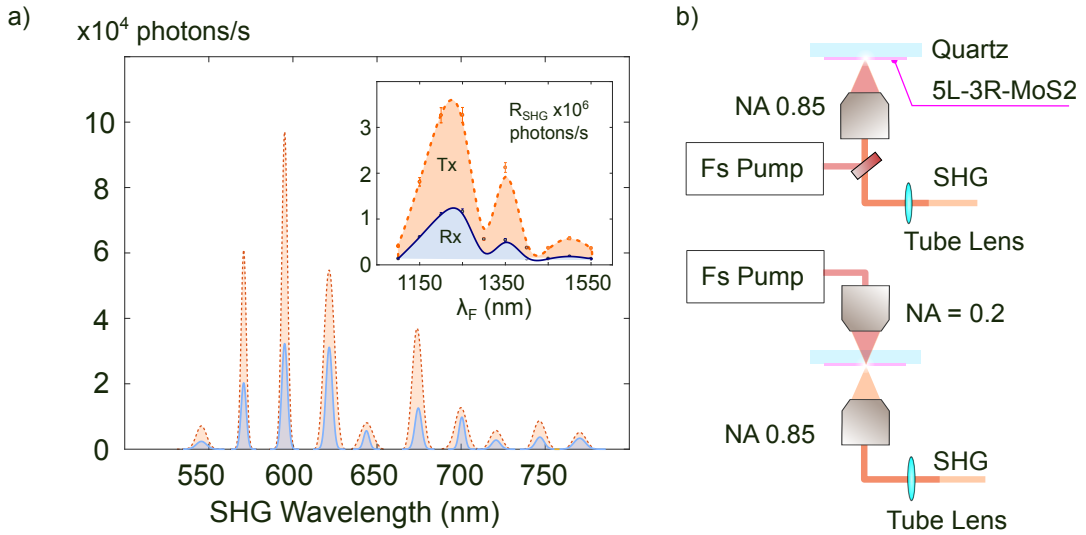


FIGURE 4.19: Dispersion of the SHG response from multi-layer 3R-MoS2 for normal incidence in a transmission geometry. (a) SHG power spectral densities measured in transmission with close-to-normal pumping (dashed blue lines) and in reflection with a large high numerical aperture (solid orange lines). The inset shows the corresponding integrated photon flux in photons/s. The expected bimodal response shows two peaks in correspondence of the A and B exciton of the material where the frequency doubling is resonantly enhanced. (b) Schematics of the measurement setups for the reflection geometry used as a control experiment (top) and the transmission (bottom).

the inset of fig. 4.19 (a), we see that the integrated photon flux has the expected bimodal shape with peaks in correspondence of the well known A and B excitons of the material [7]. The nature of these two peaks is also confirmed later in fig. 4.22 of section 4.6.5 with one-photon photoluminescence measurements. Despite the differences in effective areas between reflection and transmission, the optical intensities were kept constant. The difference in magnitude between the two responses is attributed to different collection efficiencies, as well as errors in the power measurements.

4.6.3 Brightness of SPDC in 5L MoS2

Since these SHG results represent the average photon-rate at the second-harmonic, they can be directly used in eq. (2.46b) to calculate the material effective $\chi^{(2)}$ under the assumption of perfect phase-matching. Average values and error-bars are shown in fig. 4.20 (a) for both the transmission (blue) and reflection (orange) geometries. The resonant $\chi^{(2)}$ in correspondence of the A or B exciton is nearly one order of magnitude stronger than the one calculated in monolayer WSe₂ under resonant pumping as detailed in eq. (4.28). Applying the model detailed in section 2.6, we calculate the expected rate of SPDC photon pairs for illumination in the wavelength range 550-750 nm. From fig. 4.20 (b) the upper and lower bounds for illumination at 625 and 675 nm respectively, are

$$0.03 \pm 0.01 \leq \bar{R}_{\text{SPDC-MoS2}} \leq 0.38 \pm 0.20, \quad (4.32)$$

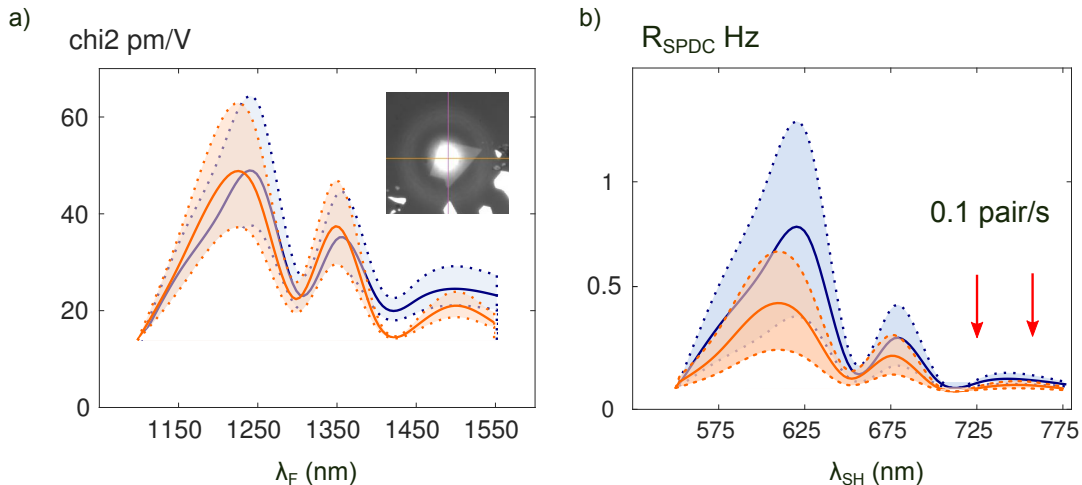


FIGURE 4.20: (a) The calculated $\chi_{\text{eff}}^{(2)}$ from five-layer MoS₂ inherits the peaks of the second-harmonic response in correspondence of the A and B excitons. The shaded areas represent the uncertainty associated with the calculations, while the inset shows an image of the overlap between the two-dimensional flake and the nearly normally-incident pump. (b) The longer interaction length of the 5 layer stack, as well as higher nonlinear susceptibility increase the expected SPDC pair rate more than three orders of magnitude compared to what can be achieved in monolayer WSe₂ (see fig. 4.14), with average values in transmission (blue solid line) and reflection (orange solid line) respectively in the range 0.1-1.3 Hz, and 0.1-0.38 Hz.

calculated assuming mode-locked illumination with repetition rate, pulse duration, and peak intensity respectively 80 MHz, 225 fs, and $7.1 \times 10^9 \text{ W cm}^{-2}$, equivalent to $1 \times 10^{-3} \text{ W}$ average power concentrated in a 1 μm spot, and a linear refractive index of $n_{\text{SH}} = n_{\text{F}} = 4.62$. This is substantially higher than obtained in monolayer WSe₂ (see fig. 4.14), in part due to the higher $\chi^{(2)}$ of MoS₂, and partly due to the increased interaction length which in five-layer MoS₂ is 36 times longer than monolayer WSe₂ 0.7 nm.

4.6.4 Measured Coincidences from 5L MoS₂

Section 4.6.3 showed that illuminating the material in the wavelength range of the measured second-harmonic generation (550-775 nm), we expect to generate signal-idler photon pairs at the corresponding fundamental wavelength (1100-1550 nm). In order to prove this experimentally, we illuminate five-layer 3R MoS₂ with the same low numerical aperture setup used in the transmission SHG experiments of fig. 4.19. The stack of filters F1 in fig. 4.21 (a) rejects any trace of near-infrared light generated inside the laser cavity which would otherwise reach the detectors.⁵ On the emission path, the pump is first removed by a second interference filter, F2, and then analyzed with a Hanbury-Brown and Twiss interferometer. A mode-locked Ti:Saph pump with central wavelength $\lambda_{\text{P}} = 725 \text{ nm}$, and peak intensity $5 \times 10^7 \text{ W cm}^{-2}$ ⁶ is expected to down-convert in a continuum of radiative modes

⁵This consists of a combination of three short-pass filters, with a combined extinction ratio in excess of 10^9 and a 725 nm band-pass filters with extinction ratio of 10^5 .

⁶corresponding to an average power of $6.38 \times 10^{-4} \text{ W}$ concentrated to a spot diameter of $\approx 8.9 \mu\text{m}$.

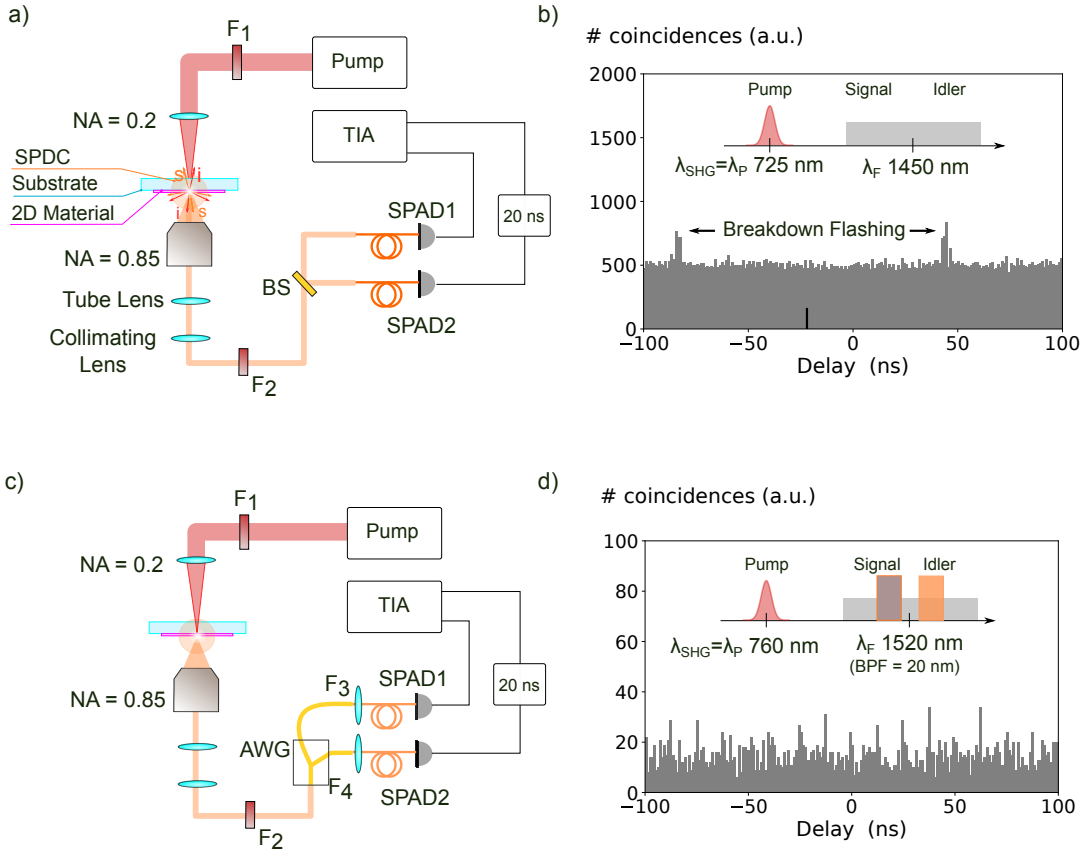


FIGURE 4.21: Attempts to measure spontaneous parametric downconversion from five-layer 3R MoS₂, with close-to-normal pump illumination. (a-b) Optical arrangements and results of photon coincidences (unfiltered signal and idler). Pump photons at 725 nm are expected to down-convert, and generate signal-idler photons in a neighborhood of the fundamental wavelength (1450 nm). These split at a beam splitter (BS), are detected with a pair of single-photon avalanche photodiodes (SPADs), and expected to result in a sharp peak at $\tau = -20$ ns. (b) Data collected over 24 hours emission shows no sign of temporal correlation, with the exception of two peaks corresponding to breakdown flashes as explained in section 4.1. When two band-pass filters are tuned at opposite sides of twice the fundamental (c-d), the two peaks disappear below the noise floor which dominates the autocorrelation.

at $\lambda_{\text{SPDC}} = 1450$ nm over a bandwidth of a few hundreds of nm. However, the SPADs sensitivity limits their detection to a 200 nm window, as it is negligible beyond 1650 nm as shown in fig. 3.14 (b). The long-pass filter F₂ has a cut-off close to 1250 nm, and was used to further reduce accidental coincidences.

The raw coincidence-histogram obtained over the course of 24 hours is shown in fig. 4.21 (b). The two peaks symmetric around the fixed electronic delay of $\tau = -20$ ns⁷ dominate an otherwise flat autocorrelation trace, and correspond to emissions from the active area of the SPADs as detailed in section 4.1. The same measurement performed on bare quartz showed an almost clear histogram, indicating that the incoherent detections that dominate the trace result from the interaction of the pump with the MoS₂ multilayer. Given the absence of a peak at $\tau = -20$ ns

⁷This was purposely introduced to avoid fictitious peaks in $\tau = 0$ deriving from minor software bugs in the firmware of the time-interval analyzer (TIA).

in fig. 4.21 (b), the measurement fails to prove the generation of energy-time entangled photons. It is however possible that these are generated, but could not be detected because of a comparatively brighter background. To confirm this, we start from the expected rate of photon pairs of fig. 4.20, and apply loss to estimate the corresponding rate of true coincidences, which we then compare against the observed rate of accidental coincidences. The rate of pairs at the sample plane expressed in eq. (2.53b) is related to that of true coincidences via the square of the total loss in the system $L_T = 88.8$ (see for instance section 4.5.4). For $\lambda_P = 725$ nm, $\chi^{(2)} = 1.66 \times 10^{-11} \text{ m V}^{-1}$, peak pump power $\hat{P}_{\text{SH}} = 37.7$ W, and effective area $A_{\text{eff}} = 7.5 \times 10^{-11} \text{ m}^2$, and 512.8 average accidentals/bin over 24 hours we find

$$R_{\text{AC}} = 5.9 \times 10^{-3} \text{ Hz}, \quad (4.33\text{a})$$

$$R_{\text{TC}} = 2.7 \times 10^{-8} \text{ Hz}, \quad (4.33\text{b})$$

$$\text{CAR} = 4.55 \times 10^{-6}. \quad (4.33\text{c})$$

In order to reduce the rate of accidentals we introduce two 20 nm spectral filters symmetrically around λ_{SPDC} , by replacing the beam-splitter with a three-port array waveguide grating (AWG). Although we expect to collect $\approx 270/20 = 13.5$ less signal (assuming a uniform signal-idler spectrum over a bandwidth of 270 nm see eq. (2.54)), if the background emission follows a different spectral distribution the overall CAR will be higher. We also increase the peak intensity to $1.34 \times 10^{10} \text{ W cm}^{-2}$, a similar value used in mono-layer MoS₂. From this, as well as the presence of the spectral filters (additional loss of 13.5) we expect to generate pairs at a rate of $\bar{R}_{\text{SPDC}} = 4.88 \times 10^{-2} \text{ Hz}$ at the sample plane. From the results obtained over 12 hours under $\lambda_P = 760$ nm illumination fig. 4.21 (d), we find an average of 15.4 accidentals/bin over an integration time of 43 200 s corresponding to

$$R_{\text{AC}} = 3.5 \times 10^{-4} \text{ Hz}, \quad (4.34\text{a})$$

$$R_{\text{TC}} = 4.6 \times 10^{-7} \text{ Hz}, \quad (4.34\text{b})$$

$$\text{CAR} = 1.3 \times 10^{-3}, \quad (4.34\text{c})$$

a noise rate 18 times weaker than what would have been measured in monolayer WSe₂ with the same power density. Note that the CAR improved 100-fold compared to monolayer WSe₂ in eq. (4.31a). In the next two sections we take steps to explain the nature of such background emission, and attempt detection gating in the time domain as a way to reduce the accidentals and increase the CAR.

4.6.5 Background Characterization

In this section we present single-photon spectral measurements of the temporally-uncorrelated emission that impaired the detection of SPDC from multilayer MoS₂ under 730 nm excitation. The results of these study in the spectral range 1300-1650 nm informs an improved detection-gated measurement. We first illuminate five-layer MoS₂ above its band-gap and confirm that its visible photoluminescence (PL) spectrum shows two peaks in correspondence with the material A and B exciton. We then repeat the experiment of section 4.6.4 in the wavelength range 550-750 nm, and find that the background intensity peaks in correspondence to the material resonances. Single-photon spectroscopy in the range 1470-1610 nm shows a spectrum

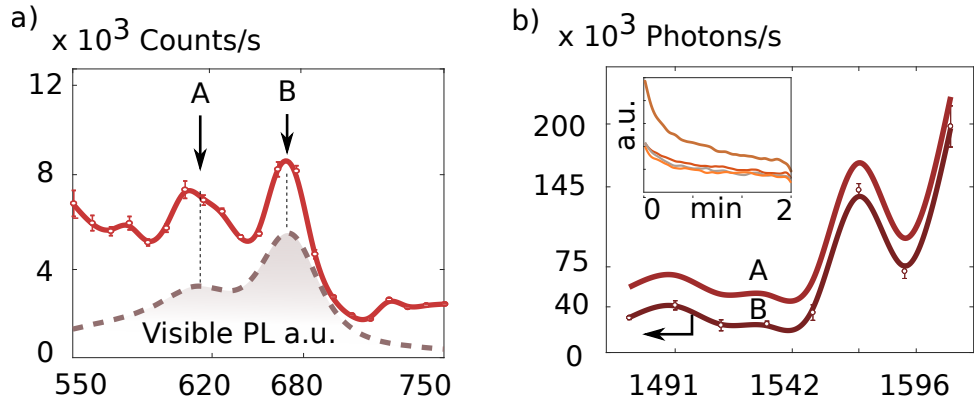


FIGURE 4.22: a) NIR emission from five-layer 3R-MoS₂ revealed by single-photon detectors. Emission follows the same features of the one-photon photoluminescence curve and peaks when the pump is resonant with the A and B excitons. Illumination with femtosecond pump 80 MHz, 235 fs and detection in the spectral region 1300 to 1700 nm. A dark-count limited signal is recorded from the quartz substrate. b) Power spectral density of NIR emission from multi-layer 3R-MoS₂ for illumination two-photon resonant to the A and B exciton. Emission peaks above 1540 nm and appears to increase towards lower photon energy. The overall spectral shape does not depend on the particular transition, and shows discrete temporal stability (inset).

mostly concentrated around 1560 nm, and suggests that the emission is even stronger at longer wavelengths.

The photoluminescence measurement was performed in reflection under 535 nm illumination through a high numerical aperture lens, and a 550 nm long-pass dichroic filter to reject the pump. As expected, the PL spectrum exhibits two peaks in correspondence of the A and B excitonic resonances of the material as shown in the dashed line in fig. 4.22 (a). In order to test the contribution of electronic resonances to the near-infrared background that dominates the histograms of fig. 4.21, we correlate the intensity of the latter with the energy difference between the pump and the two excitonic peaks. The optical arrangement used in this measurement differs from that shown in fig. 4.21 (a) only for the use of a single SPAD in place of the Hanbury-Brown and Twiss interferometer. The pump is generated by frequency-doubling the OPO in the wavelength range 550-750 nm, and its average power limited to 100 μ W, approximately one sixth of that used in fig. 4.21 (a). The background (not shown) was acquired by illuminating the quartz substrate and found to be dark-count limited (\approx 30 Hz). The solid line in fig. 4.22 (a) reveals a similar bi-modal response whose peaks align to the A and B resonances of the material, indicating a strong contribution of the two resonances to the overall strength of the near-infrared emission. To measure its energy distribution, we perform single-photon spectroscopy in the range 1470-1610 nm in 20 nm steps through an fiber-coupled array waveguide grating connected to a NIR SPAD. Results are shown in fig. 4.22 (b), where the photon rate at the sample plane was obtained from the count rate by taking into account all loss in the system. Emission is concentrated at 1560 nm and might extend after 1600 nm where we report a maximum of 200×10^3 photons/s. Finally, the overlap between the two curves in fig. 4.22 b) indicates that the qualitative spectral response is independent from the energy of the excitonic resonance. We tentatively attribute this to non-direct bandgap transitions of the material which are known to red-shift

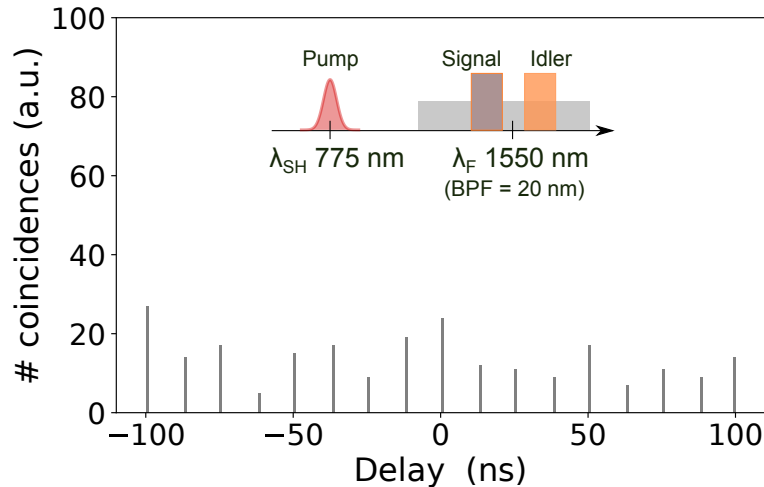


FIGURE 4.23: Gated single photon coincidences from five-layer MoS₂ under non-resonant pumping, acquired over the course of 195.5 hours. The histogram is a sampled version of the one obtained in fig. 4.21 (b) and (d), with the same period as the pump (12.5 ns). A constant delay was added to the arms of the single-photon Hanbury-Brown and Twiss (HBT) interferometer, so that true coincidences appear at $\tau = -37.5 \text{ ns}$. The experimental setup and alignment procedure is detailed in section 3.7.

to the wavelength range 800-950 nm (1.3-1.55 eV) with increasing material thickness [205], although a more detailed study would be necessary to confirm the exact contribution of these resonances.

4.6.6 Detection gating in 5L MoS₂

A consequence of the quasi-instantaneous nature of SPDC is that there cannot be any energy-time entangled photon pair in the time between two consecutive pulses. Thus, photons detected in such intervals must be background and can be discarded. In addition to applying this technique, here we tune the excitation to 740 nm, and collect signal and idler in the spectral windows $1470 \pm 20 \text{ nm}$ and $1510 \pm 20 \text{ nm}$, corresponding to the minima of fig. 4.22 b). The temporal alignment and the optical setup is similar to that described in section 3.7, where the arrival time of photons on each channel of the time-interval analyzer is checked against the reference clock of the laser. With a tolerance time window of $\pm 0.5 \text{ ns}$ and a nominal repetition period of 12.5 ns, the accidental coincidences can thus be reduced 25 times at most. Given the way the delays are processed, true coincidences are expected to appear as a sharp peak at $\tau = -37.5 \text{ ns}$, not dissimilar from that of fig. 4.18. Results collected over more than 8 days are shown in fig. 4.23. The absence of a dominant peak at $\tau = -37.5 \text{ ns}$, indicates that if generated, SPDC photon pairs lead to a number of true coincidences much smaller than that of the accidentals. From the average bin height of 13.9 and the total integration time, we calculate

$$R_{\text{AC}} = 1.97 \times 10^{-5} \text{ Hz}, \quad (4.35\text{a})$$

$$\text{CAR} = 3.6 \times 10^{-2}, \quad (4.35\text{b})$$

which despite indicating a 20-fold reduction in accidentals (close to the maximum achievable of 25), it shows that the measurement is still background limited. While experiments cannot confirm the presence of SPDC, we can equalize for the total loss in the system and advance the hypothesis that if present, the true rate of photon pairs generated at the sample plane must be smaller than $R_{AC}|t_{bin}/(L_T)^2| = 0.155 \text{ Hz}$.

4.7 Discussion

In this chapter we described the measurement of energy-time entangled photons pairs via spontaneous parametric downconversion (SPDC) in two-dimensional transition-metal dichalcogenide (TMDC) films deposited on quartz, and probed in free-space with a tunable femto-second laser. After calculating collection, propagation, and detection efficiencies, we presented results of SHG and SPDC photon coincidences for both monolayer WSe₂ and five-layers MoS₂ with a carefully engineered 3R stacking. When illuminated at their respective A-excitons, we measured an effective $\chi^{(2)}$ of $50 \times 10^{-12} \text{ m V}^{-1}$ from five-layers MoS₂, 7.6 times higher than $6.6 \times 10^{-12} \text{ m V}^{-1}$ measured in monolayer WSe₂.

SPDC results

From accurately designed SHG measurements, we inferred the SPDC potential of monolayer WSe₂ and multilayer MoS₂. For monolayer WSe₂ we calculate a maximum pair-rate of $\bar{R}_{SPDC} = 0.002 \pm 0.0016$ pairs/s in correspondence of the material A-exciton, limited by the damage threshold of the material. This increases to 0.38 ± 0.20 when the pump is aligned to the A-exciton of the second material, thanks to its carefully engineered symmetry, as well as its higher second order non-linear response. At the same pump intensity, the CAR was systematically increased from 1.5×10^{-5} to 1.3×10^{-3} and 3.6×10^{-2} in monolayer WSe₂, 5L-MoS₂ with 20 nm filters, and 5L-MoS₂ with 20 nm filters and detection gating respectively. Since it was not possible to reach values of CAR above 10, no conclusion can be made on the generation of entangled photon pairs from atomically-thick materials, or on the laws that describe their dependence on the experimental and material parameters. Interestingly, all measurements were background-limited. In MoS₂, the intensity of such background was found to be higher above 1540 nm, and when the pump was resonant to the A and B excitons of the material.

Effect of detection gating

Finally, we combined detection gating with spectral filtering. The reduction in accidentals depends on the repetition rate of the pump as well as the lifetime of the temporal statistics of the background emission. With a gate window and a repetition rate of 0.5 ns and 12.5 ns respectively, and a background uniformly distributed the maximum CAR increase is 25. We measured 20, indicating that the actual emission is more likely to happen soon after a pulse reaches the material.

Effect of spectral filtering

SPDC sources that are embedded in waveguides such as quasi-phase matched bulk crystals and integrated photonic circuits, benefit from a precise controlling of the

linear dispersion and thus of phase matching. In these systems, the joint quantum state can be engineered for specific QIP applications by tailoring its polarization, momentum, and spectral degrees of freedom [206]. An experimental consequence of this, is the ability to spectrally isolate signal and idler modes from the background, thus greatly reducing the rate of accidental coincidences $R_{\text{AC-bkg}}^{\text{nn}}$ (section 4.2). In contrast the small interaction volume in a 2D material in free-space, leads to a weak but broadband SPDC response (see eq. (2.54) and eq. (4.29) for monolayer WSe₂). For this reason, if the CAR is limited by background radiative emission eq. (4.18), any spectral filtering is likely to simultaneously attenuate both the signal and the noise (background), leading to limited if not null net gain.

Detection Challenges

All single-photon measurements were conducted with state-of-the-art NIR single-photon avalanche photodiodes. The low efficiencies expected from such small effective areas imposes long observation times, introducing many practical challenges related to the size of the data to be processed, and the stability of the electronics. One unexpected consequence of long integration times was the detection of symmetric features in the autocorrelation of the detection times between two SPADs in the HBT interferometer. These were found to come from radiative recombinations of hot-carriers in the active area, a phenomenon known as breakdown flashing. Although rarely encountered, these effects can dominate the coincidence measurements of sub-Hz signals. We also showed that a consequence of hybrid active/pассив quenching in SPADs, is a small uncertainty in the flashing time, which enables effective time-domain filtering.

Chapter 5

Conclusions

The century-old discovery of SPDC has enabled a deeper understanding of light-matter interactions and has been instrumental to the development of quantum mechanics. Although SPDC has been observed in bulk and integrated structures and its scaling laws unveiled both theoretically and experimentally, measurements have been limited to interaction volumes larger than λ^3 leaving unclear how the process would scale in the presence of just a few atomic layers. Moreover, in integrated photonic chips the waveguide provides the necessary optical nonlinearity, while simultaneously ensuring that the all optical modes propagate with the same group velocity (phase-matching). A direct consequence is that both the linear and nonlinear optical properties of the medium must be simultaneously engineered, often resulting in narrow-band and non-reconfigurable operation. Thanks to their high nonlinearity and quantum-confined nature, two-dimensional materials could be useful for the generation of entangled photon pairs via spontaneous parametric down-conversion. In this thesis we have been particularly interested in transition-metal dichalcogenides (TMDCs) primarily for their record-high nonlinearity [1–7]. The second order susceptibility reported for WSe₂ and MoS₂ are comparable to monolayer GaAs which is known to be between $12 \times 10^{-11} \text{ m V}^{-1}$ and $50 \times 10^{-11} \text{ m V}^{-1}$ in the range 500–1500 nm [108], and up to one order of magnitude larger than the material of choice for optical entanglement generation via spontaneous parametric downconversion, namely LiNbO₃, whose largest component of $\chi^{(2)}$ is known to be $6 \times 10^{-11} \text{ m V}^{-1}$ [16]. Moreover, with simple fabrication techniques, these materials can be stacked to form more complex heterostructure, and be embedded into linear waveguides or resonant optical cavities, while their thickness (many times smaller than the wavelength on light) ensures broadband light matter interaction.

In this thesis we study the potential of these materials to generate pairs of correlated photons by means of SPDC in a conventional free-space arrangement. While this simplifies fabrication, the resulting small interaction volume leads to highly inefficient conversions, rendering the measurement of photon simultaneity elusive. Experiments require detectors with high quantum efficiencies, as well as near-unity collection efficiency, to bound the observation time to a reasonable value and guarantee a large coincidences over accidental ratio (CAR). Moreover, loss imposes integration times that may extend to many tens of hours, forcing the detection and data-analysis systems to manifest unexpected behaviors. One such example is the observation of temporally localized features in the coincidence histogram, related to radiative recombinations of hot-carriers in the active area of the SPADs, a phenomenon known as breakdown flashing. In our experimental conditions the emission probability was found to be 12%, or equivalently 1 radiative recombination every 8.3 detections. If not appropriately filtered, these may be erroneously interpreted

as a signature of photon-simultaneity and thus spontaneous parametric downconversion. Their narrow autocorrelation implicates a small uncertainty of the lag between detection and emission, and was attributed to the fast quenching electronics in ID230s, in sharp contrast to the exponentially decaying trace that commonly reported in passively-quenched SPADs. These results show that breakdown radiation can be deterministically filtered in the time domain without the use of expensive and narrow-band non-reciprocal elements, and ultimately be leveraged to gate the measurement of the emission spectrum with unprecedented spectral resolution.

Our first attempt to detect photon pairs was in a planar film of atomically-thick transition-metal dichalcogenides. From the efficiency of a carefully designed SHG measurement in mono-layers WSe₂, we calculated the maximum SPDC pair rate to be 0.0020(16) Hz (or 1 pair every 16.7 minutes on average), under 1570 nm femtosecond illumination at a pump peak intensity of $3.6 \times 10^9 \text{ W cm}^{-2}$. When all losses are accounted for, the average time between detected coincidences with off-the-shelves InGaAs SPADs was expected to be tens of hours. While this is many orders of magnitude smaller than what is routinely obtained in phase-matched bulk crystals [200, 201], we show that a CAR greater than 10 could in principle be achieved, assuming that the thermal noise in the detectors was the only source of disturbance. We reach this conclusion by taking into account all losses, including the mismatch between the expected radiation pattern of the down-converted light, and the high NA free-space collection cones, which we carefully calculated by means of numeric simulations. We find that pairs generated in the substrate have sharper departure angles and a higher probability to experience total-internal reflection at the quartz-air interface, and normal pump incidence was found to lead to isotropic emission of signal and idler photons and a consequent higher probability to collect a pair from free-space. If successful, such a measurement would set a record for observation of SPDC in 2D materials, and enable the experimental exploration of scaling laws in quantum-confined structures. However, results reveal a relatively brighter and time-uncorrelated background, present even when great care was taken to spectrally isolate illumination and detection.

In order to improve the measurement, we engineered five-layer MoS₂ leveraging four simultaneous improvements: 1. the quadratic scaling of SPDC with the thickness of the nonlinear medium (provided that inversion-symmetry braking is preserved), 2. the higher damage threshold of few-layer crystals compared to monolayers, 3. the exponentially lower probability of detecting spontaneous radiative emissions as a result of a stronger Coulomb screening, 4. the stronger second-order nonlinear susceptibility of MoS₂ compared to WSe₂. Finally, we explored detection-gating as a way to further suppress the background. In all these attempts, the detection was found to be limited a background relatively brighter to the expected SPDC signal. In the best experimental configuration we were able to implement, the detection bandwidth for signal and idler was limited to 20 nm and the integration time set to 192 hours. However, even with such extreme observations, the rate of accidentals was estimated to be around 30 times stronger than the maximum expected rate of 4.88×10^{-2} pairs/s.

With hindsight, it appears that the quadratic dependence of the pair generation rate on the interaction length is the main limiting factor. One way to extend the interaction length the nonlinear sheets can be coupled with a suitably phase-matched photonic structure (e.g. a waveguide). The immediate consequence of this is the

narrowing of the spectral bands where photon pairs can be generated, which is desirable in photon heralding applications. If we indicate with G the gain resulting from a longer interaction length, and include all sources of loss in a term called γ (phase-matching, absorption, and coupling loss), we can write

$$\frac{d_{wg}}{d_{2D}} = \gamma\sqrt{G}, \quad (5.1)$$

where d_{wg} is the interaction length in the waveguide and d_{MoS2} the thickness of the TMDC used, in this case MoS₂. Thus, in order to increase the pair rate for MoS₂ from 4.88×10^{-2} Hz to 1 MHz we would need a gain $G \approx 2 \times 10^8$ (from $d_{MoS2} = 3.5 \times 10^{-9}$ m). However, it is unlikely that the pump intensity at the point of contact between the 2D sheet and the waveguide, can be any close to that achievable on the 2D material from free-space, without permanently damaging the substrate. This is likely to require an interaction length one order of magnitude longer than what calculated. Another factor of 10 is likely to arise from coupling inefficiencies, thus placing an estimate for γ at around 100. In a 22 μm long waveguide the authors in [145] reported a SHG gain of 280 with a $\frac{d_{wg}}{d_{2D}} \approx 3.8 \times 10^4$ 22 μm long waveguide, corresponding to $\gamma \approx 120$, which appears to be in the same order of magnitude estimated above. With these considerations the waveguide length d_{wg} required to achieve a pair rate of 1 MHz would be 5.9×10^{-3} m. Despite the challenges related to the fabrication of such large-area atomically-thick sheets, these materials could still prove useful to achieve highly integrated and bright sources of photon pairs on chip.

Although the generation of SPDC photon pairs in free-space TMDCs could not be confirmed, our results provide a performance benchmark for more advanced structures based on these ultra-thin materials, which could lead to experimentally confirm the scaling of quantum-classical relations when the nonlinear media are deeply sub-wavelength. Moreover, this work presents the first detailed analysis of all factors that need to be taken into account when designing such experiments, as well as their impact on the overall CAR.

5.1 Outlook

These results highlight the complexity of such single-photon quantum measurements, and suggest to explore alternative means to reduce undesired spontaneous emissions. Possible avenues include changing the material, explore cooling to deplete the lattice phonon population and thus lower the background, resonantly enhancing the downconversion by depositing the surfaces on optical cavities, or increase the interaction length by coupling the material to photonic waveguide. Another way to increase the interaction efficiency is to explore different materials with WSe₂ once such potential candidate, with $\chi^{(2)} = 580 \times 10^{-11}$ m V⁻¹, up to 100 times larger than that reported for WSe₂ [6, 207]. Another less explored material is, 4-N N-dimethylamino 4-N methylstilbazolium tosylate (DAST), whose nonlinear susceptibility was reported to be $\chi^{(2)} = 202 \times 10^{-11}$ m V⁻¹ [208]. Perovskites might also be worth exploring, with MFOGeI₃ reported in [209] to have an effective nonlinearity $\chi^{(2)} > 30 \times 10^{-11}$ m V⁻¹ up to 22000 times stronger than AgGaSe₂ which was reported to be $\chi^{(2)} = 0.3 \times 10^{-11}$ m V⁻¹ [210]. Since linear loss has a quadratic effect on CAR in single-photon coincidence measurements, it is important to minimize it.

In reflection geometries the collection loss can easily be minimized by placing a mirror at the right distance from the surface as shown in [211]. Detection loss can also be greatly reduced by using superconducting nanowire SPADs, which in the near-infrared achieve quantum efficiencies greater than 0.9. A careful design of the illumination and collection apparatus could also help reduce the propagation loss. By combining all these factors together the total pair loss of $(88.8)^2 = 7885.44$ could be lowered to $(10)^2 = 100$, corresponding to a nearly 80-fold CAR increase. While many of the advantages related to their tunable electro-optical properties remain attractive for the generation of entangled photon pairs, the small footprint of two-dimensional TMDC materials does not seem to motivate their use over well-understood integrated platforms. It remains to be seen if and how the quantum-confined nature of these materials affect the dependence of the efficiency of spontaneous parametric downconversion on the material geometry such as interaction length.

Bibliography

- ¹L. M. Malard et al., "Observation of intense second harmonic generation from MoS₂ atomic crystals", *Physical Review B* **201401**, 1–5 (2013).
- ²G. Wang et al., "Giant Enhancement of the Optical Second-Harmonic Emission of WSe₂ Monolayers by Laser Excitation at Exciton Resonances", *Physical Review Letters* **114**, 097403 (2015).
- ³X. Yin et al., "Edge nonlinear optics on a MoS₂ atomic monolayer.", *Science* **344**, 488–90 (2014).
- ⁴Y. Li et al., "Probing Symmetry Properties of Few-Layer MoS₂ and h-BN by Optical Second-Harmonic Generation", *Nano Letters* **13**, 3329–3333 (2013).
- ⁵R. I. Woodward et al., "Characterization of the second- and third-order nonlinear optical susceptibilities of monolayer MoS₂ using multiphoton microscopy", *2D Materials* **4**, 011006 (2017).
- ⁶C. Janisch et al., "Extraordinary Second Harmonic Generation in tungsten disulfide monolayers.", *Scientific reports* **4**, 5530 (2014).
- ⁷M. Zhao et al., "Atomically phase-matched second-harmonic generation in a 2D crystal", *Light: Science & Applications* **5**, e16131–e16131 (2016).
- ⁸Q. Zhang et al., "Repository Giant valley drifts in uniaxially strained monolayer MoS₂", *Phys Rev B* **88**, 245447 (2013).
- ⁹P. Johari and V. B. Shenoy, "Tuning the Electronic Properties of Semi-conducting Transition Metal Dichalcogenides by Applying Mechanical Strains", *ACS Nano*, 5449–5456 (2012).
- ¹⁰S. Horzum et al., "Phonon Softening and Direct to Indirect Bandgap Crossover in Strained Single Layer MoSe₂", *Phys Rev B* **87**, 125415 (2013).
- ¹¹B. Radisavljevic et al., "Single-layer MoS₂ transistors", *Nature Nanotechnology* **6**, 147–150 (2011).
- ¹²J. X. et. al. Al, "Tunable band gaps in bilayer transition-metal dichalcogenides", *Phys Rev B* **84**, 205325 (2016).
- ¹³H.-j. Sung et al., "Effects of van der Waals interaction and electric field on the electronic structure of bilayer MoS₂", *Journal of Physics: Condensed Matter* **26**, 405302 (2014).
- ¹⁴E. Knill et al., "A scheme for efficient quantum computation with linear optics", *Nature* **409**, 46–52 (2001).
- ¹⁵R. L. Sutherland, *Handbook of Nonlinear Optics* (2003).
- ¹⁶R. W. Boyd, *Boyd Non Linear Optics 3rd Ed*, Third (2007), p. 600.
- ¹⁷M. Planck, "Ueber das Gesetz der Energieverteilung im Normalspectrum", *Annalen der Physik* **309**, 553–563 (1901).

- ¹⁸A. Einstein, "Über einen die Erzeugung und Verwandlung des Lichtes betreffenden heuristischen Gesichtspunkt", *Annalen der Physik* **322**, 132–148 (1905).
- ¹⁹H. J. Kimble et al., "Photon Antibunching in Resonance Fluorescence", *Physical Review Letters* **39**, 691–695 (1977).
- ²⁰H. Fearn and R. Loudon, "Theory of two-photon interference", *Journal of the Optical Society of America B* **6**, 917 (1989).
- ²¹T. Legero et al., "Time-resolved two-photon quantum interference", *Applied Physics B* **77**, 797–802 (2003).
- ²²T. Rudolph, "Why I am optimistic about the silicon-photonic route to quantum computing", *APL Photonics* **2**, 030901 (2017).
- ²³D. Bonneau et al., "Silicon Quantum Photonics", in *Topics in applied physics*, Vol. 122, April (2016), pp. 41–82.
- ²⁴B. P. Abbott et al., "Observation of Gravitational Waves from a Binary Black Hole Merger", *Physical Review Letters* **116**, 061102 (2016).
- ²⁵S. T. Intervals and T. Photons, "Measurement of subpicosecond time intervals between two photons by interference", **59**, 2044–2046 (1987).
- ²⁶C. Santori et al., "Indistinguishable photons from a single-photon device.", *Nature* **419**, 594–597 (2002).
- ²⁷H. B. and Twiss, "A test of a new type of stellar interferometer on Sirius", *Nature* **178**, 1046 (1956).
- ²⁸G. Baym, "The physics of Hanbury Brown–Twiss intensity interferometry: from stars to nuclear collisions", 1–35 (1998).
- ²⁹M. Fox, *Quantum Optics: An Introduction*, Vol. 6 (2006).
- ³⁰R. J. Glauber, "The Quantum Theory of Optical Coherence", *Physical Review* **130**, 2529–2539 (1963).
- ³¹J.-W. Pan et al., "Experimental Entanglement Swapping: Entangling Photons That Never Interacted", *Physical Review Letters* **80**, 3891–3894 (1998).
- ³²Q. Zhang et al., "Distribution of time-energy entanglement over 100 km fiber using superconducting singlephoton detectors", *Optics Express* **16**, 5776 (2008).
- ³³S. Ramelow et al., "Discrete Tunable Color Entanglement", *Physical Review Letters* **103**, 253601 (2009).
- ³⁴I. Marcikic et al., "Time-bin entangled qubits for quantum communication created by femtosecond pulses", *Physical Review A* **66**, 062308 (2002).
- ³⁵B. Brecht et al., "Photon Temporal Modes: A Complete Framework for Quantum Information Science", *Physical Review X* **5**, 041017 (2015).
- ³⁶V. Giovannetti, "Quantum-Enhanced Measurements: Beating the Standard Quantum Limit", *Science* **306**, 1330–1336 (2004).
- ³⁷J. D. Franson, "Nonlocal cancellation of dispersion", *Physical Review A* **45**, 3126–3132 (1992).
- ³⁸A. M. Steinberg et al., "Dispersion cancellation in a measurement of the single-photon propagation velocity in glass", *Physical Review Letters* **68**, 2421–2424 (1992).

- ³⁹J. M. Lukens et al., "Orthogonal Spectral Coding of Entangled Photons", *Physical Review Letters* **112**, 133602 (2014).
- ⁴⁰V. Giovannetti et al., "Quantum-enhanced positioning and clock synchronization", *Nature* **412**, 417–419 (2001).
- ⁴¹C.-Y. Lu and J.-W. Pan, "Push-button photon entanglement", *Nature Photonics* **8**, 174–176 (2014).
- ⁴²A. Aspect et al., "Experimental Tests of Realistic Local Theories via Bell's Theorem", *Physical Review Letters* **47**, 460–463 (1981).
- ⁴³R. J. Young et al., "Improved fidelity of triggered entangled photons from single quantum dots", *New Journal of Physics* **8**, 29–29 (2006).
- ⁴⁴N. Akopian et al., "Entangled Photon Pairs from Semiconductor Quantum Dots", *Physical Review Letters* **96**, 130501 (2006).
- ⁴⁵C. Santori et al., "Indistinguishable photons from a single-photon device", *Nature* **419**, 594–597 (2002).
- ⁴⁶W. Yao, "Molecules in flatland", *Nature Physics* **11**, 448–449 (2015).
- ⁴⁷O. Benson et al., "Regulated and Entangled Photons from a Single Quantum Dot", *Physical Review Letters* **84**, 2513–2516 (2000).
- ⁴⁸R. J. Young et al., "Improved fidelity of triggered entangled photons from single quantum dots", *New Journal of Physics* **8** (2006) 10.1088/1367-2630/8/2/029.
- ⁴⁹M. Müller et al., "On-demand generation of indistinguishable polarization-entangled photon pairs", *Nature Photonics* **8**, 224–228 (2014).
- ⁵⁰Y. Chen et al., "Wavelength-tunable entangled photons from silicon-integrated III-V quantum dots.", *Nat. Commun.* **7**, 10387 (2016).
- ⁵¹P. Grangier et al., "Experimental evidence for a photon anticorrelation effect on a beam splitter: a new light on single-photon interferences", *EPL (Europhysics Letters)* **1**, 173 (1986).
- ⁵²C. K. Hong and L. Mandel, "Experimental realization of a localized one-photon state", *Physical Review Letters* **56**, 58 (1986).
- ⁵³L. Caspani et al., "Integrated sources of photon quantum states based on nonlinear optics", *Light: Science & Applications* **6**, e17100 (2017).
- ⁵⁴C. K. Hong and L. Mandel, "Theory of parametric frequency down conversion of light", *Physical Review A* **31**, 2409–2418 (1985).
- ⁵⁵D. C. Burnham and D. L. Weinberg, "Observation of Simultaneity in parametric production of optical photon pairs", *Physical Review Letters Rev* **25**, 84–87 (1970).
- ⁵⁶J. C. Howell et al., "Realization of the Einstein-Podolsky-Rosen Paradox Using Momentum- and Position-Entangled Photons from Spontaneous Parametric Down Conversion", *Physical Review Letters* **92**, 210403 (2004).
- ⁵⁷M. Edgar et al., "Imaging high-dimensional spatial entanglement with a camera", *Nature Communications* **3**, 984 (2012).
- ⁵⁸J.-P. W. MacLean et al., "Direct Characterization of Ultrafast Energy-Time Entangled Photon Pairs", *Physical Review Letters* **120**, 053601 (2018).

- ⁵⁹D. Klyshko, "Coherent Photon Decay in a Nonlinear Medium", *ZhETF Pisma Redaktsiiu* **6**, 490 (1967).
- ⁶⁰S. E. Harris et al., "Physical review lett krs 1", *Physical Review Letters* **18**, 732–734 (1967).
- ⁶¹D. Magde, "Study in Ammonium Dihydrogen Phosphate of Spontaneous Parametric Interaction Tunable from 4400 to 16 000 Angström", *Physics Review Letters* **18**, 905–907 (1967).
- ⁶²A. L. Migdall et al., "Tailoring single-photon and multiphoton probabilities of a single-photon on-demand source", *Physical Review A - Atomic, Molecular, and Optical Physics* **66**, 4 (2002).
- ⁶³J. H. Shapiro and F. N. Wong, "On-demand single-photon generation using a modular array of parametric downconverters with electro-optic polarization controls", *Optics Letters* **32**, 2698 (2007).
- ⁶⁴X. S. Ma et al., "Experimental generation of single photons via active multiplexing", *Physical Review A - Atomic, Molecular, and Optical Physics* **83**, 1–8 (2011).
- ⁶⁵J. Mower and D. Englund, "Efficient generation of single and entangled photons on a silicon photonic integrated chip", *Physical Review A* **84**, 052326 (2011).
- ⁶⁶A. Christ and C. Silberhorn, "Limits on the deterministic creation of pure single-photon states using parametric down-conversion", *Physical Review A* **85**, 023829 (2012).
- ⁶⁷T. Jennewein et al., "Single-photon device requirements for operating linear optics quantum computing outside the post-selection basis", *Journal of Modern Optics* **58**, 276–287 (2011).
- ⁶⁸H. Herrmann et al., "Source of non-degenerate , polarization entangled photon pairs", **103005** (2011).
- ⁶⁹J. Kawashima et al., "Type-I Quasi-Phase-Matched Waveguide Device for Polarization-Entangled Twin Photon Generation", **21**, 566–568 (2009).
- ⁷⁰T. Suhara et al., "Generation of Polarization-Entangled Photons by Type-II Quasi-Phase-Matched Waveguide Nonlinear-Optic Device", **19**, 1093–1095 (2007).
- ⁷¹T. Suhara et al., "Quasi-Phase Matched Waveguide Devices for Generation of Postselection-Free Polarization-Entangled Twin Photons", **1**, 3–4 (2009).
- ⁷²K. Thyagarajan et al., "Generation of polarization- entangled photons using type-II doubly periodically poled lithium niobate waveguides", 1–8 (2009).
- ⁷³S. Tanzilli et al., "PPLN waveguide for quantum communication", *The European Physical Journal D - Atomic, Molecular and Optical Physics* **18**, 155–160 (2002).
- ⁷⁴T. Honjo et al., "Generation of energy-time entangled photon pairs in 15- μm band with periodically poled lithium niobate waveguide", *Optics Express* **15**, 1679 (2007).
- ⁷⁵D. Bonneau et al., "Fast path and polarization manipulation of telecom wavelength single photons in lithium niobate waveguide devices", *Physical Review Letters* **108**, 1–5 (2012).
- ⁷⁶H. Jin et al., "On-Chip Generation and Manipulation of Entangled Photons Based on Reconfigurable Lithium-Niobate Waveguide Circuits", *Physical Review Letters* **113**, 103601 (2014).

- ⁷⁷A. S. Solntsev et al., "Spontaneous Parametric Down-Conversion and Quantum Walks in Arrays of Quadratic Nonlinear Waveguides", *Physical Review Letters* **108**, 023601 (2012).
- ⁷⁸C. S. Hamilton et al., "Driven Quantum Walks", *Physical Review Letters* **113**, 083602 (2014).
- ⁷⁹A. Vallés et al., "Generation of polarization-entangled photon pairs in a Bragg reflection waveguide", *Optics Express* **21**, 10841 (2013).
- ⁸⁰R. T. Horn et al., "Inherent polarization entanglement", 1–5 (2013).
- ⁸¹P. Filloux et al., "Direct Bell States Generation on a III-V Semiconductor Chip at Room Temperature", **160502**, 1–5 (2013).
- ⁸²P. Sarrafi et al., "High visibility two-photon interference of frequency-time entangled photons generated in a quasi-phase-matched AlGaAs waveguide", *Optics Letters* **39**, 5188–5191 (2014).
- ⁸³C. Autebert et al., "Integrated AlGaAs source of highly indistinguishable and energy-time entangled photons", *Optica* **3**, 143–146 (2016).
- ⁸⁴L. G. Helt et al., "How does it scale? Comparing quantum and classical nonlinear optical processes in integrated devices", *Journal of the Optical Society of America B* **29**, 2199 (2012).
- ⁸⁵J. U. Fürst et al., "Quantum Light from a Whispering-Gallery-Mode Disk Resonator", *Physical Review Letters* **106**, 113901 (2011).
- ⁸⁶M. Förtsch et al., "Highly efficient generation of single-mode photon pairs from a crystalline whispering-gallery-mode resonator source", *Physical Review A* **91**, 023812 (2015).
- ⁸⁷T. Nosaka et al., "Cross-polarized twin photon generation device using quasi-phase matched LiNbO₃ waveguide", *IEEE Photonics Technology Letters* **18**, 124–126 (2006).
- ⁸⁸G. Fujii et al., "Bright narrowband source of photon pairs at optical telecommunication wavelengths using a type-II periodically poled lithium niobate waveguide", *Optics Express* **15**, 954–956 (2007).
- ⁸⁹D. R. Hamel et al., "Direct generation of three-photon polarization entanglement", *Nature Photonics* **8**, 801–807 (2014).
- ⁹⁰T. Guerreiro et al., "Nonlinear Interaction between Single Photons", *Physical Review Letters* **113**, 173601 (2014).
- ⁹¹L. K. Shalm et al., "Three-photon energy–time entanglement", *Nature Physics* **9**, 19–22 (2013).
- ⁹²H. Hübel et al., "Direct generation of photon triplets using cascaded photon-pair sources", *Nature* **466**, 601–603 (2010).
- ⁹³S. Krapick et al., "On-chip generation of photon-triplet states", *Optics Express* **24**, 2836 (2016).
- ⁹⁴L. G. Helt et al., "Spontaneous parametric downconversion in waveguides: what's loss got to do with it?", *New Journal of Physics* **17**, 013055 (2015).
- ⁹⁵K. S. Novoselov, "Electric Field Effect in Atomically Thin Carbon Films", *Science* **306**, 666–669 (2004).

- ⁹⁶W. Wu et al., "High mobility and high on/off ratio field-effect transistors based on chemical vapor deposited single-crystal MoS₂ grains", *Applied Physics Letters* **102**, 142106 (2013).
- ⁹⁷S. Kim et al., "High mobility and low power transistors based on multilayer MoS₂", *Nature Communications* **3**, 1011–1017 (2012).
- ⁹⁸M. Zhang et al., "Two-Dimensional Molybdenum Tungsten Diselenide Alloys: Photoluminescence, Raman Scattering, and Electrical Transport", *ACS Nano* **8**, 7130–7137 (2014).
- ⁹⁹A. H. Castro Neto et al., "The electronic properties of graphene", *Reviews of Modern Physics* **81**, 109–162 (2009).
- ¹⁰⁰M. J. Allen et al., "Honeycomb Carbon: A Review of Graphene", *Chemical Reviews* **110**, 132–145 (2010).
- ¹⁰¹X. Yu et al., "Graphene-based smart materials", *Nature Reviews Materials* **2**, 17046 (2017).
- ¹⁰²H. Zhang et al., "Measuring the refractive index of highly crystalline monolayer MoS₂ with high confidence.", *Sci. Rep.* **5**, 8440 (2015).
- ¹⁰³M. Chhowalla et al., "The chemistry of two-dimensional layered transition metal dichalcogenide nanosheets", *Nature Chemistry* **5**, 263–275 (2013).
- ¹⁰⁴M. Wanunu et al., "Rapid electronic detection of probe-specific microRNAs using thin nanopore sensors", *Nature Nanotechnology* **5**, 807–814 (2010).
- ¹⁰⁵G. Danda et al., "Monolayer WS₂ Nanopores for DNA Translocation with Light-Adjustable Sizes", *ACS Nano* **11**, 1937–1945 (2017).
- ¹⁰⁶J. Wilson and A. Yoffe, "The transition metal dichalcogenides discussion and interpretation of the observed optical, electrical and structural properties", *Advances in Physics* **18**, 193–335 (1969).
- ¹⁰⁷A. V. Kolobov and J. Tominaga, "Two-Dimensional Transition-Metal Dichalcogenides Alexander V. Kolobov and Junji Tominaga", *MRS Bulletin* **42**, 471 (2017).
- ¹⁰⁸S. Sharma et al., "Linear and second-order optical response of III-V monolayer superlattices", *Physical Review B* **67**, 165332 (2003).
- ¹⁰⁹K. F. Mak and J. Shan, "Photonics and optoelectronics of 2D semiconductor transition metal dichalcogenides", *Nature Photonics* **10**, 216–226 (2016).
- ¹¹⁰D. Xiao et al., "Coupled spin and valley physics in monolayers of MoS₂ and other group-VI dichalcogenides", *Physical Review Letters* **108**, 1–5 (2012).
- ¹¹¹K. F. Mak and J. Shan, "Photonics and optoelectronics of 2D semiconductor transition metal dichalcogenides", *Nat. Photonics* **10**, 216–226 (2016).
- ¹¹²M. M. Ugeda et al., "Giant bandgap renormalization and excitonic effects in a monolayer transition metal dichalcogenide semiconductor", *Nature Materials* **13**, 1091–1095 (2014).
- ¹¹³H. S. Lee et al., "Identifying multiexcitons in MoS₂ monolayers at room temperature", *Physical Review B* **93**, 6 (2016).
- ¹¹⁴K. F. Mak et al., "Tightly bound trions in monolayer MoS₂.", *Nature materials* **12**, 207–11 (2013).

- ¹¹⁵J. S. Ross et al., "Electrical control of neutral and charged excitons in a monolayer semiconductor.", *Nat. Commun.* **4**, 1474 (2013).
- ¹¹⁶Y. Lin et al., "Dielectric screening of excitons and trions in single-layer MoS₂", *Nano Letters* **14**, 5569–5576 (2014).
- ¹¹⁷J. L. Verble and T. J. Wieting, "Lattice Mode Degeneracy in MoS₂ and Other Layer Compounds", *Physical Review Letters* **25**, 362–365 (1970).
- ¹¹⁸J. Verble et al., "Rigid-layer lattice vibrations and van der waals bonding in hexagonal MoS₂", *Solid State Communications* **11**, 941–944 (1972).
- ¹¹⁹G. Lucovsky et al., "Infrared-Reflectance Spectra of Layered Group-IV and Group-VI Transition-Metal Dichalcogenides", *Physical Review B* **7**, 3859–3870 (1973).
- ¹²⁰T. Sekine et al., "Dispersive Raman Mode of Layered Compound 2H-MoS₂ under the Resonant Condition", *Journal of the Physical Society of Japan* **53**, 811–818 (1984).
- ¹²¹Z. Wang et al., "Brillouin scattering study of low-frequency bulk acoustic phonons in multilayer graphene", *Carbon* **46**, 2133–2136 (2008).
- ¹²²R. T. Harley and P. A. Fleury, "Surface Brillouin scattering from layered metals and semimetals", *Journal of Physics C: Solid State Physics* **12**, L863–L868 (1979).
- ¹²³K. Akintola et al., "Raman and Brillouin scattering studies of bulk 2H-WSe₂", *Journal of Physics: Condensed Matter* **27**, 395401 (2015).
- ¹²⁴S. Ge et al., "Coherent Longitudinal Acoustic Phonon Approaching THz Frequency in Multilayer Molybdenum Disulphide", *Scientific Reports* **4**, 5722 (2015).
- ¹²⁵W. Wu et al., "Piezoelectricity of single-atomic-layer MoS₂ for energy conversion and piezotronics", *Nature* **514**, 470–474 (2014).
- ¹²⁶H. Zhu et al., "Observation of piezoelectricity in free-standing monolayer MoS₂", *Nature Nanotechnology* **10**, 151–155 (2015).
- ¹²⁷S. Bhattacharyya and A. K. Singh, "Semiconductor-metal transition in semiconducting bilayer sheets of transition-metal dichalcogenides", *Physical Review B* **86**, 075454 (2012).
- ¹²⁸A. P. Nayak et al., "Pressure-induced semiconducting to metallic transition in multilayered molybdenum disulphide", *Nature Communications* **5**, 1–9 (2014).
- ¹²⁹T.-R. Chang et al., "Prediction of an arc-tunable Weyl Fermion metallic state in Mo_xW_{1-x}Te₂", *Nature Communications* **7**, 10639 (2016).
- ¹³⁰J. T. Ye et al., "Superconducting Dome in a Gate-Tuned Band Insulator", *Science* **338**, 1193–1196 (2012).
- ¹³¹J. N. Coleman et al., "Two-Dimensional Nanosheets Produced by Liquid Exfoliation of Layered Materials", *Science* **331**, 568–571 (2011).
- ¹³²V. Nicolosi et al., "Liquid Exfoliation of Layered Materials", *Science* **340**, 1226419–1226419 (2013).
- ¹³³N. Liu et al., "Large-Area Atomically Thin MoS₂ Nanosheets Prepared Using Electrochemical Exfoliation", *ACS Nano* **8**, 6902–6910 (2014).
- ¹³⁴Q. Ji et al., "Chemical vapour deposition of group-VIB metal dichalcogenide monolayers: engineered substrates from amorphous to single crystalline", *Chemical Society Reviews* **44**, 2587–2602 (2015).

- ¹³⁵Y. Shi et al., "Recent advances in controlled synthesis of two-dimensional transition metal dichalcogenides via vapour deposition techniques", *Chemical Society Reviews* **44**, 2744–2756 (2015).
- ¹³⁶M. Yi and Z. Shen, "A review on mechanical exfoliation for the scalable production of graphene", *Journal of Materials Chemistry A* **3**, 11700–11715 (2015).
- ¹³⁷J. Shi et al., "3R MoS₂ with Broken Inversion Symmetry: A Promising Ultrathin Nonlinear Optical Device", *Advanced Materials* **29**, 1701486 (2017).
- ¹³⁸P. E. Powers, *Fundamentals of Nonlinear Optics* (2011).
- ¹³⁹N. Kumar et al., "Second harmonic microscopy of monolayer MoS₂", *Physical Review B - Condensed Matter and Materials Physics* **87**, 1–6 (2013).
- ¹⁴⁰D. Li et al., "Multimodal Nonlinear Optical Imaging of MoS₂ and MoS₂ -Based van der Waals Heterostructures", *ACS Nano* **10**, 3766–3775 (2016).
- ¹⁴¹H. Chen et al., "Enhanced second-harmonic generation from two-dimensional MoSe₂ on a silicon waveguide", *Light: Science & Applications* **6**, e17060 (2017).
- ¹⁴²G. A. Wagoner et al., "Second-harmonic generation in molybdenum disulfide", *Journal of the Optical Society of America B* **15**, 1017 (1998).
- ¹⁴³K. L. Seyler et al., "Electrical control of second-harmonic generation in a WSe₂ monolayer transistor", *Nat. Nanotechnol.* **10**, 407–411 (2015).
- ¹⁴⁴H. Zhang et al., "Measuring the Refractive Index of Highly Crystalline Monolayer MoS₂ with High Confidence", *Scientific Reports* **5**, 8440 (2015).
- ¹⁴⁵H. Chen et al., "Enhanced second-harmonic generation from two-dimensional MoSe₂ on a silicon waveguide", *Light: Science & Applications* **6**, e17060 (2017).
- ¹⁴⁶D. Liang et al., "Hybrid Integrated Platforms for Silicon Photonics", *Materials* **3**, 1782–1802 (2010).
- ¹⁴⁷M. Lafrentz et al., "Second-harmonic generation spectroscopy of excitons in ZnO", *Physical Review B* **88**, 235207 (2013).
- ¹⁴⁸K. F. Lee et al., "Photon-Pair Generation with a 100 nm Thick Carbon Nanotube Film", *Advanced Materials* **29**, 1605978 (2017).
- ¹⁴⁹K. He et al., "Tightly Bound Excitons in Monolayer WSe₂", *Physical Review Letters* **113**, 026803 (2014).
- ¹⁵⁰L. G. Helt and M. J. Steel, "Effect of scattering loss on connections between classical and quantum processes in second-order nonlinear waveguides", *Optics letters* **40**, 1460–1463 (2015).
- ¹⁵¹S. M. Eichfeld et al., "Rapid, non-destructive evaluation of ultrathin WSe₂ using spectroscopic ellipsometry", *APL Materials* **2**, 092508 (2014).
- ¹⁵²M. Liscidini and J. E. Sipe, "Stimulated emission tomography", *Physical Review Letters* **111**, 1–5 (2013).
- ¹⁵³A. Eckstein et al., "High-resolution spectral characterization of two photon states via classical measurements", *Laser & Photonics Reviews* **80**, 76–80 (2014).
- ¹⁵⁴B. Fang et al., "Fast and highly resolved capture of the joint spectral density of photon pairs", *Optica* **1**, 281 (2014).
- ¹⁵⁵I. Jizan et al., "Bi-photon spectral correlation measurements from a silicon nanowire in the quantum and classical regimes", *Scientific Reports* **5**, 12557 (2015).

- ¹⁵⁶D. Grassani et al., "Energy correlations of photon pairs generated by a silicon microring resonator probed by Stimulated Four Wave Mixing", *Scientific Reports*, 8–13 (2016).
- ¹⁵⁷L. A. Rozema et al., "Characterizing an entangled-photon source with classical detectors and measurements", *Optica* **2**, 430–433 (2015).
- ¹⁵⁸L. Zhang et al., "Heralded generation of single photons in pure quantum states", *Journal of Modern Optics* **59**, 1525–1537 (2012).
- ¹⁵⁹P. Mosley et al., "Generation of pure state single photon wavepackets", in Efec '05. european quantum electronics conference, 2005. (2006), pp. 268–268.
- ¹⁶⁰H. Haus, "Mode-locking of lasers", *IEEE Journal of Selected Topics in Quantum Electronics* **6**, 1173–1185 (2000).
- ¹⁶¹S. T. Cundiff and J. Ye, "Colloquium : Femtosecond optical frequency combs", *Reviews of Modern Physics* **75**, 325–342 (2003).
- ¹⁶²T. Edition, *Handbook of Biological and Confocal Microscopy* () .
- ¹⁶³E. Hecht, *Optics* (2002).
- ¹⁶⁴Princeton Intruments, *NIRVANA 640 Specs*, tech. rep. (Princeton Intruments, 2016), pp. 1–8.
- ¹⁶⁵M. D. Eisaman et al., "Invited Review Article: Single-photon sources and detectors", *Review of Scientific Instruments* **82**, 071101 (2011).
- ¹⁶⁶N. V. Wheeler et al., "Low-loss Kagome hollow-core fibers operating from the near- to the mid-IR", *Optics Letters* **42**, 2571 (2017).
- ¹⁶⁷S.-j. Im et al., "Guiding properties and dispersion control of kagome lattice hollow-core photonic crystal fibers", *Optics Express* **17**, 13050 (2009).
- ¹⁶⁸K. A. Fischer et al., "Dynamical modeling of pulsed two-photon interference", *New Journal of Physics* **18**, 113053 (2016).
- ¹⁶⁹M. Beck, "With Different Coincidence Detection Techniques", **24**, 2972–2978 (2007).
- ¹⁷⁰H.-A. Bachor and T. C. Ralph, "A Guide to Experiments in Quantum Optics", *WileyVCH* **64**, 434 (2004).
- ¹⁷¹J. J. Thorn et al., "Observing the quantum behavior of light in an undergraduate laboratory", *Am. J. Phys.* **72**, 1210 (2004).
- ¹⁷²M. Born and E. Wolf, *Principles of Optics*, 7th ed. (1999).
- ¹⁷³S. Inoué, "Foundations of confocal scanned imaging in light microscopy", in *Handbook of biological confocal microscopy* (2006), pp. 1–19.
- ¹⁷⁴L. Novotny and B. Hecht, *Principles of Nanophotonics* (2006).
- ¹⁷⁵T. Wilson, "Confocal microscopy", Academic Press: London, etc **426**, 1–64 (1990).
- ¹⁷⁶R. H. Webb, "Confocal optical microscopy", *Reports on Progress in Physics* **59**, 427 (1996).
- ¹⁷⁷B. E. A. Saleh et al., *Fundamentals of photonics*, Vol. 22 (1991).
- ¹⁷⁸L. Marini et al., "Constraints on downconversion in atomically thick films", *Journal of the Optical Society of America B* **35**, 672 (2018).
- ¹⁷⁹T. Niehörster et al., "Multi-target spectrally resolved fluorescence lifetime imaging microscopy.", *Nat. Methods* **13**, 257–262 (2016).

- ¹⁸⁰G. Gariepy et al., "Single-photon sensitive light-in-fight imaging", *Nature Communications* **6**, 6021 (2015).
- ¹⁸¹A. McCarthy et al., "Kilometer-range depth imaging at 1,550 nm wavelength using an InGaAs/InP single-photon avalanche diode detector.", *Optics express* **21**, 22098–113 (2013).
- ¹⁸²R. H. Hadfield, "Single-photon detectors for optical quantum information applications", *Nat. Photonics* **3**, 696 (2009).
- ¹⁸³G. Ulu et al., "Influence of hot-carrier luminescence from avalanche photodiodes on time-correlated photon detection.", *Opt. Lett.* **25**, 758–760 (2000).
- ¹⁸⁴M. a. Albota et al., "Three-Dimensional Imaging Laser Radars with Geiger-Mode Avalanche Photodiode Arrays", *Lincoln Lab. J.* **13**, 351–370 (2002).
- ¹⁸⁵C. Kurtsiefer et al., "The breakdown flash of Silicon Avalanche Photodiodes - backdoor for eavesdropper attacks?", *J. Mod. Opt.* **48**, 2039–2047 (2001).
- ¹⁸⁶I. Rech et al., "A New Approach to Optical Crosstalk Modeling in Single-Photon Avalanche Diodes", *Photonics Technology Letters, IEEE* **20**, 330–332 (2008).
- ¹⁸⁷N. Calandri et al., "Optical crosstalk in InGaAs/InP SPAD array: analysis and reduction with FIB-etched trenches", *IEEE Photonics Technol. Lett.* **28**, 1 (2016).
- ¹⁸⁸A. Meda et al., "Backflash light characterization to prevent QKD zero-error hacking", arXiv:1605.05562v1, 1–6 (2016).
- ¹⁸⁹H. Dautet et al., "Photon-counting techniques with silicon avalanche photodiodes", *Appl. Opt.* **32**, 3894–3900 (1993).
- ¹⁹⁰ID Quantique Single Photon Avalanche Photodiodes, *ID230*.
- ¹⁹¹S. Cova et al., "Avalanche photodiodes and quenching circuits for single-photon detection.", *Applied optics* **35**, 1956–1976 (1996).
- ¹⁹²B. Korzh et al., "Free-running InGaAs single photon detector at telecom wavelengths with 1 cps dark count rate", *081108*, 1–4 (2013).
- ¹⁹³L. Marini et al., "Deterministic filtering of breakdown flashing at telecom wavelengths", *Applied Physics Letters* **111**, 213501 (2017).
- ¹⁹⁴G. Wang et al., "Exciton dynamics in WSe₂ bilayers", *Applied Physics Letters* **105**, 182105 (2014).
- ¹⁹⁵G. Marino et al., "Sum-Frequency Generation and Photon-Pair Creation in Al-GaAs Nano-Scale Resonators", in *Conference on lasers and electro-optics*, Vol. 2, V (2017), FTu4D.2.
- ¹⁹⁶R. Trebino et al., "Measuring ultrashort laser pulses in the time-frequency domain using frequency-resolved optical gating", *Review of Scientific Instruments* **68**, 3277–3295 (1997).
- ¹⁹⁷Rick Trebino, *Frequency-Resolved Optical Gating: The Measurement of Ultrashort Laser Pulses* () .
- ¹⁹⁸I. Amat-Roldan et al., "Ultrashort pulse characterisation with SHG collinear-FROG", *Optics Express* **12**, 1169 (2004).
- ¹⁹⁹L. Caspani et al., "Integrated sources of photon quantum states based on nonlinear optics", *Light: Science & Applications* **6**, e17100 (2017).

- ²⁰⁰X.-l. Wang et al., "Experimental Ten-Photon Entanglement", *Physical Review Letters* **117**, 210502 (2016).
- ²⁰¹L.-K. Chen et al., "Observation of ten-photon entanglement using thin BiB₃O₆ crystals", *Optica* **4** (2017) 10.1364/OPTICA.4.000077.
- ²⁰²K. P. Dhakal et al., "Confocal absorption spectral imaging of MoS₂: optical transitions depending on the atomic thickness of intrinsic and chemically doped MoS₂", *Nanoscale* **6**, 13028–13035 (2014).
- ²⁰³K. F. Mak et al., "Atomically Thin MoS₂: A New Direct-Gap Semiconductor", *Physical Review Letters* **105**, 136805 (2010).
- ²⁰⁴J. K. Ellis et al., "The indirect to direct band gap transition in multilayered MoS₂ as predicted by screened hybrid density functional theory", *Applied Physics Letters* **99**, 261908 (2011).
- ²⁰⁵R. Suzuki et al., "Valley-dependent spin polarization in bulk MoS₂ with broken inversion symmetry", *Nature Nanotechnology* **9**, 611–617 (2014).
- ²⁰⁶O. Kuzucu et al., "Joint Temporal Density Measurements for Two-Photon State Characterization", *Physical Review Letters* **101**, 153602 (2008).
- ²⁰⁷M. Weismann and N. C. Panoiu, "Theoretical and computational analysis of second- and third-harmonic generation in periodically patterned graphene and transition-metal dichalcogenide monolayers", *Physical Review B - Condensed Matter and Materials Physics* **94** (2016) 10.1103/PhysRevB.94.035435.
- ²⁰⁸X. Liu et al., "Molecular Structures and Second-Order Nonlinear Optical Properties of Ionic Organic Crystal Materials", *Crystals* **6**, 158 (2016).
- ²⁰⁹C. C. Stoumpos et al., "Hybrid germanium iodide perovskite semiconductors: Active lone pairs, structural distortions, direct and indirect energy gaps, and strong nonlinear optical properties", *J. Am. Chem. Soc.* **137**, 6804–6819 (2015).
- ²¹⁰R. C. Eckardt and R. L. Byer, "<title>Measurement of nonlinear optical coefficients by phase-matched harmonic generation</title>", in *Spie*, Vol. 1561 (1991), pp. 119–127.
- ²¹¹X.-L. Chu et al., "Experimental realization of an optical antenna designed for collecting 99% of photons from a quantum emitter", *Optica* **1**, 203 (2014).

Glossary

MoS₂ molybdenum disulfide. 4, 7, 10, 15, 16, 25, 26, 27, 29, 30, 31, 32, 35, 78, 102, 106, 107, 108, 109, 110, 111, 112, 114, 117, 118, 119

WSe₂ tungsten diselenide. 4, 6, 10, 15, 16, 25, 27, 29, 30, 31, 32, 34, 36, 37, 78, 97, 98, 99, 100, 101, 103, 104, 105, 106, 108, 111, 114, 117, 118, 119

AFM atomic-force microscope. 27

AWG array waveguide grating. 46, 111, 112

BFP back-focal plane. 50, 64, 65

BPF band-pass filter. 70, 71

CAR coincidences over accidental ratio. 6, 7, 10, 55, 62, 64, 69, 77, 78, 84, 85, 86, 87, 88, 89, 90, 91, 94, 95, 102, 104, 106, 111, 114, 117

CCD charge-coupled device. 39, 94

CLSM confocal laser-scanning microscope. 56, 71, 72, 73, 75

CLSM confocal laser-scanning microscopy. 74

CVD chemical-vapor deposition. 27, 106

DFG difference-frequency generation. 13

DFT density functional theory. 99, 106

FROG frequency-resolved optical gating. 6, 39, 43, 78

FWHM full-width at half-maximum. 45

FWM four-wave mixing. 40

HBT Hanbury-Brown and Twiss. 6, 9, 85, 86, 97, 103, 109, 112

HOM Hong-Ou-Mandel. 61

LPF long-pass filter. 70

MMF multi-mode fiber. 54, 55, 56, 61, 62, 72, 73, 75, 76

NA numerical aperture. 44, 63, 65, 66, 70, 72, 74, 107, 109, 112

NDF neutral-density filter. 71

OPO optical parametric oscillator. 107

pdf probability density function. 71, 88, 89, 91

PSF point spread function. 61, 62, 74, 76

QIP quantum information processing. 19

RTT round-trip time. 43

SFG sum-frequency generation. 13, 19, 40

SFWM spontaneous four-wave mixing. vii, 21, 22, 33, 69, 88

SHG second-harmonic generation. vii, 4, 6, 7, 9, 10, 12, 13, 15, 16, 29, 30, 34, 36, 37, 41, 43, 78, 95, 96, 97, 106, 107, 109, 119

SMF single-mode fiber. 61, 75, 76

SNR signal to noise ratio. 10, 50, 55, 56, 58, 59, 69, 71

SPAD single-photon avalanche photodiode. 6, 7, 39, 54, 55, 60, 61, 62, 67, 68, 69, 73, 75, 77, 85, 87, 90, 91, 94, 103, 110, 109, 112, 115, 117, 118, 119

SPD single-photon detector. 89

SPDC spontaneous parametric downconversion. vii, 3, 4, 5, 6, 7, 9, 10, 12, 16, 20, 21, 22, 25, 31, 33, 35, 36, 46, 55, 68, 69, 70, 71, 77, 78, 85, 86, 87, 91, 94, 95, 97, 103, 105, 106, 108, 110, 113, 114, 117, 118, 119

SPTCS single-photon time-correlated spectrometer. 56, 57

THG third-harmonic generation. 43

TIA time-interval analyzer. 54, 55, 56, 67, 68, 69, 70, 73, 87, 103, 104, 110, 113

TMDC transition-metal dichalcogenide. vii, 4, 6, 7, 9, 10, 15, 16, 25, 26, 27, 29, 31, 32, 36, 71, 77, 85, 90, 99, 104, 106, 114, 117, 119

TPE two-photon emission. 88

TTL transistor-transistor logic. 70

van der Waals van der Waals. 25, 27